Modelocking of THz quantum cascade lasers : dispersion control and non-linearities

Valentino Pistore

To cite this version:

Valentino Pistore. Modelocking of THz quantum cascade lasers : dispersion control and non-linearities. Condensed Matter [cond-mat]. Sorbonne Université, 2019. English. NNT : 2019SORUS302 . tel-03141220

HAL Id: tel-03141220
https://theses.hal.science/tel-03141220

Submitted on 15 Feb 2021

Sorbonne Université

Ecole doctorale 397

LPENS / Equipe Nano-THz

Modelocking of THz quantum cascade lasers: dispersion control and non-linearities

Par **Valentino Pistore**

Thèse de doctorat de Physique de la Matière Condensée

Dirigée par Sukhdeep S. Dhillon

Présentée et soutenue publiquement le 28 Novembre 2019

Devant un jury composé de :

M. Riccardo DEGLI INNOCENTI	Rapporteur
M. Gaël MOURET	Rapporteur
M. Alberto BRAMATI	Examinateur
M. Benoît DARQUIÉ	Examinateur
Mme. Pascale ROY	Examinateur
M. Jérôme TIGNON	Membre invité
M. Sukhdeep DHILLON	Directeur de thèse

Table of contents

Introduction

Mode-locking is a technique for the generation of short light pulses from a laser source. This technology has permitted numerous applications of ultrashort and intense pulses of light in many fields of science [1] [2] [3] and industry [4]. In the optical domain their use is well established (e.g. telecommunications [5]) with semiconductor-based platforms for ultrashort pulse generation in the near-infrared frequency range [6]. However, this is not the case in the terahertz (THz) range (0.5-10THz) [7] domain despite its proven applications in areas such metrology, imaging and non-destructive testing [8] [9]. Current technological solutions for the generation of ultrashort THz pulses such as ultrafast excitation of photoconductive switches [10] or nonlinear crystals [11] offer only low average powers (~μW), low frequency modulation and broadband emission with little control of the spectral bandwidth. As a result, their application and commercial diffusion is hindered by a lack of flexibility.

Since their first realization in 2002 [12], quantum cascade lasers (QCLs) operating in the THz range have proven to be one of the only compact high-power THz semiconductor sources with a controllable bandwidth. The latter can be entirely engineered from the design of the active region of the device. Therefore, QCLs have been considered a promising platform for the generation of intense and ultrashort THz pulses. Owing to their fast gain recovery time [13], however, passive modelocking of THz QCLs has so far proved to be difficult. On the contrary, active modelocking with a microwave modulation [14] has been successfully applied, leading to the generation of ~10-20ps pulses. The pulse duration, however, has been arduous to reduce below these values despite years of research [15] [16]. Only recently (2017), THz pulses as short as 4ps have been generated by our group with the application of an integrated structure (a Gires-Tournois Interferometre, (GTI)) aiming to reduce the chromatic dispersion of THz QCLs [17]. The research in this thesis starts from this point, the route taken to build on these state-of-the-art results, and new phenomena in the ultrafast operation of these devices.

In particular, I will present dispersion engineering in THz QCLs with on-chip geometries in order to prevent pulse stretching and to obtain very short pulses even from relatively narrow-band devices. This is achieved using proven active modulation methods that can tune the QCL emission from high to low dispersion regimes. I will also show that THz QCLs can present a strong amplitude modulation of their emission profile and that they can spontaneously emit pulses as a result of a self-locking mechanism, contrary to the expected frequency modulated response. As a consequence, this provides an indication that the fast gain recovery time is not necessarily a limiting factor for the generation of pulses. I will also show this passive self-locking scheme for passive pulse generation in the framework of the first demonstrations of harmonic modelocking of THz QCLs.

Finally, a new phenomenon in THz QCLs will be presented at the end of this thesis where the modes of a free running and modelocked THz QCL can beat together to generate free space microwave emission extending from tens to hundreds of gigahertz. This nonlinear down-conversion effect of THz emission into millimetric waves will potentially raise interest for low-noise microwave generation for telecommunication applications, as well as extending the operational range of THz QCL.

This thesis is divided in six chapters that are introduced below:

Chapter 1 – THz Quantum Cascade Lasers and Modelocking: The THz domain and a short overview of the history of QCLs, will be presented. Details are provided about the physics behind these devices and the types of band structures that can be designed with particular advantages and disadvantages. This is followed by a description of the waveguides and the post-processing steps. The basic concepts of mode-locking and the related field of frequency combs in THz QCLs, which are the two main subjects of the thesis, are then presented in the second part of the chapter.

Chapter 2 – THz Time Domain Spectroscopy (TDS) of Quantum Cascade Lasers: The main focus of this chapter will be the techniques and experimental setups that are used to detect the time resolved emission of THz QCLs. In detail, THz TDS systems are initially described with an emphasis on its THz generation and detection parts. The injection seeding technique is then explained as the preferential method to detect the temporal emission of QCLs in TDS systems. The various modelocking techniques are then analysed and the implementation of active modelocking for short pulse generation is detailed both in its principles and in its practical aspects.

Chapter 3 – Dispersion in THz QCLs: The chapter begins with a theoretical analysis of the sources of chromatic dispersion in THz QCLs. It continues with a description of the integrated dispersion compensation schemes which have been studied during this thesis. The concept of an external tunable scheme is then presented via the experiments performed by our collaborators at CNR NEST (Pisa, IT) and by electromagnetic simulations from our group. This will illustrate the improvements in the performances that the device shows when dispersion compensation is achieved. Finally, the effect of dispersion on THz QCLs operating in active modelocking conditions is studied by means of numerical simulations performed by our collaborators at Queensland University (AU).

Chapter 4 – Modelocking of THz QCLs - active and free running operation: The experimental results obtained from THz QCLs characterized by injection seeding will be presented. The first instance, where I participated at the beginning of my PhD, will consist in the successful application of an integrated dispersion compensation scheme – a THz Gires Tournois Interferomenter (GTI) – which led to the generation of 4ps pulses. This is followed by a detailed experimental study of the effect of the GTI length, and therefore the dispersion, on the emission spectrum of a modelocked THz QCL. Another effect, a spontaneous pulse generation phenomenon occurring in a free running QCL will be shown, and when combined with active modelocking condition leads to the generation of a 3.4ps pulse train. In the final section, an individual 1.3ps pulse is obtained by active modelocking on a broadband device, providing practical insights on the importance of spectral bandwidth and dispersion compensation.

Chapter 5 - Harmonic modelocking in THz QCLs: The onset of harmonic modelocking in THz QCLs is studied in the case of active modelocking and free running operation for the first time. In the first section it is shown that the active modelocking technique can be used at a harmonic of the fundamental round-trip frequency to force a QCL to emit multiple pulses per round-trip. In the second part of the chapter, the analysis of the free running emission of a range of devices reveals that THz QCLs can spontaneously operate in a harmonic state even without the need of an external modulation. A simple theoretical model, based on a synchronization condition of the THz waves with the GHz modulation derived from their beating, is used to explain this phenomenon.

Chapter 6 - Microwave generation in THz QCLs: The final chapter of the thesis describes a new operating regime for THz QCLs, where the beating of the THz modes can generate a free space RF signal up to a few hundred GHz, detected by the TDS setup. This in particular shows the strong second order nonlinearity and how the RF generated signal can be engineered by a suitable THz spectral profile.

1

Terahertz Quantum Cascade Lasers and Modelocking

Quantum cascade lasers (QCLs) are light sources whose emission is based on intersubband transitions in semiconductor quantum wells. They were first demonstrated in 1994 [18] over 20 years after their initial theoretical proposal, and since then their performances have been constantly improved and expanded. In 2002 the first QCL emitting in the terahertz range was produced [12] opening up the extension of laser applications to the far-infrared region where previously these were limited technologies. This is made possible by the unique way the light is amplified in these devices: electronic transitions take place between two engineered subband energy levels, as a result of quantum confinement of the electrons in a set of quantum wells. The wavelength of the emitted radiation can therefore be tailored by tuning the energy separation between the levels, i.e. by controlling the width of the quantum wells. This is in principle independent of the material system used, in contrast to conventional semiconductor lasers which are bound to the properties of their band structure and in particular their bandgap.

One of the most recent features of QCLs is their inherent capability of generating frequency combs via four wave mixing. A frequency comb is a laser spectrum consisting of a series of extremely evenly spaced frequency lines with a certain phase relation. This generally results in a time profile of the electric field that has a periodic behaviour. Frequency combs have revolutionised the fields of optical synthesis and metrology [19] and display an evergrowing range of applications such as optical and radio-frequency arbitrary waveform generation[20], molecular spectroscopy[21] and optical clocks [22].

Another important line of research in the QCL field and related to frequency combs is the generation of short pulses of light by (active) mode-locking [16], i.e. the condition for which the longitudinal modes of a laser have a fixed phase relationship and also results in a frequency comb. Indeed, the stabilization of a pulse train is a method to realize frequency comb operation [23] where the phase relation between each mode becomes fixed to the same value for all modes. Several mode-locking techniques exist [24] [25] that are widely used to generate ultra-short and intense pulses from lasers. Many applications have developed thanks to the improvements of mode-locked lasers and technology such as exotic nonlinear effects [26], high precision metrology [19] and fundamental physics studies.

For the main part, in the visible and near-infrared ranges, passive mode-locking [27] is extensively used to generate ultrashort pulses and it is typically realized by a saturable absorber element within the laser cavity. However, conventional passive mode-locking techniques are extremely difficult to apply to THz QCLs because of the ultrashort gain recovery time (about 5 to 20ps) [13] when compared to the cavity round-trip time of the laser (~100 ps for a few mm cavity). This extremely fast dynamic of the gain can be exploited, however, for active mode-locking. In this technique, the gain of the laser is modulated at the cavity round-trip frequency by a microwave electrical signal. This has demonstrated the generation of pulses from THz QCLs, although they have been relatively long (~10 to 20 ps) [16] [14] [28] [29].

The first part of this chapter is devoted to a brief introduction to quantum cascade lasers and to the THz range in general. Section **1.2** will detail the principles of cascaded inter-subband transitions which are the basis to understand the quantum cascade laser operation. The main types of active regions will also be discussed. Section **1.3** provides a description of the THz waveguides and their relevance to QCL operation. The second part of the chapter, from section **1.4,** aims to give an overview to modelocking in THz QCLs. More details about the principles of modelocking and frequency combs are then discussed in section **1.5**.

Chapter 1

1.1 The Terahertz range

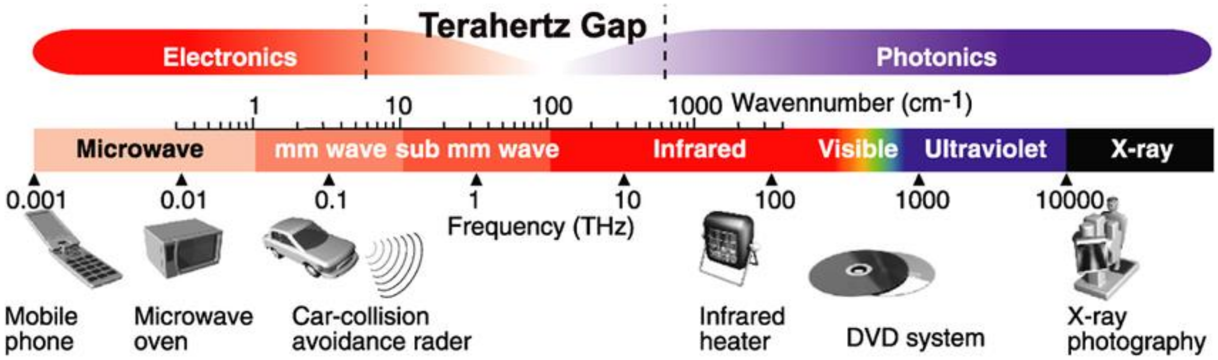

Figure 1.1: The electromagnetic spectrum with highlighted the electronic and photonic ranges separated by the THz gap. Applications from various parts of the spectrum are represented in the lower layer of the picture. Source: [3]

The unit of the frequency corresponding to 10^{12}Hz is known as Terahertz (THz), and when referred to photons it corresponds to a wavelength of 300μm and a single photon energy of ~4.1meV [7].

The Terahertz range is loosely defined as that part of the electromagnetic spectrum comprised in between 0.5THz and 10THz. It is sandwiched between the microwave and mid-infrared ranges for electronic and photonic methods, respectively, to generate directly electromagnetic radiation (see fig. 1.1). It has been called for many years the “THz gap” because of the lack of semiconductor based sources and detectors capable of working at these frequencies, rendering it the least developed region of the electromagnetic spectrum. In fact, electronic devices can directly generate frequencies up to some hundreds of GHz but performances suffer greatly beyond 1THz. At the same time, no material system currently exists that allows a natural band gap of a few THz to be used for a lasers emitting at THz frequencies. This happens in spite of the many unique properties of THz waves for applications (penetration into opaque materials for non-destructive imaging, strong gas absorption, etc.) as well as their suitability to study many fundamental effects with low energy phenomena (spin excitations, plasmons, superconductors etc).

The first quantum cascade laser (QCL) [18] was realized In 1994 at Bell Laboratory by *J. Faist* et al, over 20 years after the initial theoretical proposition. This unipolar semiconductor device showed emission in the mid-infrared (~4μm, 2340 cm-1). Its structure was based on inter-subband transitions in quantum wells [30] in contrast to inter-band transitions between conduction and valence bands that is a characteristic and a limitation of standard laser diodes [31], [32] as their emission wavelength depends on the material used for their fabrication. QCLs

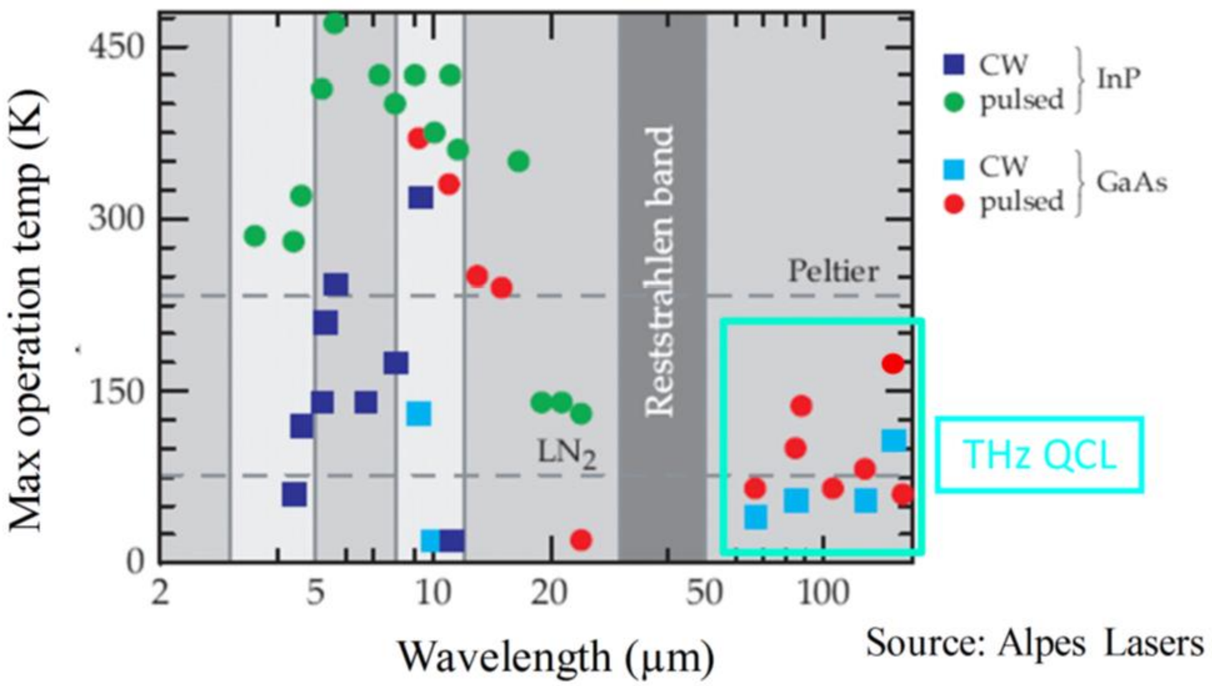

Figure 1.2: QCL maximum operating temperature as a function of the wavelength of the emitted radiation (2016). The THz range is situated at longer wavelengths than the Reststrahlen band and THz QCL performances are highlighted in the light blue area

emission frequencies and bandwidth can be instead easily engineered by tuning the width of the quantum wells rather than changing the semiconductor material system altogether. This simple fact was a breakthrough in semiconductor laser technology for the mid-infrared as it provided a simple and consistent way to overcome the ‘bandgap slavery’ limitation of the emission of diode lasers. Since their realization, MIR QCLs have been continuously improved achieving significant performances in many of their properties like frequency range [33], maximum operating temperature [34] [35] (fig. 1.2) and output power [36].

QCLs emitting in the THz range, i.e. THz QCLs, were first demonstrated by *Köhler* et al at Scuola Normale Superiore of Pisa in 2002 [12]. This was the first compact semiconductor laser source to emit at these frequencies and has proved to be breakthrough to potentially enable a plethora of different applications. This chapter will be henceforth dedicated to THz QCLs. The following sections will illustrate their working principle, the type of active region which can be fabricated, the most used waveguide geometries and their fabrication technologies.

1.2 Quantum cascade laser principles

1.2.1 Inter-subband transitions

Lasers exploit stimulated recombination processes to sustain their emission. In inter-band lasers these occur when an incoming photon interacts with an electron of the conduction band stimulating its transition to the valence band through the recombination with a hole. An additional photon, with the same energy and phase of the initial one, is emitted. As fig. 1.3a illustrates, the photon energy must be equal to the energy difference of the bottom of the conduction band to the top of the valence band, i.e. to the bandgap. Therefore, laser emission [31] is completely determined by the material system employed in the fabrication of the device. In this sense, the expression "bandgap slavery" has been used to underline this limitation inherently belonging to diode lasers.

Typical semiconductor materials present bandgaps ranging from about 0.3eV to a few eV. It is then possible to have diode lasers emitting from the mid-infrared to the ultraviolet by choosing an appropriate material system [32]. However, no semiconductor exists whose bandgap is as small as a few meV which is the energy range corresponding to THz radiation.

A suitable solution is that of using the intraband energy levels of quantum wells. The difference in energy between two levels (*subbands*, fig. 1.3b) in a quantum well of the conduction band can be as small as a few meV. Therefore, an electronic (*inter-subband*) transition from the upper to the lower state will emit a photon that can be designed to be in the THz range.

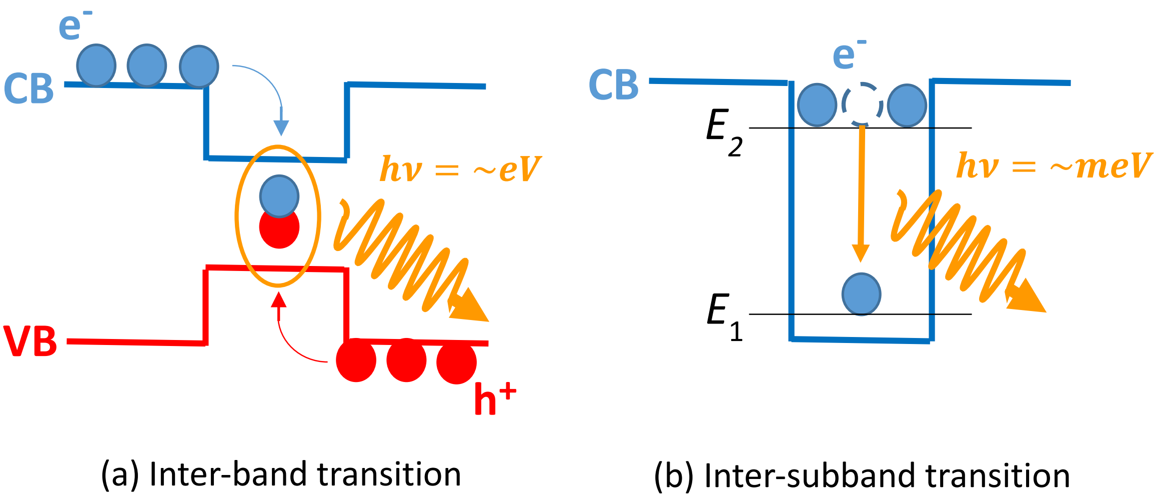

(a) Inter-band transition

(b) Inter-subband transition

Figure 1.3: Schematic of carrier transitions in semiconductor quantum wells. (a) Inter-band of an electron from the conduction band with a hole from the valence band. The emitted radiation has an energy on the order of a eV. (b) Inter-subband transition from the upper to the lower energy level of a quantum well in the conduction band. The emitted radiation has an energy in the order of ten meV (for THz).

From a quantitative point of view, one can write the eigen-energy of electrons in a quantum well whose smaller dimension is L and where the direction of the confinement is along the *z* axis as:

$$E_n = \frac{\hbar^2\pi^2 n^2}{2m^* L_z^2} \qquad (1)$$

where $\hbar$ is the reduced Planck constant, m^* (m^*=0.067m for GaAs) is the effective electron mass in the quantum well, *n* is the quantum number, $E_{z,n}$ is the eigen-energy of the *n*th order sub-band level and L_z is the quantum well thickness [37].

Therefore, for a transition from the energy level m+1 to the level m of the quantum well, the energy of the transition can be written as:

$$E_{\Delta m} = \frac{\hbar^2\pi^2(2m+1)}{2m^* L_z^2} \qquad (2)$$

It is then possible to tailor the energy difference in between the levels by tuning the size of the quantum well without the need of changing the constituent materials. For GaAs, about 10nm are generally sufficient to provide for the photons emitted from the aforementioned transitions to have a frequency in the THz range. These transitions are generally referred as “inter-sub-band transitions” and the simplicity of their design represents one of the greatest advantages over classical inter-band transitions.

The first THz QCL was fabricated according to these principles and successfully demonstrated in 2002. There are several THz QCL bandstructure designs and these will be discussed in the next sections.

1.2.2 Cascaded inter-subband transitions

As presented in the previous section, inter-subband transitions can be designed to correspond to THz frequency emission by choosing a suitable thickness of the quantum wells.

In order to observe laser action ; however, two conditions must be also satisfied:

1) the concentration of the electrons on the upper level has to be higher than that on the lower, i.e. the population inversion condition has to be realized;
2) the gain has to be sufficiently strong to overcome the losses.

The first condition needs to be considered carefully as there are many non-radiative scattering processes which result in extremely short carrier lifetimes of the upper subband (~10ps). Examples are optical phonon emission, electron-electron, ionized-impurity and interface scattering [38], [39]. These ultrafast dynamics are inherent to inter-subband transitions as the typical lifetimes for inter-band transitions are on the order of nanoseconds.

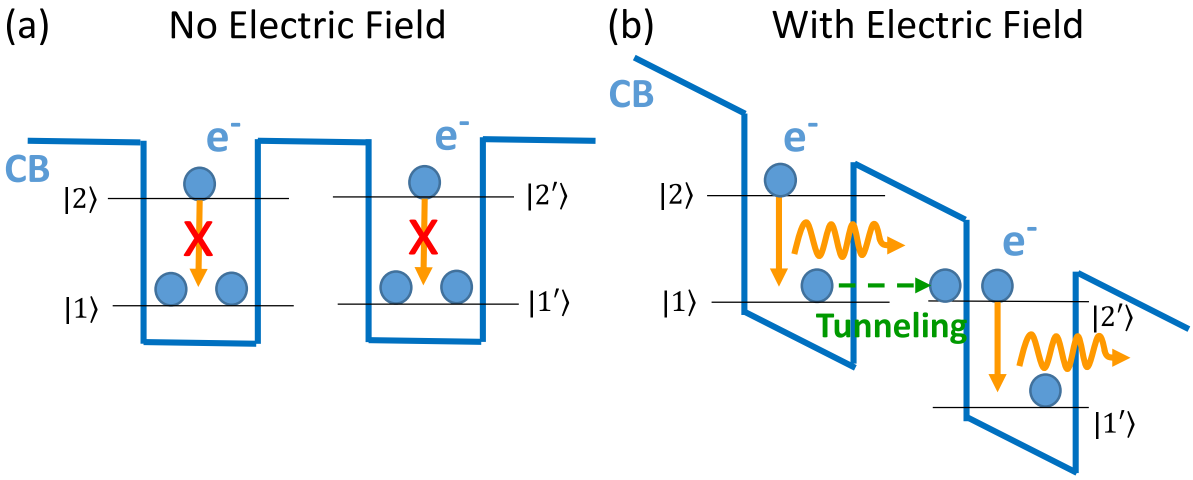

Figure 1.4: (a) Two quantum wells separated by a barrier in the absence of electric field. No carrier cascading is realized. (b) Two quantum wells in presence of an applied electric field. When the lower level of the first well is aligned to the upper level of the second well, electrons can tunnel through the barrier creating a cascade effect.

For a simple two levels system in a quantum well with the fundamental level $|1\rangle$ and upper level $|2\rangle$, one can achieve population inversion only if the lifetime τ_2 associated to the upper level is longer than the lifetime τ_1 of the fundamental one, i.e. $\tau_2 > \tau_1$. This is typically realized by using the non-radiative mechanisms to reduce the τ_1 lifetime, such as miniband scattering [40] and longitudinal optical (LO) phonon depopulation [41] that reduce τ_1 to the sub-picosecond scale. Further details will be provided during the description of the active regions.

The second condition can be met by coupling a set of quantum wells – a period – designed with a population inversion and then stacking ***N*** periods in a single active region (figure 1.4a). ***N*** is typically 100-200 for a THz QCL resulting in active region thicknesses > 10μm. In this way, the gain of a single period is multiplied by a factor ***N***, as well an ensuring a good overlap with the optical mode.

To electrically inject carriers into the upper laser level, a designed bias is applied across the quantum well structure. The permits to ‘tilt’ the potential of the quantum wells and to resonantly tunnel into the upper state, as well as allowing the alignment of the fundamental level of the first well $|1\rangle$ with the upper level of the second well $|2'\rangle$ (fig. 1.4b). Thus, for ***N*** quantum wells, ***N*** photons can be emitted, increasing the gain and permitting laser action.

The emitted photons will be tranverse magnetic (TM) polarized due to the inter-subband selection rules, having the electric field component parallel to the growth direction [42], [43]. This consideration is important for type of waveguides that are employed for the confinement of the THz mode in the active region. These will be discussed in section **1.3**

1.2.3 Active regions of quantum cascade lasers

All the THz QCLs analyzed in this thesis are based on the GaAs/AlGaAs (well/barrier) material system. In the following, the main active region types employed in THz QCLs are described. These are:

1) Bound-to-continuum (low threshold current, narrow spectral bandwidth)
2) LO-phonon depopulation (high threshold current, broad spectral bandwidth)
3) Hybrid LO-phonon and bound-to-continuum (intermediate characteristics)

Bound-to-continuum scheme

Fig 1.5 illustrate the band structure of a bound-to-continuum THz QCL centered at 2 THz under a bias of 1.5 kV/cm [44]. In this figure, 2 periods of the band structure are showed and each of them consists of typically 8 quantum wells (GaAs) and barriers (AlGaAs). The horizontal axis presents the position of the quantum wells and barriers along the direction of growth and the vertical axis the energy potential of the subbands. The various coloured curves represent the square of the electronic wavefunctions in the quantum wells and are obtained according to the Schrödinger equation. The laser transition occurs in the orange zones. The inter-subband energy gap there is about 9 meV corresponding to a frequency ~2.1 THz. After the emission, the electron is transported from the fundamental level to the mini-band (the light blue zones). These are used to transport the electrons between any two neighbouring periods. The light green zones are called injector wells and their purpose is to collect electrons from the bottom of the mini-bands and resonantly inject them onto the excited levels of the electronic transitions. The injector well has to be next to the quantum well where the excited level is localized so that the two wave functions overlap strongly to guarantee efficient resonant tunneling.

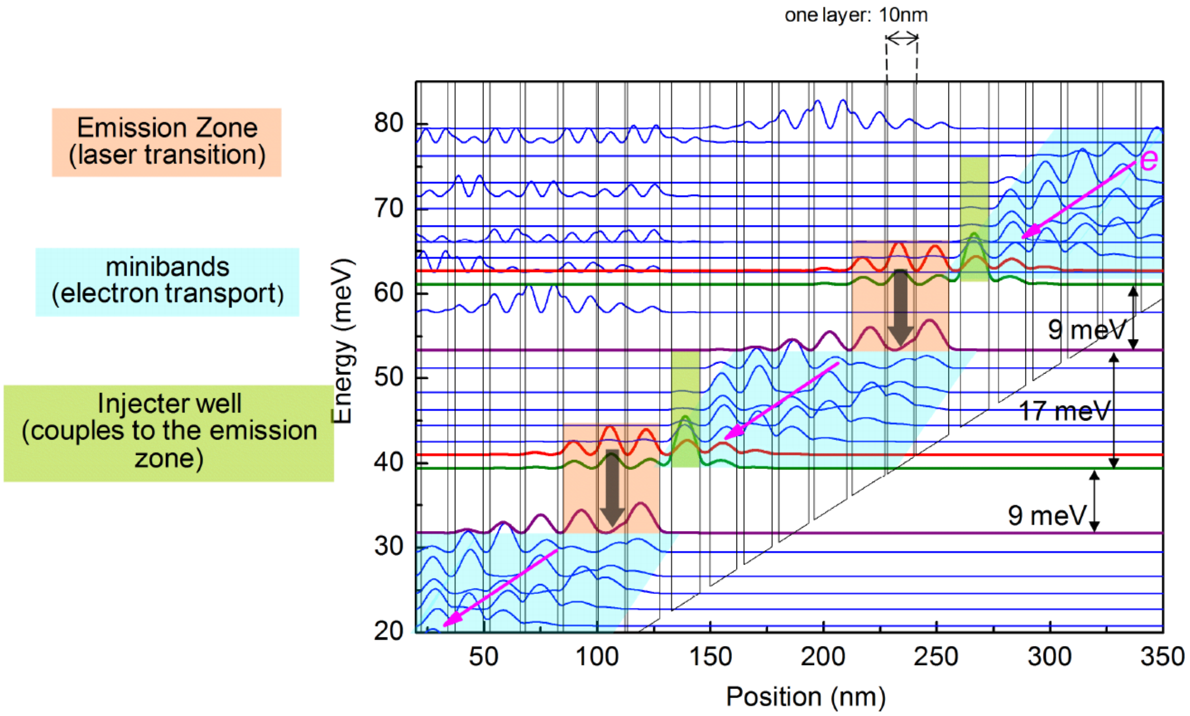

Figure 1.5: Band structure of a bound-to-continuum THz QCL. Laser transitions take place in the orange zones. The mini-bands are coloured in light blue. The injectors, which are the quantum wells that collect electrons from the mini-band and bring them to the excited levels, are represented in green.

The THz QCLs based on bound-to-continuum design allows for low operating voltages due to the small fields that it is necessary to apply to achieve the alignement of the levels. However, this design typically results in relatively low temperature operation and narrow gain bandwidth owing to the miniband depopulation of the lower state. This fact results in a relatively long lifetime while the narrow bandwidth of these structures limits their use for short pulse generation.

LO-phonon depopulation scheme

Compared to the previously discussed bound-to-continuum design, LO-phonon depopulation active regions typically consist of an injector well and a transition zone while also having less wells per period [45]. The example of the band structure of fig. 1.6 is designed for an emission frequency centered at 2.4 THz under a bias of 8 kV/cm. There are just 3 quantum wells per period. The green, the blue and the red wavefunctions represent the injector, the excited and the fundamental level of the laser transition respectively. The energy difference between the fundamental level of one period and the injector level of the following period is roughly 36 meV corresponding to the transition energy of a GaAs LO phonon. This choice results in a

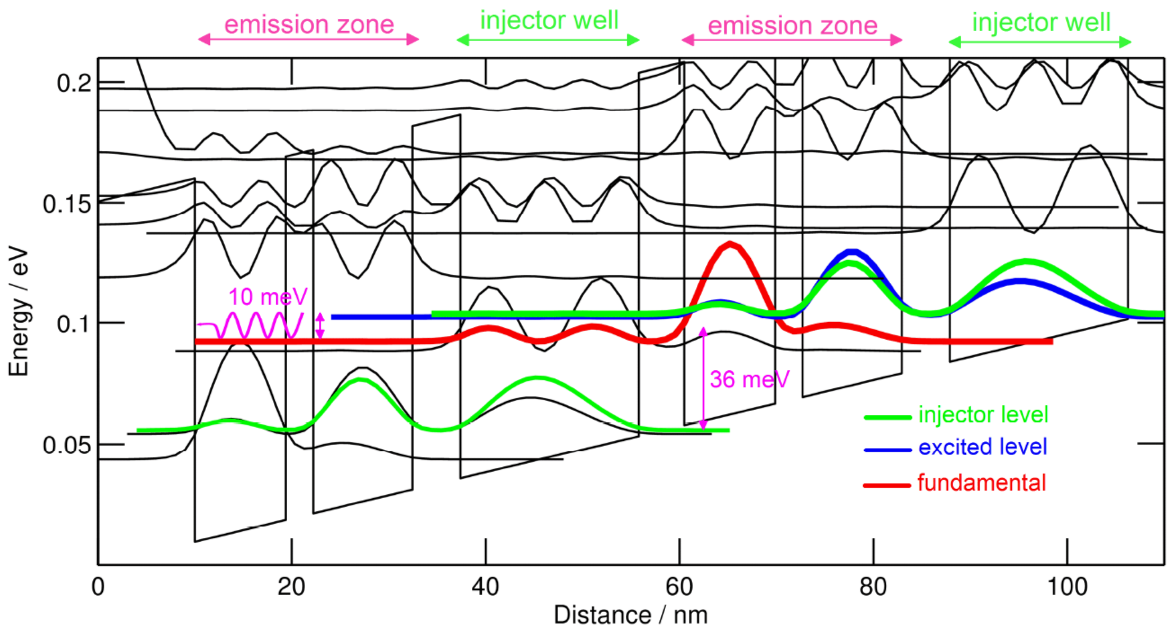

Figure 1.6: Band structure of a LO-phonon depopulation active region of a THz QCL. The emission zones are the wells where the laser transitions occur. The injector wells are those that collect the electrons from the fundamental level of the previous period and bring them to the excited level of the following period.

resonant depopulation of the lower laser state and a very short lifetime (~0.2 ps). Population inversion can therefore be ensured. In addition, such a short lifetime results in a broad spectral gain bandwidth, making these active regions ideal candidates for ultra-short THz pulse and also permits the highest temperature operation of a QCL (~210 K) [46]. The main drawback, however, is that the large applied field, as well as high currents, induces a large power dissipation, normally preventing high duty cycle and CW operation at high temperatures. This is also a disadvantage when it comes to active modelocking as it is difficult to strongly modulate the structure if the power requirements are large. This structure is used in parts of the current thesis.

Hybrid LO-phonon and bound-to-continuum scheme

An example of the band structure of this hybrid design, for an emission frequency centered at ~3.2 THz under a bias of 9 KV/cm, is presented in fig 1.7. As the name suggest, this scheme can be considered a combination of a bound-to-continuum and a LO-phonon structure [47]. As with the LO phonon design discussed above, the injector level (in green) collects the electrons from the fundamental level of the previous period by resonant tunneling and injects them into the excited level (in blue) of the following one. The laser transitions take place between the single excited band level (blue) and the fundamental continuum levels (in red). The fundamental

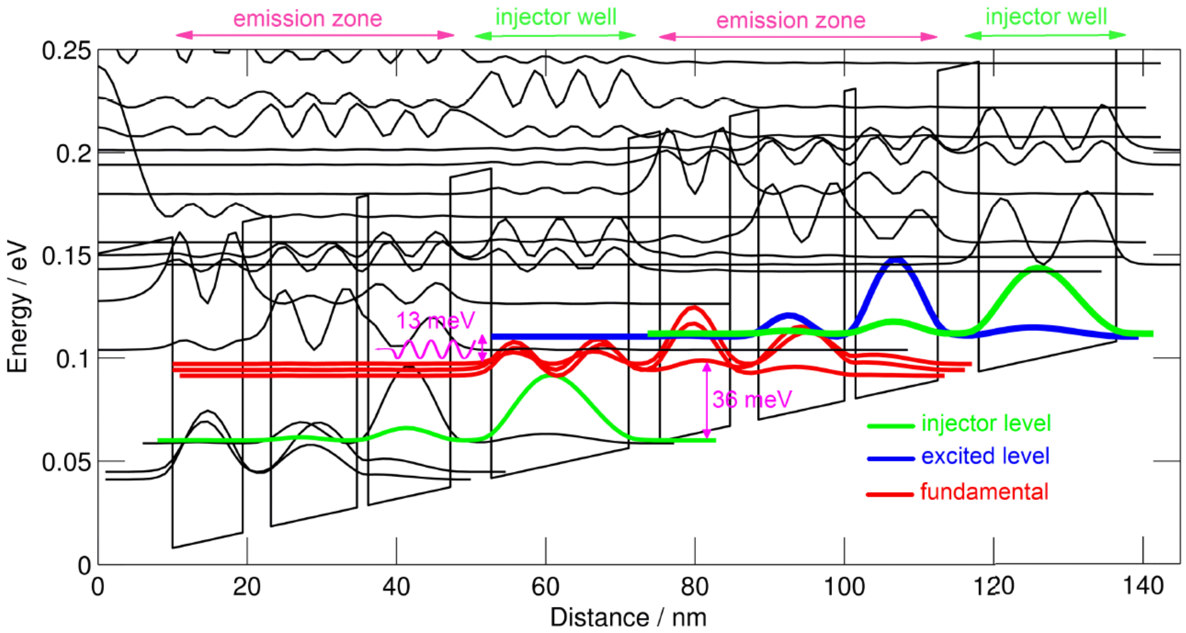

Figure 1.7: Band structure of a THz QCLs based on hybrid depopulation that combines LO phonon and bound-to-continuum schemes The emission zones are the wells where the laser transitions occur. The injector wells are those that collect the electrons from the fundamental level of the previous period and bring them to the excited level of the following period.

levels behave as a miniband transporting the electrons to the injector level of the next period where they are resonantly depopulated by LO phonon interaction. This hybrid depopulation scheme results in an electron lifetime of the fundamental level being slightly longer than that of pure LO phonon design. This fact directly results in a gain bandwidth that lies between the pure LO-phonon and bound-to-continuum active region designs. However, its advantage is that a stronger field than LO phonon based devices is required for operation. As a consequence, QCLs based on this design are easier to modulate with the current. Moreover, to compensate, multiple active regions centered at different frequencies can be stack on each other to increase the spectral gain bandwidth. Most of the devices presented in this thesis employ this type of active region that offers greater than 1THz spectral bandwidth with low electrical power requirements. As will be presented, this opens up the possibility of the ultra-short pulse generation and new phenomena in their ultrafast operation.

1.3 Technology

1.3.1 Waveguides for THz light confinement

Due to the very large wavelengths of THz radiation (~50µm in GaAs) compared to the size of the active regions (~10-15µm), conventional dielectric cladding for the confinement of light is impractical. This is because THz waves would require a large thickness of the dielectric layer to achieve a good confinement while their overlap to the active region would still be very poor. As discussed in the previous chapter, though, the photons generated by the inter-subband transitions are TM polarized. This fact can be exploited to design surface plasmon based waveguides that have distinctive properties for the THz photon confinement [12].

Two main kinds of waveguides are currently used in THz QCL technology with certain advantages/disadvantages:

1) Single-plasmon waveguides – Low modal confinement; directional beam; not suitable for microwave modulation
2) Double-metal waveguides – High confinement; highly diverging beam; simultaneous waveguide for microwave modulation

In this thesis, all the described QCLs are fabricated with the second type of waveguides. The reason is that double-metal structure are more adapted to carry the high-frequency electrical modulations necessary for mode-locking. The growth of the samples investigated originated from the University of Leeds, UK, except for wafer ‘ART2758’ from Thales Research and Technology, France.

Single-plasmon waveguides

In single-plasmon QCLs, the active region is put in between a metallic top layer (typically Ti/Au of 10nm/200nm thicknesses) and two doped layers at the top and bottom (~700nm thick), as shown in fig. 1.8b. The combination of the top metal layer and the bottom doped layer can a surface plasmon mode that provides the confinement of the TM polarized THz emission in the laser cavity. The generated single-plasmon mode is illustrated in the inset of fig 1.8b as calculated by COMSOL Multiphysics. It loosely confines the THz mode to the laser cavity, with the majority of the optical mode penetrating into the GaAs substrate (the bottom thick light-grey layer in the figure).

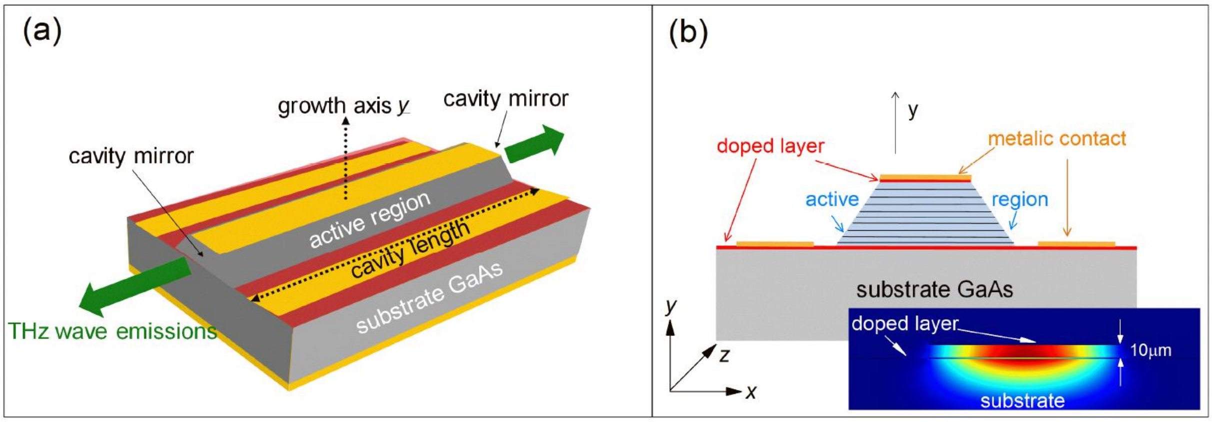

Figure 1.8: (a) Schematic as a 45° view of single-plasmon THz QCL (b) Cross section of a single-plasmon QCL. Inset: THz electric field intensity distribution in the cross section of a single-plasmon waveguide.

The confinement factor Γ is used to describe the modal overlap to the active region and can be defined [39] as:

$$\Gamma = \frac{\int_{active} dx\, dy\, E^2(x,y)}{\int_{x,y=\infty} dx\, dy\, E^2(x,y)} \tag{3}$$

where x, y are respectively the horizontal and vertical direction of QCL's cross-section as shown in fig 1.8 and E is the electric field. For a single-plasmon QCL, the confinement factor typically lies between 0.1 – 0.5 [48].

The losses in the system are normally due to the mirror and waveguide, α_m and α_w respectively. The gain required for lasing action in a QCL is then defined as [49]:

$$g_{th} = \frac{\alpha_m + \alpha_w}{\Gamma} \tag{4}$$

One can see that the lower the confinement, the higher the gain has to be to reach the threshold typically meaning higher current thresholds and, as a consequence, the maximum operating temperature decreases.

Moreover, it is also necessary to mention that the ridge width of a single-plasmon QCLs has to be generally large (more than 150 μm). In fact, if it is too narrow, the THz mode will be pushed further into the substrate and be less confined to the active regime, further increasing the threshold current.

However, there are also some advantages related to the low confinement of single-plasmon waveguides: for example, it permits an easy out-coupling of the power which in turn allows the QCL to be easily applied to applications such as spectroscopy or imaging [53]. It also favours high coupling efficiencies of external radiation and especially the injection of THz waves into the QCL's cavity. This last point is quite important for time resolved coherent detection (see chapter **2**).

Double-metal waveguides

Double metal waveguides, also known as metal-metal (MM) waveguides, differ from the previously described single-plasmon structures, for having the active region directly sandwiched between two metallic layers [44]. This design usually employs top gold layers with a thickness of about 300µm and bottom gold layers of 600µm. As the active region is sandwiched between two metal layers, the THz mode is confined in the active region and the confinement factor is close to 1, as the inset of fig 1.9b illustrates by showing the electric field intensity distribution of the THz radiation in the double-metal cavity.

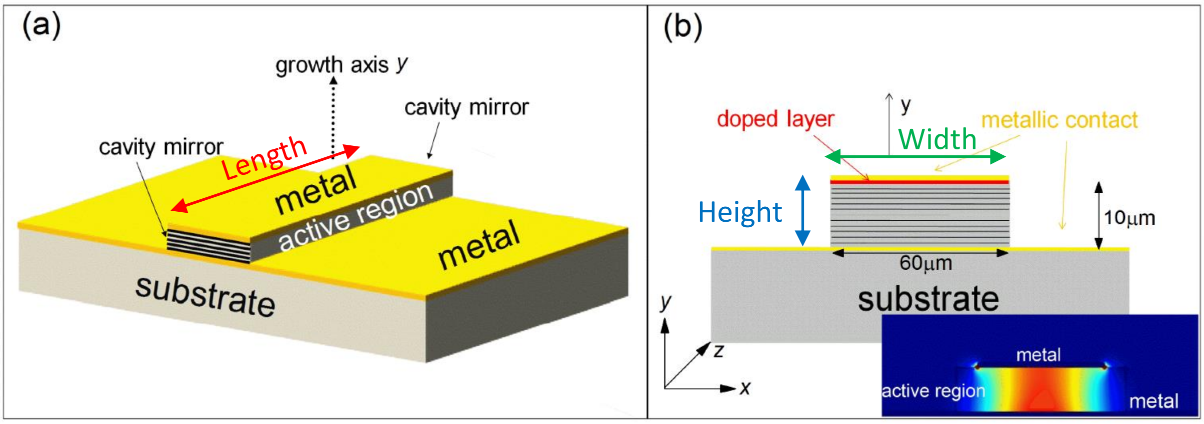

Figure 1.9: (a) Schematic of a double-metal THz QCL as a 45° view (b) Cross section of the double-metal waveguide QCL. The red, blue and green arrows report the dimensions of a QCL cavity as they will be used to describe the samples. Inset: THz electric field intensity distribution in the cross section of a double-metal waveguide.

Since the confinement is so large, the threshold is typically lower than that of the single-plasmon QCLs and this feature has allowed for the highest temperature operation up of QCLs, up to 210 K [46]. The ridge width of THz QCLs based on MM waveguide can be much narrower (< 40 µm) than that of single-plasmon QCLs owing to the strong confinement. However, a consequence of the strongly confined modes is the huge impedance mismatch with free space radiated modes. This leads to highly diffracted far-field patterns, poorly out-coupled powers and low injection coupling efficiencies. These are all aspects that must be considered from the experimental point of view as well as that of the applications.

One last advantage that is worthy to be highlighted is that these waveguides are more suitable to carry high frequency electronic modulations than their single-plasmon counterpart since they are essentially GHz (strip) waveguides. For this reason, double-metal THz QCLs are the only kind of device that are presented in this thesis. More details can be found in following sections and in chapter 2 where active modelocking will be discussed.

Finally, side-absorbers are usually employed in double-metal QCLs to avoid lasing at higher orders lateral modes which significantly reduces the output power of the device [50]. These consist in strips of highly doped GaAs layers that are left exposed along the waveguide edges by a top-metalization set-back. Their effect is that of increasing the losses of the lateral modes and so increasing their threshold gain. Recently, further studies on this topic have revealed that the addition of a thin (a few nm) metallic layer on top of the side-absorbers can increase the lateral modes losses to the point of effectively suppressing them entirely [51]. In this thesis, all of the characterized QCLs present side-absorbers as the descriptive tables at the beginning of

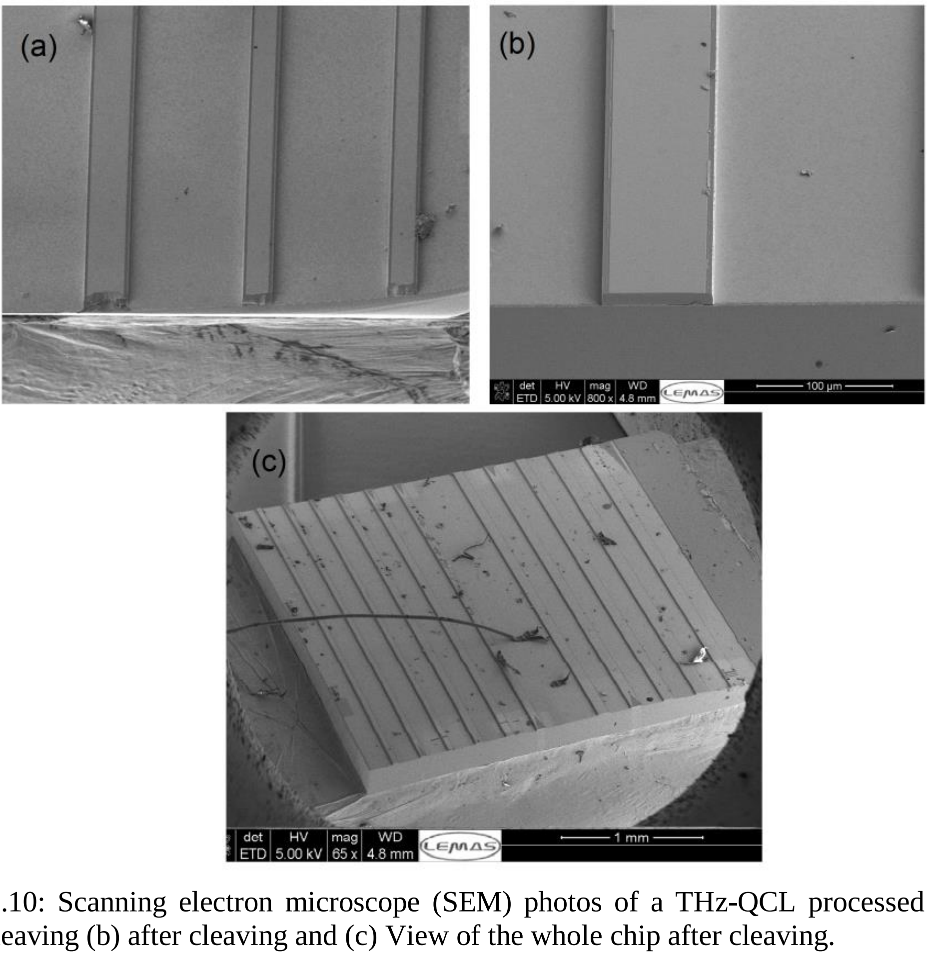

Figure 1.10: Scanning electron microscope (SEM) photos of a THz-QCL processed chip (a) before cleaving (b) after cleaving and (c) View of the whole chip after cleaving.

each chapter will show. No metallic deposition has although been performed unless specifically indicated.
A simplified representation of the fabrication process of a double-metal waveguide QCL can be found in Annex 1 while a more complete description is available in [52]. Samples were processed either at C2N (Group of R. Colombelli) or at SNS, Pisa (Group of M. Vitiello).

1.3.2 QCL post-processing

After the fabrication, the device is mechanically cleaved with a diamond tip. This is done in order to bring the cavity to the desired length and to realize the end mirrors of the cavity (the facets). Figure 1.10a shows the terminating part of three QCLs prior to cleaving and panel b) the facet of one of them just after. This is generally done on both sides so that the final result is similar to that of fig. 1.10c.

After the cleaving, the QCL is glued on a copper block as those shown in fig. 1.11a by means of an indium foil. The choice of indium is related to its exceptional thermal conductivity properties that are helpful to maintain the device at cryogenic temperatures by easing the thermal exchange with the coldfinger. The mounted device can be seen in fig. 1.11b. It can also be noticed that the electrical connection is established by connecting the device through micro wire bonding to a coplanar waveguide integrated to a high-speed SMP connecter. This allows for high frequency electrical modulations up to ~26GHz to be brought to the QCL for mode-locking. Once the mounting is completed, the QCL is ready to be mounted on a continuous flow He cryostat for characterization.

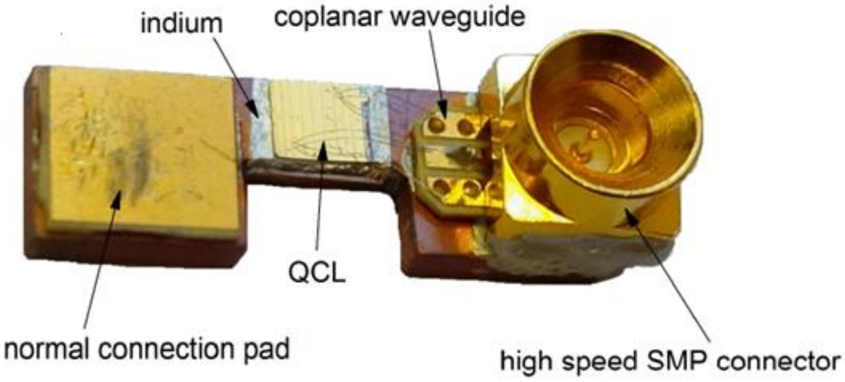

Figure 1.11: THz QCLs mounted on a copper block with high-speed coplanar transmission line waveguide and integrated SMP connector.

1.4 Introduction to mode-locking

Mode-locking is a widely used technique to generate ultra-short and intense pulses of light from a laser [1]. The resonant frequencies which can be sustained by a laser cavity are called longitudinal modes and are determined by the cavity length and the refractive index of the active medium of the laser. If all of them are in phase, the electric field of all these modes will interfere constructively in a small region in time. This will result in an ultra-short and intense pulse in the cavity which will propagate back and forth in the active medium and will then be partially coupled out from the mirrors at every round-trip time. In the time domain, a train of pulses with a separation given by the cavity round-trip time will be obtained. This kind of result corresponds to what is generally referred as mode-locking.

Historically speaking, mode-locked lasers have been first demonstrated in the 1970s, and since then they have undergone considerable developments that have permitted uncountable scientific and industrial applications spanning from fundamental physics to medicine, e.g. refractive surgery [53] and optical data storage [54]. THz ultra-short pulses are especially attractive due to the unique properties of the THz range. They can be generated by photoconductive antennas, but due to the low average power output, difficulty in the control of the spectral properties and the necessity of femtosecond Ti:Sapphire lasers, their diffusion remains limited.

Since the first demonstration of THz QCL in 2002, research groups have investigated methods to induce these devices to generate pulses. This goal was first achieved in 2011 by S. Barbieri et al [14] at University of Paris-7, followed up by our group [16] [28] [29] at École Normale Supérieure (2013). *S. Barbieri et al* showed the active mode-locking of a 2.7THz QCL referenced to a mode-locked erbium-doped fiber laser. The electric field amplitude of the QCL was sampled and mode-locking could be analyzed in the frequency domain. The work from our group demonstrated instead mode-locking by the direct measurement of the THz pulses in the time domain thanks to the injection seeding technique described in chapter **2.** This technique can also investigate the transition between free-running and modelocked operation. In both articles the presented THz pulses displayed a duration greater or equal to 10 ps. This resulted in a narrow spectrum which is detrimental to most applications.

Further developments led to the understanding that the generation of ultra-short pulses in THz QCLs is intrinsically hindered by the chromatic dispersion of the active medium. Recently, thanks to the design and integration of proper dispersion compensation schemes, it has been possible to reduce the duration of the pulses generated by THz QCLs to the much lower value of 4ps [17].

One of the main aims of this thesis (chapter **3**) will be to fully address the role of dispersion to deepen our insights and to evaluate the possible solutions to further shorten the pulse duration of modelocked QCLs. A more extensive discussion on this topic will be provided in chapter **4**. In this chapter, instead, the principles of mode-locking will be introduced that are essential to understand the experimental results and how they relate with my work on dispersion compensation.

1.5 Mode-locking and frequency combs

1.5.1 Principles of mode-locking and frequency combs

A frequency comb is a laser spectrum characterized by a constant and fixed spacing of its modes. One can describe a frequency comb with the simple expression:

$$f_n = f_0 + nf_\Delta \tag{5}$$

where f_0 is the carrier offset frequency, $n = 1,2, \ldots$ is an integer and f_Δ is the frequency spacing of the comb. In other word, one can univocaly define an ideal comb just by its two main parameters f_0 and f_Δ. A popular way to generate a frequency comb is through a stabilized femtosecond mode-locked laser. In this case, the waveform is a pulse train as the phase of the laser modes are fixed to each other by a modelocking mechanism. Conversely, frequency combs based on the non-linear Kerr (or Four Wave Mixing FWM) effect result in a quasi-CW profile with minimal amplitude modulation.

Owing to the close relationship between frequency combs and pulse generation, it is important to provide a minimum standard according to which we may refer to the one or the other (or both). Starting with a general expression for the emission of a generic laser with n modes, one can write the time profile of the electric field as:

$$E(t) = \sum_1^n E_n(t) = \sum_1^n A_n e^{2\pi i[(f_n+\delta_f)t+\phi_n]} + c.c.$$

$$= \sum_1^n A_n e^{2\pi i[(f_0+nf_\Delta+\delta_f)t+\phi_n]} + c.c \tag{6}$$

$$= \sum_1^n A_n e^{2\pi i[(f_0+nf_\Delta)t+\delta_f t+\phi_n]} + c.c$$

where E_n is the electric field of the n^th^ mode, A_n its amplitude, ϕ_n a time-independent phase offset, $f_n + \delta_f$ its frequency expressed as a deviation δ_f from the n^th^ line of a frequency comb. For a Fabry-Perot laser, such as a QCL, the parameter f_0 of the comb may correspond to the lowest-frequency mode of the spectrum (if one allows n to start from zero) while f_Δ is the free-spectral range which can be written as:

$$f_{\Delta} = \frac{c}{2n_0 l} \qquad (7)$$

with n_0 being the refractive index of the material (or the group refractive index when dispersion is present) and l the cavity length. The frequency detuning, δ_f, of a mode from its ideal position in the comb can then be made to account for all the factors that generally lead to a non-constant mode spacing, e.g. chromatic dispersion. It is in fact well known that the refractive index of a material is generally not constant with the frequency. This is particularly true for the THz QCLs due to the proximity of the reststrhalenband (~8THz) which leads to a rapidly changing value of the refractive index. If n_0 is not constant, the free spectral range will change across the spectrum. This detuning δ_f, which can be computed for each mode of frequency f, allows to differentiate a frequency comb to a generic spectrum in a compact way. We can then analyze three different scenarios according to the values which δ_f and ϕ_n can assume for the modes of a generic laser spectrum:

1) $\delta_f \neq 0$ and ϕ_n is random for all the modes

   In this situation the modes are not evenly spaced and the phase is different for each one of them. The time profile will then be given by independently emitting modes and a random waveform approaching CW emission will be the result. Most importantly, no periodic profile of sort can be identified. It is generally the result of uncompensated dispersion and the absence of any mechanism which can maintain the mode coherence.

2) $\delta_f = 0$ and ϕ_n is fixed but different for all the modes

   This case corresponds to a frequency comb. Mode spacing is in fact constant as a result of successfully compensated dispersion and/or the presence of a sufficiently strong mechanism that can keep the modes at a fixed frequency, e.g. cascaded four wave-mixing [55] and is often referenced as modelocking. The time profile of the electric field will then be periodical (with a periodicity given by the free spectral range f_{Δ}), but since ϕ_n is different for all the modes (but fixed), the waveform will most unlikely result in a pulse behaviour. Indeed, it has been reported [56] [57] that the emission would be frequency modulated. In chapter **5** this subject will be treated in more details.

3) $\delta_f = 0$ and ϕ_n is fixed and identical for all the modes

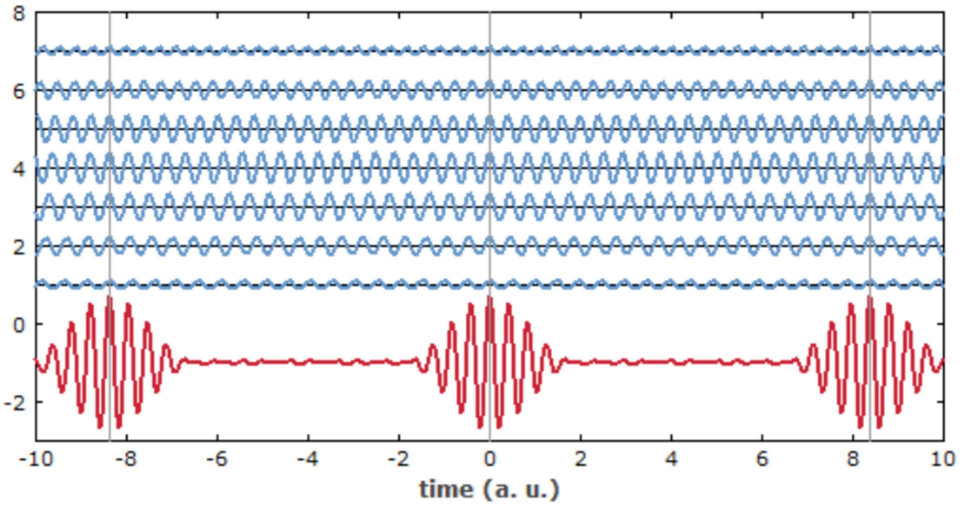

Figure 1.12: Short pulse generation (red) by mode-locking of 7 different modes (in blue). The time independent phase offset is ϕ_n identical for all the modes (case 3) which are evenly spaced ($\delta_f = 0$). A periodic, stable pulsed profile is generated. Source: [https://www.rp-photonics.com /mode_locking.html]

> This last case corresponds to a frequency comb with a well defined temporal profile which is periodically repeated. The notable difference with respect to the previous case is that all the modes are in phase with each other for at least once per round-trip so that they interfere constructively resulting in a short laser pulse. This is also referred to as mode-locking.

There are also other cases that can be experimentally obtained which are a mix of those described above. For instance, one might have a pulsed time profile for which not all the modes are in phase with each other or have a perfectly constant spacing. When this happens, the generated pulse may be deformed and be broader than its “Fourier-transform limited” value (meaning that it has the minimum duration granted by its spectrum under a Fourier transform. This is obtained typically only if all the modes are mode-locked in the case of situation 3). A train of pulses which are not transform limited is in practise the signature that the dispersion is not compensated over the entire spectrum. For this very reason, increasing the bandwidth of a THz QCL is usually not a viable way to procede towards the generation of shorter pulses if a solution to maintain the mode coherence has not been implemented. Needless to say, the broader the spectrum the broader this solution will need to be, which generally tends to result in complex designs with increasing issues of limited reliable reproducibility on the experimental side. In chapter **3**, a section will be devoted to the evaluation of different schemes to compensate the dispersion.

Moreover, one can also think at a situation for which a laser source, such a Ti:Sa laser for example, emits a not perfectly stable train of pulses with slightly different amplitude and duration from each other, but never reverts to CW operation. Some kinds of instability [58] or noise [59] may be responsible for this behaviour. The modes of the laser have to be in-phase with each other or the resulting electric field waveform would not be pulsed, and so one could consider the laser to be operating in a mode-locked condition but may not say its spectrum to be a proper frequency comb due to fluctuations in the mode positions or linewidth which de facto corrupt the main properties of the comb making it unusable to many applications.

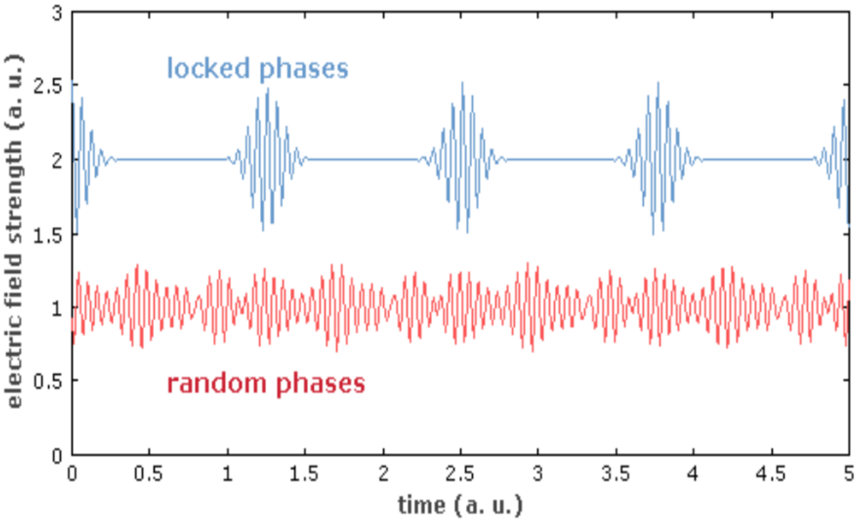

Figure 1.13: Comparison between the cases 2 (in red) and 3 (in blue) described in this section. In the blue curve, the modes are all in phase with each other every 1.25 time units, and clearly represents a mode-locked laser. In the red curve the modes are fixed but are randomly set with respect to each other. The same periodicity exists also in this case but the time profile is much closer to a CW output. Source: [https://www.rp-photonics.com/mode_locking.html]

At this regard, it may be appropriate to recall here that frequency combs have started a revolution in many fields and this is especially true in optics and metrology as they establish a phase-coherent link between the microwave and optical domains[60]. One very recent example of a frequency comb emitted by a THz QCL can be found in the work of L. Consolino et al [61] which has been an interesting advancement towards the use of THz QCLs for metrological applications. The reason for mentioning this particular study is due to the fact that the device employed in the experiments presented in the cited paper is the Sample 1 described in this thesis, and it was first characterized as a part of my work on broadband QCLs. The related results from free running and mode-locking experiments will be discussed in chapter **3** and **4**.

Another important application of frequency combs which is of particular relevance for THz QCLs is molecular spectroscopy due to presence of a plethora of unique molecular fingerprints in this frequency range. In general, frequency combs spectroscopy has already surpassed the speed and precision of Fourier spectrometers. However, these combs are realized by systems made of several optical components [62] [63] [64] which limits the practicity of their use. QCLs, on the other hand, have proved to be able to generate frequency combs both in the MIR [55] and in the THz [65] range while having the advantages of being compact and electrically-controlled devices. For these reasons they have attracted an ever-growing attention during the last few years.

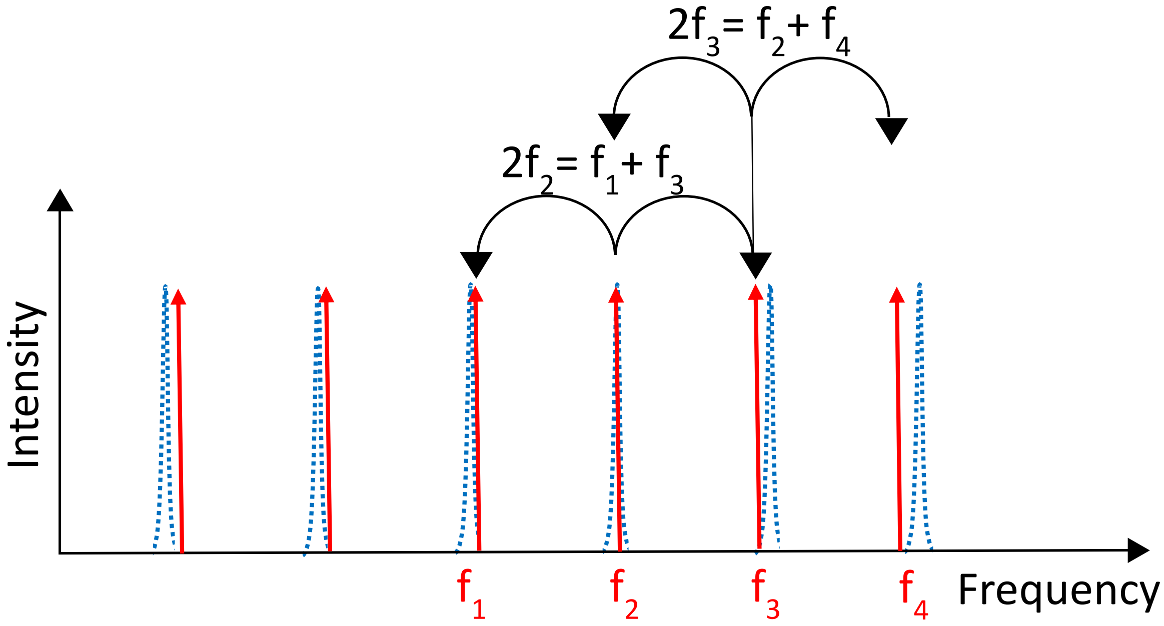

Figure 1.14: Simplified schematic of a frequency comb formation by FWM starting from a single mode at f_2. The dashed gaussians represent the positions the mode would have accounting for dispersion (uneven mode spacing). The red arrows show how FWM favours the generation of new modes with a constant mode spacing, thus a frequency comb. After emission at f_1 and f_3 has started, also processes such as $f_1 + f_3 = f_2 + f_4$ become possible, further enhancing the cascading process.

As a final remark for this section, the nature of the frequency combs generated by a QCL will be addressed. It was very briefly mentioned in point 2, that a mechanism capable of maintaining a fixed phase-relationship between the modes can spontaneously arise in QCLs that help limiting the detrimental effects of dispersion and allow for comb formation. This third order non-linear effect, four wave mixing (FWM), is also responsible for mode proliferation together with the spatial hole burning effect. As extensively explained in the work of J.B. Khurgin et al [57], these mechanisms are at the base of the multimode nature of the emission of QCLs which otherwise would favour single mode emission owing to the ultra-fast gain recovery time of the active medium. However, for the same reasons, the time profile of the electric field of a free-running QCL should be nearly constant, as any pulse-like feature travelling in the cavity gets smoothed over time by the fast gain relaxation. Due to this very fact, passive modelocking is asserted to be nearly impossible to achieve in QCLs. Multimode operation and nearly constant temporal output are a signature of a periodic frequency-modulated signal, i.e. a frequency comb where the phases are fixed in time from one mode to the other but cannot be used to generate pulses.

These considerations will be particularly important in chapter **4** where I will present a novel case of a spontaneously mode-locked THz QCLs displaying a strong and long-lasting amplitude modulation i.e. pulse generation of the emitted electric field, in contrast with the currently most accepted interpretation of the roles of the gain and FWM in shaping the emission profile of QCLs suggesting other processes are at work.

Currently, modelocking in THz QCLs has only been reported through active modulations of the bias current (active modelocking). The stable train of pulses with the shortest duration which can be found in the literature have been obtained in 2017 by A Mottaghizadeh et al. [66] and F. Wang et al. [17] and have a single pulse duration of 5ps and 4ps respectively. Single pulses as short as 2.5ps have also be reported [51] but they tend to broaden as a consequence of chromatic dispersion, limiting their practical utility. In this work, I will present a pulse train with a record duration of 3.4ps by combining active modelocking and dispersion engineering. I will also show that single pulses as short as 1.3ps can be generated from QCLs displaying ultra-broadband emission.

1.5.2 Electrical beatnote

As it was explained in the previous part, FWM and SHB allow the QCL to be multi-mode despite the presence of an ultra-fast gain that would instead strongly favour single mode emission. When the modes in the cavity of the QCL beat together, and owing to the fast QCL dynamics, an electrical beating results “the beatnote” that appears as a modulation of the current bias. The exact frequency of the beatnote in the spectrum depends on the mode spacing, so ultimately on the cavity length and the refractive index of the gain material. For example, a 3mm long cavity will have fabry perot modes separated by ~13 GHz and therefore a beatnote at this frequency is expected to be found. If the mode spacing is not identical across the whole spectrum, however, the beatnote will have a large linewidth or not observed. On contrary, if the mode spacing is identical as in the case of a modelocked source, extremely precise and stable in time, the beatnote will be extremely narrow. In other words, one can use the information obtained from the beatnote to assess the quality of the modelocked/frequency comb source. A precise measurement of the beatnote linewidth with a electrical spectrometer is in fact one of the fundamental methods employed by the vast majority of the QCL community to demonstrate comb operation [57].

Chromatic dispersion is one of the main factors which can destabilize a frequency comb. As it will be explained in detail in the next chapter, one of the most important sources of dispersion in a THz QCL is the one provided by the gain. Since the gain depends on the bias [67], it is necessary to measure the beatnote frequency and intensity as a function of the bias applied. When this is done, one generally plots the results in a « beatnote map » that allows to verify in which conditions a QCL works in comb operation. Extensive work has also been performed in the recent years to limit the dispersion with different approches and improve the formation of combs in QCLs [68].

The behaviour of a generic beatnote is such to be very narrow at low biases, where the number of modes are limited, and where mode stablization processes dominate the frequency properties of the spectrum thus ensuring a constant mode spacing. As the current is increased, new modes arise that may be too far away from the center of the spectrum to be well locked and the beatnote linewidth will start to broaden. As the dispersion keeps increasing with bias, the modes are generally dispersed that the beatnote becomes a very broad plateau, signature that no more coherence exists in the spectrum.

In general, frequency combs will be treated several times in this thesis due to the fact that pulsed lasers, one of the main subjects of my work, are ultimately comb sources. However, an important difference is that by having access to the electric field time profile of the THz QCLs, usually all the required information is obtained by time resolved experiments rather than by the observation of the quality of the beatnote. Further, this permits to study if the QCL is frequency or amplitude modulated. In fact, stable pulse trains can only be produced by a very specific kinds of combs (having modes with identical phase). Several examples of beatnote spectra and maps can be found throughout the thesis. They are also useful because the beatnote position is a good initial guess for the frequency modulation to apply for active modelocking, which will be discussed in the next section.

1.6 Conclusions

In this chapter, some introductory information about THz QCLs have been provided. In particular, a comparison has been carried out on the fundamental mechanisms of traditional diode lasers and QCLs to illustrate the main features that distinguish the latter from conventional optical devices.

A discussion of the processes upon which the quantum cascade effect is based has been proposed. The main kind of active region designs and waveguide structures have been outlined. In particular this thesis will concentrate on spectrally broad structures for short pulse generation with MM waveguides that simultaneously confined the THz modes and the microwave modulation used for active modelocking.

In the second part of the chapter, modelocking and frequency combs were presented and compared on a simple theoretical basis. Criteria for the attribution of the QCLs emission to each of them were defined and will be used to describe the experimental results presented in this thesis.

The following chapter will discuss the experimental setup and techniques which were used for the characterization of the THz QCLs. This will provide the basic information to understand the experiments and the results provided from chapter **3**.

2

Terahertz Time Domain Spectroscopy of Quantum Cascade Lasers

In order to characterize the emission of THz quantum cascade lasers with a high temporal resolution, ultrafast detection systems with a sub-picosecond responsitivity are needed. Although direct techniques currently do not exist, Terahertz time domain spectroscopy (THz-TDS) allows the generation and detection of THz pulses on a femtosecond (fs) times scale by exploiting coherent sampling schemes with NIR ultrafast lasers. This can be adapted to measure the emission of THz QCLs, on the condition that the synchronization of the QCL emission with the THz pulses from the TDS system is established. To ensure this condition, in 2010 our group developed a technique called "*Injection seeding*" [69] The main principle of this system is to inject a phase-resolved THz pulse, generated from a *fs* optical pulse excitation of a photoconductive antenna, into the cavity of a QCL to initiate laser action. In this way, the phase of the QCL can be synchronized to the THz emitter and thus to the *fs* probing pulses. The electric field of the phase-controlled QCL radiation can be then detected in both amplitude and phase using, for example, electro-optic sampling. This permits to investigate the temporal profiles of free-running and modelocked QCLs.

In this chapter, the fundamental principles of THz-TDS will be introduced in section **2.1**. In the following part (section **2.2**), the injection seeding technique will be discussed to illustrate how it is used to detect the electric field of the THz QCL emission in the time domain. In section **2.3**, some results of the measured THz QCL emission will be analyzed. From the second part of the chapter, modelocking techniques that allow a laser to generate short pulses will be described in section **2.4**. Focusing on active mode-locking, the implementation of this technique to the THz-TDS system will be detailed in section **2.5**. The information provided in these two sections represent the basis to understand the experimental results which will be presented in the next chapters.

Chapter 2

2.1 Terahertz detection

As already stated in the previous chapter, the THz range is a less developed part of the electromagnetic spectrum due to the lack of promising sources and detectors. In particular, regarding the latter, the commonly used THz detectors [70] [9] such as pyroelectric detectors and Golay cells can only respond to a very slow modulation frequency of less than 50 Hz that is extremely far-away from the most basic requirements for ultrafast detection. Other THz detectors, for example hot electron bolometers, are capable of achieving much higher response frequencies from a few kHz to a few GHz, but they cannot attain frequencies above 10 GHz [71]. To further investigate the ultrafast properties of THz QCLs, such as their dynamics and short pulse generation, high-speed detectors or detection systems with a faster response are required.

Terahertz time domain spectroscopy (THz-TDS) is a system capable of sampling a THz signal in time with a resolution of less than 20fs. This can be done as a result of its detection system, which transfer the information of a phase-locked THz electric field to an ultrashort (sub-100fs) near-infrared probe pulse thanks to a non-linear process and allows for detection using more conventional infrared detectors. The retrieved information, using a delay line to obtain the temporal behaviour, consist in both the phase and the amplitude of the THz field. More details are provided in the next section.

Other ultra-fast techniques have very recently been developed that allow to measure the time profile of THz QCLs emission. For example, it has been shown that it is possible to coherently detect the QCL’s emission by locking the QCL beatnote to a harmonic of the repetition rate of a fs laser and by actively modulating the bias current applied to the device [14]. However, this limits the use of the technique to the study of actively modelocked QCLs and not free running devices. Other methods include shifted wave interference Fourier transform (SWIFT) [72] and photon correlation measurements with sub-cycle time resolution [73]. The interesting point of the injection seeding technique used here is that the THz waveform can be sampled from the build-up of amplification to steady-state laser action, as well as not requiring locking the repetition rate of a QCL to any reference. They will be described in section **2.2**.

However, for these systems to work on QCLs, it is vital to synchronize the phase of the QCL emission with that of the probe pulses, lest all the measured values for the field at a specific time average to zero. This implies that one must not allow the spontaneous emission to start the lasing process as that is will produce photons with a random phase. In order to solve this problem, a coherent detection technique called *« injection seeding »* [69] [74] [75], was developed by our group allowing us to detect the time-resolved emission of THz QCLs.

The technique is based on injecting a broadband THz pulse generated by a photoconductive antenna [76], excited by a Ti:Sapphire *fs*-laser pulse, into the cavity of QCLs to start the laser action and replace the QCL's spontaneous emission. In this way, the phase can be fixed by the injected THz pulse. Once the emission phase is controlled, we can coherently detect the electric field of the QCL emission, using standard electro-optic sampling [77] described later in this chapter.

2.2 Terahertz time domain spectroscopy

Terahertz time domain spectroscopy (THz-TDS) is a spectroscopic technique that allows us to coherently detect the time-resolved electric field of THz radiation with a resolution in the order of the tens of fs [72]. A THz-TDS setup is typically composed of three parts: a femtosecond optical/near-infrared laser, a THz generation system and a THz detection system. One of the most commonly used generation systems is based on THz pulses generated by photoconductive antennas while the detection system used in this work is electro-optic sampling [71].

This setup is sensitive to the amplitude and phase of the THz electric field and can be used on specific materials and nanostructures to study their electrical and optical properties. At first, some details about the THz generation and detection parts of the setup are presented. They will be followed by a proper description of the complete system.

2.2.1 THz photoconductive antennas

Several techniques exist that allow to generate THz pulses with femtosecond lasers. Examples are frequency mixing in nonlinear crystals, plasma generation in air and photoconductive antennas [7] [78] [79]. In our group photoconductive antenna are typically employed to generate broadband THz pulses covering the frequency range from 0.1 – 4 THz [76]. Such a device, in its simplest form, consists of 2 metal electrodes deposited on a GaAs semi-insulating substrate as schematically illustrated in fig 2.1. A femtosecond infrared laser pulse, typically produced from a Ti:sapphire laser (λ ~800nm), having a photon energy larger than the band-gap of the material, can be used to promote the electrons in the valence band of the GaAs substrate in between the electrodes to the conduction band where they become free carriers. With the antenna biased, a transient photocurrent *IPC* will be consequentially generated. This time-dependent photocurrent I_{PC} will then be proportional to the applied static electric field and to the temporary optical pulse profile [7].

By applying the Hertzian dipole antenna model to the system, it is possible to recover its time-dependent emission expression in free space [7]. If the spatial terms are not considered, the emitted electric field time profile results to be dependent on the time differential of the photocurrent:

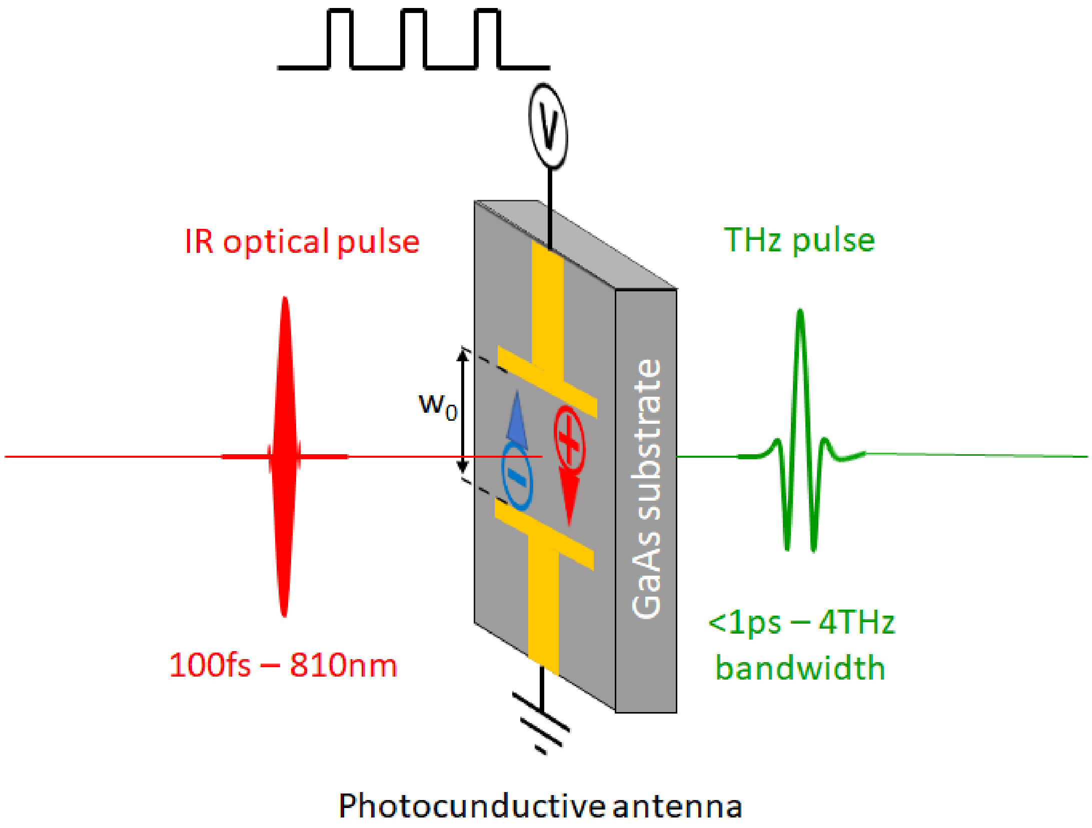

Figure 2.1: Schematic representation of a photoconductive antenna for THz generation under excitation from an ultrashort near-infrared pulse

$$E_{THz}(t) \propto \frac{dI_{PC}(t)}{dt} \tag{8}$$

For example, for a ~100fs IR laser pulse, the transient photocurrent will generate an electric field also lasting a few hundred femtoseconds (the exact value is dependent on the dynamics of the material used for the substrate), which corresponds exactly to the THz frequency range. Generally, the THz pulses produced in this way are centered at about 1 to 1.5THz with a broad bandwidth of ~3-4 THz and a typical average power of ~20μW.

For different applications, different electrode geometries and fabrication processes are employed to engineer the properties of the emitted THz radiation [10]. In this thesis, I used the large area interdigitated photoconductive antenna [80] owning to its high average radiative power of tens of μW under an infrared excitation power of about 500mW and a modulation frequency of a few tens of kilohertz. For a given photoconductive antenna, its output electric field is proportional to the bias voltage and the optical excitation power (unless the response saturates at high values).

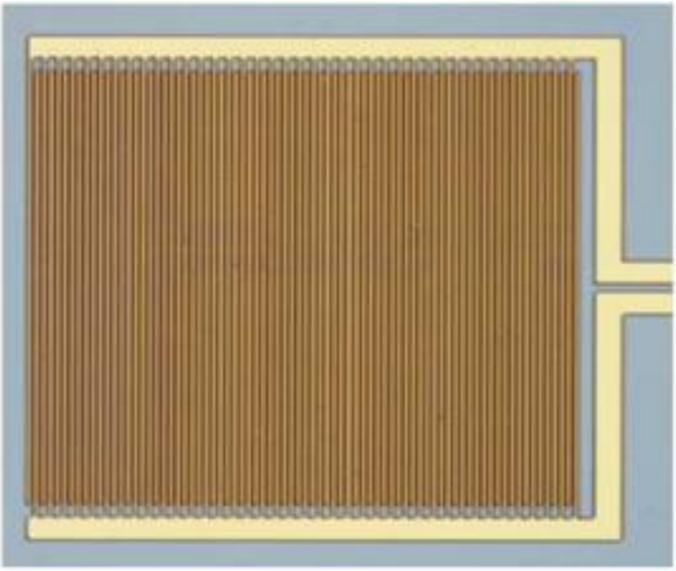

Figure 2.2: Example of a large area interdigitated photoconductive antenna. [http://www.batop.de/products/terahertz/photoconductive-antenna/photoconductive antenna-1060nm.html].

2.2.2 THz electro-optic detection

There are several techniques to detect THz waves using ultrafast lasers. Examples are photoconductive switches [81], plasma based air photonics [82] and non-linear crystals [83]. In our group, we employ electro-optic crystals as they allow for detection on a relatively broad spectral bandwidth when compared to photoconductive devices.

Electro-optic (EO) sampling permits to measure the electric field of the THz radiation using a second order non-linear effect called Pockel effect. From the analysis of the second order non-linear polarization for the Pockels effect one can find a proportionality between the susceptibility tensor and the static electric field amplitude which induces birefringence in a EO crystal [3]. Therefore, by measuring the birefringence, one can quantitatively assess the applied electric field.

The EO sampling of the THz electric field works exactly in this way. We can analyze in more details the measurement process by considering the components necessary to the detection system. A schematic representation can be found in fig. 2.3. We can start with the NIR ultrashort pulses (in red) from the Ti:Sa laser impinging on the EO crystal, which in our case is a ZnTe crystal. We can assume at first that these pulses are linearly polarized. If no THz electric field (in green) passes through the crystal at the same time as the NIR pulses, then no birefringence is induced and the polarization of the pulses will not change. After the crystal, the quarter-wave plate will make their polarization become circular. The Wollaston prism will split the two components of the polarization, which are identical, and the photodiode will make the difference between them. The result in this case is always zero (plus noise).

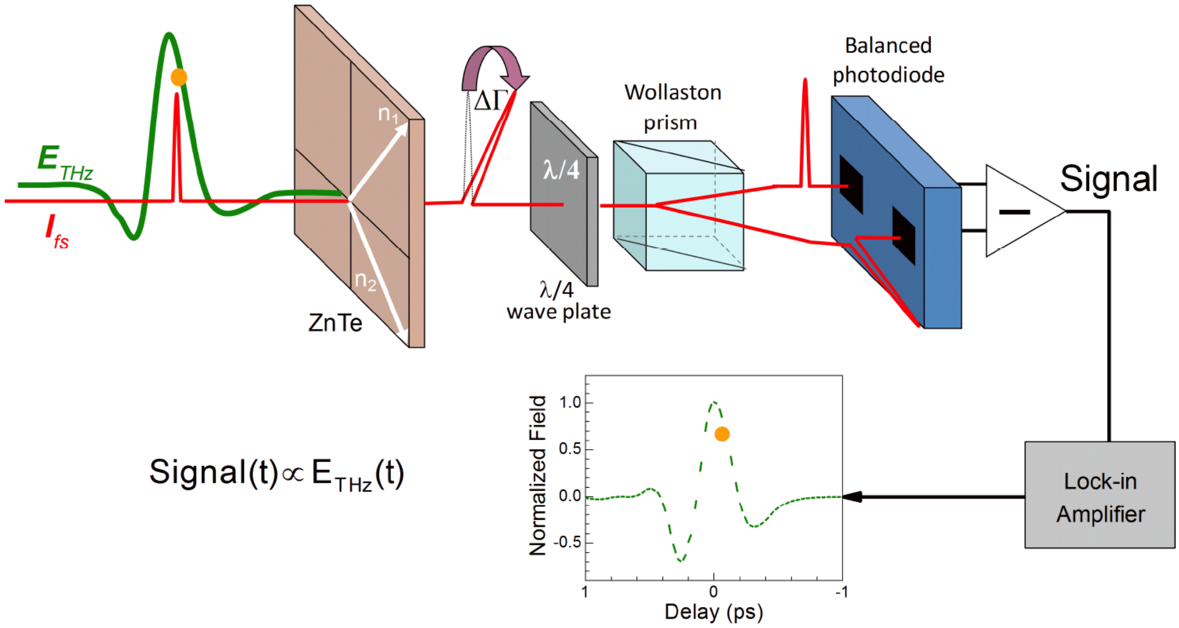

Figure 2.3: Schematic diagram of an electro-optic sampling system for THz electric field detection. List of components: ZnTe crystal: nonlinear crystal for Pockels effect. λ/4 wave plate: lens changing the polarization of the NIR pulses. Wollaston prism: it separates the horizontally and vertically polarized components of the NIR optical pulses after the quarter-wave-plate. Balance photodiode: it detects respectively the horizontal and vertical components of the NIR pulses. Their difference is determined and then sent to a Lock-in amplifier for detection.

If instead a THz electric field passes through the crystal together with the NIR pulse, due to the phenomenon of the induced birefringence, the latter will experience a different refractive index along the n_1 and n_2 directions (the white arrows on the crystal in the figure). Passing through a crystal of thickness L, a phase delay is introduced between the linearly polarized components of the n_1 and n_2 axis, which is given by [3]:

$$\Delta\phi = (n_1 - n_2)\frac{\omega L}{c} = n_O^3 r_{EO} E_{THz}\frac{\omega L}{c} \tag{9}$$

where n_O is the refractive index at the frequency of the pulse and r_{EO} is the EO coefficient. The NIR pulse will then become elliptically polarized after the quarter-wave plate with components:

$$I_x = \frac{I_O}{2}(1 - \sin\Delta\phi) \approx \frac{I_O}{2}(1 - \Delta\phi) \tag{10}$$

$$I_y = \frac{I_O}{2}(1 + \sin\Delta\phi) \approx \frac{I_O}{2}(1 + \Delta\phi) \tag{11}$$

where I_O is the intensity of the optical pulse. The Wollaston prism will separate these components and they will be detected by the balance photodiode. The result of the difference is:

$$I_s = I_y - I_x = I_O\Delta\phi = n_O^3 r_{EO} E_{THz} \frac{I_O \omega L}{c} \tag{12}$$

The signal resulting from the photodiode is therefore proportional to the value of THz electric field at the moment the NIR pulse passed through the crystal. This is represented in fig. 2.3 by the yellow point on the plot after the lock-in amplifier, which is modulated at the frequency of the THz emitter (the antenna, in the easiest case). If the arrival time of the pulse to the crystal is changed by a mechanical delay-line, another point of the THz electric field will be sampled. We can then entirely scan the THz profile just by changing the delay of the NIR pulse and so reconstruct its shape in the time domain. Typical fields that are detected are on the order of tens of V/cm.

Finally, regarding the different kinds of EO crystals, the ZnTe [36] and GaP [84] are the mostly commonly used as the group velocity of the near-infrared optical pulse is roughly equal to the phase velocity of the THz pulse in these materials. This phase-matching condition allows to maximize the Pockels effect and permits to treat the varying THz waves as a static electric field. However, their phase velocities are slightly different for different THz frequencies, resulting in an optimal thickness of the crystal for broadband detection. For instance, a 200µm thick ZnTe crystal is used to detect THz frequencies from a few hundreds of GHz to more than 3 THz. Thicker crystals will give a larger signal but this will also reduce the detection bandwidth.

2.2.3 THz time domain spectroscopy setup

A schematic diagram of the complete setup of the THz time domain spectroscopy system can be seen in fig. 2.4. In our group, we use a Ti:sa laser with a central wavelength of about 810nm which is employed to generated optical pulses of ~100fs duration with a repetition rate of ~76 MHz. The optical pulses are divided into 2 parts by a 50/50 beam splitter as illustrated in the figure (component named *BS*). One of these parts goes to a delay line, consisting of a motorized movable plate and 4 dielectric mirrors *M1 – M4*, and then to the EO crystal (via the mirrors *M5* and *M6* and a small hole on the parabolic mirror *PM4*).

The second part of the fs laser beam is focused onto the THz emitter (the PC antenna) by the mirror *M9*. A THz pulse will then be generated as introduced in section **2.2.1**. In this way the THz pulses from the antenna are always in phase with the *fs* optical pulses. (Typically, a 25KHz square signal of 3V_{pp} and 50% duty cycle is applied to the electrodes of antenna). Four parabolic mirrors (*PM1* to *PM4*) focus the THz waves onto the nonlinear EO crystal ZnTe which has a typical thickness of 200μm to 500μm. When the THz and the first optical pulse overlap and travel through the ZnTe crystal at the same time, the electric field of THz waves can be measured by the EO sampling system (section **2.2.2**). By continuously moving the mirrors on the delay line to adjust the optical paths length (delay) of the NIR pulses, we can then change

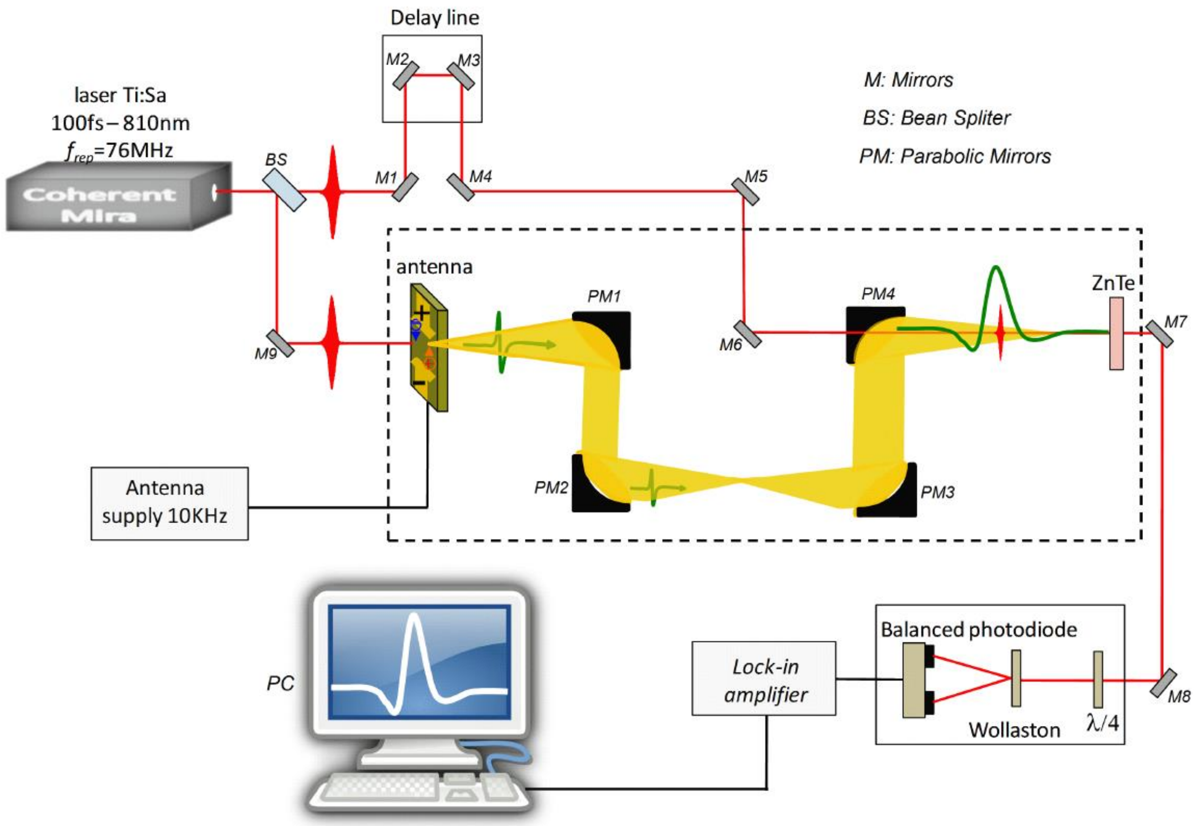

Figure 2.4: Schematic diagram of a time domain spectroscopy setup for THz electric field generation and detection. The components represented are: Coherent Mira: *fs* laser generating NIR pulses of 100*fs* duration, 810nm central frequency, 76MHz repetition frequency and ~1.2W average output power. Delay line: mirrors installed on a motorized movable stage to change the length of the optical path (delay) of the *fs* pulses. Loçk-in amplifier: it allows to coherently detect and amplify the 25KHz signals (the modulation frequency of the photoconductive antenna) after the balance photodiode. PC: computer to record the data from the lock-in amplifier. Red pulse (line): *fs* optical pulse (path). Green pulses: THz waves. Yellow zones: THz wave path. Black line: electrical connections. The photoconductive antenna, 4 parabolic mirrors and nonlinear crystal ZnTe are placed in a closed glass box and purged by compressed dry air.

the relative positions and phase relations between them and the THz pulses. Therefore, the actual THz electric field can be reconstructed in time domain step by step as presented in fig. 2.5a-b. These pictures show two time positions of the delay line of the optical pulse that can sample different time positions of the THz profile.

It is particularly important to underline that as the THz pulses are locked in phase to the NIR ones, the signal measured at a given phase delay is the average of thousands of samplings (repetitions), all at exactly the same conditions. This method greatly reduces the noise and then improves the signal-noise ratio as schematically shown in fig. 2.5 for five pulses separated by ~13 ns.

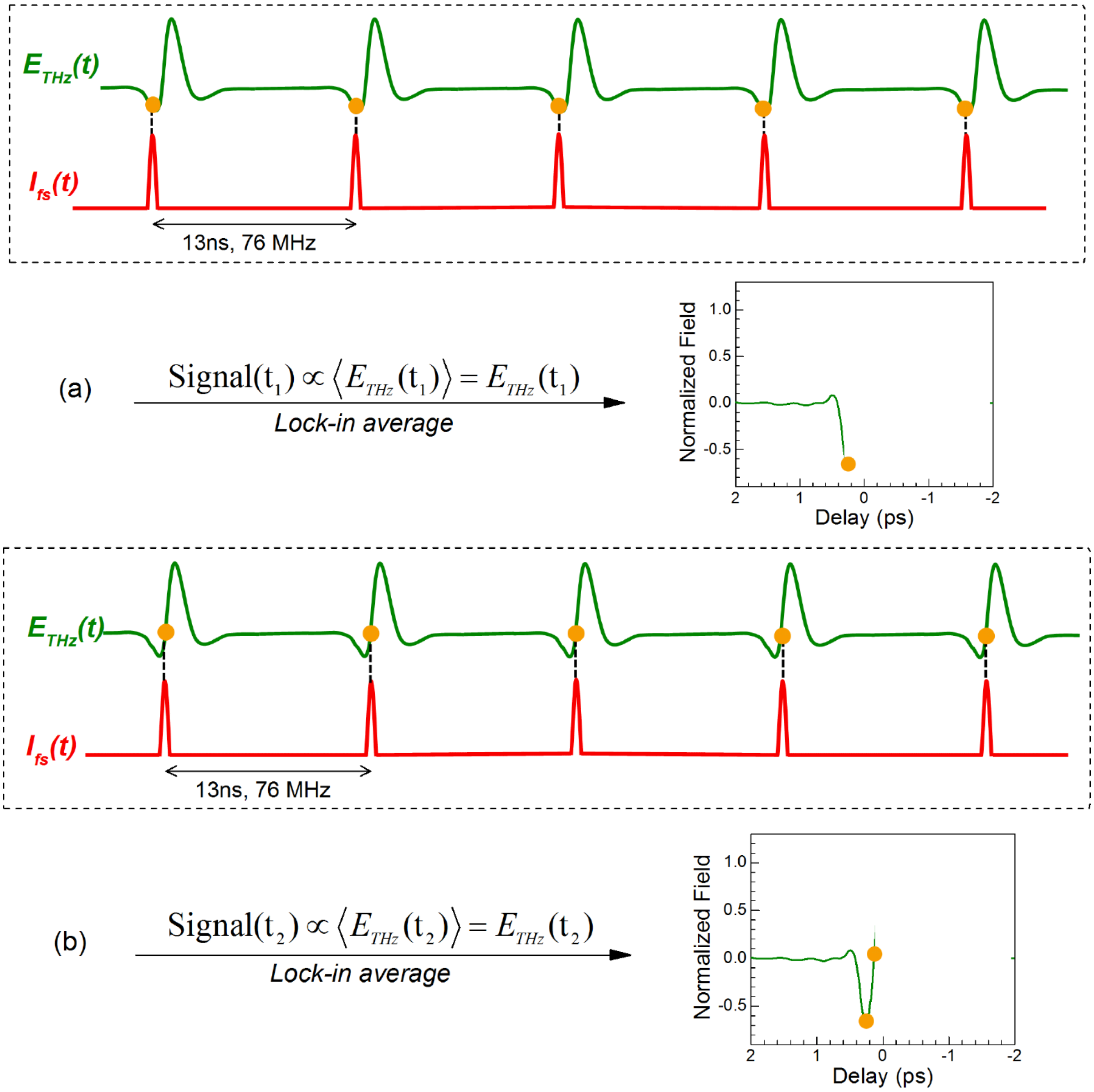

Figure 2.5: Electro-optic sampling processes of the THz electric field for different delays of the NIR pulses. The THz pulses are sampled by the *fs* optical pulses, having a repetition rate of 76MHz. Moving the delay line from (a) to (b), the electric field at different times can be measured and this allows to reconstruct the full time profile of the THz pulse.

Figure 2.6a shows a typical time domain scan of the THz pulse from a GaAs photoconductive antenna under a ~100 *fs* optical pulse excitation with an average power of ~400mW and a central wavelength of about 810 nm. A ZnTe crystal of 300µm was used for the electro-optic sampling. In fig. 2.6b it is reported the spectrum of the photoconductive antenna emission obtained by applying a fast Fourier transform (FFT) to the temporal signals in (a). For this photoconductive antenna, the duration of the THz pulse is about ~1 ps and the frequency response is centered at ~1.2 THz, covering the range from 0.1 THz to 3.8 THz. The grey zone in fig. 2.6b represents the spectral range between 2 to 3THz, corresponding to most of the QCL frequencies that will be investigated in the latter chapters. The photoconductive antenna described in this paragraph is the external THz source that will be employed to inject THz pulse into QCLs as discussed in the next section.

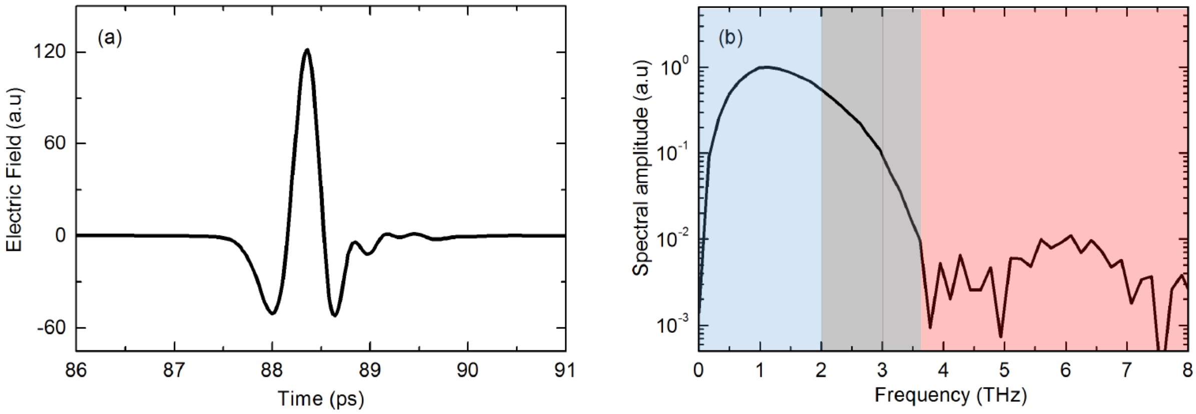

Figure 2.6: Measured (a) Time domain and (b) Spectrum of a THz pulse generated from a GaAs photoconductive antenna. The gray area represents the frequency range where the QCLs operate in this thesis. The antenna emission at lower frequencies is on a blue background. The red area shows that the system does not present significant emission at frequencies above 3.8THz

2.3 Injection seeding of THz QCLs

In the previous chapter it was shown how it is possible to measure the THz electric field of a photoconductive antenna and reconstruct its time profile. To understand the ultrafast properties of QCLs and study the generation of short pulses, it is necessary to do the same for these devices.

However, it cannot be done by just substituting the photoconductive antenna with a THz QCL and measuring its output. It was presented at the end of section **2.1** that by doing so one would measure a random QCL phase for each point in femtosecond pulse. In fact, even by

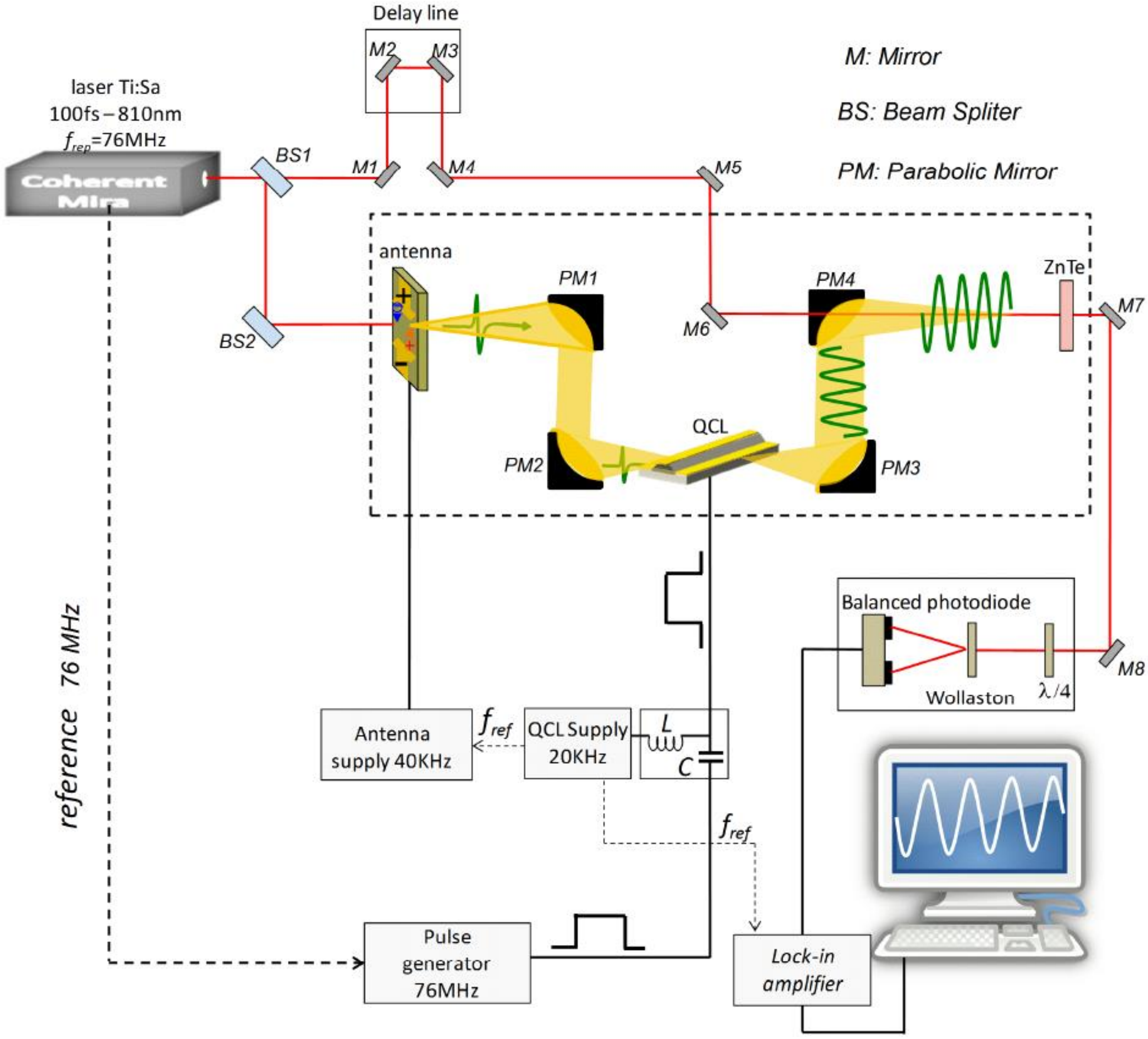

Figure 2.7: Injection seeding setup for time-resolved detection of THz QCL emission. QCL supply 20kHz: a quasi-DC bias at 20kHz frequency and 5μs width is applied to maintain a QCL slightly below its lasing threshold. Pulse generator 76MHz: electrical pulses trigged by the NIR pulses are employed to bring the QCL above its threshold at a repetition frequency of 76 MHz (13 ns). Antenna supply 40kHz: current square waves with a width of 5μs and a frequency of 40kHz are applied to the electrods of a photoconductive antenna. Red pulse (line): *fs* NIR pulse (paths). Green pulses: THz waves emitted by the photoconductive antenna and QCLs. Yellow zones: THz pulse path. Black line: electrical connections.

synchronizing the switch-on of the QCL to the NIR pulses, the spontaneous emission which initiates laser action will ensure that the phase of the electric field is random every time the device starts emitting. Therefore, the averaging of hundreds of measurements for each point in time, the mechanism inherent to the TDS technique, will ultimately result in a zero value. The solution is to fix the phase of the electric field emitted by the QCL by locking it to that of the NIR pulses. To this aim, our group developed the technique known as “injection seeding”.

Fig 2.7 shows the injection seeding setup for the time-resolved detection of THz QCL. Based on THz-TDS, a QCL is placed at the focus point of the parabolic mirrors *PM2* and *PM3*. The principle is to inject a phase-resolved ‘‘seed’’ THz pulse emitted by a photoconductive antenna into the QCL cavity to initiate its laser action through the phase-resolved external THz source, instead of the QCL’s random spontaneous emission [79] [67]. In this way, with switch on the QCL synchronized to the input pulse, the phase of the QCL electric field can be fixed and synchronized to the THz pulses from the photoconductive antenna, and therefore also to the *fs* optical pulses. Once its emission phase is controlled, the electric field of the QCL can then be detected in the time domain by using EO sampling.

As one can notice in fig. 2.7, the setup is similar to that illustrated in fig 2.4 and described in the previous section. In the case depicted here, the antenna is biased by square signals with an amplitude of 3V, a frequency of 40KHz and a duty cycle of 20%. The QCL is maintained just below its threshold by a square electrical signal with a frequency of 20KHz and a duty cycle of 10% The THz pulses generated by the photoconductive antenna are collected by the gold parabolic mirror *PM1* and then injected into the THz QCL by the parabolic mirror *PM2*. Simultaneously, when the THz pulse (seed pulse) is coupled into the QCL, the device is brought above threshold by a radiofrequency (RF) electrical pulse, trigged by the NIR laser pulses via a high-speed photodiode within the Ti:Sapphire laser, as illustrated in fig. 2.8. These RF pulses are short electric pulses with a width of 6ns at the same repetition rate (76 MHz) as the Ti:sa laser. They allow to switch the QCL off and on alternately for coherent sampling between each fs pulse. By synchronizing the injection of the seed pulses to the switch-on of the QCL, these will be amplified until the laser action of QCL will be initiated by the injected THz pulses, and therefore its phase can be completely controlled. In other words, every time the QCL is switched on, its emission has always the same fixed phase directly determined by the *fs* optical pulses. This is shown in fig. 2.8 where the terahertz electric field in green is the emission of the QCL. Since the phase between each THz pulse is the same, the THz electric field can be sampled

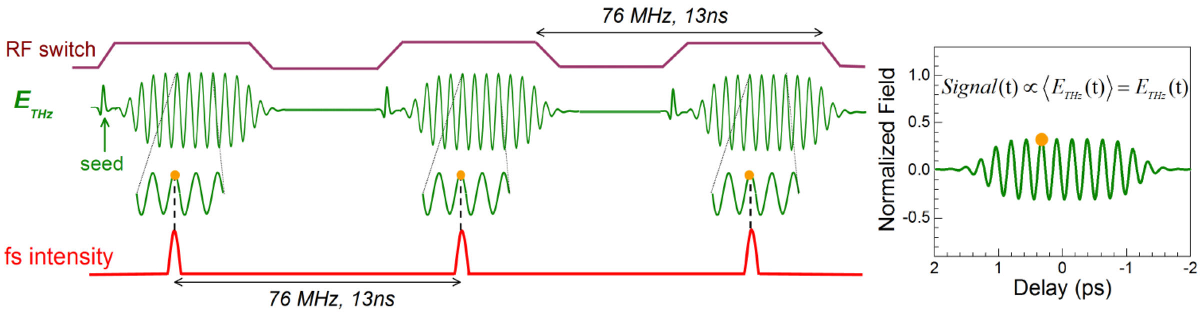

Figure 2.8: Schematic diagram illustrating an example of electro-optic sampling of THz pulses emitted by a QCL synchronized to the NIR pulses. The RF switch curve at the top represents the electrical pulses employed to switch the QCL on and off alternately at the same repetition frequency of the *fs* optical pulses (76MHz). The green curve is the electric field of the QCL emission in the time domain. The seed pulse represents the THz radiation emitted by the photoconductive antenna and coupled into the QCL cavity for the injection seeding technique. The red curve is the 100 *fs* optical pulses generated by the Ti:Sa laser. In the right panel: measured electric field obtained by varying the delay between *fs* optical pulses and THz QCL emission.

always at the same time for each NIR pulse. Averaging at a fixed position will therefore allow the electric field to be recorded with a high signal-to-noise ratio.

The time-resolved electric field of the QCL emission can then be reconstruct by continuously adjusting the delay between the THz field and the *fs* optical pulses, as described above for the case of the antenna. Moreover, it is also possible to determine the entire dynamic of the QCL from the amplification range (generally up to 600ps after the injection of the THz seed) to the steady state regime.

With the injection seeding technique, one retains all the advantages of the typical TDS system, such as a field resolved broad detection bandwidth. Further, this not only allows us to perform the active mode-locking of THz QCLs but also grants access to the ultrafast dynamics of QCLs. For instance, fig. 2.9, which is taken from the original paper demonstrating this technique [69], shows the typical time-resolved electric field emission of a single-plasmon bound-to-continuum THz QCL. The represented device has a central frequency of 2.15THz which is measured thanks to the injection phase seeding technique. In panel (a) one can see the electric field of the QCL recorded from 0 ps to 1500 ps. The THz seed pulse radiated by antenna is injected into the QCL at around -30 ps. Propagating along the laser cavity, the seed gets amplified. When it arrives at the facet opposite to the one where the seed was injected into the waveguide, part of the THz pulse is coupled out and then detected by the TDS, which provides the trace reported in fig. 2.9a at around 0 ps. The delay with respect to the injection represents the propagation time of about 25 ps which corresponds to a single pass through a 2mm long QCL (the refractive index of the material can be assumed to be around 3.6 as a first order approximation). The remaining part of the pulse is reflected back into the cavity and continues to be amplified. After one more round-trip and another reflection at the first facet, it will again be partly coupled out and this is detected as the second pass (in the figure at about 50ps). The process continues in this way resulting in the quasi-periodic pulse-like train that one can see in the first (<600ps) part of fig. 2.9a, with each pulse separated by a round-trip. One can notice that after each round-trip inside the Fabry-Pérot cavity, the pulse is broadened in time owing to the limited gain spectral bandwidth, until the THz wave completely fills the laser cavity. In fact, the dynamic range of the QCL spans from 0ps to 600ps and corresponds to the range where the electric field is broadened and amplified. After 600ps, the QCL emission becomes stable as the gain of QCL saturates (as it gets clamped to the losses) and the amplification ceases. In fig. 2.9b the

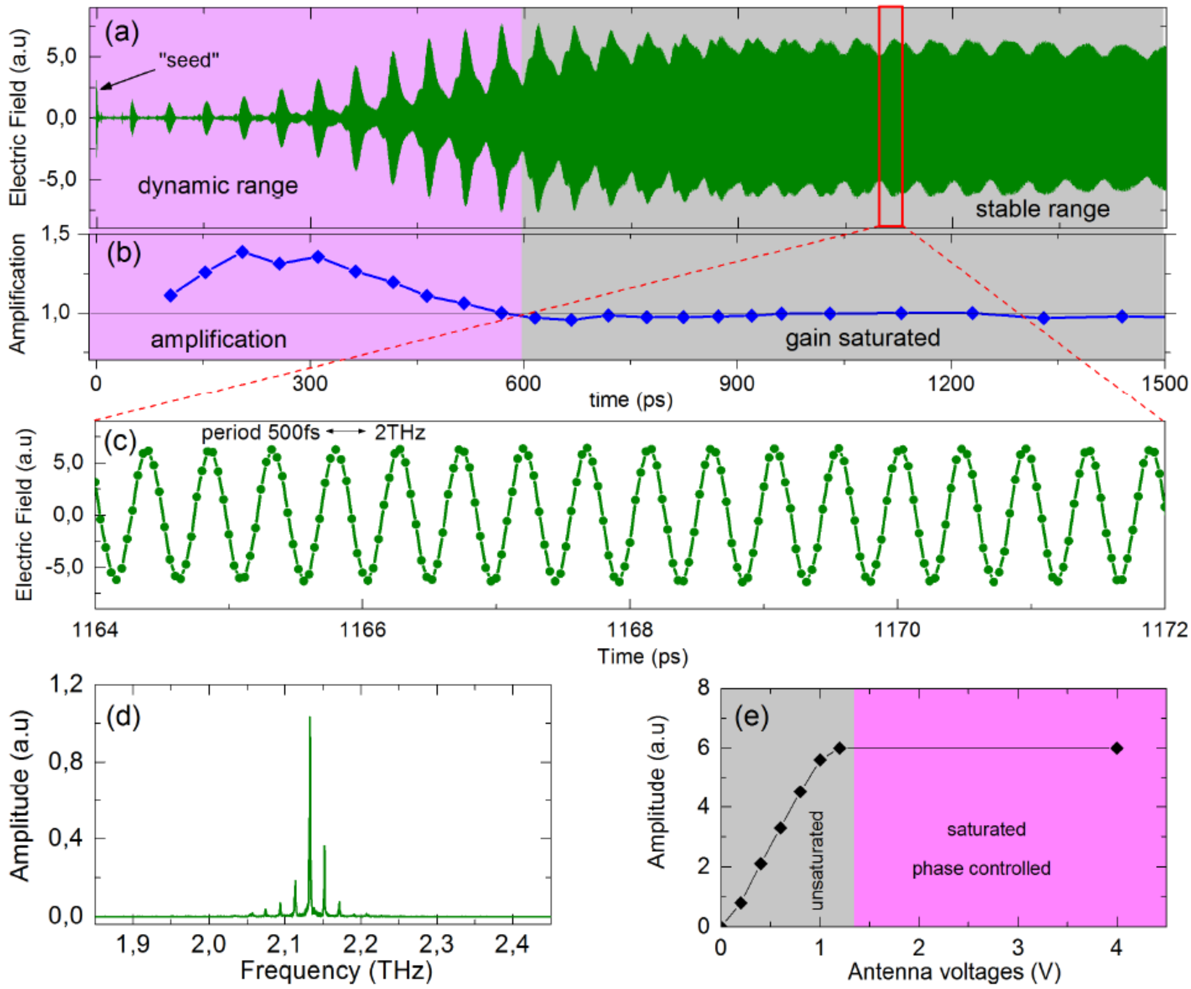

Figure 2.9: Time-resolved emission of a THz QCL measured by the injection phase seeding technique. (a) Electric field of the QCL emission from 0 ps to 1500 ps. (b) The amplification efficiency of the QCL as a function of time (c) Zoom of the electric field of the QCL emission from 1164 ps to 1172 ps. (d) Spectrum of QCL emission obtained by the fast Fourier transform of the trace in (a). (de Amplitude of the electric field of the QCL emission at 1ns as a function of the THz seed power, proportional to the antenna voltage. [Source: *Oustinov et al. "Phase seeding of a terahertz quantum cascade laser". Nat. Commun.1:69(2010)*]

amplification efficiency of the QCL as a function of time is shown, which is calculated by comparing each pulse with the previous one. Before 600ps, the amplification is not clamped to the total losses and thus is above 1. Afterwards, when there is no more amplification it becomes equal to 1 69].
In panel (c) one can find a zoom of the electric field in (a), for the times from 1164 ps to 1172 ps and with the green dots representing each point measured with the TDS. Clear oscillations of the electric field can be reconstructed, having a time period of ~500 ps which corresponds to a frequency of about 2THz. By applying a fast Fourier transform (FFT) on the time trace in (a), it is possible to recover the spectrum of QCL's emission, as shown in panel (d). As previously said, the emission band is centered at 2.14 THz and has a bandwidth of about 150GHz.

One of the most important issue to verify is if the QCL emission is fully seeded by the input pulse. In fact, if the injected power is too weak, the laser action of the QCL will be only partially initiated by the injected THz seed and it will also be partly started by the spontaneous emission. In this detection scheme, only the emission that is phase-locked to the probe pulses can be detected, while the portion of the emission that is initiated by the spontaneous emissions will remain undetected. On contrary, if the injected THz power is strong enough, laser action will be dominated by the seed pulse and the part caused by the spontaneous emission will be inhibited. If this is true, increasing the injected THz power will not lead to an increase of the THz electric field when the gain is clamped and it is possible to use this method to verify the condition of the phase-locking of the emission. Therefore, it is of the utmost importance to inject enough THz power into the laser cavity to totally seed its emission phase and carry out measurements in the saturated region, as shown in the purple zone of fig 2.9e. In this picture, one can see the amplitude of the THz electric field of the QCL at about 1ns as a function of the photoconductive antenna voltage, which is proportional to the electric field amplitude of the THz seed pulse.

The injection seeding technique, that is now well established, is able to entirely characterize the THz emission of QCLs in the time domain from dynamic amplification until gain clamping in the stable range. It represents the main tool employed in this thesis to study the free-running emission and mode-locking characteristics of THz QCLs on femtosecond time scales.

2.4 Mode-locking techniques

Several techniques exist that allow to modelock a laser. According to the laser source, one may be preferred over the others. They can generally be divided in three categories: active, passive and hybrid modelocking. For what concerns the THz QCLs, section **1.5** showed that no stable pulse formation should be able to occur and survive for long in the active medium due to the fast gain recovery time that favors single mode emission. It was also stated that as a consequence of this fact, the output of a QCL always resembles that of a frequency modulated laser, with the (eventual) formation of spectral combs but strictly constant output. Indeed, the measurement of the free-running emission of some of the THz QCLs analyzed with seeding experiments seems to confirm this claim. Therefore, the use of active modelocking has been so far the only available solution to force a QCL to emit pulses. However, since it will be shown in chapter **4** that a QCL can spontaneously generate pulses as opposed to all the previously reported evidence, it is useful to describe all three categories of modelocking techniques.

2.4.1 Active mode-locking technique

Active modelocking is a technique to force a laser to generate pulses by modulating its gain and losses or round-trip phase change at a frequency close to the round-trip frequency. Active modelocking can be realized in several ways, e.g. with Mach–Zehnder integrated optic modulators [85], acousto-optic and electro-optic modulators [86] [87] or with a direct current modulation [88].

The first report of an active modelocked THz QCLs was presented by S. Barbieri et al [14] in 2011 and was soon followed by our group [28]. The employed technique in both works was direct current modulation, which is also the same method I have used in my work. The main idea is to fix the separation and the phase of the modes by applying an electrical modulation that is monochromatic and as close as possible to the round-trip frequency of the laser cavity. It is possible to describe the effect of such a modulation both in the time and frequency domain. Starting from the latter, one can see in fig. 2.10a a simplified representation of a free-running QCL spectrum with three unevenly separated modes.

When the current modulation is applied, the central frequency at f_2 will transfer a part of its energy to its sidebands at $f_2 \pm f_M = f'_1, f'_3$ that are very close in frequency to the two free running

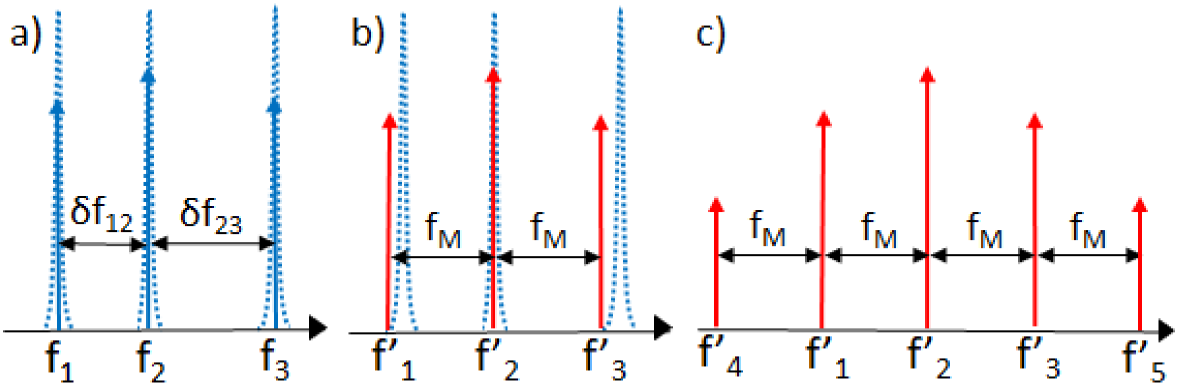

Figure 2.10: Active modelocking acting on the modes of a THz QCL. (a) Three modes are represented from a generic device that are not evenly spaced (separations $\delta f_{12} \neq \delta f_{23}$). (b) The application of a current modulation at frequency f_M enforces a constant mode spacing between the modes. (c) Each mode transfers part of its energy to the neighbouring modes at a separation f_M inducing the rising of side bands. In this way, a mode-locked spectrum is formed

modes f_1 and f_3. If the modulation is strong enough, this will induce the lasing modes at f_1 and f_3 to move towards the sidebands frequencies positions until they totally (fig. 2.10b) overlap and the mode spacing will be locked to the modulation frequency f_M. As represented in fig. 2.10c, the same concept can be applied starting from either f_1 and f_3 so that other side-bands are created from these modes and a mode-locked spectrum with a gaussian envelope tends to form.

In the time domain, one can visualize the effect of the current modulation as schematically presented in fig. 2.11. The QCL is biased just below threshold so no emission can take place.

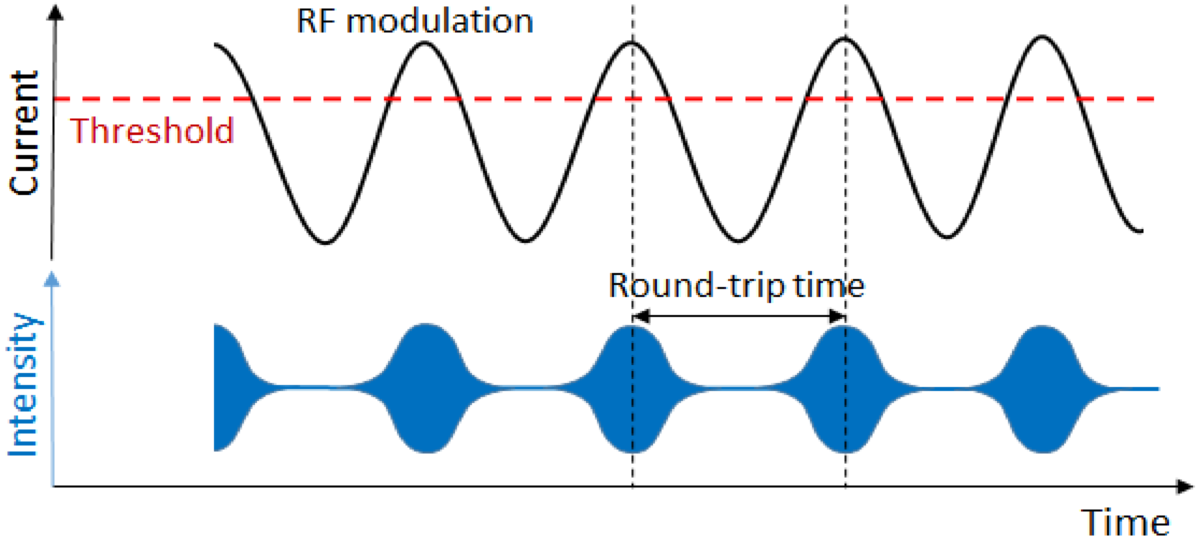

Figure 2.11: Effect of current modulation in the time domain. If the QCL is biased close to threshold (dashed red line), the application of an additional sine wave (solid black curve), with frequency equal to the round-trip frequency to the current, will allow the device to be above threshold for a narrow time window each round-trip. Since emission can only occur when the device is above threshold, a train of relatively short pulses is generated.

When a modulation with a frequency equal to the round-trip frequency is applied, a small portion of the active region will be above threshold in correspondence of the maximum of the sinusoidal waveform, forming a local gain region surrounded by losses. Radiation will then be generated in this small part of the cavity and will start to propagate. Since the round-trip frequency coincides with the frequency of the modulation, the light can propagate following the gain region and be amplified, while the portion of the light which is outside of gain region will experience losses and be quickly suppressed. In this way a pulse is formed which travels rigidly with the sine-wave modulation, meaning that the only modes that are favoured by this mechanism are those in-phase to the current profile. In other words not only the mode spacing but also the phase offset of the modes is fixed to an identical value for all the modes thanks to the active modulation. Therefore, the QCL is modelocked.

The emission profile of an active modelocked QCL is of course a train of pulses separated by the cavity round-trip time (blue curve in fig. 2.11). Owing to the sinusoidal profile of the modulation, however, the obtain pulse duration is generally longer than by employing other modelocking techniques. Since the cavity of a QCL is generally quite short (we usually employ cavities about 3mm long), the frequency of the modulation tends to be quite high (~13GHz for a 3mm cavity) that requires the use of fast electronics and connection lines.

As it was explained in the presentation of the electrical beatnote, its position in the spectrum is generally equal to the round-trip frequency value. It is then important to obtain a beatnote spectrum that can be used to identify the frequency range where it is suitable to choose the frequency of the current modulation for active modelocking. Moreover, if the laser is amplitude

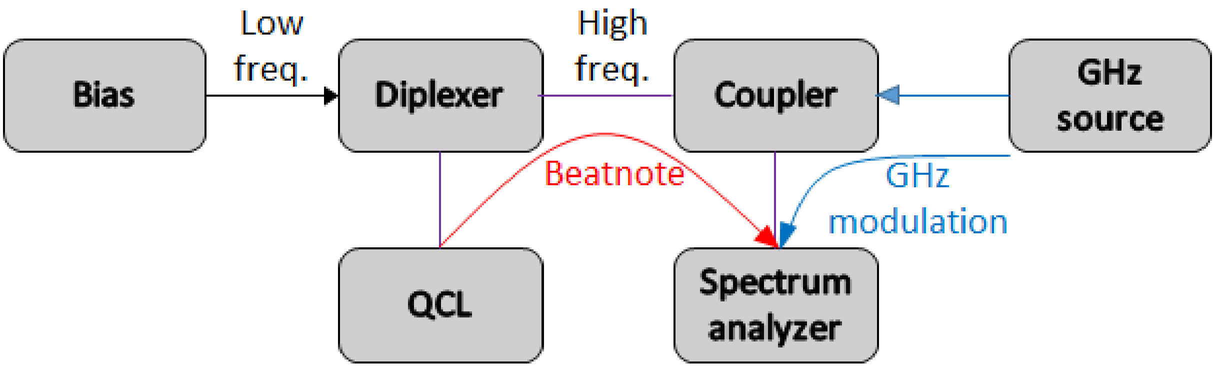

Figure 2.12:Experimental setup for beatnote and injection locking measurements. The source applies a quasi-DC bias to the QCL (black arrow) through a diplexer. The GHz sources sends a high frequency modulation close to the beatnote frequency (blue and purple lines) to a spectrum analyzer and to the QCL through a coupler and the diplexer. The beatnote of the QCL is finally brought to the spectrum analyzer for measurement through the same high frequency line (in purple).

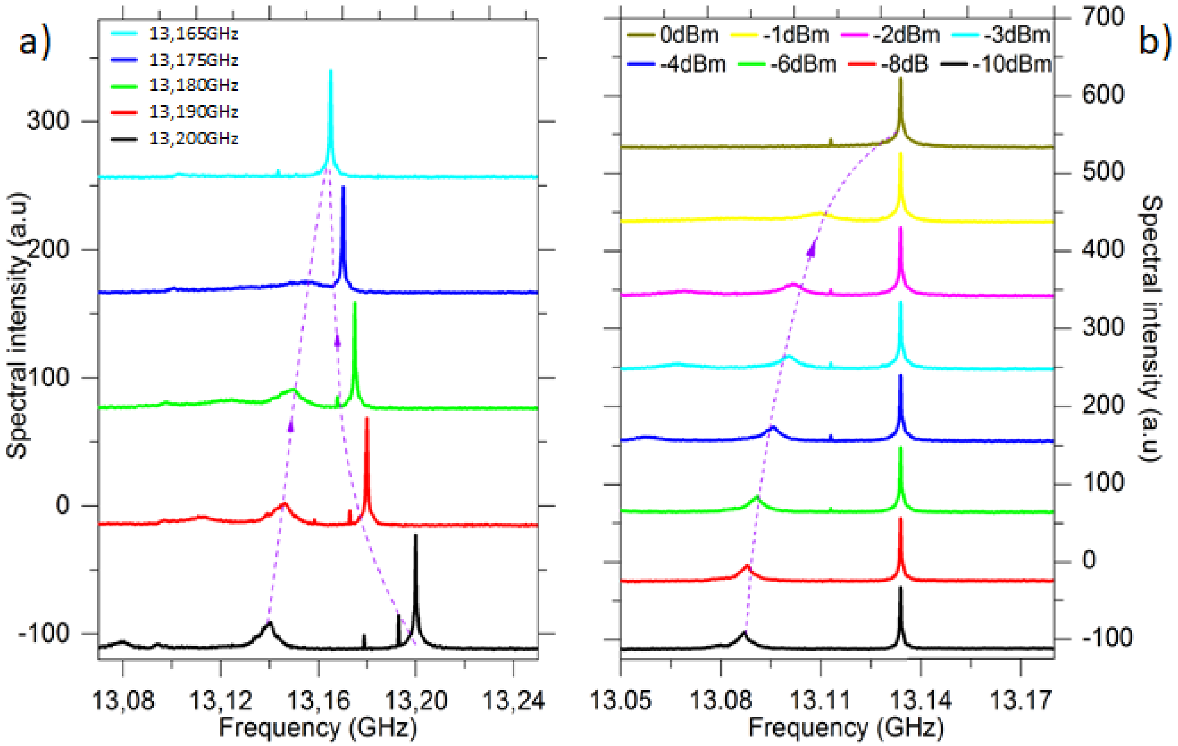

Figure 2.13: Beatnote pulling experiments. (a) A GHz modulation of constant power is applied close to the beatnote. As its frequency is moved towards the beatnote, the latter is pulled towards the modulation frequency. (b) A GHz modulation of constant frequency is applied close to the beatnote. As its power increases, the beatnote is pulled towards the modulation frequency.

modulated, and not purely frequency modulated, its modes must be producing a beatnote at the round trip frequency. One can then prove that active modelocking is achieved only when the beatnote is locked to the active modulation, i.e. the QCL beatnote gets ‘pulled’ to the active modulation. This demonstration is an important preliminary step to determine if a QCL is or can be modelocked.

In this experiment, whose setup is schematically represented in fig. 2.12, a quasi-DC bias is employed to bring a QCL above threshold and a diplexer is employed to combine the low frequency bias and the high frequency modulation produced by a GHz generator which is used to actively mode-lock the device. Thanks to a broadband high-speed spectral analyzer it is possible to display the beatnote of the QCL and GHz modulation frequencies applied on the QCL at the same time. As shown in fig 2.13a, which illustrates the case of a 3mm long QCL, the broad peak at the left side is the beatnote frequency and the thin line on the right is the GHz modulation frequency. The locking range a QCL, which is the frequency range in which the free running oscillator can be locked to the injected power, can be defined [89] as:

$$\Delta f_{lock} = \frac{2f_0}{Q}\sqrt{\frac{P_{inj}}{P_0}} \tag{13}$$

where f_0 is the free-running oscillation frequency, Q is the oscillator Q-factor, P_{inj} and P_0 are the injected power and the free-running oscillator power respectively. From eq. 13 the locking range can be broadened for higher injection powers and this means that it is possible to vary the modulation frequency in a wide range to modelocked the laser. In general, the modulation power required for actively modelock a QCL depends on the optical intensity inside its cavity and the Q-factor of its cavity.

In fig. 2.13a, the pulling effect of the GHz modulation on the beatnote can be made visible in the following way. At first the microwave power is fixed at 0 dBm and its frequency is tuned towards the beatnote. This induces the latter to shift or be ‘pulled’ towards the modulation frequency without undergoing significant changes in amplitude and shape. At the end, the beatnote and the modulation frequency become a single narrow peak when they fall into the locking range. This indicates that the free running mode spacing is locked to the modulation frequency. Even though pulses are not directly demonstrated, this is an indication that active mode-locking has been achieved. Equation 13 also shows that the same pulling mechanism can also be realized by increasing the power of the modulation while keeping its frequency constant. This is demonstrated in fig. 2.13b for a modulation frequency of 13.13 GHz. The modulation power is then increased from -10 dBm to 0 dBm forcing the broadband beatnote to move toward the modulation frequency. When the modulation power is strong enough, the locking range will also be extended such that the beatnote is locked.

2.4.2 Passive and hybrid mode-locking techniques

Passive modelocking [90] is a technique to generate short pulses from a laser source by means of a saturable absorber. To explain the principle of passive modelocking we can consider a laser source whose steady state already displays a pulse propagating in the cavity, and a fast saturable absorber. Every time the pulse passes through the absorber, if it is intense enough it saturates the absorption reducing the losses for a very short time (see fig. 2.14). If the gain is

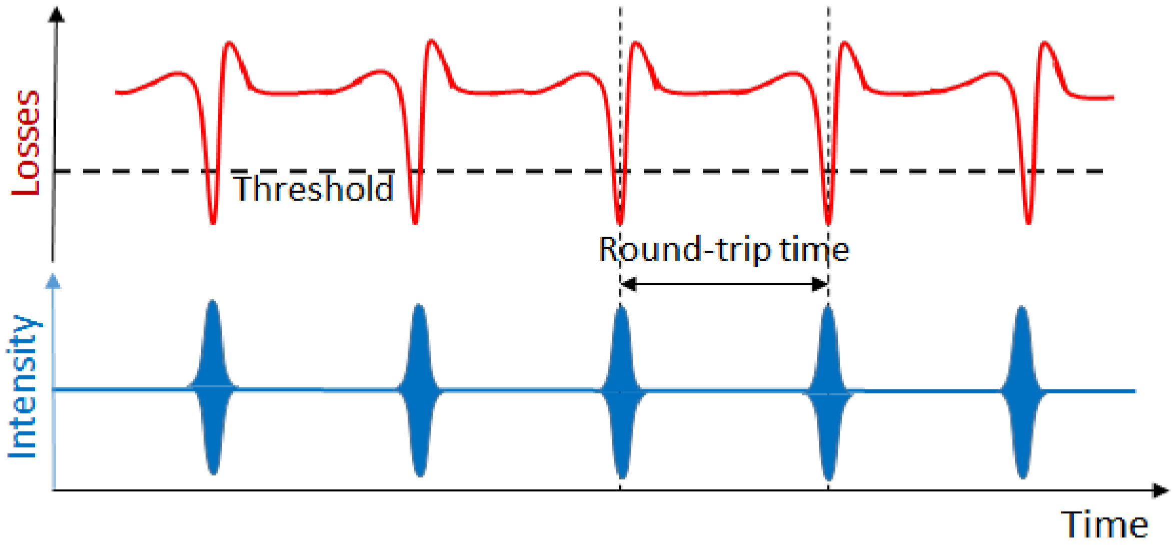

Figure 2.14: Passive modelocking representation. The red line indicates the losses of the saturable absorber. In blue, the electric field time profile of laser source is shown. When a pulse hits the absorber saturating the absorption, a small time window is opened for the transmission of a pulse. As a result, only the central part of each pulse is transmitted while the tails are suppressed thus shortening the pulse. The final duration of the pulse is given by the balance between the shortening and the broadening effects (i.e. dispersion).

correctly adjusted, only at this time the losses can be sufficiently low to open a short time window to let light through for amplification. All the light which enters the absorber before or after the pulse will not have a sufficient intensity to saturate the absorption and will experience a net negative gain throughout a single round-trip, getting consequenctly suppressed. This permits a single pulse to exist in the cavity, and as in the case of active modelocking, this means that both the mode-spacing and the offset phases of the modes must have identical values for all the modes. Moreover, each time the pulse enters the saturable absorber, its tails will tend to be absorbed more than its peak so that very short pulse durations can be achieved as opposed to active mode-locking schemes [91]. The final pulse duration will be given by the balance of the shortening effect of the losses modulation and the other effects which tend to elongate the pulses, e.g. chromatic dispersion.

Passively modelocked lasers can sometimes have start-up difficulties [92] which is not a concern for actively modelocked devices. Moreover, by applying an active modulation on top of an already existing passive modelocking scheme, one can stabilize the phase noise of the laser and, as it was shown with the pulling effect on the laser beatnote, also permits to tune the mode separation at values inside the locking range. Therefore, the combination of active and passive modelocking, i.e. hybrid modelocking [93], is a technique capable of delivering the advantages of both schemes, at the price of additional complexity on the design of the device and in the controlling systems.

2.5 Active mode-locking setup

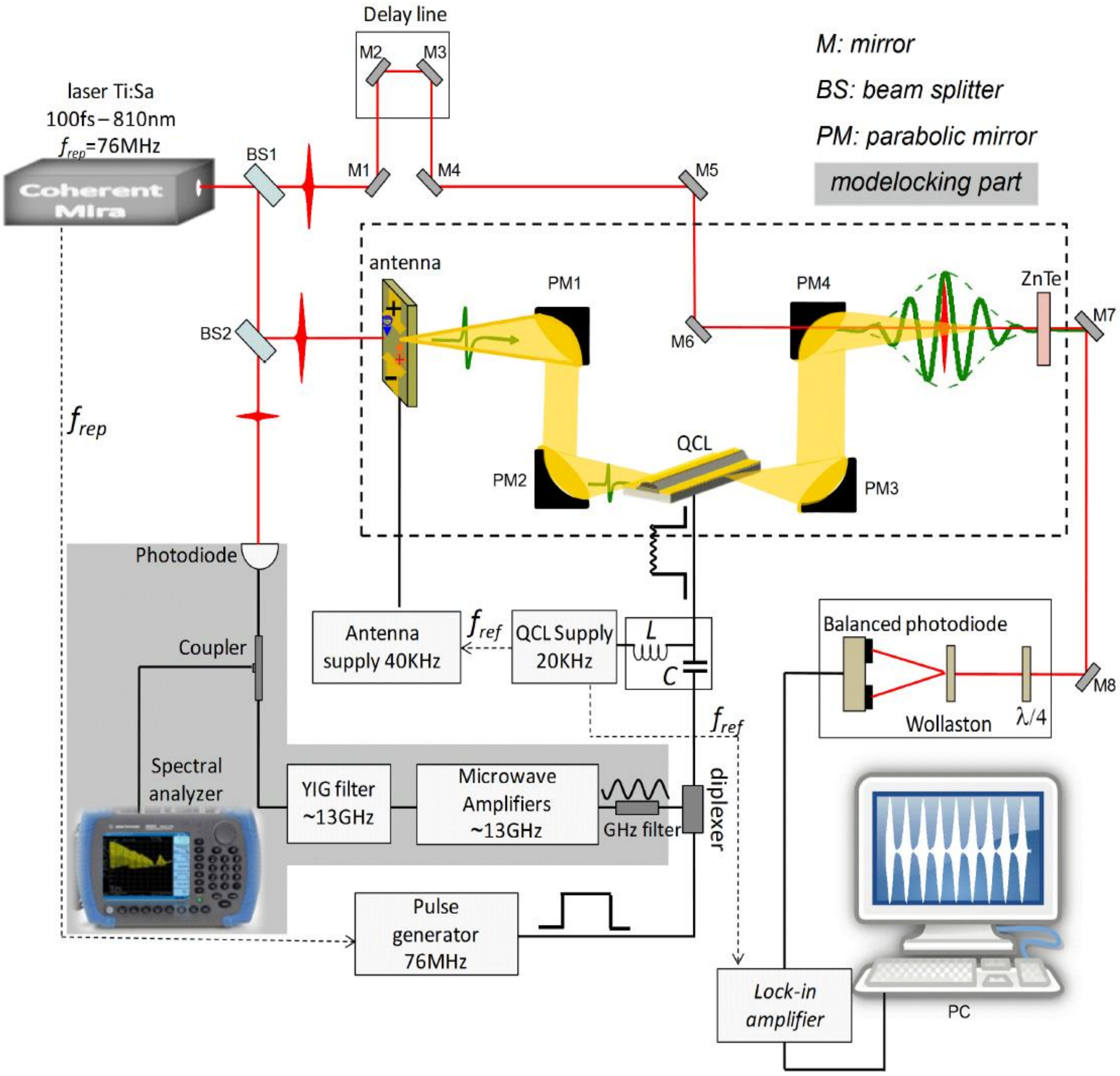

Figure 2.15: Complete experimental setup for injection seeding for free-running and modelocking operation of QCLs. The free running part is the same as portrayed in fig. 2.7. The part of the setup for modelocking is on a gray background.

The experimental setup for the active modelocking of THz QCLs consists in the injection seeding setup presented in chapter **2** with the addition of all the components necessary to apply a GHz modulated current on top of the quasi-DC bias and the RF pulses used in the seeding technique. Figure 2.15 shows in fact the same experimental setup of fig. 2.7 where only the parts in the grey background have been added. The reason is that it is still necessary to fix the phase of the emission of the QCL to the TI:Sa pulses (red lines and pulses) used to sample it. Concerning the parts already described in the previous chapter, the black lines correspond to the electrical connections and dashed gray line to the trigger reference for the 76MHz pulse generator. The green pulses represent the THz pulses from the photoconductive antenna (on the left of the QCL) or the THz QCL (before the ZnTe crystal) and the yellow zones represent the THz optical path. The photoconductive antenna, parabolic mirrors, nonlinear crystal ZnTe and QCL are all inside a sealed box (dashed rectangular region) which allows for purging with a compressed dry air or N_2 system.

The new part of the setup for the generation of the GHz modulation includes a fast infrared photodiode, a coupler, a spectrum analyzer, a YIG filter and some microwave amplifiers. Just before the antenna, a pick off mirror (BS2) is divides the laser beam into two parts, corresponding respectively to 98% (~500mW) and 2% (~10mW) of power. The ~10mW

(a) unsychronized

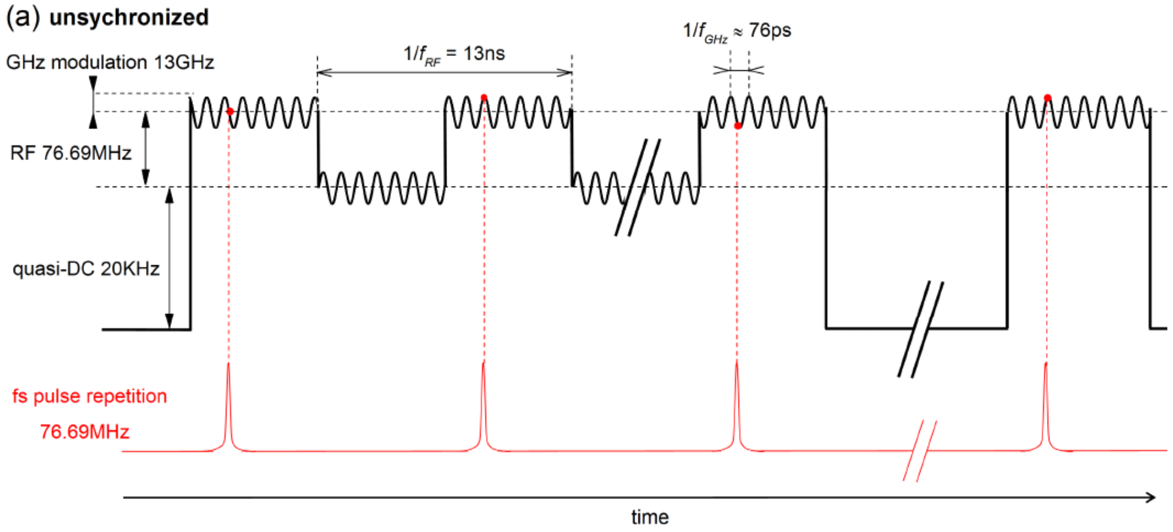

(b) sychronized

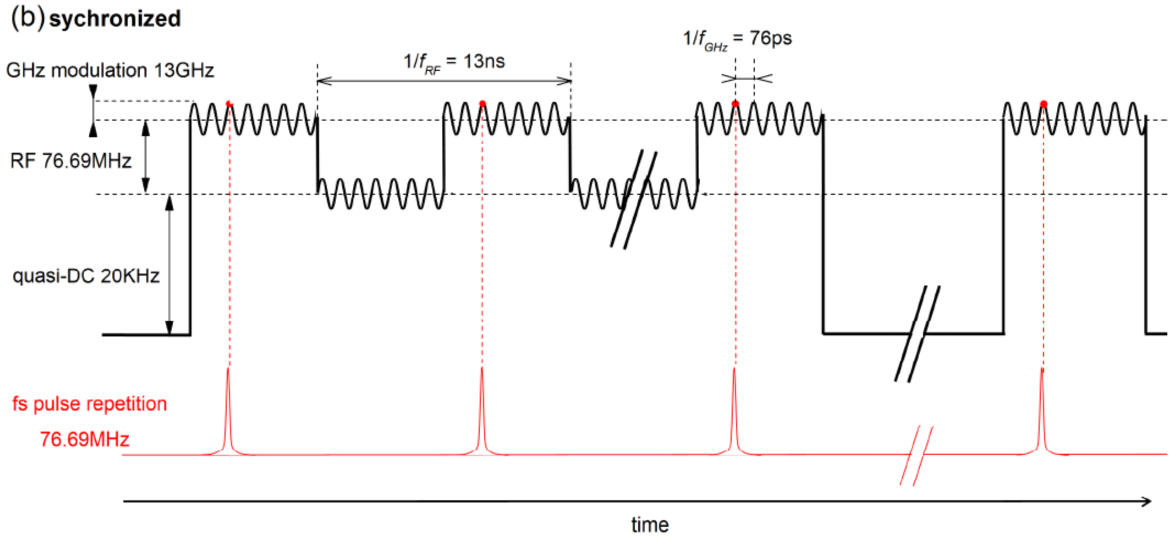

Figure 2.16: Time domain representation of the electrical modulation applied tn a QCL for active modelocking experiments. (a) In the case the GHz modulation phase is asynchronous with respect to the probing fs pulses, the sampling process will lead the average of all the samples to converge to zero. No detection can be successfully be performed in this condition despite the device being modelocked. (b) A synchronous GHz modulation modelocks the QCL and allows for coherent detection

infrared laser beam is then focused on an ultra-fast photodiode (HAMAMATSU GaAs MSM Photodetector G4176-03). The optical pulses will then produce short electrical pulses. Using a high speed spectrum analyzer (Agilent N9344C 20GHz Handheld Spectrum Analyzer), it is possible to measure a comb of electrical signals from around 76 MHz spreading to 20 GHz (the upper limit of the bandwidth of our spectrometer) with a mode separation of 76.69MHz which is the femtosecond pulses repetition rate. A frequency tunable Yttrium-iron-garnet filter (Micro lambda wireless MLFP-1593PD) is then used to isolate a single one of this lines. For instance, the one closer to 13GHz is the 169th harmonic frequency. In this way, a pure sinewave at said frequency is generated. As the power at 13 GHz directly after the YIG filter is rather low (-50dBm), microwave power amplifiers (the most important of them is a Quinstar QPJ-06183846-B0 because of its very high amplification) are used increase the signal power up to ~30dBm. This high power modulation is combined with the 20 KHz DC-bias and the 76 MHz RF pulses by means of a suspended substrate diplexer (11 SZ10 - 6000 /T 18000-O/O) and injected into the QCL to start the active modelocking process.

One of the most important points to make here is that it is not possible to use any GHz generator to apply the active modulation and the reason is that our coherent detection system requires the GHz modulations to be synchronized with the 76 MHz RF pulses or, equivalently, to the infrared femtosecond laser pulses. If an external unsynchronized generator is employed, the QCL emission will be sampled at different times for each round-trip period, as illustrated in fig. 2.16a, and this will result in a “zero” after thousands of averages by the lock-in amplifier. On contrary, when the 169th harmonic frequency of the RF pulses is used, the RF pulses and GHz modulations have a fixed phase relationship every time the QCL is switched on by the RF pulses as shown in panel b). In order to carry the electrical signals that have frequencies at kHz, MHz and GHz, Mini-circuits high speed cables covering the band DC – 18GHz are employed in the setup, thus limiting the loss and distortions the high frequency modulation would experience in unsuitable cables.

The setup configuration presented here is the one employed for the experiments presented in the following chapters.

2.6 Conclusions

In this chapter, the time domain spectroscopy system was presented that provides the basis of investigating the temporal response of QCLs. Its main components were described in detail, with a particular attention devoted to explain the working principles of the THz generation and THz detection parts. An example of the sampling of the signal from a photoconductive antenna was presented to illustrate the concept that allows to record the amplitude and phase information of the THz electric field.

One of the main points discussed in this chapter was that it is not possible to detect the emission of a THz QCL by simply using it as the THz source in TDS in place of the photoconductive antenna. The reason is that the QCL's emission shares no phase relationship with the NIR pulses used for detection. Therefore, no measurement of the THz field is possible unless the QCL is phase-locked to them. The problem is solved by means of the injection seeding technique, whose principles and implementation in the setup have been presented in detail. Particular importance was given to the control of the QCL's emission properties, in particular regarding the conditions to achieve full phase seeding and ensure the complete characterization of the THz electric field from a QCL.

The implementation of an active modelocking system to the TDS setup was thoroughly described. In particular, the use of an active modulation synchronized to the Ti:Sa round-trip frequency was highlighted as the major requirement for this kind of measurements. The next chapter will introduce the concept of chromatic dispersion in THz QCLs and its importance related to the generation of ultra-short pulses in THz QCLs.

The next chapter will introduce the concept of chromatic dispersion in THz QCLs and its importance related to the generation of ultra-short pulses in THz QCLs.

3

Dispersion in THz QCLs

The refractive index of a material is generally not constant with the frequency. As a result, the phase velocity and the group velocity of the optical radiation travelling through a medium are frequency dependent. This phenomenon is referred to as chromatic dispersion. In the time domain, the effect of dispersion is that different optical components will propagate at different speeds, thus broadening an optical pulse as it will acquire a chirp while passing through a dispersive medium.

The chirp of a pulse can be considered as the time dependence of its instantaneous frequency. When a pulse is unchirped, its instantaneous frequency is constant and it has minimum duration for a given bandwidth. It is therefore of great importance to reduce or eliminate the chromatic dispersion to enable the generation of ultrashort pulse trains. This can be done by introducing specific dispersion compensating elements, such as grating pairs, photonic crystal fibers, prism pairs and chirped mirrors for radiation in the visible range. In the THz range, very few solutions exist as a result of the immaturity of the domain and difficulties of working at such long wavelengths.

In this chapter, sources of dispersion and their compensation in THz QCLs are investigated, as well as their implication in pulse generation. In particular, a theoretical derivation of the material and QCL gain dispersion is presented in section **3.1**. Dispersion compensation schemes investigated in this thesis are analysed in section **3.2**, with a focus on integrated Gires-Tournois interferometers (GTI) and other GTI-like structures. Full electromagnetic simulations are shown to improve our knowledge beyond the conventionally employed analytical approach. As well as an integrated approach, section **3.3** shows the simulations a novel concept of tunable dispersion compensation using an external cavity, that was successfully implemented, in collaboration with Scuola Normale Superiore, Pisa (IT). Finally, the effects of the dispersion on pulsed QCL emission are investigated in section **3.4** by means of numerical simulations of active modelocking, performed in collaboration with the University of Queensland (AU).

	Sample 1	**Sample 7**
Growth code	L1458	L857
Processing lab	CNR (Pisa)	C2N (Paris)
Active region (periods)	2.5THz(55) 3THz(40) 3.5THz(40)	3THz(180)
Active region scheme	Hybrid structure [94]	Hybrid structure [47]
# wells	9	4
Waveguide	Double Metal	Double Metal
Length/width/height	2.9mm/85µm /17µm	2.7mm/100µm /12µm
Side absorbers (width)	6.5µm	2µm

Table 3.1: Properties of the samples employed in chapter **3.** The dimensions refer to those described in fig.1.9

The THz QCL which is employed to study the effect of the tunable GTI in section **3.3** will be henceforth referenced in the text as “Sample 1”. Despite the fact that the experimental results from Sample 1 presented in this chapter were obtained in Pisa, I first characterized it with the THz TDS at LPENS. The design is based on a multiple stack geometry to enhance the spectral bandwidth. The latter experimental results will be presented in section **4.5** of the next chapter as they show a significant advancement towards the generation of sub-ps pulses. Details about the QCL design, growth and geometry used in this chapter to illustrate the effect of dispersion can be found in Table 3.1. Dispersion compensation is particularly important for these samples as the spectral bandwidth is large. The LIV curves, obtained from a pyroelectric detector, and the beatnote spectrum can be found in Annex **3.1.1**. In a similar way, the numerical simulations of section **3.4** bases some parameters on those of the device described in [17]. The device will then be called “Sample 7” and its characteristics are once again reported in Table 3.1. Its LIV and beatnote map are reported in Annex **3.1.8**.

Chapter 3

3.1 Sources of dispersion in THz Quantum Cascade Lasers

With regard to the radiation traveling through a THz Quantum Cascade Laser, three main sources of dispersion can be identified as the material, the gain and the waveguide [95]. In the following subsections, each one of these contributions will be analysed from a theoretical point of view. The results obtained here will be employed in section **3.4** to show the global effect of dispersion on pulsed QCL emission.

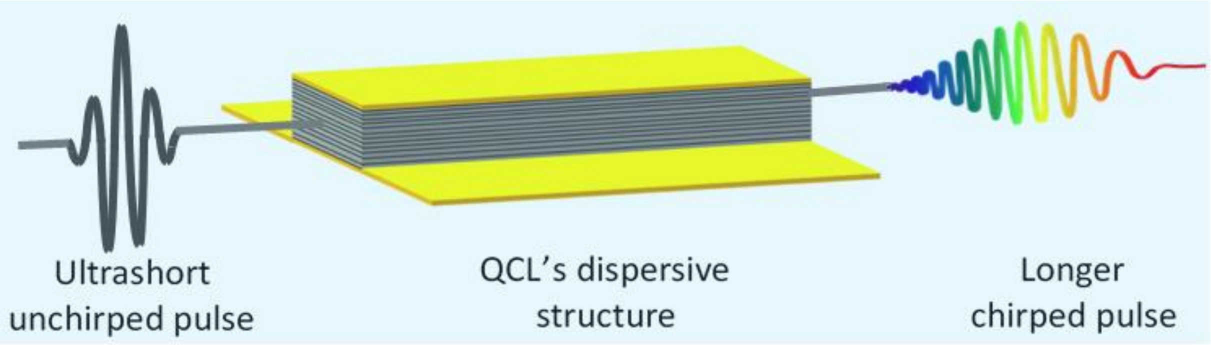

Figure 3.1: Graphical representation of the effect of the QCL's dispersion on an ultrashort pulse. The broadening of the ultra-short pulse injected in the cavity from the left facet is displayed as a long pulse emitted from the right facet.

3.1.1 Material dispersion

THz QCLs cavities are made of a stack of quantum wells usually based on the GaAs/AlGaAs material system. These materials do not possess a constant refractive index with frequency, especially in the THz range due to the proximity of the reststrahlenband at ~8THz, and as a consequence the light travelling in the cavity experiences strong chromatic dispersion.

The function representing the dispersion profile of the material can be obtained from the frequency dependent refractive index. For the sake of simplicity, the material of the cavity can be treated as bulk GaAs and a Drude-Lorentz model can be applied to derive the formula of the refractive index. Experimental values for the fundamental constants can then be plugged into the latter and used to extract the dispersion as detailed below.

The expression for the dielectric function, according to the Drude-Lorentz model, can be written as:

$$\varepsilon_r(\omega) = \varepsilon_1(\omega) + i * \varepsilon_2(\omega) = \varepsilon_\infty + \frac{\Omega_{TO}^2(\varepsilon_0 - \varepsilon_\infty)}{\Omega_{TO}^2 - \omega^2 - i\gamma\omega} \qquad (14)$$

where ε_∞ and ε_0 are the high frequency and static dielectric functions of GaAs respectively, Ω_{TO} is the frequency of the transverse optical vibrations in GaAs and γ is the damping factor. Values that are generally used are reported in Table 3.2.

Using the following notations for the refractive index and the dielectric constant

$$\tilde{n}(\omega) = n(\omega) + i * k(\omega) \tag{15}$$

$$\varepsilon_r(\omega) = \varepsilon_1(\omega) + i * \varepsilon_2(\omega) \tag{16}$$

the real part of the complex refractive index can be written [96] as

$$n(\omega) = \sqrt{\frac{\sqrt{\varepsilon_1^2(\omega) + \varepsilon_2^2(\omega)} + \varepsilon_1(\omega)}{2}} \tag{17}$$

and it is plotted in fig. 3.2. The imaginary part is reported in Annex **2.1**.

Property	Value	Unit
ε_∞	10.60	1
ε_0	12.74	1
Ω_{TO}	8.2	THz
γ	3.5	cm^{-1}

Table 3.2: Material constants of GaAs

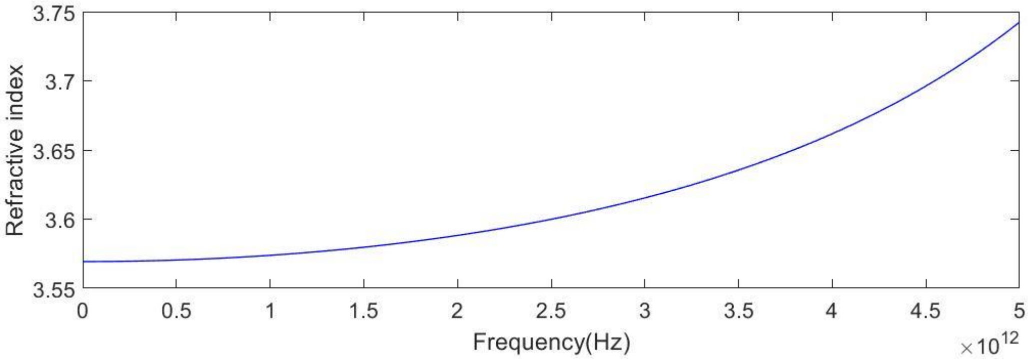

Figure 3.2: Frequency dependence of the refractive index of GaAs as resulting from equation (17) with the parameters of Table 3.2

The group velocity is then obtained from

$$v_g(\omega) = \frac{c}{n(\omega) + \omega\left(\frac{dn(\omega)}{d\omega}\right)} \tag{18}$$

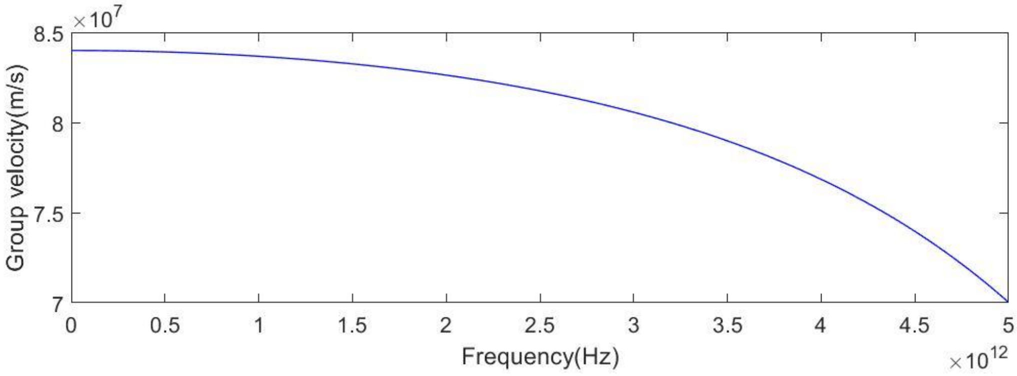

Figure 3.3: Frequancy dependence of the group velocity of GaAs as obtained from equation (18)

Finally, the dispersion per unit of length, called Group Velocity Dispersion (GVD), can be written as:

$$GVD(\omega) = \frac{d}{d\omega}\left(\frac{1}{v_g(\omega)}\right) \tag{19}$$

and shown in fig. 3.4.

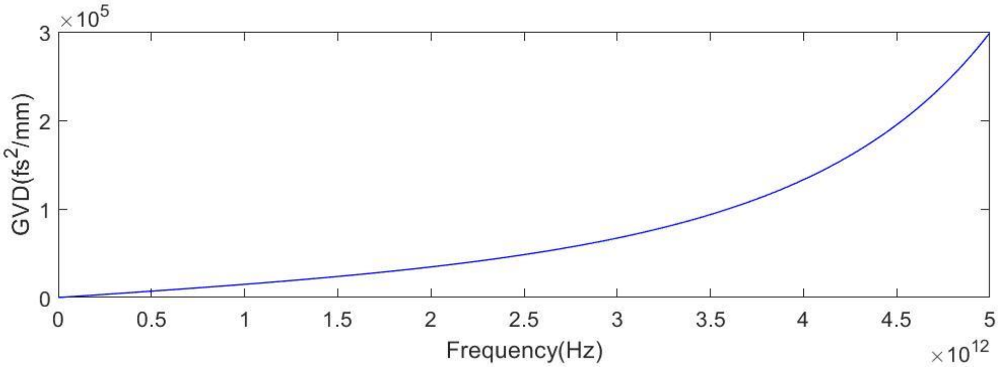

Figure 3.4: Frequency dependence of the group velocity dispersion of GaAs as resulting from equation (19)

For the radiation travelling in the medium for a certain length, the GDD (Group Delay Dispersion) can be used to address the total amount of dispersion it has accumulated:

$$GDD(\omega) = GVD(\omega) * l \tag{20}$$

being "l" the distance that the light has travelled across.

Overall, the material introduces a slow varying GDD to the dispersion experienced by the radiation propagating into the cavity. While not negligible, this is usually less significant than that provided by the gain for the range of frequencies we are interested in (from 1.5THz to 3.5THz). This will be further discussed in the following section.

3.1.2 Gain dispersion

The gain of the laser is another factor to consider in order to compute the total dispersion function of a QCL due to the fact that it introduces a variation to the refractive index in correspondence of the spectral gain bandwidth. It is possible to write the gain as a function of the imaginary part of the susceptibility χ(ω), that in turn is related to the relative dielectric function by the following expressions:

$$\chi(\omega) = \chi'(\omega) + i * \chi''(\omega) = \varepsilon_r(\omega) - 1 \tag{21}$$

$$\tilde{n}(\omega) = \sqrt{\big(1 + \chi'(\omega)\big) + i * \chi''(\omega)} \simeq 1 + \frac{1}{2}\big(\chi'(\omega) + i * \chi''(\omega)\big) + \cdots \tag{22}$$

by developing the square root in series and approximating up to the linear components, we get the real part of the refractive index being equal to

$$n(\omega) \simeq 1 + \frac{\chi'(\omega)}{2} \tag{23}$$

and the real part of the susceptibility can be derived from the imaginary part from the Kramers-Krönig relations [97]:

$$\chi'(\omega) = \frac{2}{\pi}\int_0^{\infty} \frac{\omega' * \chi''(\omega')}{\omega'^2 - \omega^2} d\omega' \tag{24}$$

By approximating the gain to its first order expansion, one gets

$$\alpha \simeq -\frac{\chi''(\omega) * \omega}{c} \tag{25}$$

It is then possible to obtain the refractive index change which is introduced as long as a suitable expression for the gain is provided. A common choice consists in approximating the gain with a Lorentzian function [98]:

$$\alpha(f) = \frac{\alpha_g}{1 + \left(\frac{f - f_c}{\gamma}\right)^2} \tag{26}$$

where α_g is the maximum value of the gain, f_c the central frequency of the Lorentzian and γ its HWHM (half width at half maximum).

In this case, the real part of the susceptibility reads:

$$\chi'(f) = \frac{\alpha_g c}{\pi^2 n_m(f)} \int_0^{\infty} \frac{1}{(f'^2 - f^2)\left(1 + \left(\frac{f' - f_c}{\gamma}\right)^2\right)} df' \tag{27}$$

$n_m(f)$ represents the real part of the dielectric function of the material. Once again, it is possible to solve this equation numerically with a dedicated software.

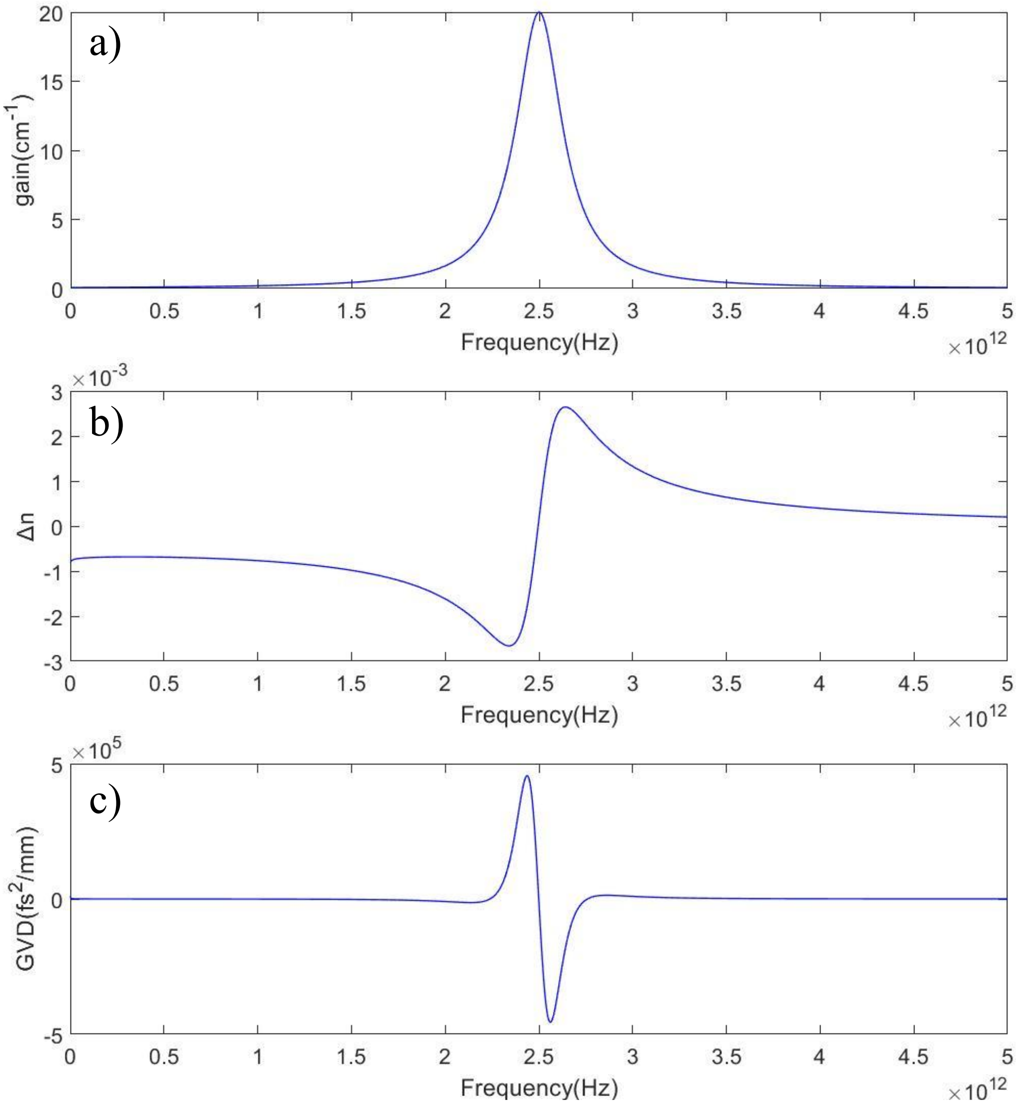

Figure 3.5: (a) Lorentzian gain from equation (26) with the parameters of Table 3.3, (b) induced refractive index change resulting from plugging equation (27) in the expression of (23) and (c) GVD profile obtained from the second derivative of (b) over the angular frequency

Parameter	Value	Unit
α_g	20	cm^{-1}
f_c	2.5	THz
γ	0.15	THz

Table 3.3: Gain parameters used to plot the curves in fig. 3.5.

The gain parameters in Table 3.3 (corresponding to the Sample 2 described in the next chapter) produce the gain profile, refractive index change and GVD reported in fig. 3.5 (a-b-c respectively).

The refractive index variation induced by the gain introduces a fast-changing modulation in correspondence to spectral gain of the laser, thus strongly affecting its operation. It has also to be noticed that despite the gain profile being symmetric with respect to its central frequency, the total dispersion is not, as the material adds a monotonously increasing offset to the one of

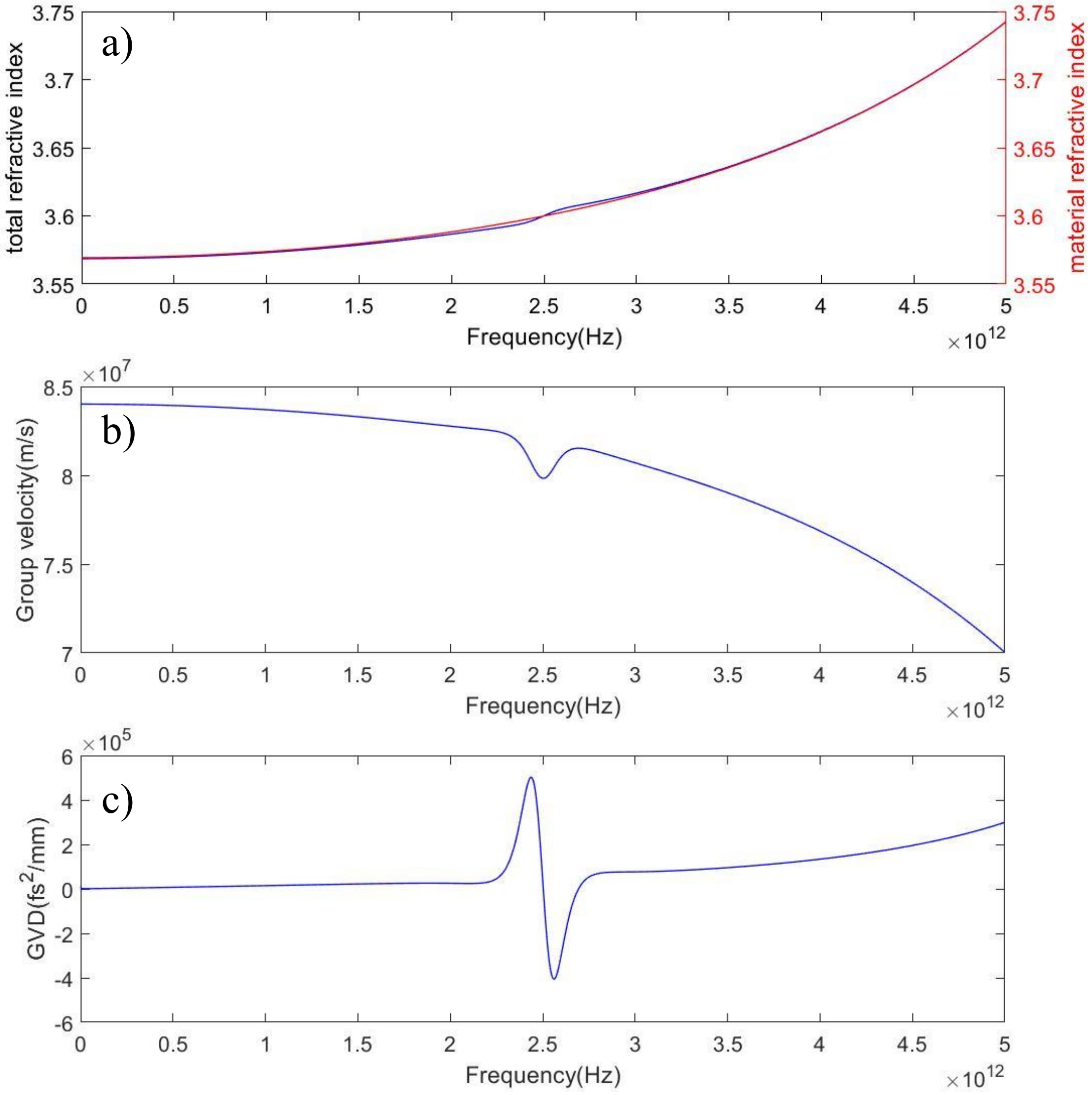

Figure 3.6: Profiles of (a) the total (material + gain) refractive index (in blue) and the GaAs refractive index (in red), (b) the total group velocity and (c) the total GVD

the gain. Moreover, the gain adds both positive and negative components in a relatively small range of frequencies. This adds to the complexity of realizing a suitable dispersion compensating method.

Figure 3.6a compares the material refractive index, in red, with the total refractive index in blue which includes both material and gain contributions. The effect of the latter appears as a small modulation centered at 2.5THz, the central frequency of the Lorentzian. Panel (b) shows the computed group velocity. Here the effects of the gain are clearer in the form of a local decrease of the group velocity centered around the designed gain. Panel c), the GVD clearly shows that the gain is the strongest contribution to dispersion in the emission band of the laser. It is therefore necessary to introduce in the system an additional element with a dispersion profile of opposite sign with respect to that induced by gain to obtain dispersion compensation.

3.1.3 Waveguide dispersion

The high confinement of the double metal waveguides, together with the better suitability for carrying RF current modulations compared to the single plasmon architecture (chapter **1**), is one of the main reasons these are employed for broadband applications. The waveguide dispersion that these structures induce has to be considered. Although an analytical approach could again be used, in order to account for more detailed geometries, a software for electromagnetic simulations is employed.

The simplest case consists of a slab of GaAs, having the frequency dependent refractive index computed in **3.1.1**, sandwiched in between two Au layers. An example of the mode profile,

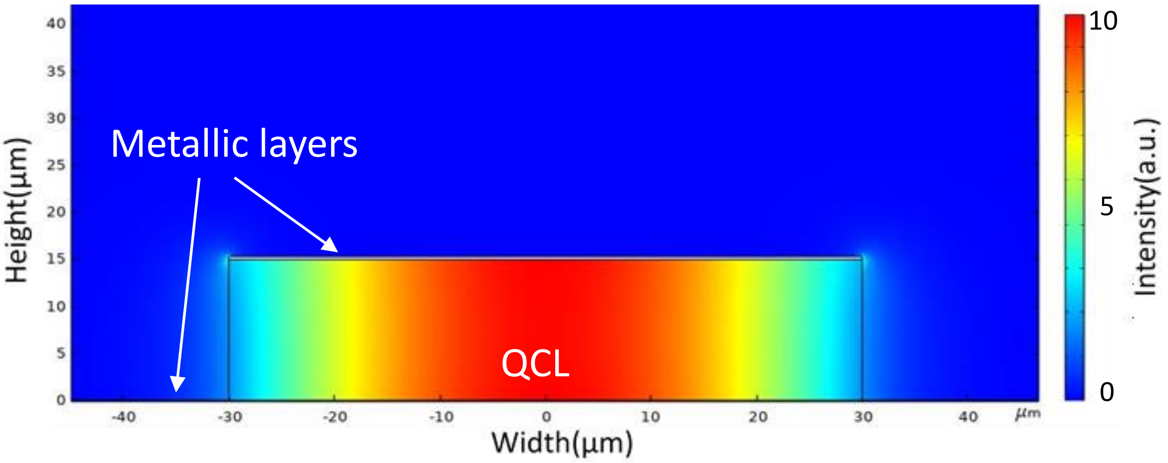

Figure 3.7: Spatial distribution of the fundamental mode intensity of a 60µm wide double metal waveguide at 3.5THz

calculated using Comsol Multiphysics, is shown in fig. 3.7 for a 60µm wide waveguide with a GaAs thickness of 15µm and gold layers thickness of 0.3µm at 3.5 THz. More complex designs, including n+ layers and side absorbers (see section **1.3.1**), are generally used but the most basic case is illustrated here for the sake of generality.

A frequency sweep can be used with a mode analysis study to retrieve the effective modal index dependence on frequency, as plotted in fig. 3.8a. This can then be used in the theoretical derivation of the dispersion in place of the original material refractive index. It is also possible to compute the contribution of the waveguide alone by considering the difference of the effective mode index to the index of GaAs. When this is done, one can find a dispersion profile similar to that of fig. 3.8b. The most important consideration that has to be made is that the waveguide does not introduce a significant amount of dispersion for frequencies greater than 1THz. For this reason, it is fair to assume in most cases that its overall contribution to the total dispersion is negligible, at least for waveguides wider than 60µm and the QCL emission at frequencies greater than 2 THz. From this point on, unless differently specified, the dispersion of the waveguide will not be considered.

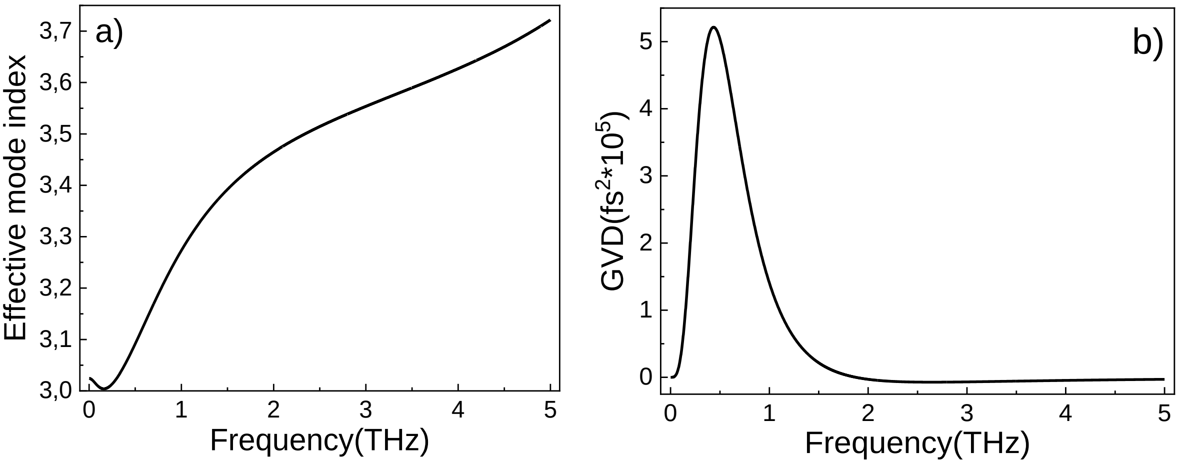

Figure 3.8: (a) Effective mode index of the waveguide and (b) waveguide dispersion profile

In conclusion, generally the most important sources of dispersion are related to the gain and the material. Since the gain becomes clamped at laser threshold, it may be thought that the dispersion it provides could undergo the same effect leading to its reduction in the lasing band (a flat gain profile adds no dispersion to the total function). As investigated in [67] though, this is not the case and the dispersion increases for higher and higher biases even if the gain remains clamped. Therefore, the calculation of the total dispersion performed in this chapter still holds. In the following section, methods to compensate the dispersion will be discussed.

3.2 Integrated dispersion compensation schemes

In the previous section the main sources of dispersion were analyzed, that result in pulse broadening in time. We can then consider dispersion compensation to be one of the major challenges we need to realize to achieve efficient short pulse generation. While at optical wavelengths varied solutions to obtain a excellent control over dispersion are available, such as grating pairs, photonic crystal fibers, prism pairs and chirped mirrors, in the THz range only a limited number has been proposed, e.g. coupled waveguides [99], double chirped mirrors [100], plasmon-enhanced waveguides [101] and Gires-Tournois interferometers [17].

In this part of the chapter, THz QCLs with integrated short cavity that acts as a GTI are investigated. This choice as the main method of compensating for the QCL dispersion relies fundamentally on their simple design and fabrication, and higher reproducibility of their effect with respect to other proposals. Before providing further details about this solution applied to QCLs, standard GTIs are presented.

3.2.1 Gires-Tournois Interferometers

GTIs are a variant of Fabry-Perot resonators whose main purpose is compensating for chromatic dispersion. Once extensively used in femtosecond lasers, these devices present a relatively simple structure, schematized in fig. 3.9a. In the ideal case, they consist of two mirrors r_1 and r_2, with r_1 having low reflectivity while r_2 being a perfect mirror, separated by a medium of refractive index *n* and thickness *d*. Therefore, they are supposed to be used in reflection, and the total reflectivity should be unity over the entire frequency range they have been designed for, while the phase φ is modulated with the wavelength according to the mirror separation as expressed by the formula the formula

$$tan\left(\frac{\varphi}{2}\right) = \frac{1+r_1}{1-r_1} tan\left(\frac{\omega\tau}{2}\right) \tag{28}$$

where $\tau = 2n_g l/c$ is the round-trip time and $r_1 = \sqrt{R_1}$ with R_1 the reflectivity coefficient for the intensity of the front mirror.

This means that the dispersion profile the GTI introduces can be written [17] as:

$$GDD = -\frac{2\tau^2(1-r_1^2)r_1 sin(\omega\tau)}{\left(1+r_1^2-2r_1 cos(\omega\tau)\right)^2} \tag{29}$$

An example for l=76µm, n_g=3.6 and r_1=0.1 is plotted in fig. 3.9b

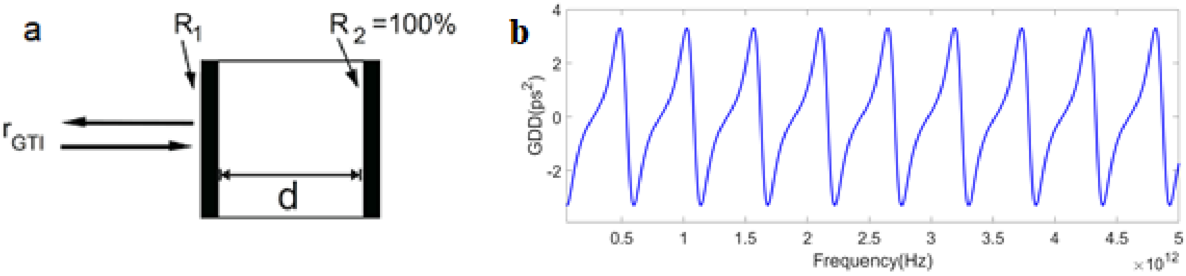

Figure 3.9: (a) Schematic of an ideal GTI; (b) example of the chromatic dispersion introduced by an ideal GTI

In a different fashion than the ideal case, the GTIs integrated to the QCLs have to work in a transmission configuration so to be employed in seeding experiments (as it will be presented from chapter **4**). This is possible as the back mirror is one of the original facets of the QCL's cavity and it is not an ideal mirror. We have then to modify equation 28 as

$$\varphi = -arctan\left(\frac{(1-r_1^2)sin(\omega\tau)}{\frac{r_1}{r_2}+r_1r_2-(1+r_1^2)cos(\omega\tau)}\right) \qquad (30)$$

to account for r_2 being lower than 1 [17]. An example of the GDD and reflectivity profiles of a non-ideal GTI are showed in fig. 3.10. As a general rule longer cavities will provide higher dispersion, but the resonances will also be closer to each other, resulting in a narrowing of the usable dispersion band.

It is important to notice here that the resonances of the GTI (Faby-Perot cavity) correspond to the minima of the reflectivity. This fact will be used later to ease the interpretation of the experimental data.

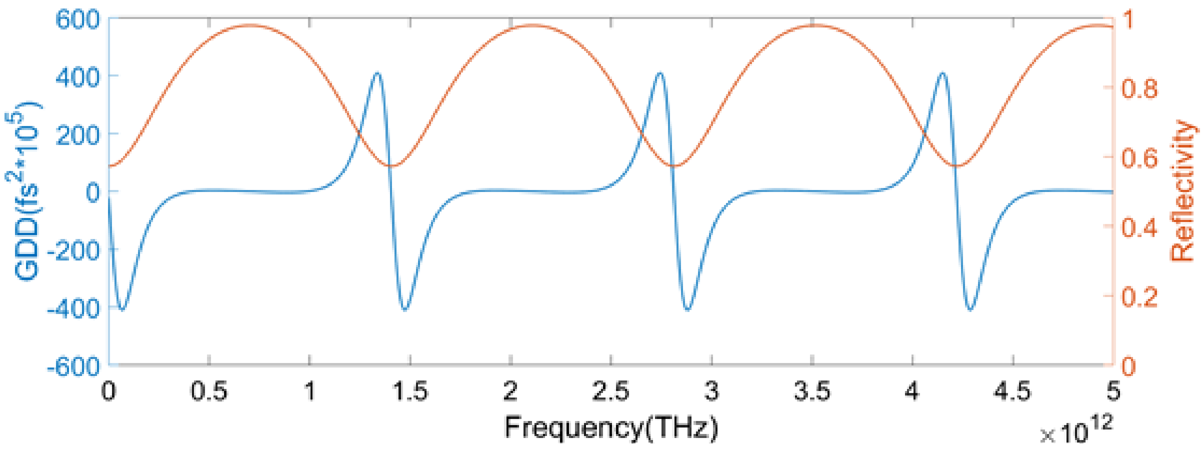

Figure 3.10: Example of the dispersion (blue) and reflectivity (orange) profiles of a non-ideal GTI

To take into account the real geometry of the GTI coupled to a QCL, detailed electromagnetic simulations on Comsol Multiphysics were performed for each structure. To confirm the reliability of our simulation tools, the dispersion of a Si cavity, acting as a Fabry-Perot resonator, was experimentally measured and compared with the theory and simulations. (As the GTIs employed for our devices were directly integrated to the metal-metal QCL cavity (see fig. 3.12), it was not possible to experimentally retrieve the GTI contribution to the dispersion). A 76µm thick, high resistivity Si wafer (HR-Si) was tested in transmission configuration in a THz-

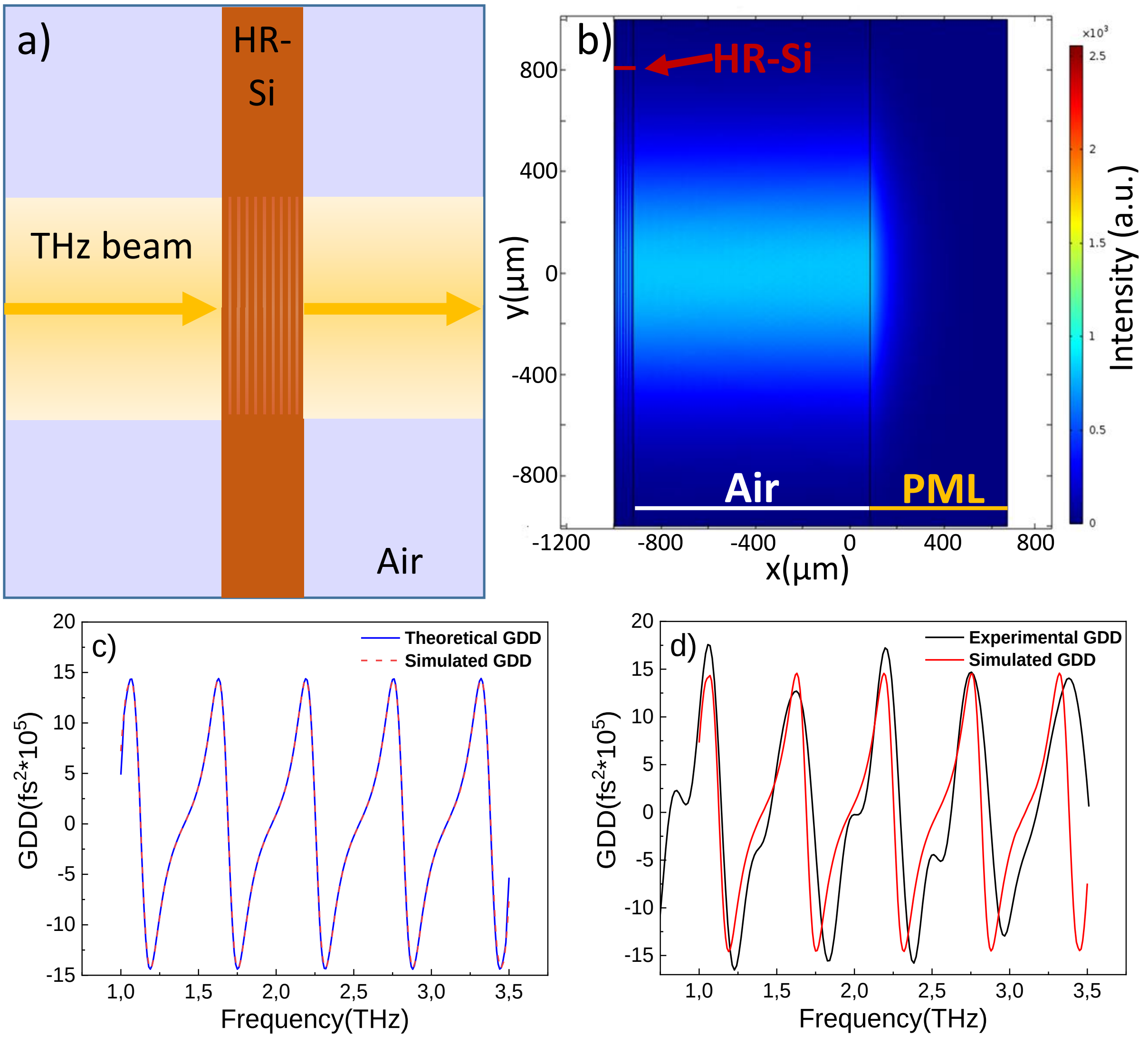

Figure 3.11: (a) Representation of the TDS transmission configuration used to retrieve the GDD from the HR-Si sample; (b) simulated electric field distribution at 3.5THz from Comsol. The input port, corresponding to the left border of the picture, is at a sub-wavelength distance from the Si wafer while on the right side a perfectly matched layer (PML) is used to ensure the absorption of the radiation. Comparison in between (c) the theoretical (plain blue) and simulated (dashed red) GDD (d) the experimental (black) and simulated (red) GDD.

TDS (fig. 3.11a) and the setup was reconstructed on Comsol to simulate the results (fig. 3.11b). A constant refractive index of 3.5 for the Si was assumed.

The simulated transmission results for a Gaussian beam impinging on a semi-infinite Si slab (with the same refractive index used for theory) were then compared with the theoretical formulae (see above). In the case of the simulations, the phase of the scattering parameter S11, corresponding to the phase of the complex reflectivity read at the injection port, is considered for the computation of the GDD. Figure 3.11c shows the almost perfect agreement between the two. The experimental results were also compared with those simulated on Comsol and are plotted in fig. 3.11d. As one can see, the constant refractive index approximation holds mainly at low frequencies, while at higher frequencies, where the refractive index diverges from 3.5, the local maxima tend to shift with respect to the simulated ones. Despite the approximation the values are in fair agreement, validating the approach for the design of dispersion based on GTI-like structures.

These will be treated in further details in the next sections, including results from both simulations and experiments. The effect of the GTIs on THz QCLs will also be presented for free-running and for modelocked emission.

3.2.2 GTI-like coupled cavities

GTIs coupled to QCLs have been previously realized by a dielectric coating for MIR devices [68]. For wavelengths corresponding to THz QCLs, however, layers on the order of ten of micron thicknesses would be necessary, that is impractical and very difficult to reproduce. In order to avoid complex fabrication processes, the structure of the QCL waveguide can be

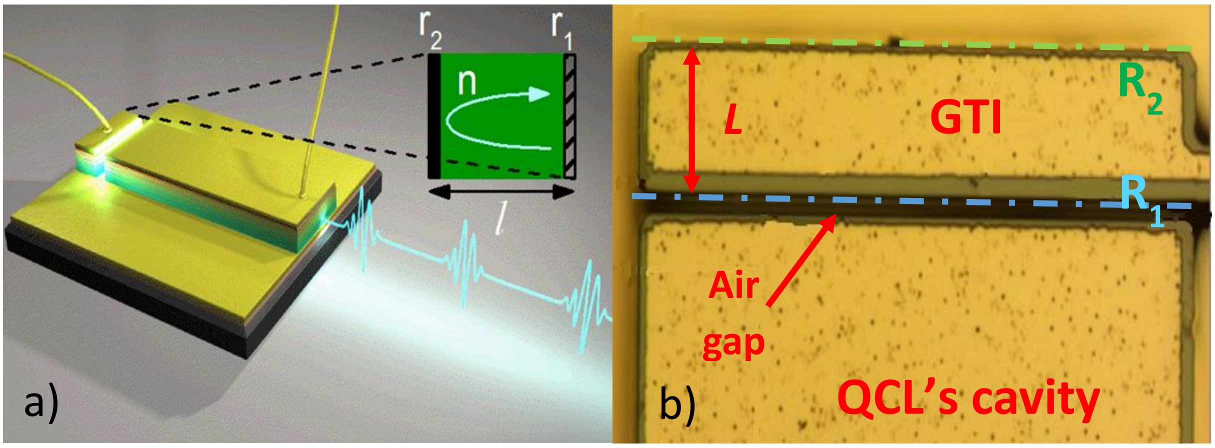

Figure 3.12: (a) Artistic representation of a QCL with an integrated GTI; (b) top-view of a 19µm long GTI-like coupled cavity etched at one end of the QCL's facets

exploited to create a separated cavity with high field confinement, that acts as a GTI. This is done by etching a thin air gap, usually about 2-4μm wide, into the active region at a specific distance '*L*' from one facet of the QCL. In this way, a GTI-like section is integrated right at one end of the QCL, as illustrated in the representation of fig. 3.12a. Figure 3.12b shows instead a top-view obtained at an optical microscope of a coupled cavity at one end of a QCL.

As previously said, the distance '*L*' from the QCL facet at which the air gap is etched is the main parameter to design the GTI, as it represents its length and therefore it is the most important factor for determining the profile of the dispersion introduced by the coupled cavity. A secondary factor is instead the size of the air gap. The effect of this parameter was studied by simulations and the results are plotted in fig. 3.13, where the dispersion profile at a resonance is reported for a gap size of 2, 4 and 6μm. As one can see, the dispersion increases with the gap size. This is a result of the higher value of the reflectivity of the front mirror r_1 which is due to the greater separation of the facet of the QCL to that of the GTI. It is then possible to tune the amount of dispersion we want to introduce in the system with the GTI also by setting the proper gap size other than just the cavity length. Values at least 4μm are generally employed to achieve compensation as the maximum GDD due to the gain and the material is usually in the order of ~1-2ps². Nevertheless, the etching process is rather complicated due to the high aspect ratio of the gap. The etching is required in fact to reach the bottom gold layer that is ~10-17μm in depth

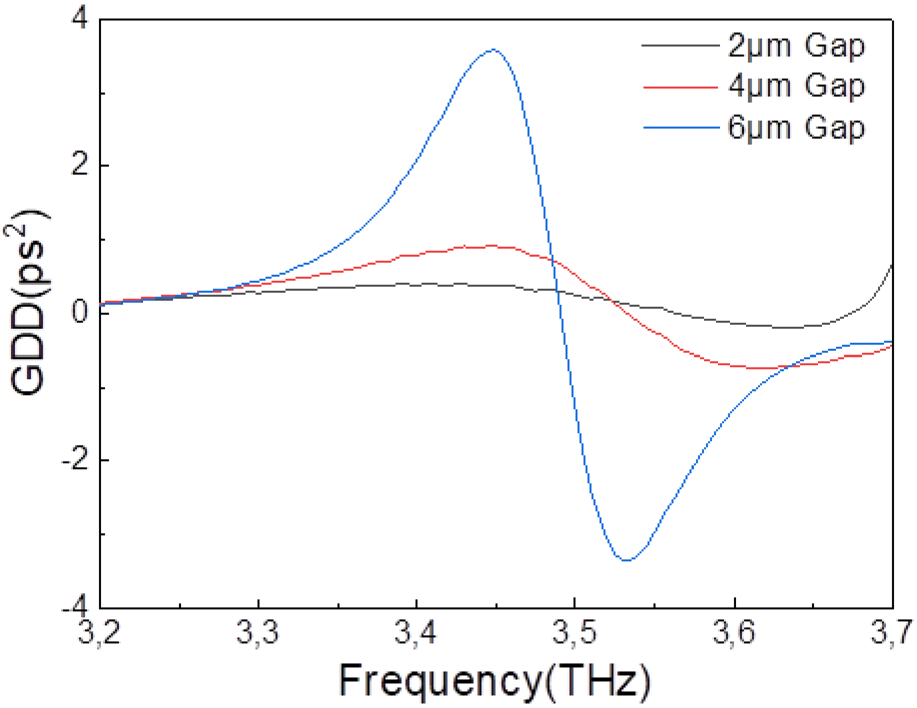

Figure 3.13: GDD profiles around 3.4THz at a resonance of a 30μm long coupled cavity for a gap size of 2μm (black), 4μm (red) and 6μm (blue).

with respect to the top of the waveguide. For this reason, other architectures of the compensation scheme were also analyzed. These will be presented in the following section.

3.2.3 Other GTI-like structures

Some variants of the previously described GTI-like structure were considered as possible candidates for integration to QCLs in order to obtain a better dispersion compensation. The reason for this further investigation is also to find a simpler structure with respect to the GTI described in the previous section, and more specifically to avoid the etching of the active region. A 30µm length is chosen for all the following structures, which were simulated in the 3D environment of Comsol, in order to allow for comparison. A waveguide width of 60µm was employed that is sufficient to minimize the effect of the waveguide dispersion.

A first simple choice for a structure can be realized by removing a strip of the Au top layer without extending the gap to the active region. This can be done by Focused Ion Beam [102], which can sputter the atoms from the surface of the metal with sub-micrometric precision, instead of chemical etching, that already simplifies the processing.

The idea behind this design is that the change of refractive index due to the removal of the gold should induce a certain degree of reflectivity at the gap interface, that could then be thought as a low reflectivity input mirror. Figure 3.14a shows a graphical representation of the device while fig. 3.14b reports the simulated dispersion profile. As it can be seen, the response is considerably different from that of an ideal GTI as two regions of high dispersion are visible at about 2.4THz and 3THz. While compensation is obviously not achievable in correspondence

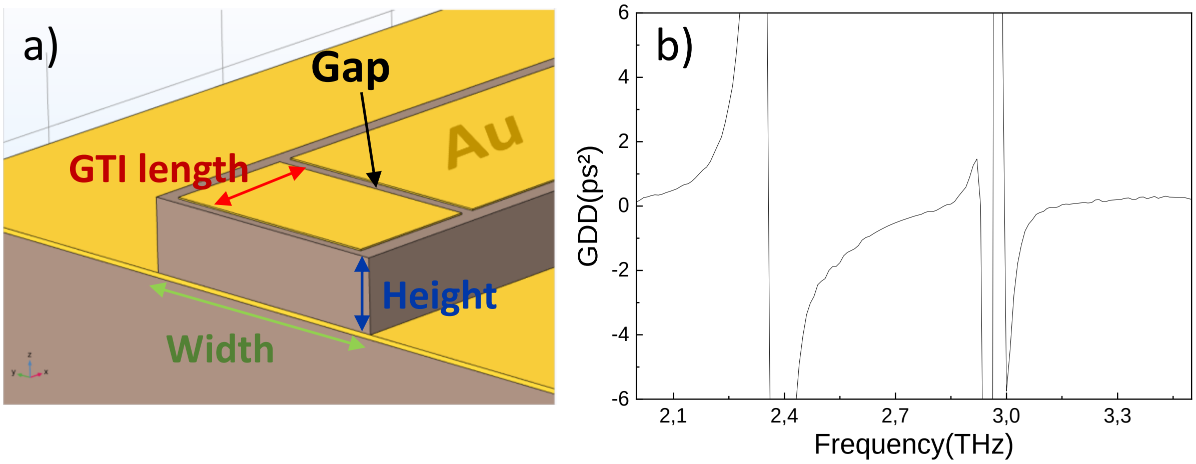

Figure 3.14: (a) Schematic of a 30µm long, 60µm wide and 10µm high cavity obtained by removing a 3µm strip of gold from the top-Au layer and (b) the simulated dispersion profile

of such a strong dispersion, the range from 2.5THz to 2.9THz is still quite adapted to be applied to a QCL designed to work at those frequencies.

Similar results can be obtained and more finely tuned by changing the length and the position of the Au layer and the size of the gap, but, as already said, the high dispersion features are unlikely to be removed thus making this kind of design still not perfectly suitable for ultra-broadband applications.

The second variant consist in etching the top gold layer on the last few microns before a facet of the QCL cavity. It can be obtained from the previous design by removing the gold after the gap. Once again, at the interface of the gold layer with the etched area, the radiation experiences reflection making this part of the cavity working similarly to a GTI. The lack of light confinement due to the missing metallic layer on the etched section of the cavity locally lowers the effective mode index significantly. The deposition of a dielectric in place of the Au, as reported in [103], is a viable option to tailor the dispersion profile but once again this would require some additional fabrication steps, making the realization of these devices less straightforward. The simulated dispersion profile for a 30μm etched GTI-like section is reported in figure 3.15b together with a representation in panel (a). In the same picture, the red curve represents the GDD introduced by a coupled cavity GTI of the kind described in section **3.2.2** having the same dimensions of the variant analyzed here.

The dispersion profile shows two resonances at about 2.5THz and 3.15THz, but one can easily notice that the one at lower frequencies exhibits a behavior that is opposite in sign with respect to that of a general GTI. The reason for this is that at those frequencies the effective mode index

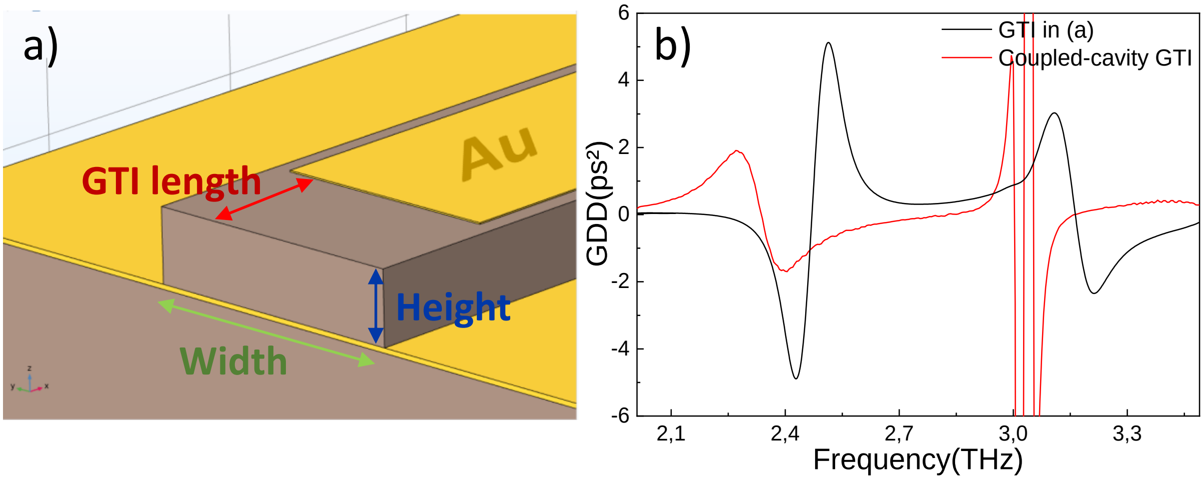

Figure 3.15: (a) Schematic of a 30μm long, 60μm wide and 10μm high cavity obtained removing the top-Au layer and (b) the simulated dispersion profile introduced by the GTI represented in (a) (black) compared to a coupled cavity GTI as described in section **3.2.2**.

in the coupled cavity defined by the missing Au layer becomes so low due to the lack of confinement that the output reflectivity R_2 is smaller than the input reflectivity R_1. In this situation, quite narrow resonances appear with the order of the oscillations inverted with respect to the usual case. For the example provided here, this unfortunately also implies that the dispersion introduced in between the two resonances results to be overally positive. On contrary, a broad negative region is visible above 3.15THz that could be employed for dispersion compensation. Moreover, the resonance at 2.5THz could also be directly applied to a QCL designed for narrow band application and high output, which will therefore have a high gain and a strong gain dispersion that can be perfectly compensated by this coupled cavity design.

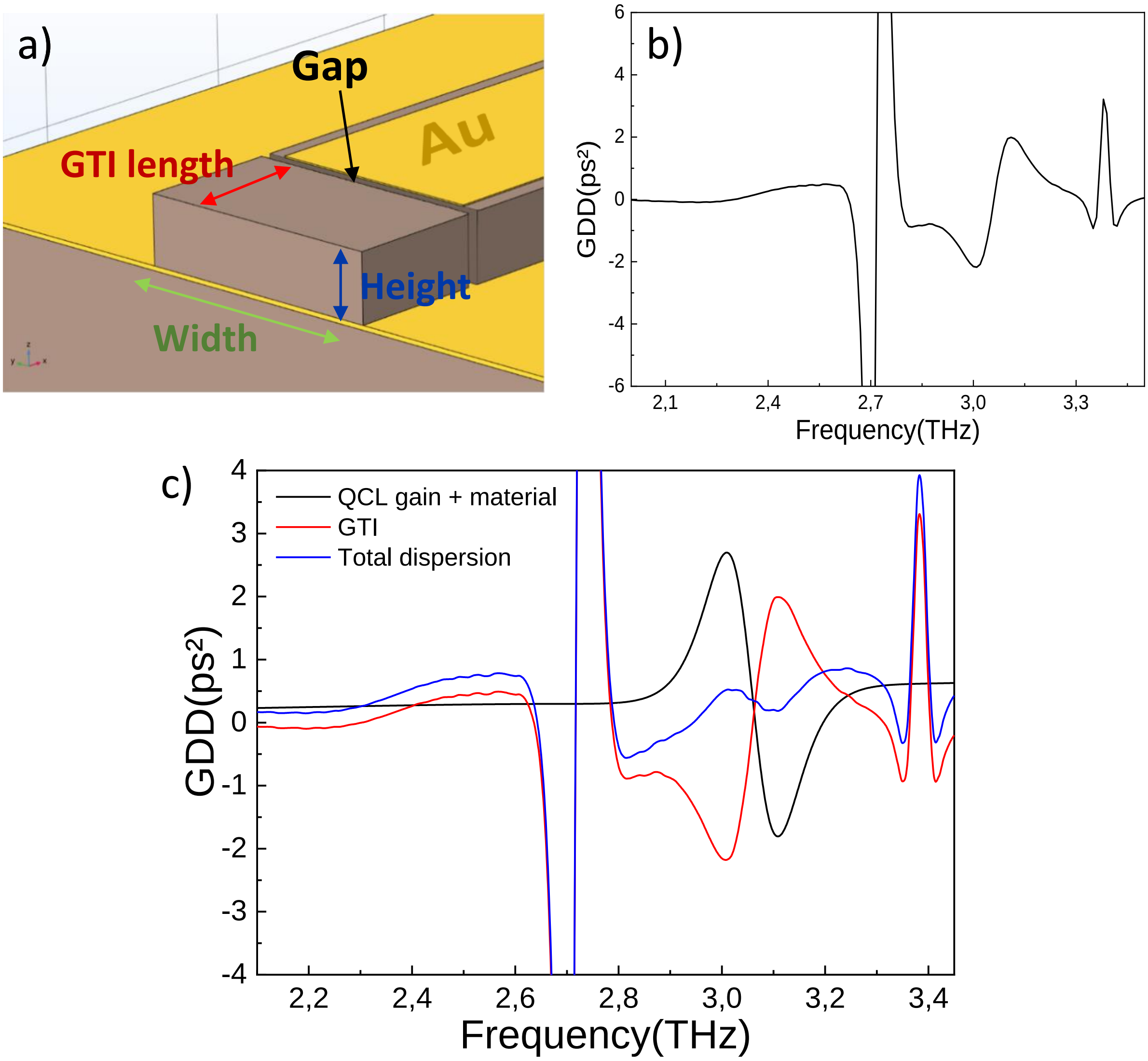

Figure 3.16: (a) Schematic of a 30μm long, 60μm wide and 10μm high cavity obtained by etching a 3μm gap in the active region and removing the top-Au layer and (b) the simulated dispersion profile it introduces. (c) An example of dispersion compensation employing this structure. The Lorentzian gain used to compute the dispersion in black has a peak value of 10cm^{-1}, a FWHM of 120GHz and a central frequency of 3.05THz. A QCL length of 3mm was employed.

An important consideration that has to be made for this structure is that the two parameters affecting its response are the length of the gold layer removed, which obviously defines the size of the cavity, and the height of the active region (for the simulations reported in this chapter, a value of 10µm was chosen for the height). The latter is essential for operation at low frequencies, as it can strongly affect the frequency position of the resonances and the overall ratio R_2/R_1 which in turn determines the behavior of the dispersion profile.

One last design was studied as a possible modification to the GTIs described in section **3.2.2** that are already integrated to several samples. The change consists in removing the top Au layer on the separated coupled cavity or, in a similar fashion, the same structure can be obtained from that of fig. 3.15a by extending the gap through the active region at the interface with the main QCL cavity. Figure 3.16a shows a graphical representation and the panel (b) of the same picture reports the dispersion profile for a 3µm gap and the usual 30µm cavity size.

The gap changes the value of the input reflectivity and the effects are reflected in the dispersion profile: the resonance at 2.4THz that was present in fig. 3.15a has not disappeared completely, but it has flatten to the point of being barely visible. This fact is accentuated by the strong oscillations at 2.7THz that were absent in the previous case. The resonance at 3.1THz has not significantly changed in magnitude, but it has now the opposite sign with respect to before. This fact means that adding the gap it is possible to keep a higher input reflectivity even at higher frequencies, resulting in a dispersion profile opposite to that of a standard GTI and that is in principle better suited for compensating the gain dispersion of a QCL as fig. 3.16c shows. However, the kinks that appear in the dispersion profile at 2.7THz and 3.4THz make the application of this design much less desirable, and given the very strong dependence of the response of these devices to the geometrical parameters, the reliance on a perfect fabrication process hinders the possibility of their consistent reproducibility. For this reason, intermediate configurations, i.e. with a partial removal of the top gold layer or a gap not reaching the bottom of the structure, were not thoroughly studied even if they could lead to better dispersion profiles for specific QCLs.

In fact, while effective in compensating the dispersion for the single QCLs they have been designed for, all of the solutions described in this section still lacks the tunability to be applied to very different devices or to finally control the dispersion. In the following part of this chapter, tunable GTIs are discussed, that could become better candidates for generalized application than integrated structures.

3.3 Tunable GTIs

In the previous section, integrated GTIs for dispersion compensation of THz QCLs were discussed. Their implementation results in very compact structures that can be realized within the typical fabrication procedure. However, each integrated GTI provides a fixed dispersion profile, and therefore needs to be carefully designed to compensate for the dispersion of the device. Moreover, as discussed in the previous sections, the gain component of the dispersion depends on the bias applied to the device such that perfect compensation can only be achieved on a limited operational current range of the QCL. The capability of tuning the dispersion introduced by the GTI is therefore desirable to extend the compensation condition to a broad bias and spectral range. A tunable dispersion compensation scheme based on an external retro-reflector was recently demonstrated [104] for MIR QCLs, but no equivalent design has been shown for THz QCLs where dispersion is high. In this section it will be showed that the same principle can be applied to THz QCLs. This work was in strong collaboration with Scuola Normale Superiore/CNR where I provided the concept and performed the analysis of the dispersion from both the theoretical and the experimental point of view, with the setup and experiments realized by Francesco Mezzapesa at Miriam Vitiello's CNR group in Pisa (IT)

3.3.1 Scheme design

The dispersion compensation structure consists in an external flat mirror in gold ($R \approx 1$) which is perpendicular and in close proximity to a facet of the QCL and whose position can be mechanically tuned by a piezoelectric actuator with micrometric sensitivity (between a few microns to ~ 200µm from the QCL end). An artistic representation of the system is in figure 3.17. This concept allows for the implementation of a GTI-like structure, where the medium in between the mirrors, one being the golden mirror and the other the facet of the QCL itself, is air.

The limited feedback into the cavity when using a flat external mirror affects the response of the system that is different from a standard GTI. It can be shown, in fact, that in the case of a spherical mirror with curvature roughly equal to the reciprocal of the distance of the mirror from the QCL, the back-coupling of the radiation into the cavity is almost 100% and the GDD profile is exactly the same as a perfect GTI (see Annex **2.2**). In the case of a flat mirror, the amount of radiation coupled back into the QCL depends on the divergence of the output beam,

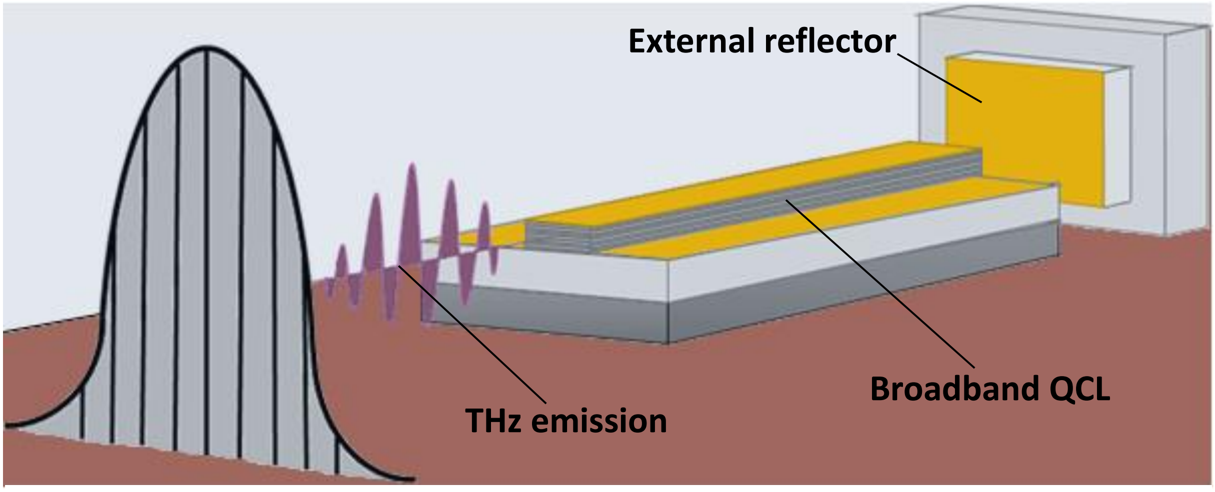

Figure 3.17: Representation of a QCL with a tunable dispersion compensation scheme. The double-metal THz QCL is depicted at the center of the picture on its substrate (not in scale). The external retro-reflector is on the top right corner and can move closer or further from the QCL facet thanks to a micrometric step-motor (not represented). The emission of the device is pictured as a purple wave on the left and its spectrum as comb with a gaussian envelope on a gray background.

and thus on the frequency considered. The structure has been simulated using Comsol to retrieve the GDD it provides (figure 3.18b)). A comparison with the gain GDD for the studied QCL (Sample 1), figure 3.18a, shows that compensation is indeed achievable. In contrast to the integrated GTI, however, this structure only provides significant dispersion when it is on-resonance i.e. at the minimum of the reflectivity. Indeed, while in the integrated GTIs the dispersion profile around the off-resonance position possesses the correct magnitude to compensate for the QCL dispersion, in the case of this tunable scheme this is only available around the on-resonance position. For the experimental procedure, this was in fact the condition

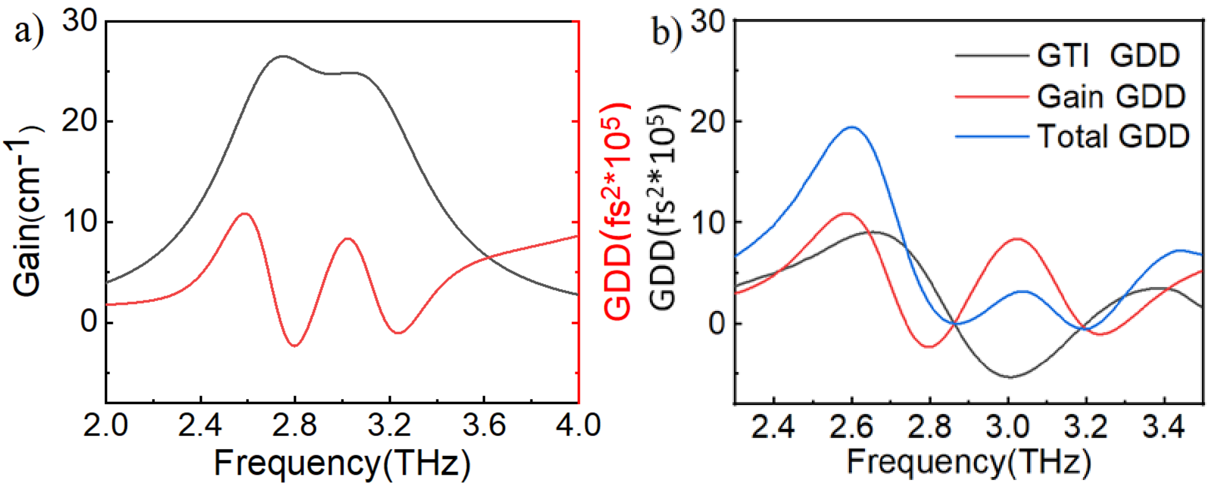

Figure 3.18: (a) gain and GDD profile of the QCL; (b) Gain (red), GTI (black) and total (blue) GDD profiles for a 55μm distance of the gold mirror from the QCL facet. The same scale is applied to all three vertical axis

employed to obtain compensation. In the following part, the setup used for experiments is described and the results are analyzed and compared with simulations.

3.3.2 Comb operation experiments

Beatnote spectroscopy measurements (see section **2.4.1**) at different points on the current-voltage characteristic were performed to analyze the mode coherence of the free running continuous wave THz QCL. The beatnotes were recorded from a bias-tee connected to a commercial Rohde & Schwarz spectrum analyser in its root mean square (RMS) acquisition mode. The beatnote map of the pristine (i.e. without the external reflector) sample is shown in figure 3.19a, with very wide beatnote signatures that indicates non-uniform mode spacing. Figure 3.19b shows the effect of the external reflector on the beatnote. The QCL was kept at a constant current value of 700mA and the gold mirror was moved with respect to its facet (from a starting position of about 40µm that is accounted as an offset). Figure 3.19b shows two strong narrow beatnotes at about 50µm and 110µm corresponding to the on-resonance conditions of the GTI with the lasing band. For the first of these, the simulated GDD profile is shown in figure 3.18b, showing that the dispersion introduced by the feedback can compensate for the intrinsic one when the GTI is operated on resonance. (A similar GDD profile is achieved for a distance of 110µm).

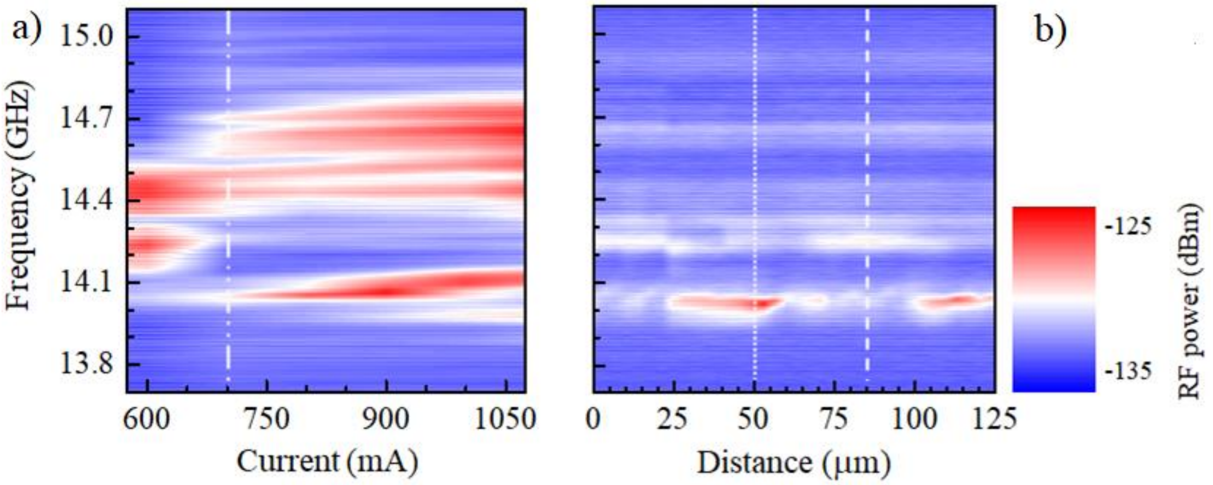

Figure 3.19: (a) Beatnote map of the pristine sample; (b) beatnote map of a fixed CW QCL bias at 700mA as a function of the gold mirror position, with an offset of about 40µm.

In fig. 3.20, the beatnote maps for the pristine sample (black, bottom panel), off-resonance at 85µm distance for the mirror (blue, middle panel) and on-resonance at 55µm distance (red, top panel) are compared. While the pristine sample show a single, narrow beatnote only up to

530mA, and in the off-resonance case this is reduced to 520mA, when the GTI is in on-resonance condition this is observed up to 580mA. The effect of dispersion compensation is also strongly observed in the results above 580mA. In the pristine sample in fact, above this current the so called "high phase noise" regime takes place, for which the dispersion is high enough to prevent the modes locking together. As a result, a large number of broad beatnotes can be found in the spectrum. Similarly for case with the off-resonance GTI: no clear beatnote can be identified and the overall behaviour of the visible ones appear chaotic. On contrary, when the mirror is put in resonance, a strong and relatively narrow single beatnote persists up to 980mA, an extremely broad range which illustrate the effect of dispersion compensation. Such a strong behaviour is observed in spite of the limited feedback that the flat mirror is able to provide to the device.

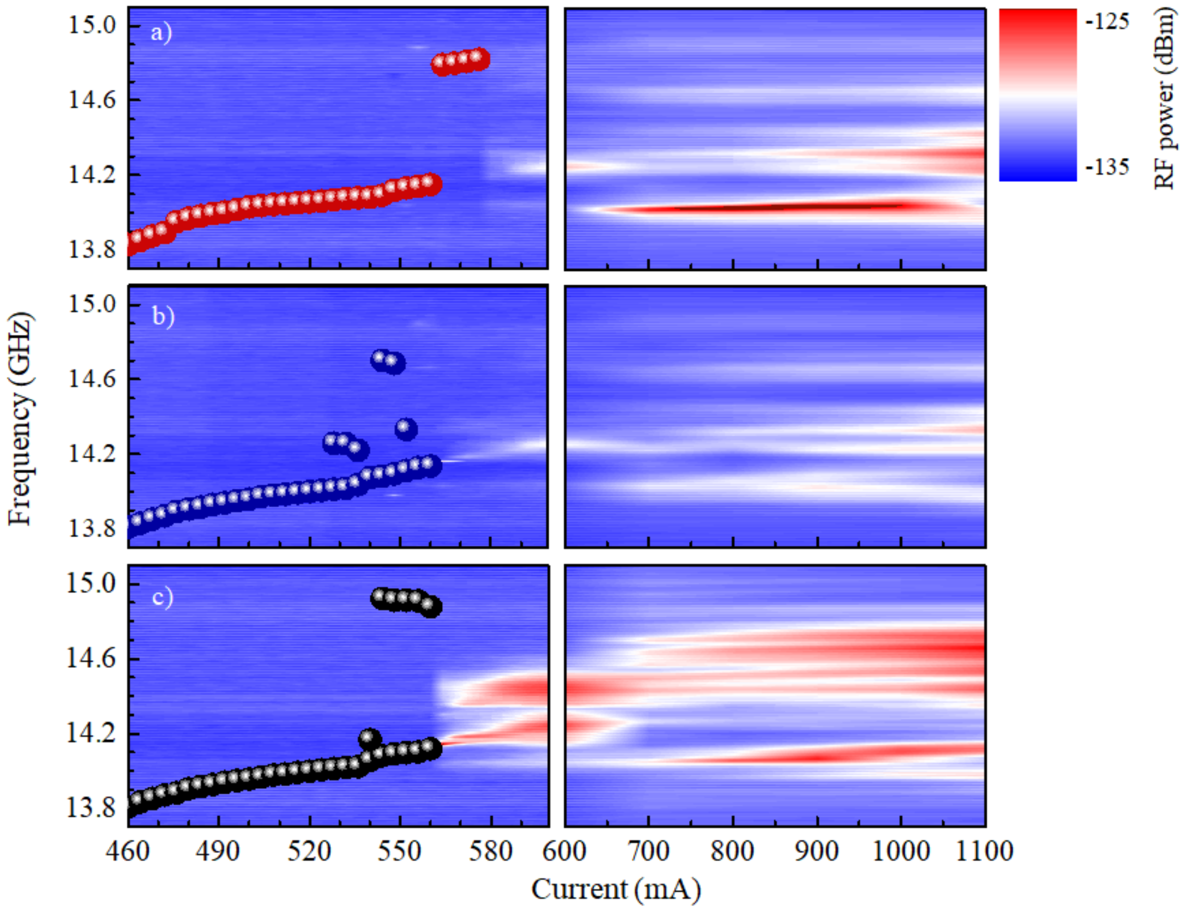

Figure 3.20: Beatnote maps showing the beatnote frequency dependence on the bias for the pristine sample (bottom panels), off-resonance (middle panels) and on resonance (top panels).

An immediate advantage of operating in on-resonance condition is that despite the beatnote broadening significantly above 580mA from 3kHz to 20MHz (see Annex **2.2**), it potentially still permits locking to a microwave reference to reduce the linewidth, as well as for active modelocking. This is not the case for the pristine and the off-resonance cases as no individual beatnote can be identified, greatly diminishing the usable dynamics of the device and the possibility of modelocking. The increase of the linewidth can be ascribed to the increase of GVD of the gain where more modes are brought about threshold that arise with the bias.

It is clear that this compact dispersion compensation scheme offers an important capability for post-processing control of the GDD. The experimental results that have been shown, thanks to our collaborators at CNR Pisa, confirm the theoretical framework for the analysis of the QCL dispersion that has been presented so far, while at the same time demonstrate a flexible solution to their integrated counterpart.

As a final remark, while the beatnote quality has been visibly improved, no time resolved measurements of the emission of the device was performed (see following chapters). The reason is that seeding experiments are generally performed in a transmission configuration, that is not adapted to the geometry of the external GTI that can only operate in a reflection geometry. Future work will be based on setting up a such a geometry.
In the final section of this chapter, the notions that have been discussed so far about dispersion will be applied to the time resolved simulations of active modelocked emission from THz QCLs.

3.4 Effect of dispersion on QCLs pulsed emission

We showed previously that the light travelling in the QCL cavity experiences a considerable amount of dispersion because of the strong frequency dependence of the material refractive index, due to the proximity of the reststrahlenband, and of the gain induced refractive index change. It is then interesting to simulate the emission of an actively modelocked THz QCL in the cases where the dispersion has been or not compensated, and to compare the results with experimental data. In this section, numerical simulations on this topic are described. These were performed by Dr Xiaoqiong Qi at the University of Queensland (AU) and are based on the QCL called Sample 7 henceforth (see Table 3.1 for more details), characterized at LPENS by THz time domain spectroscopy both for the free-running and the modelocked emission regimes.

3.4.1 Theoretical model

The theoretical framework on which the simulations were performed is obtained from the combination of the multi-mode reduced rate equations (MM-RREs) as described in [105] and the equation for pulse propagation as proposed in [106]. This allows for the modelization of both the formation of the THz pulses generated in active modelocked THz QCLs and their propagation in the laser cavity, including the influence of dispersion. In more details, RREs describes the time resolved build-up of the pulses with the microwave modulation at the round-trip frequency, while the master equation accounts for dispersion, losses and non-linearities experienced during the pulse propagation. This is described below:

In order to model the active mode-locking, the driving current can be written as

$$I(t) = I_0 + I_{RF}\cos(\omega_{RF} t) \tag{31}$$

with $\omega_{RF} = 2\pi\nu_{RT}$ and ν_{RT} is the round-trip frequency.

The MM-RRE used in the models have the form:

$$\frac{dN_3(t)}{dt} = \frac{\eta_3 I(t)}{q} - \sum_m G_m\big(N_3(t) - N_2(t)\big)\,S_m(t) - \frac{N_3(t)}{\tau_3} \tag{32}$$

$$\frac{dN_2(t)}{dt} = \frac{\eta_2 I(t)}{q} + \sum_m G_m\big(N_3(t) - N_2(t)\big)\,S_m(t) + \frac{N_3(t)}{\tau_{32}} + \frac{N_3(t)}{\tau_{sp}} - \frac{N_2(t)}{\tau_2} \tag{33}$$

$$\frac{dS_m(t)}{dt} = MG_m\big(N_3(t) - N_2(t)\big)S_m(t) + \frac{M\beta_{sp}N_3(t)}{\tau_{sp}} - \frac{S_m(t)}{\tau_p} \tag{34}$$

$$\frac{d\varphi_m(t)}{dt} = \frac{\alpha}{2}\left(MG_m\big(N_3(t) - N_2(t)\big) - \frac{1}{\tau_{p,m}}\right) \tag{35}$$

where $N_3(t)$, $N_2(t)$ are the carrier populations at upper and lower energy level of the laser transition, respectively, $S_m(t)$ and $\varphi_m(t)$ are the photon population and the phase of the slowly varying envelope of the electric field for the mode m=1, 2, …, M. The number of modes M is determined by the gain spectrum bandwidth and M=25 is chosen in this simulation to match the measured pulse spectrum of Sample 7. All the other parameters in the equations above have their usual meaning [107]-[108].

The emission power from each mode is

$$P_m(t) = \eta_m \hbar\omega_m \frac{S_m(t)}{\tau_{mp}} \tag{36}$$

and the total pulse power is

$$P(t) = \sum_m P_m(t)e^{j[\omega_m t + \varphi_m(t)]} \tag{37}$$

The resulting output power profile and its envelope are plotted in fig. 3.21, where the expression for the envelope is given by:

$$A(0,t) = |P(t)| = \sum_m P_m(t)\cos[\omega_m t + \varphi_m(t)] \tag{38}$$

and both $P_m(t)$ and $\varphi_m(t)$ are obtained from the MM-RREs.

As said before, the pulse propagation process in the laser cavity can be modelled by the master equation of modelocking. Since the RF modulation and the optical field amplification through the gain in the active region of the laser has been considered in the MM-RREs, it is only necessary to involve the losses, dispersion, and nonlinearity terms for the pulse propagation in the master equation. It is possible to directly solve it in the frequency domain if the nonlinearities are not considered. Since in the first case the master equation becomes a linear

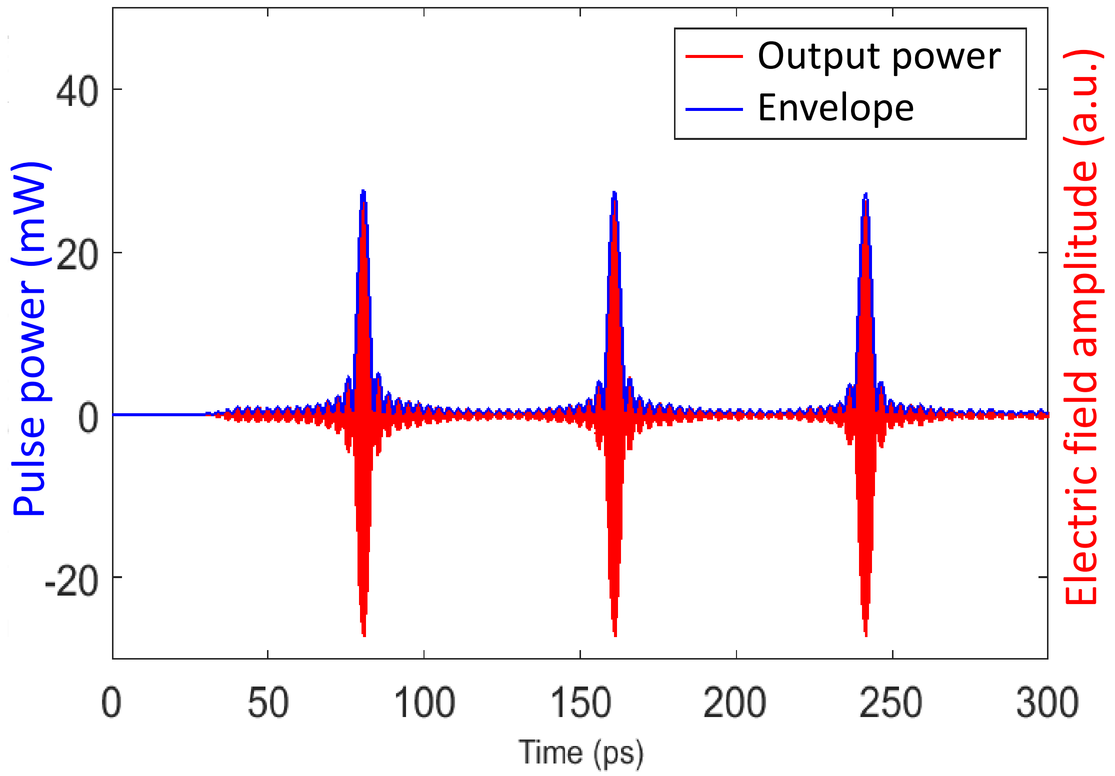

Figure 3.21: Simulated electric field (red) and pulse power (blue) obtained by solving equations from 32 to 35, i.e. the MM-RRE system

equation in frequency, it is reasonable to consider that the MM-RREs and master equation are applied to the optical field of the ultra-short pulses simultaneously.

In the absence of gain amplification and RF modulation, the master equation can be written as

$$T_R \frac{\partial A(T,t)}{\partial T} + \frac{\alpha}{2} L_R A(T,t) - \frac{j}{2}\beta_2 L_R \frac{\partial^2 A(T,t)}{\partial t^2} = j\gamma |A(T,t)|^2 A(T,t) L_R \qquad (39)$$

Where L_R is twice the length of the cavity, $A(T,t)$ is the slowly varying envelope of the electric field. α, β_2 and γ are the propagation loss, the group velocity dispersion and the nonlinearity in the laser cavity. It is noted that there are two time scales in the equation above: T is the propagation time or coarse-grained time [109] that develops on a time scale of the order of the round-trip time $T_R = L_R/v_g$ while t denotes the fast time scale of the order of the pulse width. It is assumed that the time scale associated with the pulse is sufficiently smaller than T_R so the two times are essentially decoupled.

The group velocity dispersion β_2 induced by the material and the gain in the active region for our model is shown in fig. 3.22 as from the method discussed in section **3.1**.

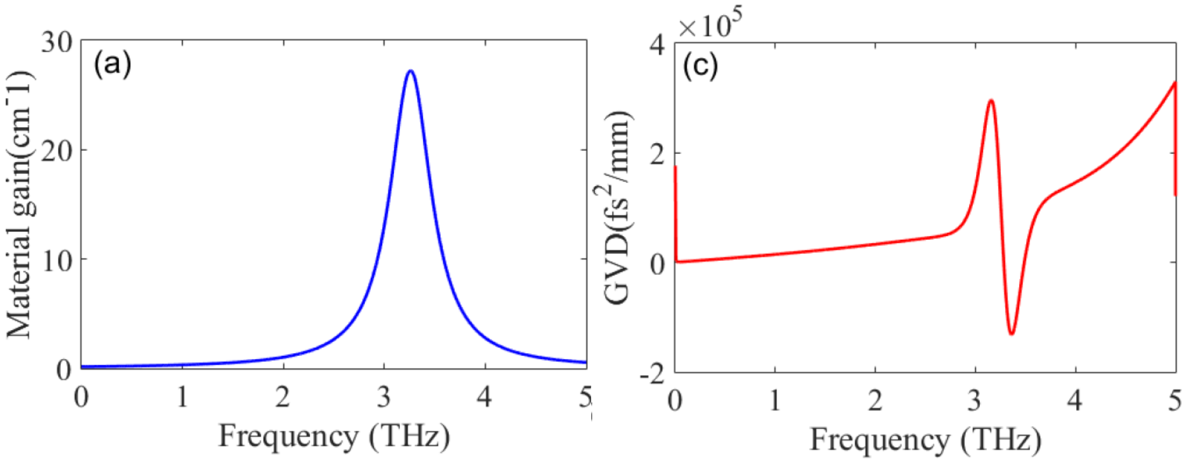

Figure 3.22: Gain (blue) and GVD profile (red) obtained with the method described in section 4.1 as used for the simulation

If the non-linearities are ignored, i.e. γ=0, it is possible to perform a Fourier Transform of equation 39 obtaining

$$T_R \frac{\partial A(T,\omega)}{\partial T} + \frac{\alpha}{2} L_R A(T,\omega) - \frac{j}{2} \beta_2 L_R (j\omega)^2 A(T,\omega) = 0 \tag{40}$$

whose solution is

$$A(T,\omega) = A(0,\omega) exp\left[\int (-\alpha + j\beta_2 \omega^2)\, v_g \, dT\right] \tag{41}$$

where $A(0,\omega)$ is the Fourier transform of the slowly varying envelope for $A(0,t)$ as shown in equation 38. (Regarding the slowly varying envelope approximation, in chapter **5** we will employ Maxwell-Block equations to resolve the electric field emitted by the device).

3.4.2 Simulation results

The spectrum employed in the simulation has a central frequency of 3.26THz and 25 longitudinal modes with a mode separation of 12.43GHz. Figure 3.23 shows the generated pulses A(0,t) from MM-RREs in frequency domain and time domain in panels (a) and (b) respectively. The green line is a Gaussian pulse reference with FWHM of 126.8 GHz, as observed in the experimental results [17].

The propagation losses and dispersion are then accounted for by plugging these results into equation (40). Figure 3.24 shows the comparison of the pulse evolution and pulse width

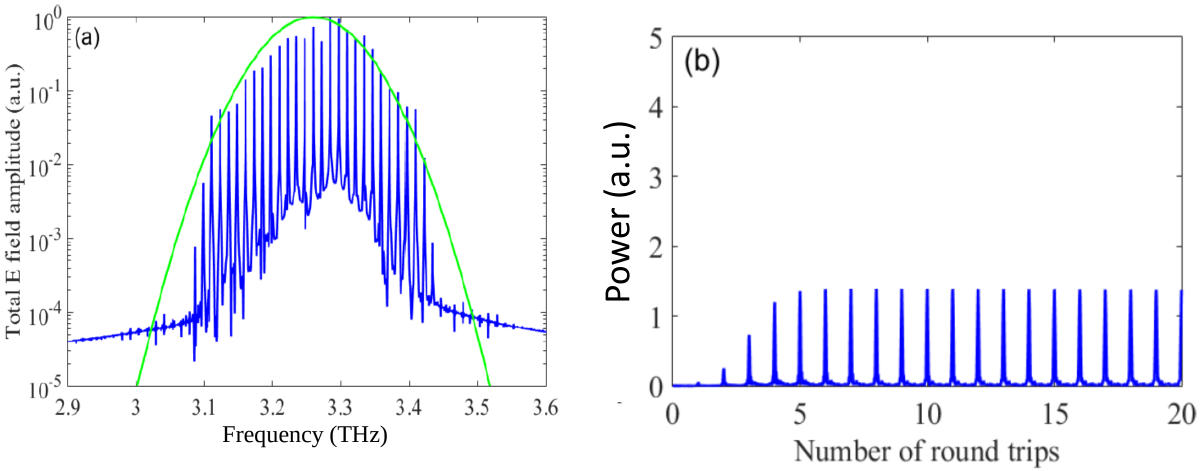

Figure 3.23: The MM-RREs generated pulses in frequency domain (a) and time domain (b), the green line in (a) is a Gaussian pulses with FWHM of 126.8 GHz.

dynamics during propagation in the laser cavity versus the number of round trips, with and without gain dispersion. In order to observe only the effect of dispersion during the propagation, two cases are considered having an identical gain profile (10cm^{-1} of peak gain) when solving the MM-RRE but two different values for the dispersion in the master equation. In the top panels (a-b) the dispersion is computed from a peak gain value of 10cm^{-1} while in the bottom panels this is brought to 27cm^{-1} thus increasing the magnitude of the dispersion by a factor 2.7.

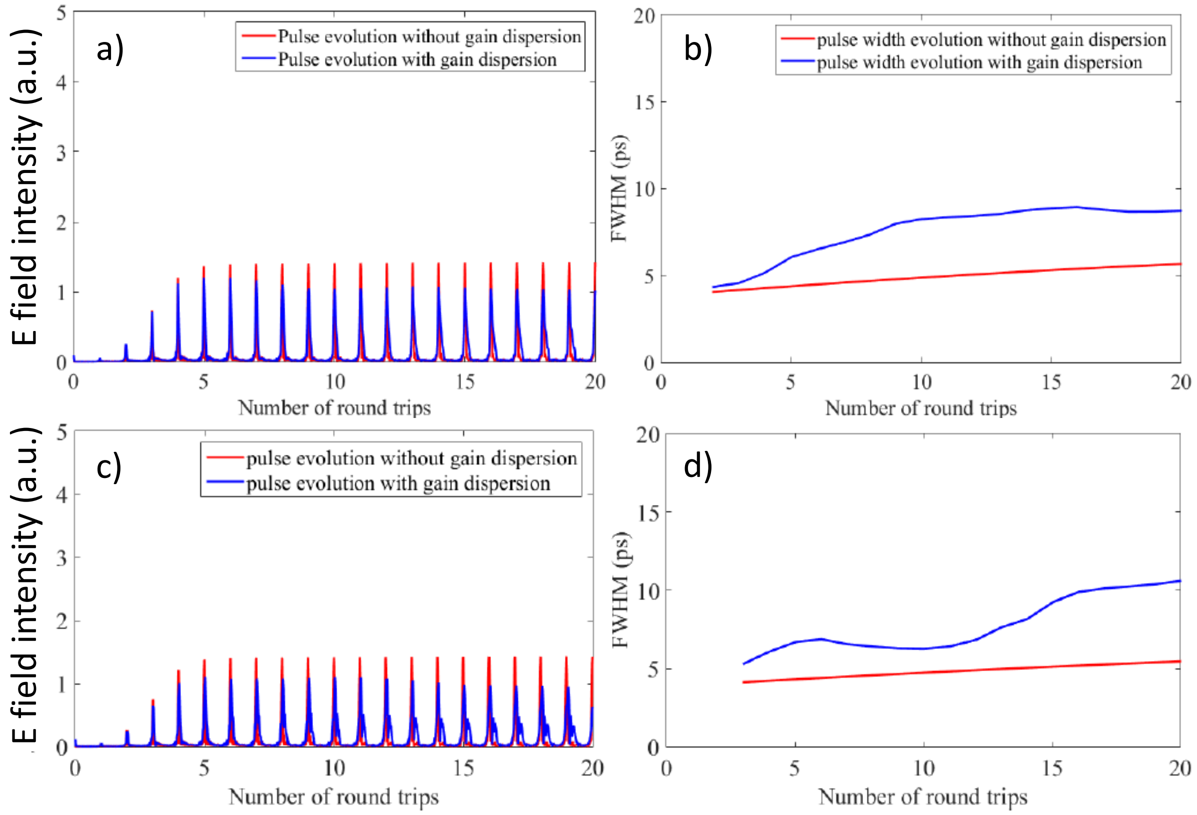

Figure 3.24: Comparison of pulse evolution (a-c) and pulse width dynamics (b-d) with (blue curve) and without (red) gain dispersion. The gain dispersion is computed from a maximum gain of 10cm-1 for (a)-(b) and 27cm-1 for (c)-(d).

For the case where the dispersion is higher it is observed that the steady state pulse width increases from 5.6 ps to 11ps. It is also noted that a higher group velocity dispersion not only leads to wider pulses but it also generates multiple pulsation after each main pulse, as it is particularly visible in panel c). However, when the dispersion is lower, the multiple pulsations tend to disappear and the steady state pulse width is decreases 8.6 ps. The MM-RREs model also allows for the analysis of the influence of peak gain and gain spectrum distribution on the transient pulse formation processes. As previously described, the gain spectrum bandwidth and

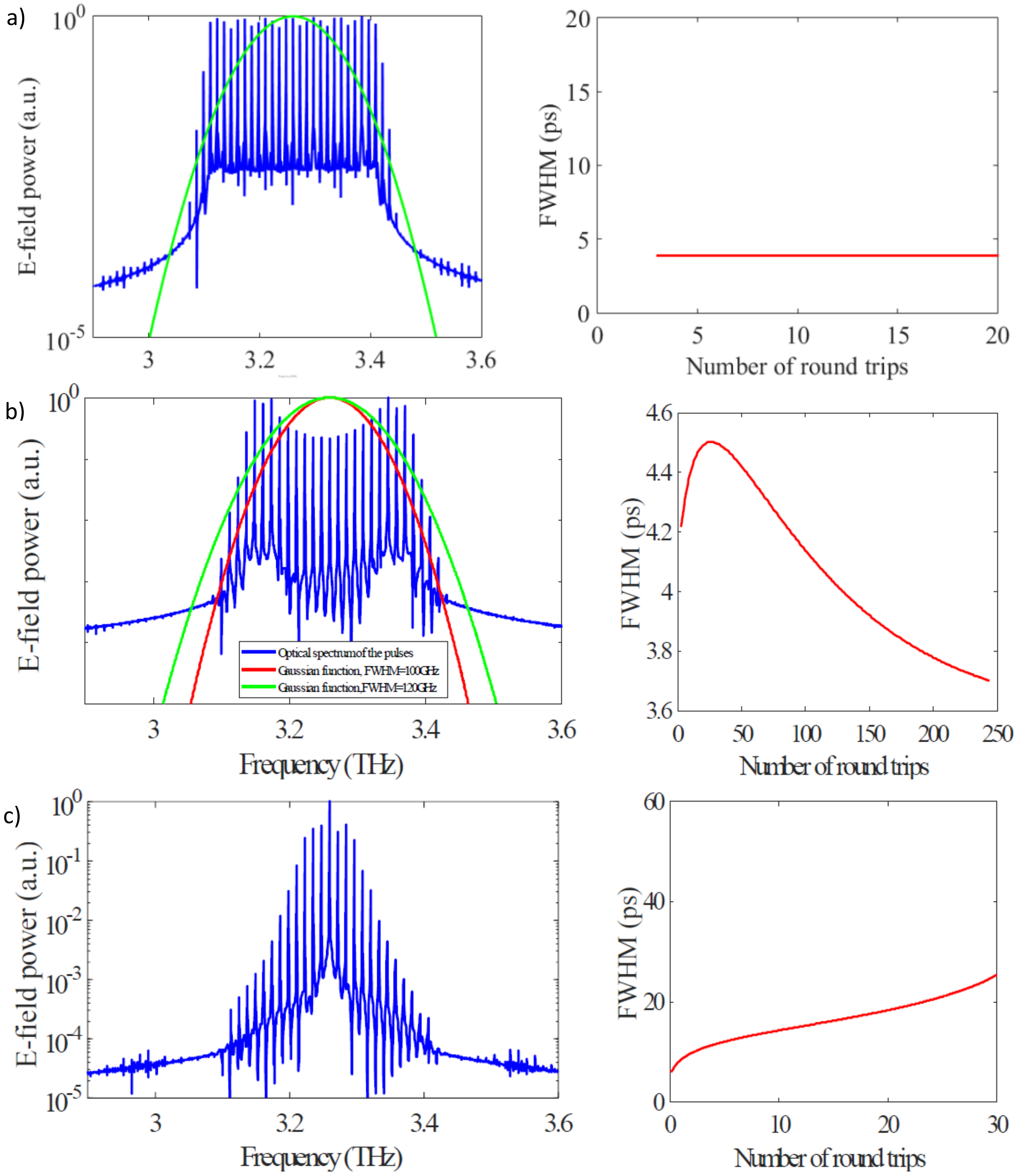

Figure 3.25: The flat (top), two-peak (middle) and sharp (bottom) spectrum profile and their corresponding pulse width dynamics

the gain threshold determine the number of laser modes that are available for modelocking. In turn, the peak gain is responsible for how quickly the steady state can be reached. The number of phase locked modes determines the pulse width: more modes are locked, the narrower the pulses that can be obtained.

Furthermore, for a fixed gain spectrum bandwidth, the pulse width dynamics are sensitive to the shape of the gain spectrum as well. As reported in fig. 3.25a for 25 phase locked modes, if the top of the pulse spectrum is flat, the pulse width value reaches steady-state at 3.9ps rapidly (it is reduced to 1.9ps when the number of modes equals 50 for the same 600GHz pulse bandwidth (not shown)). If the central modes have lower gain than the side modes (like for a two-peaks profile), as shown in panel (b), the pulse width increases quickly before dropping to a duration smaller than that of the first pulse generated in the cavity. If the central modes are instead much higher than the side modes, the pulse width increases very slowly and keeps growing even after hundreds of round trips (fig. 3.25c)
This suggests that the pulse width dynamics might be controlled by the arrangement of the multi-stack structure of the active region of a THz QCL. For example, it is possible to have either two active region stacks with peak gains side by side to generate a decreasing pulse width when the latter is propagating in the laser cavity or design a flat gain distributions among the modes to have a fast stabilization and maintain it, or even a sharp gain distribution to create an increasing pulse width along the round trips. These results show that to realise short pulses, both a large bandwidth and a good uniformity in the mode power are important factors.

3.4.3 The effect of the upper level electron lifetime

The fast gain recovery time in a THz QCL compared to the round-trip time is widely believed to be the main reason that makes conventional methods for mode locking THz QCLs a significant challenge. It is therefore of great importance to study the impact of the upper level electron lifetime on the value of this parameter for which there is currently no absolute agreement within the scientific community.
The starting consideration is that the material gain is proportional to the population inversion as shown in the relationship below:

$$G_M = \frac{4\pi e^2}{\varepsilon_0 n_{eff}} \frac{{z_{UL}}^2}{2\gamma_{UL} L_P \lambda} \Gamma(n_U - n_L) \tag{42}$$

Where $n_U - n_L$ is the electron population inversion per active region period in a sheet density form. The driving or injection current is the main electron source to reach population inversion, so the population inversion will be influenced by the RF modulation of the driving current. In addition, the upper electron lifetime is an important parameter in a THz QCL, which determines the turn-on delay. Here, we try to investigate the population inversion transient response at different upper level electron lifetime.
As used in an active mode-locking laser, the driving current is modulated at the round trip frequency as from equation 31 where here the bias current is I_0=0.75A, the modulation amplitude is I_{RF}=0.15A, and $\omega_{RF}=2\pi\Delta\nu$ and $\Delta\nu=c/2n_{eff}L_a$=12.43 GHz, as shown in fig. 3.26a. The switch-on dynamics of population inversion $N3(t)$-$N2(t)$ and the emission pulse power for various upper level electron lifetime are simulated in panel (b) and (c) respectively.

As it can be seen from fig. 3.26b, the population inversion oscillations are driven by those of the current but with some delay for the first oscillation period which depends on the upper carrier lifetime τ_3. When τ_3 is increased from 5ps to 8ps, 11ps, and 20 ps, the peak in the first oscillation period is postponed from 12.6ps, to 17.13ps, 20.83ps and 25.77ps, while instead the peak positions in the following periods are shifted to earlier times. The pulse peak power is almost coincident with the current maximum. However, extended upper lifetime can improve the pulse peak power from 0.7mW to 8.6mW, 15.1mW, and 27.1 mW respectively. This fact can be easily understood from the steady-state solutions of the single-mode RREs for the photon population, which is:

$$S_s = \frac{\frac{\eta_3 I}{q} - \frac{N_{3s}}{\tau_3}}{BG} \tag{43}$$

where B and G are the gain and population inversion respectively.

As the results show, the generation of the pulses is governed by the driving current with the gain recovery time not greatly influencing the pulse widths. However, this does not necessary translate to high peak intensity as this parameter clearly depends on the upper level lifetime, i.e. to the amount of energy stored in the cavity that can contribute to pulse formation.

In conclusion, numerical simulations based on a model combining the MM-RRE and the master equation for pulse propagations have been presented. The effect of the dispersion and of the shape of the gain on pulse broadening has been studied, which shows the appearance of multiple pulsations in case of strong dispersion and very different pulse duration evolution for single, double-peaked and flat gain profiles. This opens up to new perspectives in the possibility of designing the emission properties of THz QCLs depending on the required applications.

In addition, the switch-on dynamics of the population inversion and the emission pulse power for various upper level electron lifetime have been investigated. It has been shown that the injection driving current modulation is still the dominant effect regarding population inversion (and therefore the gain) compared to upper level carrier lifetime, although the oscillating periods slightly change when this is increased. The expression of the steady-state solution for the photon population (equation 43) also shows that larger upper level electron lifetimes also improve results in increase pulse peak power.

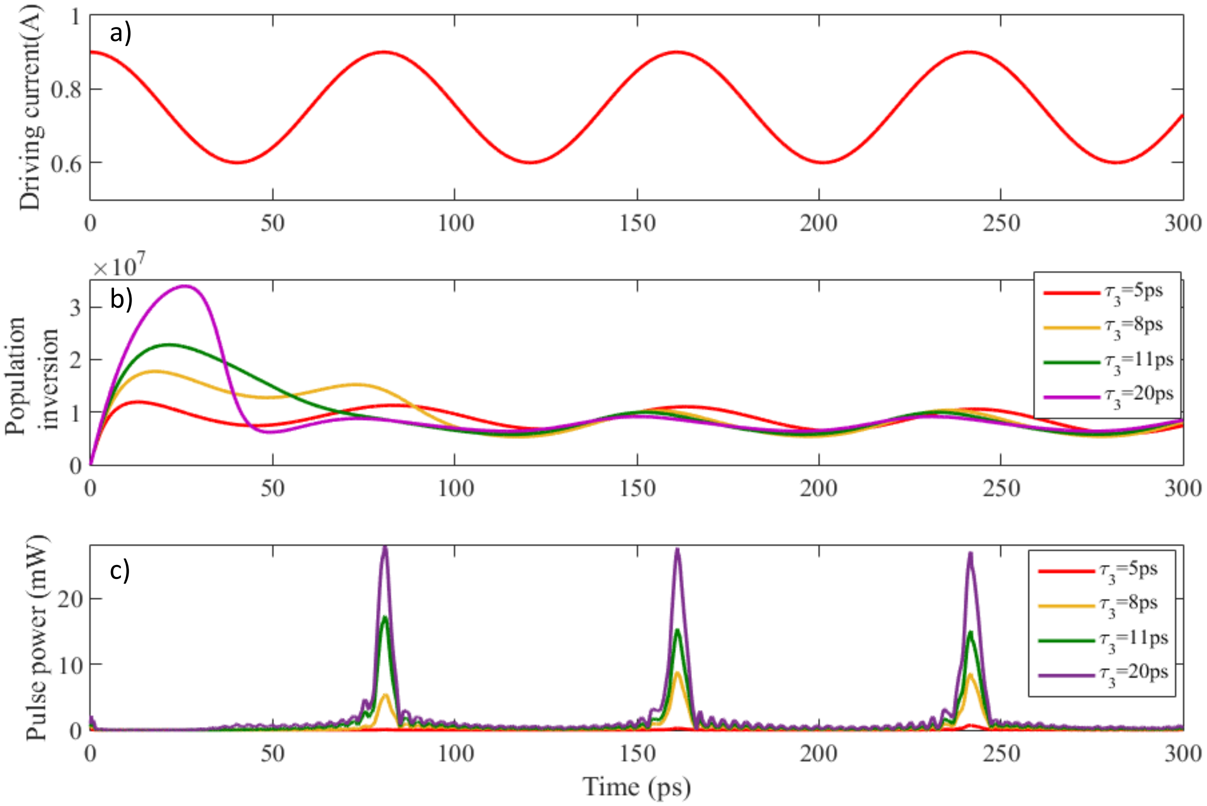

Figure 3.26: (a) Driving current time profile, (b) population inversion evolution for different upper level electron lifetimes as resulting from the modulating current on the top panel, (c) the generated pulse profiles

3.5 Conclusions

In this chapter, a complete analysis of the dispersion in THz QCLs has been carried out with theoretical and numerical tools, and the results have been compared with experimental data that have validated our approach. The simulations of a modelocked QCL emission have provided important information regarding the behaviour of the devices and how the gain shape can affect the evolution of the pulse width as the light travels in the laser cavity. These can be used to improve the design of the heterogeneous structures (i.e. realized by multi-stacks of gain regions) of broadband QCLs to further enhance their capability of generating short pulse trains. Importantly we show that the ultrafast gain is not a hindrance to the realization of short pulses from THz QCLs through active modulation, and that the dispersion is an important parameter to fully control.

Integrated dispersion compensation schemes based on GTIs were analyzed, and found to be suitable to broadband application, although limited to specific frequency ranges and dispersion profiles. A complete knowledge of the device is necessary to procede to finely tune the geometric parameters of the GTI cavities and achieve compensation. However, a large flexibility in the dispersion response of individual structures can be achieved that are compatible with standard processing procedures.

The tunable GTI made of an external mirror mechanically positioned by a piezoelectric actuator has showed remarkable results in providing for tunable dispersion compensation in a broadband design. The significant improvement in the range of the frequency comb regime has provided a demonstration of the reliability of our dispersion model, and at the same time has showed the perspective of the realization of a truly zero-dispersion, tunable, THz frequency combs.

The effect of dispersion compensation will be further experimentally investigated in the next chapters that make use of the solutions discussed here, dealing in particular with the generation of the shortest pulse trains from a THz QCL.

4

Modelocking of THz QCLs – active and free running operation

Since many years, the generation of sub-picosecond pulses from high-power semiconductor THz sources has been regarded as an important milestone still to achieve in order to enhance applications of THz technology and potentially replacing femtosecond based sources. So far, QCLs have shown to have the potential to provide for all the requirements that are necessary for this goal, in particular concerning ultra-broadband emission and Watt level output power, while bringing other advantages, such as their very compact size, and disadvantages.

Passive modelocking is a technique that induces a laser to emit pulses without the necessity of an external reference. One of the most common ways to achieve this condition is by the use of saturable absorbers. However, the fast gain recovery time of QCLs renders passive modelocking with saturable absorbers a very difficult task to achieve [110]. Some purely theoretical proposals for carefully designed schemes to obtain self-pulsations in QCLs have been reported [111] but no evidence has ever been experimentally shown. Although self-starting frequency combs through FWM have been recently demonstrated, these are not thought to be pulsed emission but rather produce a temporal profile with a nearly constant output intensity (a purely frequency-modulated laser) [56].

The aim of this chapter is to show the ultrashort pulse trains can be obtained by active modelocking THz QCLs, where chromatic dispersion has been compensated. Further new phenomenon for these devices will be reported which display spontaneous and stable pulsation in free-running experiments, i.e. without the need of an external modulation. While this is contrast with the generally accepted idea that pulses cannot be sustained in the laser cavity without a external modulation mechanism, this novel operation is observed in two samples for a scan duration of more than 2ns, highlighting the stability of the generated pulses. We will also show that this spontaneous pulsed behaviour in the free-running condition can be enhanced with active modelocking leading to the generation of shorter pulses. This will be discussed in section **4.4**, where the new record duration of 3.4ps for a pulse train will be presented.

	Sample 1	**Sample 2**	**Sample 3**	**Sample 4**	**Sample 4/66**
Growth code	L1458	L1194	L1369	L1388	L1388
Processing lab	CNR (Pisa)	C2N (Paris)	C2N (Paris)	C2N (Paris)	C2N (Paris)
Active regions (periods)	2.5THz(55) 3THz(40) 3.5THz(40)	2.5THz(200)	2.5THz(50) 3THz(36) 3.5THz(36)	2.5THz(50) 3THz(36) 3.5THz(36)	2.5THz(50) 3THz(36) 3.5THz(36)
Active region scheme	Hybrid structure [94]	LO phonon depopulation [112]	Hybrid structure [94]	Hybrid structure [94]	Hybrid structure [94]
# wells	9	3	9	9	9
Waveguides	Double Metal	Double metal	Double Metal	Double Metal	Double Metal
Length/width /height	2.9mm/85µm /17µm	3.2mm/68µm /12µm	3.16mm/56µm /15µm	3mm/56µm /15µm	3.43mm/56µm /15µm
Side absorbers (widths)	6.5µm	4µm	3.5µm	4µm	4µm

Table 4.1: Characteristics of the samples used in chapter **4.** The dimensions refer to those described in fig.1.9

In section **4.1**, the generation of ultrashort pulse trains from THz QCLs is introduced showing successful dispersion compensation on a fairly broad part of its emission spectrum. This device used was discussed in section **3.4** (Sample 2) and provided the parameters for the numerical simulations discussed there. The effect of dispersion is experimentally highlighted using different GTI lengths and its application to tuning the QCL spectra is presented in section **4.2**. Spontaneous pulsed emission from a THz QCL is studied in section **4.3** from Sample 4 both in its pristine form and with a 66μm long GTI integrated to it (Sample 4/66 to remind the reader of the presence of the GTI). Section **4.4** shows the effect of active modelocking on Sample 4/66 and the generation of an ultrashort pulse train owing to a careful design of the dispersion of the device. Finally, preliminary results from an ultra-broadband device (spectral bandwidth ~ 1THz) are discussed in section **4.5**. Here, the shortest pulse ever demonstrated from a THz QCL, having a FWHM of 1.3ps, will be presented.

As already anticipated, the QCLs that are used in this chapter are Sample 2 in section **4.1**, Sample 3 in section **4.2** and Sample 1 in section **4.5**. The Samples 4 and 4/66 are discussed in the sections **4.3** and **4.4** that will treat the topic of spontaneous pulsed emission. The LIV curves and beatnote maps for the first two devices can be found in Annex **3.1.4** and **3.15**. Those for Sample 1, 2 and 3 are given in Annex **3.1.1**, **3.1.2** and **3.1.3** respectively. The characteristics of all these devices are reported in Table 4.1.

Chapter 4

4.1 Ultrashort pulses from THz QCLs

4.1.1 State of the art

As previously stated, THz pulses are very useful tools for spectroscopy, non-destructive testing and the study of ultrafast phenomena. Having shorter pulses increases the spectral bandwidth available and it is in general assumed that the 1ps duration is the threshold below which THz applications to the industrial sector start to take place. This has led to a research domain dedicated to generate a sub-picosecond pulse trains from a THz QCL. As well as potentially replacing NIR femtosecond laser methods for applications, it is also of fundamental interest on how the QCL dynamics play a role in short pulse generation.

Figure 4.1 shows a summary of the duration of the pulses emitted from a THz QCL as reported by papers in literature. One can see that for several years since active modelocking was first demonstrated, the duration of the emitted pulses was stuck at about 10ps. The main limitation was then identified to be the dispersion, and consequently 5-4ps pulse trains started to be reported as soon as new designs were used to reduce it. If improved dispersion compensation schemes are combined to more spectrally broad structures, the durations of THz pulses from the QCLs will continuously to be reduced. Moreover, single pulses are also reported to have been generated at new record durations. These are showed as the red dots of fig. 4.1. Even if these isolated pulses are far more easy to generate than a stable train, and generally broaden or

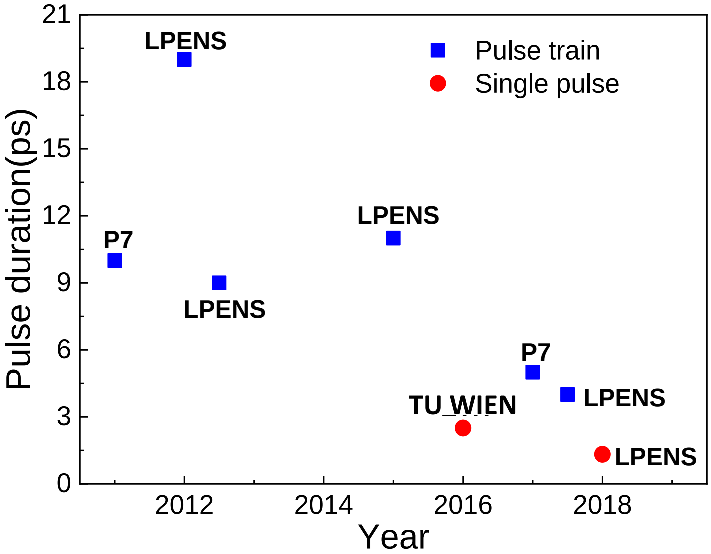

Figure 4.1: Pulse duration versus year in several publications pulse generation from THz QCL emission. The laboratory of the first author is reported on top of each point (P7=Paris 7 (FR), LPENS Paris (FR), TU Wien (AT)). Blue squares represent stable pulse trains while the red circles report the duration of a single pulse, isolated or in an unstable train.

degrade into complex profiles, they still show the potentialities of a successfully compensated broadband device.

As for the current state of the art, the shortest stable pulse train reported up to date was shown in [17] in 2017 and represents the first example of THz QCL whose dispersion has been compensated with an double-metal integrated coupled cavity, resulting in a 4ps pulsed emission. Another work which is worth mentioning is [66], where the authors explain the generation of a 5ps pulse train as a result of the use of double-metal waveguides. This pulse train, however, exhibited an additional pulsation per round-trip with a longer duration than the first one (6ps) and lower intensity. No complete explanation was reported for this unusual behaviour.

Although there has been a considerable body of work on frequency combs, no further work has been published that shows a significant improvement in terms of pulses shorter than those obtained by active modelocking to a generic THz QCL. In this section, the focus is set on the original design of [17] which constituted the starting point for the experimental part of this thesis. The original concepts and results are reported to show a practical example of a broadband QCL for which the dispersion has been, at least in part, successfully eliminated.

4.1.2 Dispersion compensated modelocked emission

The initial experimental result of this thesis was the first demonstration of an ultrashort pulse train from an active modelocked QCL with an integrated 58µm GTI structure (section **3.2.2**). This device, described in the previous chapter as Sample 2, is based on a LO phonon depopulation scheme and is designed to work at 2.5THz from a single active region in a double metal waveguide. The LIV curves and beatnotes map are available in Annex 5.1.

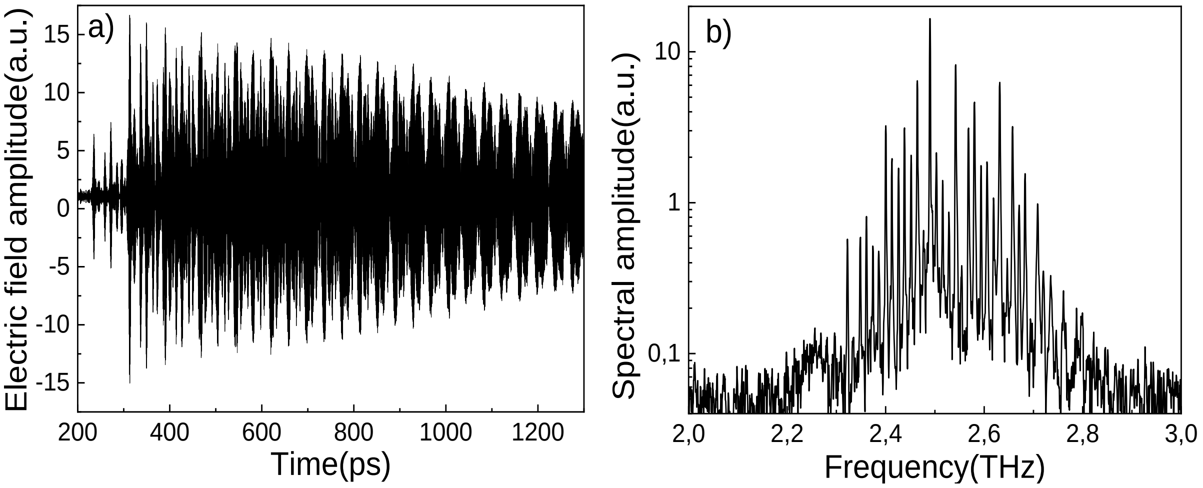

Figure 4.2: (a) Time response and (b) spectrum of free-running emission of Sample 2 with a 58µm integrated GTI

The free-running emission, shown in fig. 4.2a for 1247mA and 23dBm of RF power, and the related spectrum in fig. 4.2b present a typical example of a multimode QCL with a band spanning more than 300GHz.

When a 30dBm current modulation at a frequency close to the RF beatnote of the device is applied (12.75GHz), active modelocking is enforced and the emission of the QCL becomes pulsed as reported in fig. 4.3a. As one can see, the pulse duration remains constant at 4ps, that is almost three times less than an identical QCL but without a GTI, as showed in panel (e).

Comparing the modelocked spectrum, having a FWHM of about 172GHz, and the GTI reflectivity profile (fig. 4.3b, in red), we can see that the emission is mostly ‘off-resonance’ with reflectivity of the GTI. As a consequence, the GTI introduces a profile of dispersion that is opposite in sign compared to the one of the gain. The original computation of the dispersion components, based on a fully analytical approach (fig. 4.3c), was performed by Dr. Nathan Jukham of Bochum University and shows compensation on several hundreds of GHz in the spectral range of the device. This is shown in fig. 4.3d where the total GDD (red curve) is almost zero from 2.35THz to 2.65THz while the gain GDD (green curve) presents a 0.8ps^2 variation in the same frequency range. Electromagnetic simulations were more recently performed with the Comsol Multiphysics software which show a very good agreement with the original computation (see chapter **3**). These results clearly demonstrate that the bandwidth available to the QCL is not the main limiting factor in reducing the pulse duration. The understanding of the role of dispersion is in fact more vital as great improvements in pulse width could be obtained even from a not completely successful elimination of this detrimental factor.

The geometrical parameters and the structure of this device were employed for the simulations in the last part of chapter **3**. Their aim was to study the effect of the active modulation, upper level lifetime and gain shape on the pulse generation process. We can then see how the experimental results here fit the case described in fig. 3.26a, where a broadband QCL with a uniform mode intensity permit short pulse duration (~5ps) if the dispersion is correctly compensated.

It is worth showing, though, that the dispersion can affect the emission of the QCL in ways other than just broadening the generated pulses. This becomes clear when the dispersion profile is engineered in such a way to prevent modelocking in certain frequency ranges and induces, in turn, a tunability of the emission. This topic will be discussed in the next section.

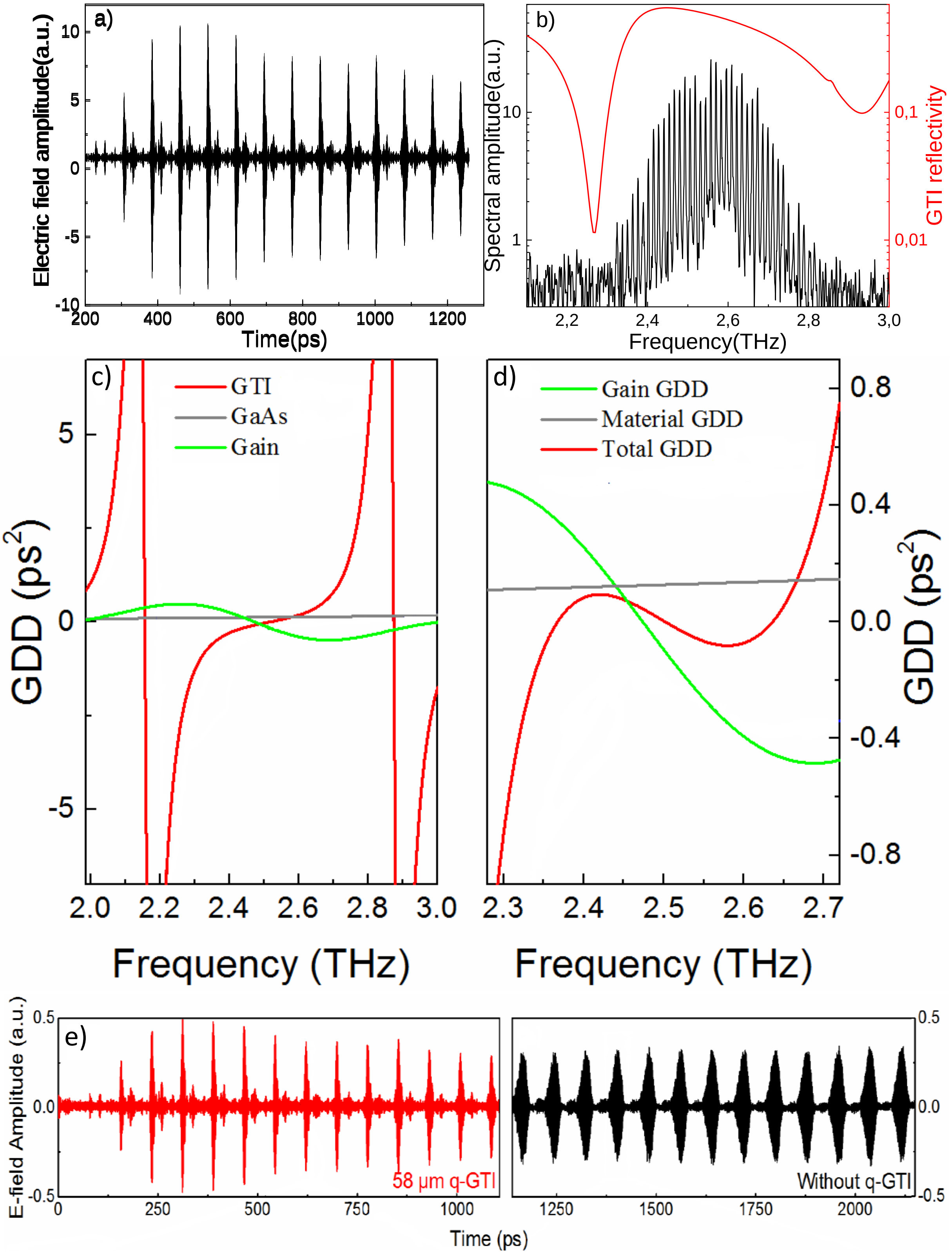

Figure 4.3: (a) Time profile of the electric field emitted by Sample 2 in active modelocking conditions and (b) its FFT spectrum with the reflectivity profile of the integrated GTI (in red). (c) Dispersion profile of the gain (green), material (gray) and the GTI (red); (d) total GDD (red) with gain (green) and material (gray) dispersion around the compensation point. (e) Comparison between the modelocking traces obtained from Sample 2 with (red, same as (a)) and without (black) the integrated GTI. The pulse FWHM decreases from 11ps to 4ps thanks to the presence of the dispersion compensating device

4.2 Effect of dispersion on the emission frequency of THz QCLs

In order to compare the effect of the dispersion introduced by GTIs on the emission properties of QCLs, 4 devices of the kind of Sample 3 were fabricated on the same chip. These devices employ the hybrid design of the active region which allow for a low current threshold and makes the modulation of the device easier. The multiple stacks of gain regions centered at different frequencies (see Table 4.1) are supposed to provide for a broad bandwidth.

The initial characterization of the free running and modelocked emission are reported in fig. 4.4. This QCL shows a ~100GHz band centered at 2.9THz in the free running case (panel c) and emission over a much larger band of 400GHz from 2.8 to 3.2THz in modelocking condition (panel d).

On three of the QCLs on this chip, GTIs with slightly different lengths, spanning from 36.1µm to 38.5µm with steps of ~1µm, were realized. The main idea behind the design of these structures was to tune the GTI around the on-resonance position with respect to the emission band of the QCL, and to observe the effects of the temporal and spectral response of the QCL

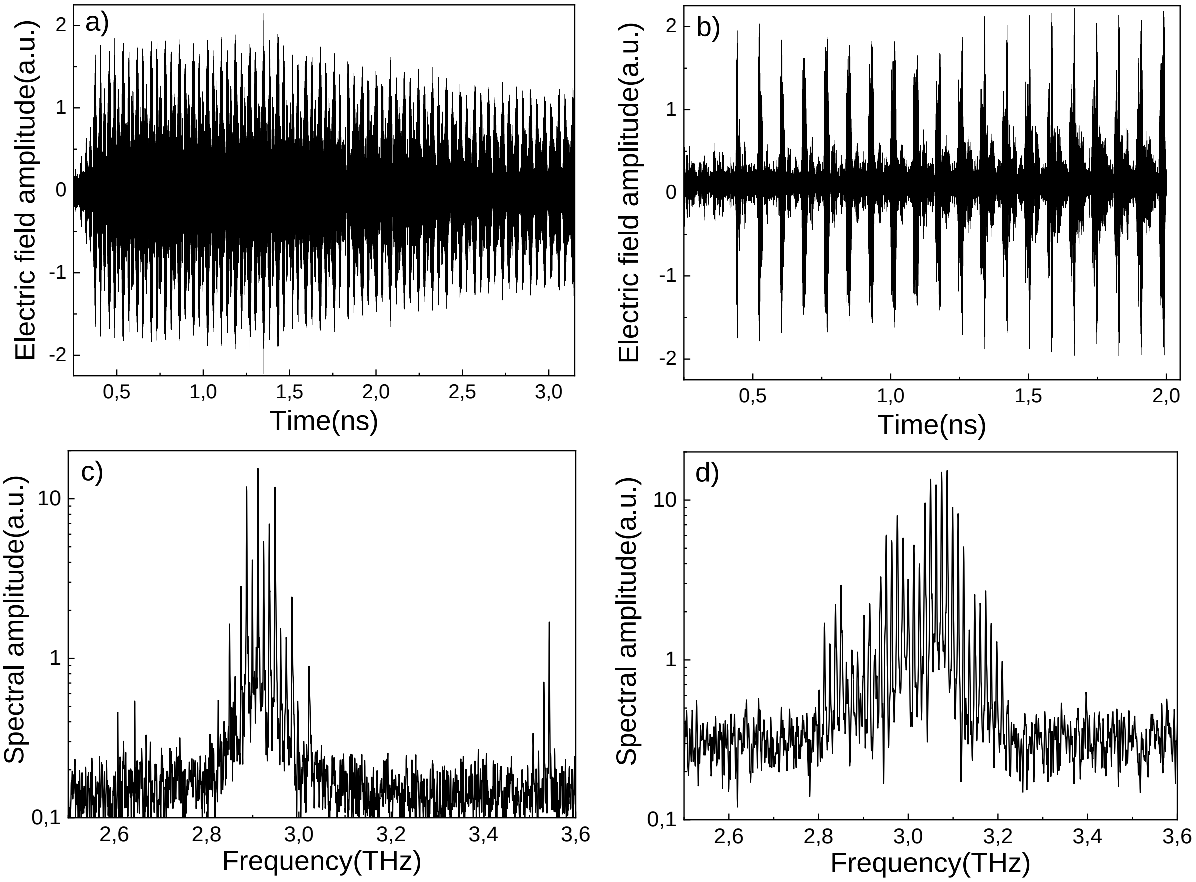

Figure 4.4: (a) free-running and (b) modelocking time traces and the correponding FFT spectrum (c-d) for the pristine Sample 3

properties. A theoretical approch was used to define the dimensions of the coupled cavities. The simulated GTI reflectivity for all the QCLs are showed in fig. 4.5 with the modelocked spectra obtained from experiments in each case. The free running emission is reported in Annex **4.1**, where only a weak effect of the GTI length is visible in the spectra.

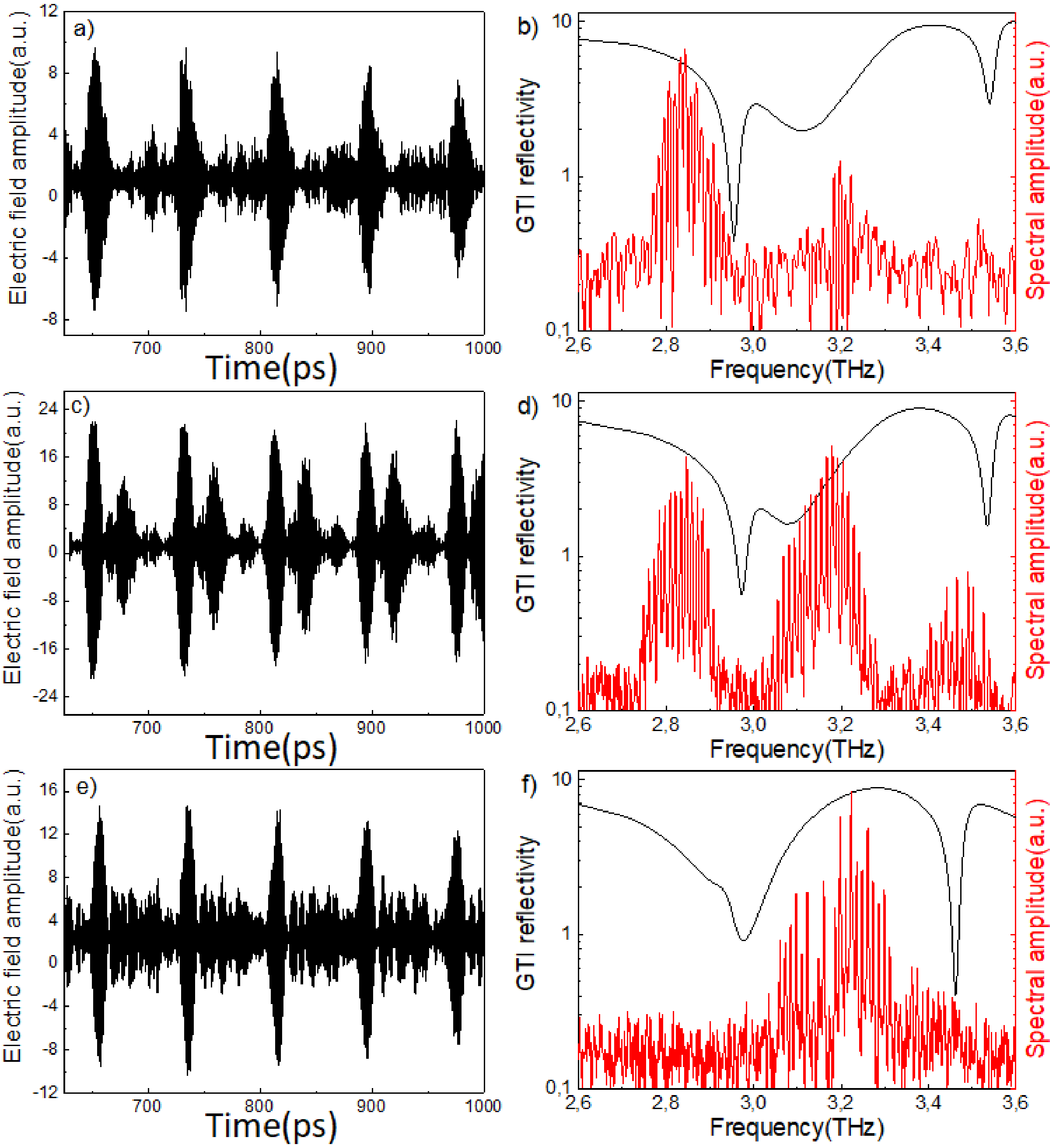

Figure 4.5: modelocking time traces (left panels), GTI reflectivity profiles (in black) and spectra (in red) (right panels) for Sample 3 with the 36.1μm (a-b), 37.1μm (c-d), 38.3μm (e-f) GTIs

The reflectivity profiles of the GTIs are shown here in place of the GDD profile to ease the interpretation of the results, as the dispersion can easily span more than two orders of magnitude in amplitude in correspondence to the resonances (which occur at minima of the reflectivity), making the understanding of the plots more difficult. The first point to notice from the comparison of fig. 4.4 with fig. 4.5 is that, despite the pristine sample emitting continuously from 2.8 to 3.2THz, all the samples with an integrated GTI show no emission around 3THz, in correspondence to the minimum in the reflectivity profile, when they are modelocked. As explained in section **3.2.1**, minima in the reflectivity correspond to resonances of the GTI and consequently to very high dispersion. Overall the shifting of the resonances to lower frequencies for longer GTI cavities is observed in the electromagnetic simulations and appears to correlate with the spectral response.

The analysis of the modelocking spectra clearly highlights the effect of the GTI on the locking mechanism: starting with the 36.1μm GTI (fig. 4.5a-b), we record a band at 2.8THz, below the minimum in the reflectivity profile, and a second weaker band at 3.2THz. Single-pulsed emission is obtained in the time domain. This situation is similar to that of the pristine case, but with the emission in between the two bands being made impossible by the great amount of dispersion introduced by the coupled cavity which prevents modelocking, as showed in fig. 4.6a.

As the high dispersion region moves to lower frequencies for the 37.1μm GTI (fig. 4.6b), the two previous bands broaden and the power gets redistributed in favor of the band at higher frequency. It is also interesting to notice that at this point the QCL shows emission in regions where the pristine sample was either very weakly or not emitting at all, attesting the occurrence of a shifting mechanism and the strong role of dispersion. The time trace shows two pulses per round-trip each of them distinctively related to one of the two main bands, as showed in more details in Annex **4.2**. Finally, at 38.3μm GTI length, a single band is present centered at 3.2THz, corresponding to the upper band of the previous case but considerably broader. This is a result of the strong positive dispersion added at 2.8THz by the GTI (fig. 4.6c), which prevents emission, and of the slow-varying negative dispersion from 3.1THz to 3.3THz which on contrary allows for modelocking to take place at higher frequencies than the pristine case.

As fig. 4.6d shows from the comparison of the modelocking spectra of all the samples, the effect of the GTI size on the emission properties of modelocked QCLs is strong. Frequency tuning seems to be possible as a consequence of the preferential emission of modelocked QCLs at lower dispersion conditions. This is particularly clear in the 38.3μm GTI case for which no emission occurs at the designed frequency of 2.9THz while a fairly broad band generated at 3.25THz, in modelocking conditions. Moreover, as the time traces show, active modelocking results to be effective even for configurations where the dispersion is quite strong in the lasing

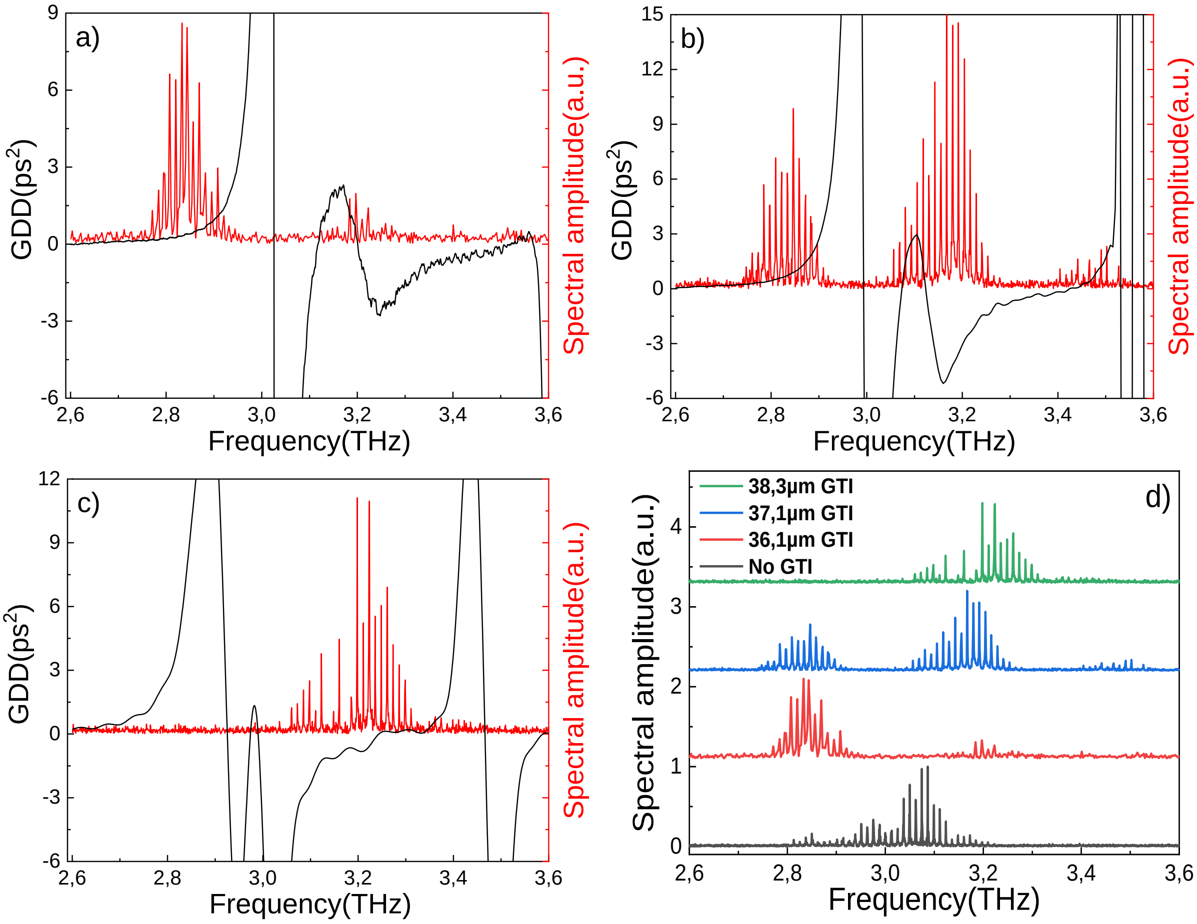

Figure 4.6: modelocking spectrum superimposed to the GDD provided by the GTIs of length 36.1µm (a), 37.1µm (b) and 38.3µm (c); (d) comparison of the previous spectra

band and it is capable of establishing and maintaining a long lasting mode coherence, provided that a sufficiently low dispersion range of frequencies is available for emission. Finally, it has been showed that the electromagnetic simulations of the GTI structures are capable of providing precise information that are essential to understand the behavior of these devices, such as the position of the resonances in the reflectivity profiles which translates into regions with strong dispersion.

This frequency shifting feature of GTIs on modelocked QCLs will be shown to allow the generation of ultrashort pulses, as described in the next section, when active modelocking will be used on ‘self-modelocked’ devices integrating a coupled cavity.

4.3 Spontaneous pulsed emission from a THz QCL

In section **1.5** it was explained that conventional passive modelocking techniques are not applicable to QCLs owing to their extremely short gain recovery time compared to the round-trip time of a photon in the cavity [113] [110]. It is clear, though, that the capability of generating short pulses from a THz QCL without the need of external electronics required for active modelocking is a highly desirable feature. Beyond the use of a saturable absorber, other propositions to induce pulse generation, mainly based on the alternation of gain and absorption sections of the cavity, were also highlighted but they still lack clear experimental results from devices where such design has been implemented [111]. The use of a saturable absorber combined with self-induced transparency was also proposed to achieve passive modelocking [114] but, as for all the other conceptual models, no demonstration has so far been presented.

In this section, observation in the time domain of self-pulsation from a THz QCL is provided. A possible explanation for this phenomenon is detailed in the broader frame to explain the harmonic states of emission in the next chapter and is potentially related to the particular geometries of the QCL and microwave waveguides. Moreover, a collaboration with the group of Dr Christian Jirauschek at TUM (DE) is currently ongoing to simulate the proposed mechanism responsible for the onset of this phenomenon by means of Maxwell-Block simulations. Nevertheless, the experimental proof of self-pulsation is irrefutable, encouraging for passive modelocking, and is discussed in the following.

4.3.1 Free-running pulsed emission of a THz QCL

Seeding experiments were performed to record the time profile of the electric field emitted by the pristine Sample 4 device in free-running conditions. This is shown in fig. 4.7a with the corresponding spectrum in panel b). A quasi-DC bias of 195mA and a RF power of 24dBm were employed during the injection seeding experiments. A very interesting fact is that Sample 4 is nominally identical to Sample 3 in terms of growth process and active region structure. The only differences are related to a slightly different growth temperature for the GaAs and especially to the geometry of the device.

The first striking feature of this time profile is its extremely pulsed behavior compared to any previously recorded free-running emission. In fact, once the steady-state is reached at 600ps, each round-trip clearly presents a main pulse surrounded by two smaller pulses. It is recalled that secondary pulsations were obtained in section **3.4** from the simulations combining the MM-RRE with the master equation of propagation in presence of dispersion. It is therefore not surprising to find these features in a device that does not include a dispersion compensation scheme. At the same time the fact that pulses are generated also means that the modes have to be locked to each other, despite the absence of an external driving mechanism. Experimentally, the mode coherence is typically assessed by the presence of a fairly strong beatnote (see Annex **3.1.4**). It is also recalled that this result is in striking contrast with the most accepted hypothesis that no stable pulse train can be spontaneously generated from a QCL owing to the presence of an ultra-fast gain recovery and strong chromatic dispersion [57] (see chapter **1**, section **1.5** for a more complete discussion on this topic).

Concerning once more the presence of the secondary pulsations, similar results are explained in [115] from numerical simulations as a side effect of SHB on the pulse shape. They can also be understood as the dephasing of the modes at the outer sides of the spectrum, where it is more difficult to establish the same phase relationship that the central modes share. It is nonetheless

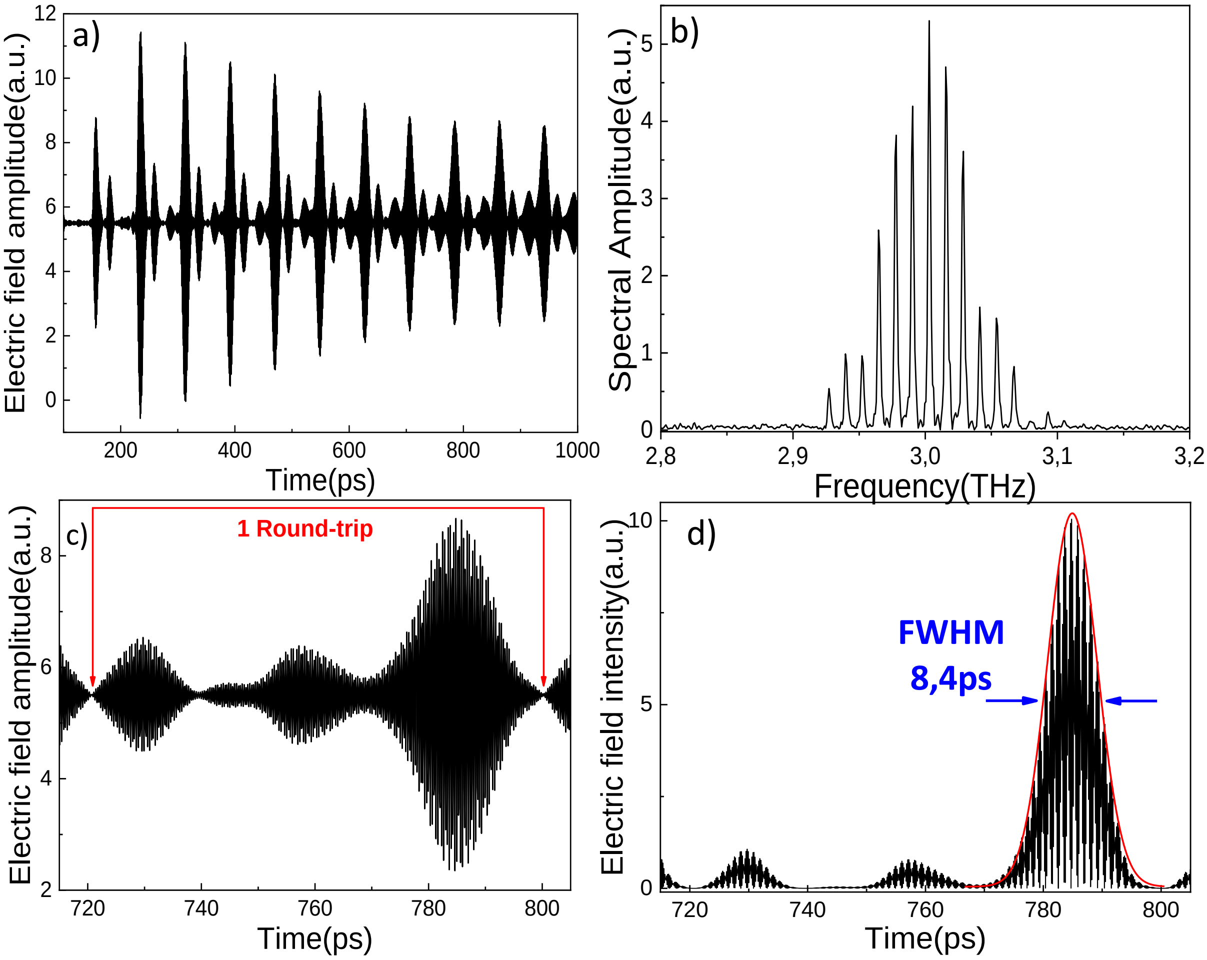

Figure 4.7: (a) Time profile of the free-running emission of Sample 4 prior to GTI integration and (b) the corresponding spectrum in the frequency domain. c) one round-trip of the time trace in a) showing the amplitude and intensity (d) of the electric field.

clear that they do not affect the overall behavior of the device even after several roundtrips as the main pulses are far stronger than the all the other features in the trace.

In the time trace of fig. 4.7a the main pulses show a FWHM of about 8.4ps in the steady-state (fig. 4.7c) while the spectrum is limited to a main band of less than 200GHz width centered at 3THz (panel b). It is therefore quite remarkable that so few modes spontaneously interfere to produce the well defined pulses visible in the intensity profile of fig. 4.7d. This is in contrast with a generic QCL's emission profile which tends to be much less modulated in amplitude. In fact, a kind of self-locking mechanism must be responsible for this emission profile which is capable of fixing the phases of the modes despite the unfavourable ultrafast dynamics of the gain of In order to further investigate this effect, active modelocking was attempted on Sample 4. In this particular case, the observed pulses clearly identify the round-trip, such that the best frequency for the active modulation could be computed directly from the reciprocal of the round-trip time (~78ps, see fig. 4.7c). A value of 12.7GHz was consequently obtained, which is close but not identical to that of the beatnote (12.3GHz). Figure 4.8 reports three modelocking traces for RF currents modulated at frequencies close to the computed one. The corresponding FFT spectra are plotted in panel b). As one can see, when modulations at 12.74GHz and 12.81GHz are applied, a pulse train is obtained which resembles the free-running trace but with a reduced appearance of the secondary pulsations. The drop in the pulse amplitude that is observed is consistent with the profile of the seeding trace and it is related to the initial transient occurring during the amplification process. Another reason for which this behavior is observed consists in the broadening of the pulses due to the uncompensated dispersion, which affects the pulses, especially at the beginning of the trace. In the steady state (>600ps), the pulses tend to stabilize their duration.

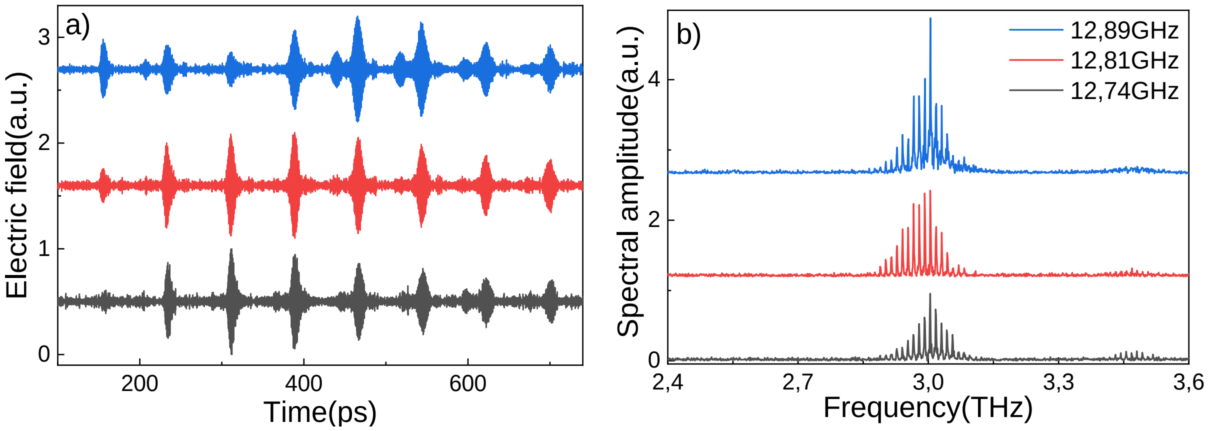

Figure 4.8: (a) Modelocking time traces and (b) spectra for a 12.74GHz (black), 12.82GHz (red) and 12.89GHz (blue) active modulation applied to Sample 4.

For a modulation of 12.89GHz instead, the amplitude of the pulses is observed to be more irregular with respect to the previous cases. It is suggested that this fact might derive from the relevant difference (~200MHz) between the natural round-trip frequency observed in the free-running case and the modulation applied, i.e. the frequency of the active modulation exits the locking range. This sample, in fact, showed a considerable sensitivity to the parameters of the active modulation: it is noticeable that for any frequency tested, the phase of the GHz signal had to be carefully set to allow for emission. For instance, for any of the traces of fig. 4.8, if the phase of the active modulation was shifted of more than $\pm\frac{\pi}{3}$ with respect to the value used to perform the measurement, no emission was observed. Some more details on how these facts relate to the locking mechanism of the beatnote of the device to the active modulation will be presented in section **4.4**.

The spectra are also not considerably different from that of the free-running case, except for a redistribution of the power among the modes which occurs depending on the frequency employed.

As the dispersion seems to be the main reason for which the pulses broaden, self-modelocking behavior of this QCL in high dispersion conditions was investigated. This was done by integrating a GTI with a length chosen to be ‘on-resonance’ (66μm) with respect to the emission band of the device. The same GTI also defines another range of frequencies for which the dispersion is compensated: in this way it was possible to test once more the frequency shifting properties of active modelocking in combination with a GTI.

4.3.2 Effect of dispersion on spontaneous pulsed emission

The 66μm long GTI integrated on Sample 4 was designed in such a way to display a strong dispersion region in correspondence to the free-running emission of the QCL, i.e. from 2.75THz to 3.1THz and at 3.4THz.

At the same time, according to the phenomenon of frequency shifting in active modelocking conditions that was described in section **4.2**, it is also expected that if a suitably low dispersion range is engineered in between the two high dispersion regions, then the application of an appropriate active modulation will create a spectral emission band in that range.

Figure 4.9 shows the dispersion and the reflectivity profile of the integrated GTI. One can see that the dispersion is strong in correspondence of the resonances of the GTI, which are the local minima of the reflectivity. A slightly negative dispersion range is instead evident from 3.05THz to 3.3THz, after which the dispersion slowly becomes positive again. If we apply an active modulation at the correct frequency so that the device is modelocked, we would expect the actively modelocked emission to occur in the blue regions. First, the free running condition was characterized for a later comparison and to verify if the dispersion is capable of destabilizing the self-locking mechanism that produced the pulsed emission in the pristine device.

Usual seeding experiments were performed to record the electric field amplitude and phase as a function of time as well as the free-running spectrum for 270mA and 14dBm of RF power applied. The emission profile is plotted in fig. 4.10a, its spectrum in panel b) and its intensity in panel c).

The intrinsically pulsed nature of the emission of the pristine Sample 4 is conserved, and the emission also takes place almost at the same frequencies even if less modes are present. This is a consequence of the fact that the dispersion is strongly increased with respect to the pristine sample and less modes are brought above threshold. Nevertheless, this is an extremely interesting observation that shows an unexpected robustness of the phenomenon of self-

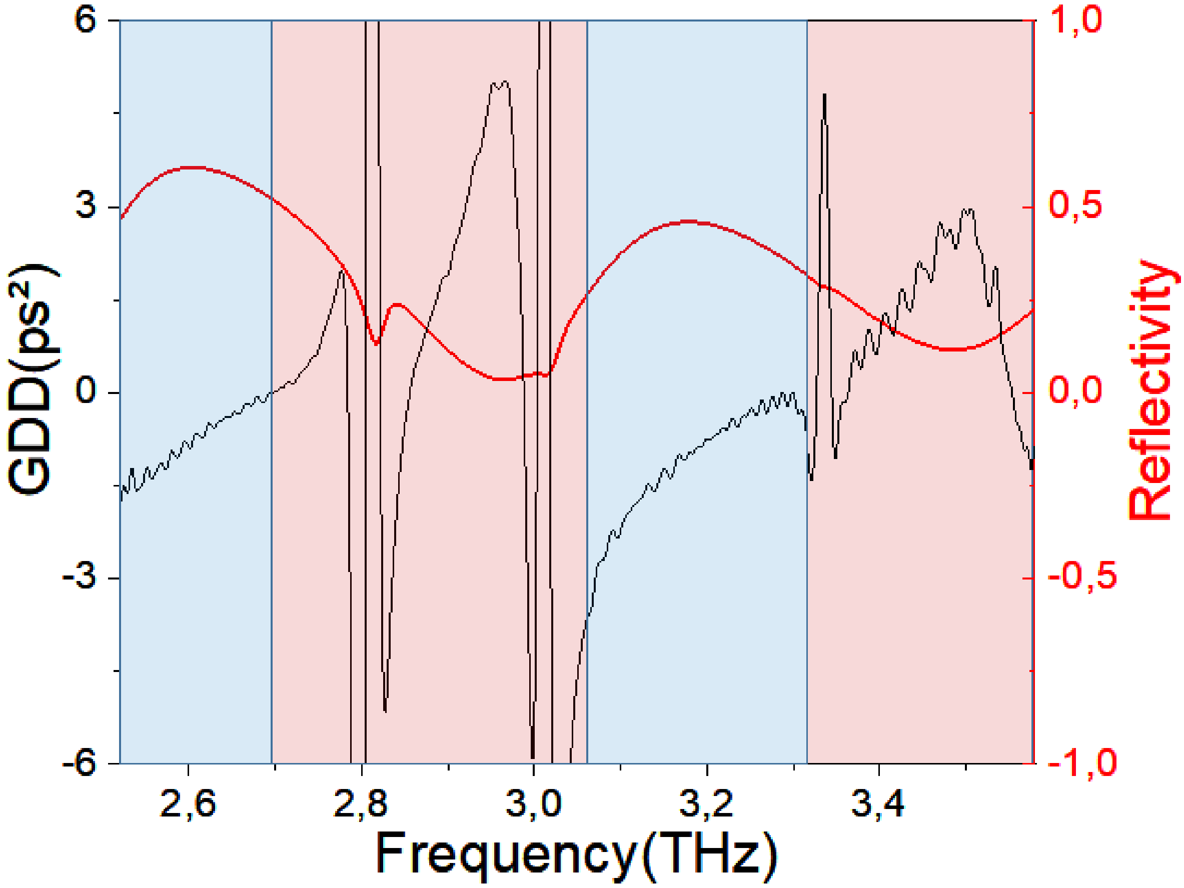

Figure 4.9: Dispersion (black) and reflectivity (red) profile of the 66µm GTI integrated to Sample 4. The ranges where strong dispersion is introduced by the GTI have a red background. Those where limited or compensated dispersion is present have a blue background

pulsation even in presence of unfavorable conditions. It has already been highlighted that dispersion is believed to be one of the main reasons for which the mode phase relationship, is lost when the bias is increased. Here instead the pulses of fig. 4.10a are strikingly well defined and stable even after 2ns. Some broadening is of course evident but appears to be limited compared to the amount of dispersion the radiation experiences owing to the GTI.

Further and more detailed analysis is necessary to deepen our understanding of this phenomenon. For this reason, instead of performing a single FFT over the entire time trace to

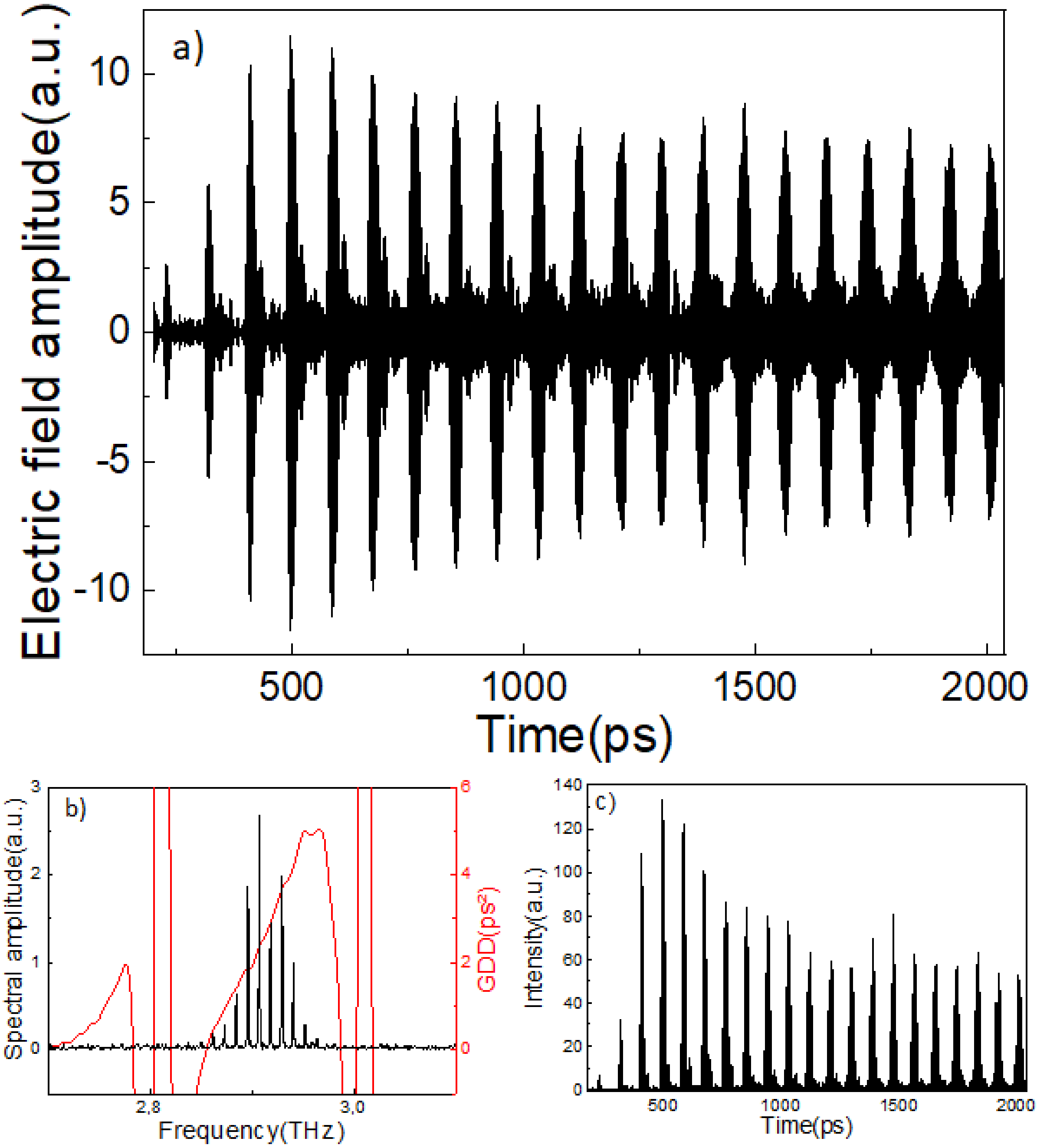

Figure 4.10: (a) Free-running emission of Sample 4/66 showing spontaneous pulse generation. (b) free-running spectrum (black) and GTI dispersion (red). (c) Intensity of the electric field as a function of time of Sample 4/66 clearly displaying a pulse train

get the spectrum of the emission, a series of FFTs on a moving range of 500ps were applied and are plotted as a colourmap in fig. 4.11. This allows us to visualize which frequency components are active at a specific time. On the time axis of this picture, the central time of each window is used. The colour code displays higher intensity with brighter colours, so that the background is black. Panel (a) corresponds to the emission of the pristine Sample 4 while panel (b) displays that of Sample 4/66.

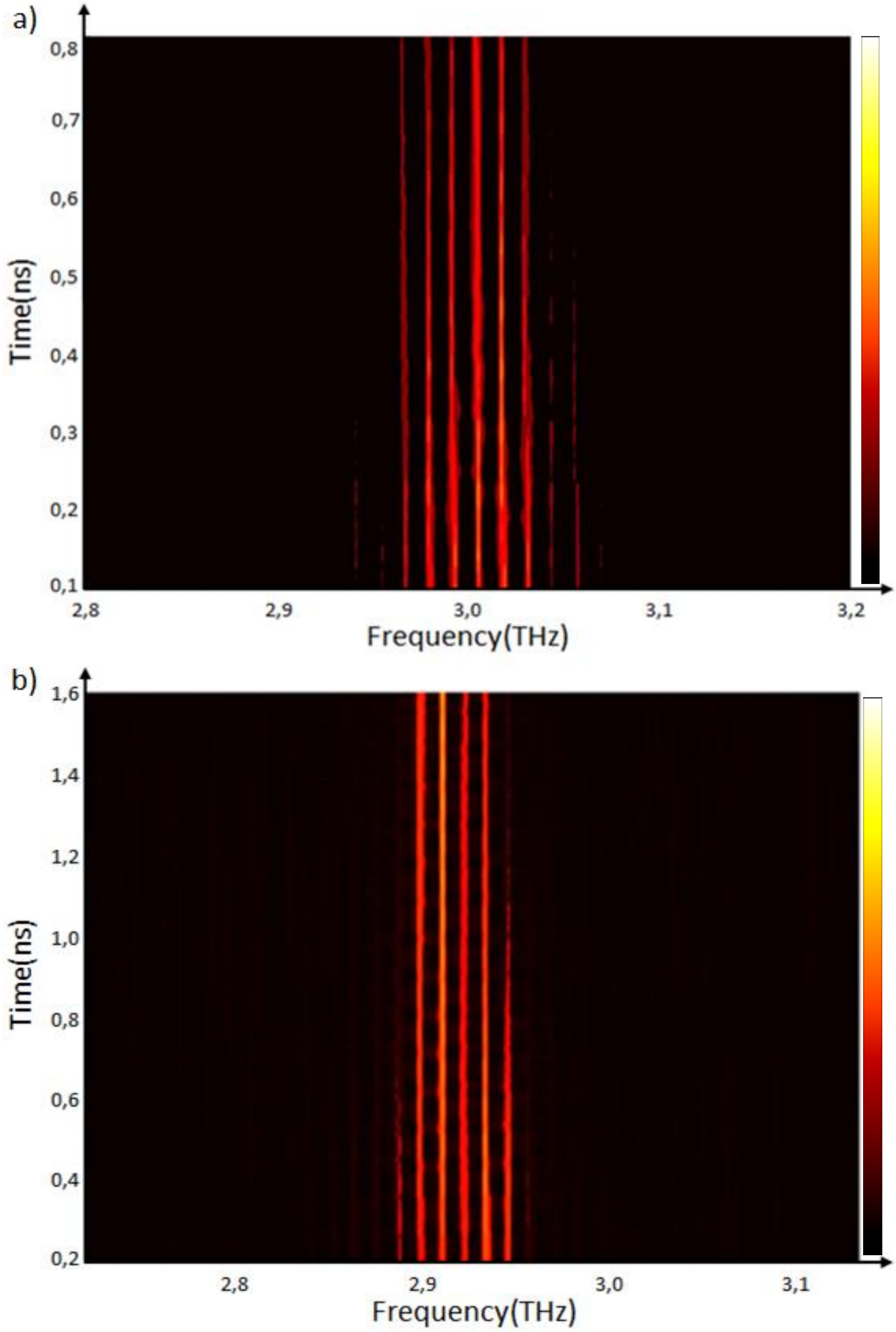

Figure 4.11: Electric field spectral evolution as a function of time for the free running emission of Sample 4 (a) and Sample 4/66 (b).

It is easy to notice that at the beginning of both traces many modes are present that decrease in number with time. In particular, the modes at the extremities of the spectrum are the first to disappear. This fact is in part expected from the nature of the seeding measurement that injects a broadband pulse whose components may temporarily survive in the cavity if they match the frequencies of the gain region. As a consequence, during the amplification transient the pulses may result to be shorter than those that are instead present in the steady-state. For these traces, this happens before 600ps.

However, the reduction of the number of the modes for Sample 4/66 (fig. 4.11b) may be induced by the GTI dispersion. For instance, the modes that are not sustained by the FWM become weaker and weaker, finally disappearing, and this process is favoured by the presence of a strong dispersion. On the other hand, the central modes look to be very strong throughout the entire trace and are capable of surviving indefinitely, leading to the stabilization of the pulse duration after 1.5ns.
Conversely, the pristine device shows remarkable stability in its spectrum already after 600ps.

Currently, no absolute explanation has been determined that allows this specific family of QCLs to defy the expected model for the QCL emission [57]. However, it is clear is that there is a set of conditions that permits a pulse to survive for an extremely long time in the cavity of a QCL. Even more interesting is the fact that the underlying mechanism is shown to be very robust and capable of fixing the phase of the modes even in presence of extremely high dispersion. A possible mechanism comes from the analysis of the harmonic emission states that are discussed in the next chapter, where certain conditions to the amplitude modulation of the QCL's emission are proposed.

After having observed the effect of the GTI on the free-running emission of a self-pulsating device, active modelocking experiments were performed. Since the device is already emitting pulses, I will refer to Hybrid Modelocking when an active modulation is applied on top of this spontaneous mechanism. This should not to be confused with the hybrid modelocking technique described in section **2.4.2** which is instead a combination of passive and active modelocking.

4.4 Hybrid modelocking

In the previous section, spontaneous pulse emission from two self-locked THz QCLs was presented and analyzed. In this part of the chapter, it will be showed that an active modulation can be used together with the frequency tuning properties of a GTI to tailor an ultrashort pulse train from a single relatively narrow emission band. This represents the first demonstration of a hybrid modelocking application to THz QCLs.

As already done in the case of the pristine Sample 4, it is possible to compute the roundtrip time from the pulses of the free-running emission of Sample 4/66 to deduce the most suitable value to employ for the frequency of the active modulation. From a round-trip time of about 87ps, the correct frequency of the RF current is around 11.46GHz that is noticeably different from its beatnote at 10.8GHz. The higher roundtrip time is due to the fact the device was not cleaved on the side where the coupled cavity was integrated, resulting to be longer than its pristine counterpart (see Table 4.1 for further details).

Figure 4.12a shows the modelocking traces obtained when a modulation of frequency 11.282GHz (in red), 11.361GHz (in purple) and 11.438GHz (in blue) is applied. Only in the last case a train of stable pulses is generated while in the other two traces the pulses tend to broaden and decrease in amplitude with each round-trip. It is possible to explain this behaviour by considering each spectrum, plotted in fig. 6.6b-d-f, and the dispersion of the integrated GTI. It is easy to notice that by getting closer and closer to 11.46GHz, the emission band shifts away from the free-running band at 2.9THz and moves into the dispersion compensated range that was originally designed in the middle of the bands of the free-running spectrum. As observed from the injection seeding experiments, the position of the free-running band is in a high dispersive frequency range due to the strong positive dispersion introduced by the GTI that sums to that from the material and gain. This phenomenon was already observed in Sample 3 for different GTI sizes, and multiple bands could be tailored according to the coupled cavity response when active modelocking was applied to the device. In this case, the shifting of the emission band by changing the frequency of the active modulation can be interpreted as a result of the pulling mechanism described in section **2.4.1**: by keeping the intensity of the GHz modulation constant, one can tune its frequency until it enters into the locking range. Once this is achieved, modelocking is possible and a stable pulse train can be obtained. The emission band tends to shift to a less dispersed spectral region, where modelocking requires less energy to be enforced. This locking happens more efficiently as the modulation gets closer to the exact round-trip frequency of the device.

It is important to highlight that in the case of the modelocking at 11.438GHz (blue trace) the pulses have totally different frequency components and a broader bandwidth than those generated in the free-running case. This capability of controlling the properties of the pulses, which is limited for passive and spontaneous modelocking as discussed in section **2.4**, is also

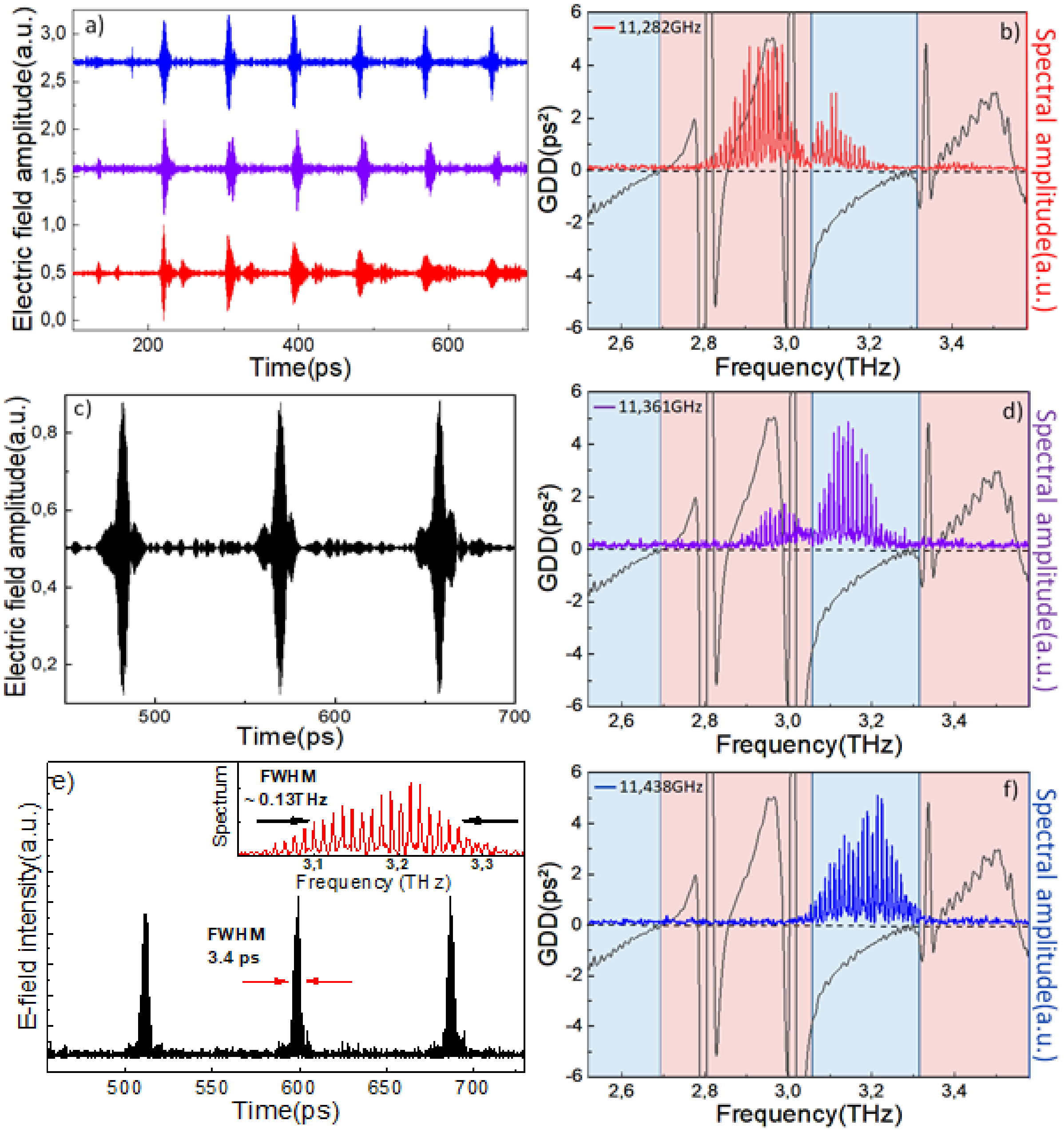

Figure 4.12: (a) Modelocking time traces for an active modulation at 11.28GHz (red), 11.36GHz (purple) and 11.43GHz (blue); (b-d-f) corresponding spectra with same colour code; (c) zoom of the first three pulses of the steady-state when a 11.43GHz modulation is applied to the device; (e) intensity of the pulses in ((c) with the spectral intensity in red in the inset. The difference in time between the pulses in panels (c) and (e), which are actually the same pulses, is due to the will to display those of the traces in (a) all at the same time to ease the comparison

what makes hybrid modelocking an interesting technique. Moreover, fig. 4.12c shows also that the secondary pulsations surrounding the main pulse observed from the pristine Sample 4 have disappeared, leaving an almost perfect example of pulse train. The FWHM of these pulses is reported in the intensity plot of fig. 4.12e, showing a record duration of 3.4ps. This is even more striking if the FWHM of their spectrum is considered, being as small as 132GHz that is 24% less than that of the 4ps pulse train discussed in section **4.1**. By assuming a gaussian profile for the pulses, this means that the recorded train is Fourier-limited. This implies that the dispersion is almost perfectly compensated, as expected from the design of the GTI. This is also the shortest stable pulse train reported in literature up to date, and represents the demonstration that an extremely large bandwidth is not necessarily required for short pulse generation if suitable dispersion compensation schemes are applied.

A final note regards the range of frequencies from 2.5THz to 2.7THz, where the dispersion profile introduced by the GTI is analogous to that from 3.1THz to 3.3THz where the emission shifts to when active modelocking is applied. In principle, both those regions could have been suitable for modelocking emission to be observed. The reason for which we do not observe any shift of the emission band into the lower compensated range at 2.6THz is probably due to the fact that the required frequency shift for the QCL would have been higher than 300GHz. Considering also the fact that the pristine sample emits at about 3THz, which is a demonstration of the presence of gain at those frequencies, the range around 3.2THz probably is simply favoured by its proximity.

Finally, with these results it has been showed that the active modelocking technique acts independently from the spontaneous pulse generation mechanism and that it is possible to combine the two to obtain extremely short pulses even from a narrow-band QCL. This includes the possibility to shift the emission spectrum to the desired frequency range in the gain region while keeping the pulsed behaviour of the free-running. The hybrid modelocking technique has also proved capable of going beyond the previous state of the art and it has the potential to be extended to broader bandwidth cases. It could then be the key to finally achieve sub-picosecond THz pulses that are coveted by the scientific and industrial community.

4.5 Active modelocking of an ultra-broadband QCL

Since, in general, the duration of a pulse is inversely proportional to its available bandwidth, a way to obtain short pulses consists in employing broadband structures, as presented in section **3.4**.

For double metal QCLs, devices with outstanding emission properties extending over one octave (i.e. with the last mode of the emission band being at more than twice the frequency of the first mode) have already been reported in literature [116]. These are based on multi-stacks of active regions that are designed to work at different but close frequencies. When all of these are lasing at the same time, emission over broad ranges of the THz spectrum becomes possible. Moreover, flatter gain profiles can be achieved that reduce the dispersion in the emission range. In this section, results from seeding and modelocking experiments on a broadband device, Sample 1 already used in section **3.3** for the study of the tunable GTI structure, will be shown. No dispersion compensation scheme was employed on this QCL and this will allow us to compare some of the simulations results previously described in section **3.4** with actual experimental data.

4.5.1 The ultra-broadband structure

Sample 1 is based on a heterostructure with three active regions, each exploiting a resonant phonon depopulation scheme but with different gain bandwidths centred at 2.5 THz, 3 THz and 3.5 THz. The expected emission is then supposed to occur from about 2.25THz to 3.75THz, covering an extremely broad range of about 1.5THz [117]

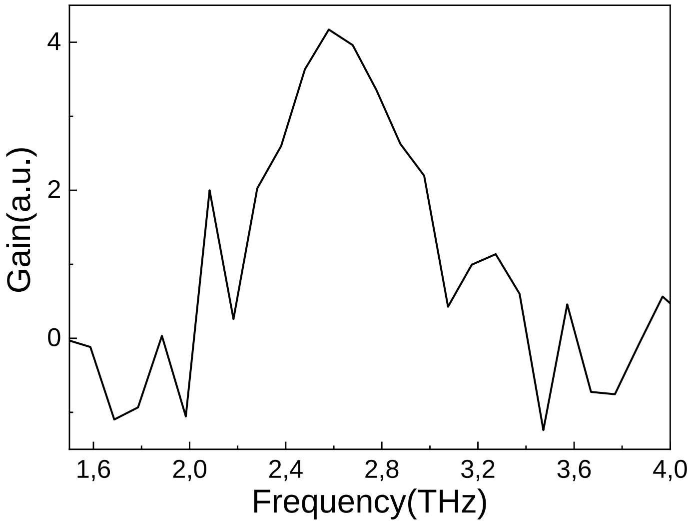

Figure 4.13: Gain profile of Sample 1 biased at 677mA using the technique described in [69]

Measurement of the gain with the technique described in [118] were also performed to experimentally assess the broadband behavior of this device. Figure 4.13 report the gain profile as measured at a bias of 677mA. The peaked profile shows the presence of gain from 2.1THz to 3.3THz, in agreement with the two lower active regions but without a strong amplification from that designed at 3.5THz.

Seeding experiments were then performed to recover the time profile of the emission of this QCL.

4.5.2 Experimental results

The free-running emission was obtained from seeding experiments. In figure 4.14 the raw time trace and related spectrum for a bias of 423mA and 32dBm of RF at 76MHz are shown.

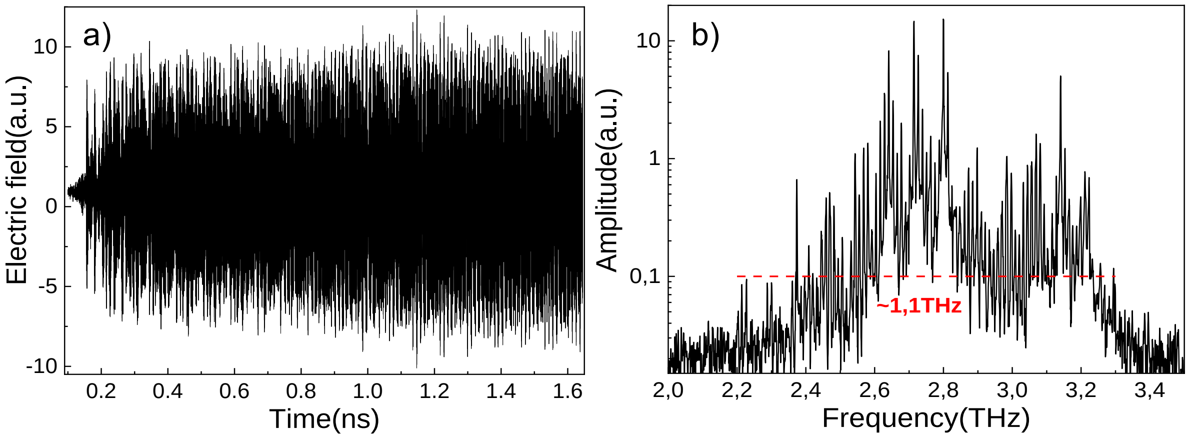

Figure 4.14: Free running emission in the time domain (a) and corresponding spectrum (b) of Sample 1 at 423mA with 32dBm of 76MHz RF applied.

Despite looking somehow compact and not so different from continuous wave emission, the time profile of the electric field shows a very complex pattern throughout the whole trace, with many small features of very short duration that are a consequence of the large number of modes involved. The spectrum in fact spans about 1.1THz, from 2.2THz to 3.2THz, in very good agreement with the expectations from the preliminary gain measurements. This means that the device has the potential to generate very short pulses if the modes are phase locked to each other.

In order to obtain pulsed emission, the QCL was tested in the active modelocking configuration. A modulation of 12.2GHz and 25dBm was applied on top of 420mA quasi-DC and 28dBm of RF for the seeding. Figures 4.15(a-b) show the raw data for the resulting time trace and the intensity of the first pulse respectively. The corresponding spectra are plotted in panels (c-d).

As the time trace shows, a single pulse is emitted during the first round-trip. This has a record duration of 1.32ps and a spectrum with FWHM of about 500GHz. It is the shortest pulse reported in literature for a THz QCL up to date. The spectrum of this pulse has a flat top, suggesting that the dispersion it experienced is still limited. The active region designed at 3.5THz seems not to be participating in the pulse formation. After another round-trip, multiple pulsations appear, increasing the pulse width considerably. This phenomenon was also observed in the simulations performed in the previous chapter in fig. 3.24. It is also interesting to notice that the whole spectrum of the trace does not differ significantly from that of the free-running case. In fact from the first pulse on, the shape of the spectrum degrades again into a peaked one, and the intensity of the modes is only slightly redistributed with respect to the case of the seeding. This can be explained from the lack of a dispersion compensation scheme that for such a broadband structure results in the stretching of the pulses after just a few round-trips, even with an active modulation applied.

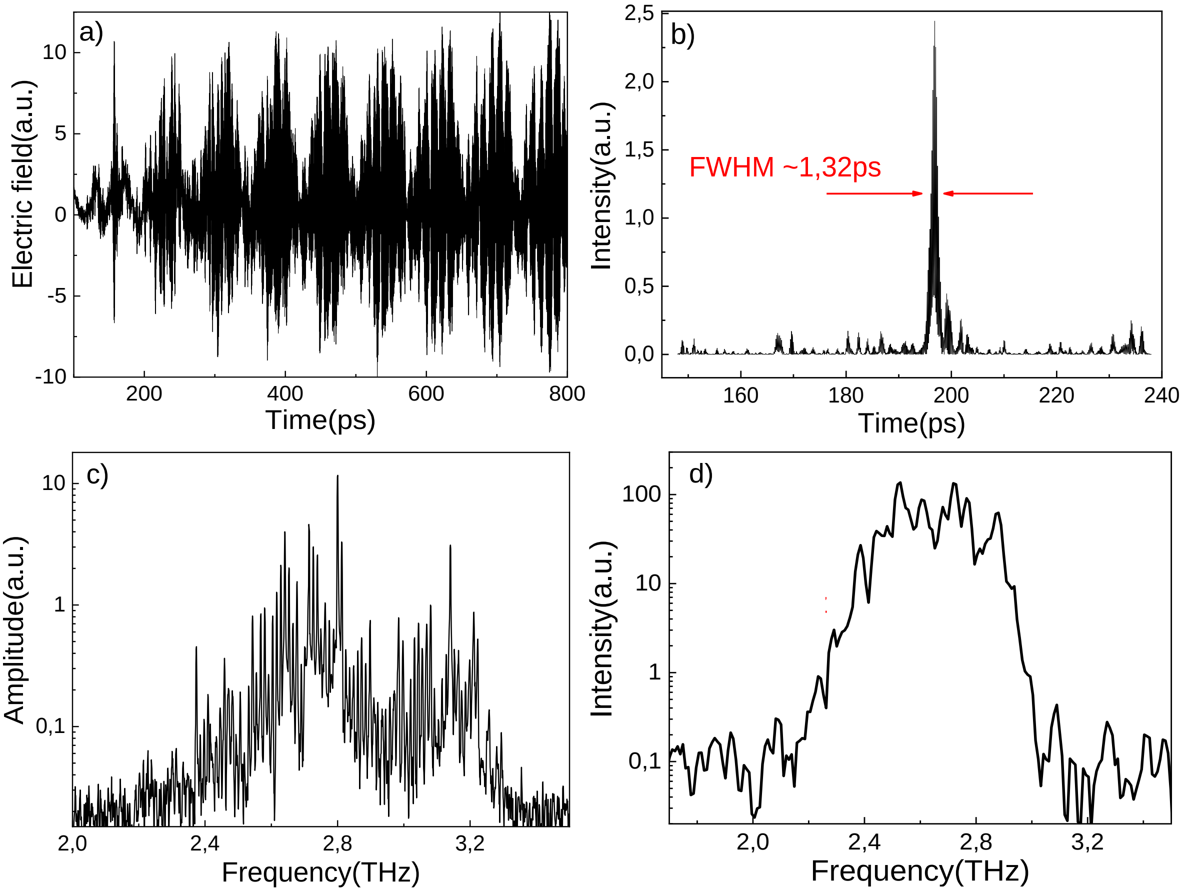

Figure 4.15: Modelocking time trace (a), first pulse intensity (b), modelocking spectrum (c) and first pulse intensity spectrum (d) of Sample 1

In conclusion, ultra-broadband structures such as Sample 1 offer very large bandwidth that allows for the formation of very short pulses, as the one showed in figure 4.15(b), but the presence of uncompensated dispersion over such a broad range of frequencies quickly stretches the pulses leading to multiple pulsation and overall pulse broadening. It is therefore of the utmost importance, especially for this kind of structures, to integrate a suitable dispersion compensation scheme capable of limiting or eliminating these undesirable effects. It is still remarkable, though, that such a short pulse, almost at the threshold of 1ps, could be simply obtained with the conventional active modelocking technique and a broadband device.

4.6 Conclusions

In this chapter it has been showed that the combination of adapted dispersion compensation schemes and active modelocking can successfully lead to the generation of ultrashort THz pulses. This was done starting from the case of Sample 2, which demonstrated to be capable of delivering a 4ps pulse train. The theoretical framework for dispersion control underlying these results was described and confirmed, in particular to that regarding the effects of the coupled cavities on the emission properties of the QCLs.

Furthermore, the combination of an active modulation and dispersion engineering has permitted the tuning of the frequency band of the emitted pulses. This is a desirable feature to add versatility to the QCLs that in general offer limited control over their emission properties post fabrication. While generally not suitable for ultrashort pulse generation, this technique can still be employed as a post processing solution that does not require to design and implement a sophisticated feedback structure.

From the study of Sample 4, the onset of spontaneous pulsed emission from a THz QCL was reported for the first time. Owing to the ultrafast time domain technique, the build-up of this phenomenon has been shown with femtosecond resolution from the moment the device is switched on to the steady state. The very fact that a THz QCL can operate in a condition reminiscent of passive modelocking, despite the pulses being quite broad compared to the active modelocked ones, represents nonetheless an advancement towards practical applications and an interesting behavior of certain QCLs. This can be considered also as a demonstration that there are some ways to overcome the short gain recovery time constraint of QCLs for the passive generation of pulses. In fact, the experimental data offer an absolutely clear proof that pulses can be stable in a QCL cavity without an external modulation.

Finally, the combination of the self-pulsing behavior with the existing techniques of active modelocking and dispersion compensation has been proved to be effective and dramatically improved the quality of the resulting pulses. A Fourier-transformed limited pulse train of 3.4ps of duration in steady state was demonstrated i.e. stable modelocked emission with the shortest pulses reported to date. This fact is even more striking if the band of the emission is taken into account where only a narrow spectral width of ~130GHz at the FWHM was employed.

This was realized by combining the dispersion profile from a suitably engineered GTI with the active modelocking technique in the same way as it was initially demonstrated in Sample 3.

Some preliminary results concerning the application of active modelocking to ultra-broadband THz QCLs were presented in the final section. This showed that pulses with a duration close to 1ps can be generated with the existing approaches. At the same time, they also show that in order to lock together many modes over a very broad range of frequencies in stable way, specific dispersion compensating schemes must be implemented. When this is not done, the initial pulse profile will degrade extremely quickly leading to the onset of multiple pulsations and a continuous broadening. Nonetheless, significant advances have been made to breach into the domain of sub-picosecond pulses. At this regard, future studies will include the design and implementation of an integrated GTI to these QCLs for dispersion compensation over the broadest spectral range.

5

Harmonic modelocking in THz QCLs

Several new phenomena unique to QCLs have been reported since their first realization in 1994. This includes, for example, ultrafast modulation and the absence of relax oscillations owing to their unconventional fast dynamics compared to other laser sources. Other new observations include coherent instabilities [119] and harmonic modelocked behavior in MIR QCLs. The latter, where QCLs emit at well-defined harmonics of the round-trip frequency, has not been previously observed in THz QCLs and will be the main topic of this chapter. More specifically, section **5.1** will discuss the first demonstrations of harmonic modelocked devices by an active modulation while section **5.2** will demonstrate an interesting behavior where THz QCLs that spontaneously modelock on a harmonic (i.e. without an external modulation).

A theoretical model based on Maxwell-Bloch equations is also proposed to explain the physical origin of the harmonic state in THz QCLs. In particular, this interpretation based on interlayed absorption and gain regions, will provide a route in understanding why certain QCL show modes separated by a specific harmonic of the fundamental round-trip frequency whilst not emitting at the natural fundamental value. A further generalization to a device with a tunable external feedback into its cavity is used to predict that the harmonic state of a device can be controlled under certain circumstances.

Although spontaneously generated harmonic frequency combs have already been presented for the QCLs operating in the MIR [120], no direct measurement or simulations of their temporal profile has been reported. (Their steady state properties have only been inferred on the basis of theoretical models and numerical simulations). This will be investigated both experimentally and theoretically for the first time here for THz QCLs that highlights the importance of considering the microwave waveguide for QCL modelocked operation. Moreover, harmonic emission may open up to the possibility of technological applications of THz QCLs such as microwave generation and broadband spectroscopy.

Two new devices, Samples 5 and 6, will be introduced in this chapter. These are based on the structures described in [47] and [94] respectively, which allow for a low threshold current. Their characteristics are presented in Table 5.1 and their LIV and beatnotes map are reported in Annex **5.1** and **5.2**. A third device, Sample 7, is briefly used to show the behavior of a conventional double-metal QCL having modes separated by the fundamental round-trip frequency. The simulations of section **3.4** were based on the spectrum of this device. Since it will not be analyzed in much detail, solely its characteristics are added to Table 5.1.

	Sample 5	**Sample 6**	**Sample 7**
Growth code	ART2758	L1456	L857
Processing lab	C2N (Paris)	CNR (Pisa)	C2N (Paris)
Active regions (periods)	2.5THz(180)	2.5THz(55) 3THz(40) 3.5THz(40)	3THz(180)
Active region scheme	Hybrid structure [48]	Hybrid structure [85]	Hybrid structure [48]
# wells	4	9	4
Waveguide	Double Metal	Double Metal	Double Metal
Length/width/height	6mm/60µm /12µm	2.2mm/63µm /17µm	2.7mm/100µm /12µm
Side absorbers (width)	4.5µm	4.5µm	2µm

Table 5.1: Characteristics of the samples used in chapter **5.** The dimensions refer to those described in fig.1.9.

Chapter 5

5.1 Harmonic modelocking in a Quantum Cascade Laser

5.1.1 Introduction

A laser sustains many longitudinal (Fabry-Perot) modes which are separated in frequency by the free-spectral range Δf :

$$\Delta f = \frac{c}{2nl} \tag{44}$$

where *n* is the effective refractive index of the material of the laser and *l* is the distance in between the laser facets. This is also the reciprocal of the round-trip time, as extensively discussed in chapter **1**. Therefore, for a sufficiently long QCL, Fabry-Perot modes will be found in the region corresponding to the designed gain of the device. This was generally the case for all the experimental results presented in the previous chapters. In the case of modelocked lasers, the mode separation and phase relation are fixed to a high precision. This is typically around bias values close to laser threshold. If the bias is raised too much, however, the chromatic dispersion produced by the gain will rise and the modes will not be evenly spaced. The emission will then become chaotic due to the loss of mode coherence. These topics were already treated in detail in section **1.5.1**.

Harmonic modelocking operation for which the mode separation is a multiple of the free-spectral range can also be observed if the time profile of the emitted radiation shows a periodicity that is an integer fraction of the round-trip time. In the case of pulsed modelocking, a harmonic state can be easily identified if more than one pulse per round-trip is emitted. In this condition, the QCL is said to be harmonically modelocked, with the number of pulses per round-trip being associated to the corresponding order of the harmonic (see the representation of fig. 5.1). The same concept can be applied to non-pulsed frequency combs, but the electric field profile in this case is expected to be only frequency modulated, with limited to no amplitude modulation [56].

A harmonic state not only permits a higher repetition rate (at the price of the loss of some modes), but it also improves the signal to noise ratio compared to fundamental state as the same signal is emitted multiple times in the same amount of time compared to the fundamental case. However, it should be noted that the comb is more sparsely spaced in frequency.

Harmonic frequency combs have very recently been demonstrated for the MIR QCLs [56] [121]. Reports from THz QCLs have still to be published. Moreover, the time behaviour of the comb emission was not been directly measured and all investigations have been based on the analysis of the beatnote linewidth and of the emission spectra. Here, thanks to the extremely high temporal resolution of a THz TDS, we will demonstrate the ultrafast dynamics of harmonic frequency combs on a femtosecond/picosecond scale as well as their evolution over a nanosecond scale. Of particular interest is the observation of a strong amplitude modulation of the electric field, instead of an expected frequency modulation, which generates short pulse-like features on a ps-scales. This is not predicted by the current models that are used to understand the temporal emission of THz QCLs.

Before discussing the experimental data, it is also important to recall that up to date the spectra obtained by TDS experiments on QCLs have generally been provided by employing an FFT over the entire time trace, effectively averaging all the modes over the whole duration of the scan. This approximation can be accepted for QCLs operating entirely at the fundamental state

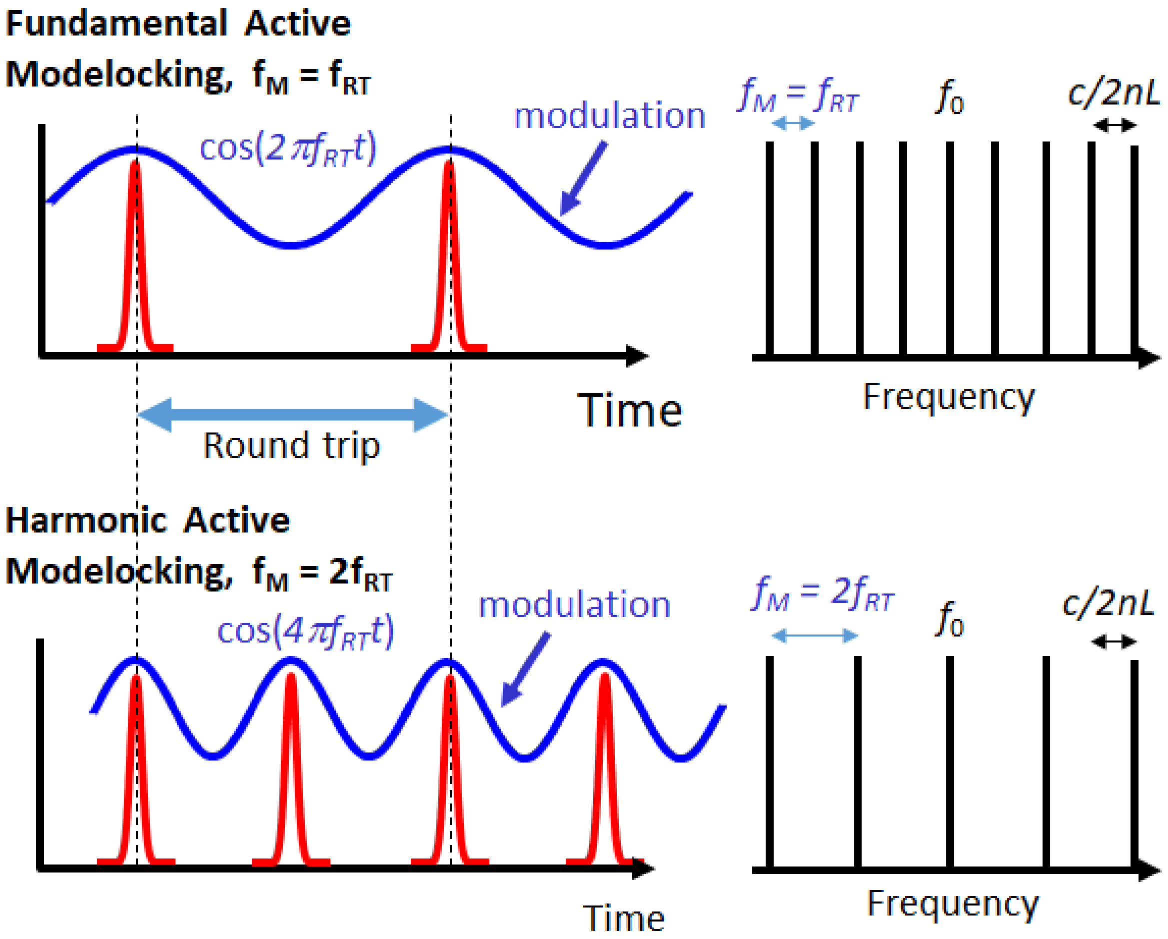

Figure 5.1: Representation in the time (left) and frequency (right) domains of the output of a QCL modelocked at its fundamental frequency (top) and at the second harmonic (bottom) of its round-trip frequency.

but becomes a limiting factor if the laser can switch from a state to another in ranges of time that are comparable to the duration of the scan. A useful tool to study the onset and progression of the mode dynamics in a QCL is the analysis of the time evolution of the emission spectrum. This can be done with a series of moving FFT of a relatively narrow portions of the electric field time profile (a few hundreds of ps). This technique was already discussed in section **4.3.2** to study the emission of Sample 4 which is a QCL working at the fundamental modelocking state. In that particular case, one could notice the lines at the modes at the extremities of the QCL spectrum fading as time goes on. This was expected due to the increase of the FWHM of the pulsations during the scan as a result of dispersion. Equivalently, from the point of view of the spectrum, it can be described as the effect of the dispersion acting on the weaker modes and therefore cannot be locked to the rest of comb up, to the point they finally disappear after several round trips. In other words, it can be described as the signature of the competition between the mechanisms inducing multimode operation (e.g. spatial hole burning) which tend to sustain these modes and the dispersion which, in tandem with the gain, leads to narrower band emission. The important feature that it is important to notice in section **4.3.2**, is that the device starts and continues its emission in the fundamental state, i.e. with all the modes separated by the round-trip frequency of the cavity.

In the next sections, experimental evidences of active and spontaneous harmonic emission in THz QCLs are reported along with an analysis of the mechanisms which can be considered that drive these devices in states other than the conventional fundamental case.

5.1.2 Active harmonic modelocking

Active modelocking is the standard technique that is employed to force a QCL to emit pulses. It was discussed in chapter **2**, where it was explained that to actively modelock the emission of a laser it is necessary to apply a current at a frequency corresponding to the round-trip frequency of the cavity. Generally, additional modes are created and the frequency separation of all the modes is determined by the active modulation.

In this section it will be shown that active modelocking can be used to induce the QCL to operate also at a harmonic of the fundamental mode separation. This can be conceptually done by multiplying the frequency of the active modulation by an integer number that will be the harmonic value at which the QCL is modelocked. There are of course additional difficulties to address that arise when the frequency of the electronics is increased significantly, as it happens for high harmonic values.

In order to avoid unnecessary changes to the standard configuration of the setup, such as introducing electronic components and dedicated connections capable of carrying modulation frequencies higher than 20GHz, the experiments were done on Sample 5, which is 6mm long. With a QCL of such length, the fundamental frequency is expected to be around 7GHz and the second harmonic to be ~14GHz. The LIV and beatnote are reported in fig. 5.2.

The electrical beatnote spectrum in fig. 5.2b shows two higher peaks at 6.9GHz and 14.5GHz when the device is switched on for a bias current of 1.12A. The line at 14.5GHz corresponds to the second harmonic beatnote, while those in between 7GHz and 9GHz can be linked to the interactions between beatnotes of different sub-combs of the spectral emission [122]. None of these features, though, seemed to correspond to an actual fundamental beatnote. No beatnote is present for the device biased below threshold at 860mA. Interestingly, the strongest feature is the beatnote at 14.5GHz, meaning that the device favours second harmonic emission over the fundamental even in its free-running state. This phenomenon has never been showed before from a THz QCL and will be addressed in the following section.

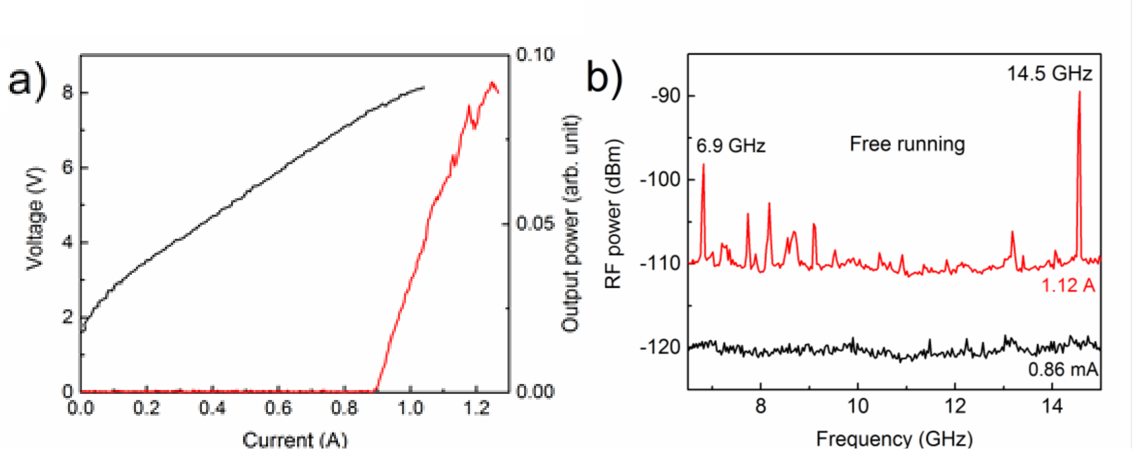

Figure 5.2: (a) LIV and (b) beatnote spectrum of Sample 5 when this is biased below (black) and above (red) threshold

As explained in chapter **3**, before modelocking a device it is necessary to prove that it is possible to lock it to an external RF reference, i.e. that its mode spacing and mode phases can be locked to an injected active modulation. Since the electrical beatnote is indicative of the uniformity of the mode distribution, one can indicate active modelocking by locking the beatnote to the external reference. This has been extensively reported for the fundamental case [89] but no demonstration has ever been done for a harmonic.

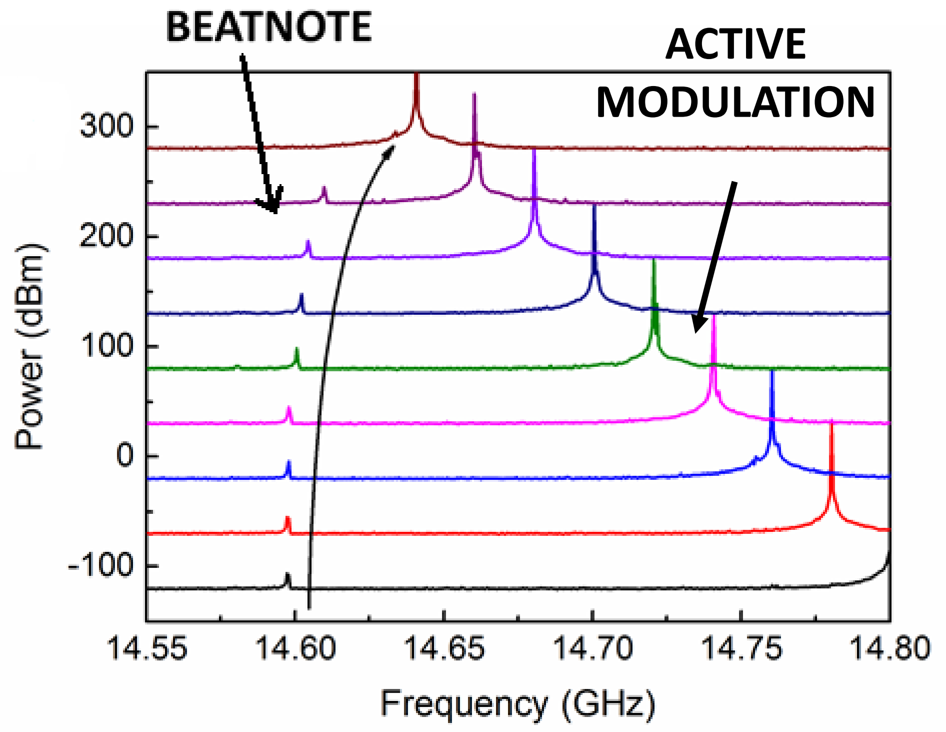

Figure 5.3: Injection locking of second harmonic beatnote of Sample 5. The beatnote is pulled towards the active modulation as their frequencies get close to each other

Therefore, an experiment was done in the same way as that in section **2.4.1**. This consisted in recording the second harmonic beatnote with a spectrum analyser while a 16dBm current with a frequency close to 14.5GHz was injected into the QCL and was then moved closer and closer to the harmonic beatnote. Figure 5.3 shows how the latter is pulled to the RF reference with a non-linear dependency and finally gets locked to it, thus proving in principle the feasibility of active harmonic modelocking. Free-running, fundamental and second harmonic active modelocking were consequently performed on the device.

The time traces for these experiments are shown in fig. 5.4a with their spectrum in panel (b). In the free-running state with for a bias close to the threshold, the QCL shows only a few modes, mainly around 2.45THz and 2.35THz, which results in a mostly continuous emission. When a 18dBm current modulated at 6.51GHz is applied, the device enters the fundamental modelocking state which is evident from the single pulse per roundtrip in the time trace and all the new spectral lines appearing in the spectrum, which share that frequency spacing at the round-trip frequency. If modulated at 13.80GHz, instead, the QCL emits two pulses per round-trip, and the spacing of the modes doubles as well.

The comparison of the three traces allows one to clearly identify the emission state of the device even without knowing in advance the frequency of the modulation applied. This constitutes a clear demonstration of active harmonic modelocking, which in perspective can be used at even higher harmonic orders.

By observing the part of the free-running spectrum in the blue box of fig. 5.4b, it can also be noticed that the modes are separated by a multiple of the fundamental frequency. One can compare it with the spectra of the fundamental and second harmonic states to see that in general one mode over two appears to be missing in the free-running emission. This is also consistent with the power distribution in the beatnote map: the second harmonic state tends to be favoured over the fundamental one even in the absence of an active modulation. Since only a few modes are above threshold in the free-running spectrum, though, the phenomenon is not obvious.
In order to verify this spontaneous harmonic emission observation, further experiments were performed on Sample 5 at higher biases. A complete discussion on this topic will be done in the following part of the chapter.

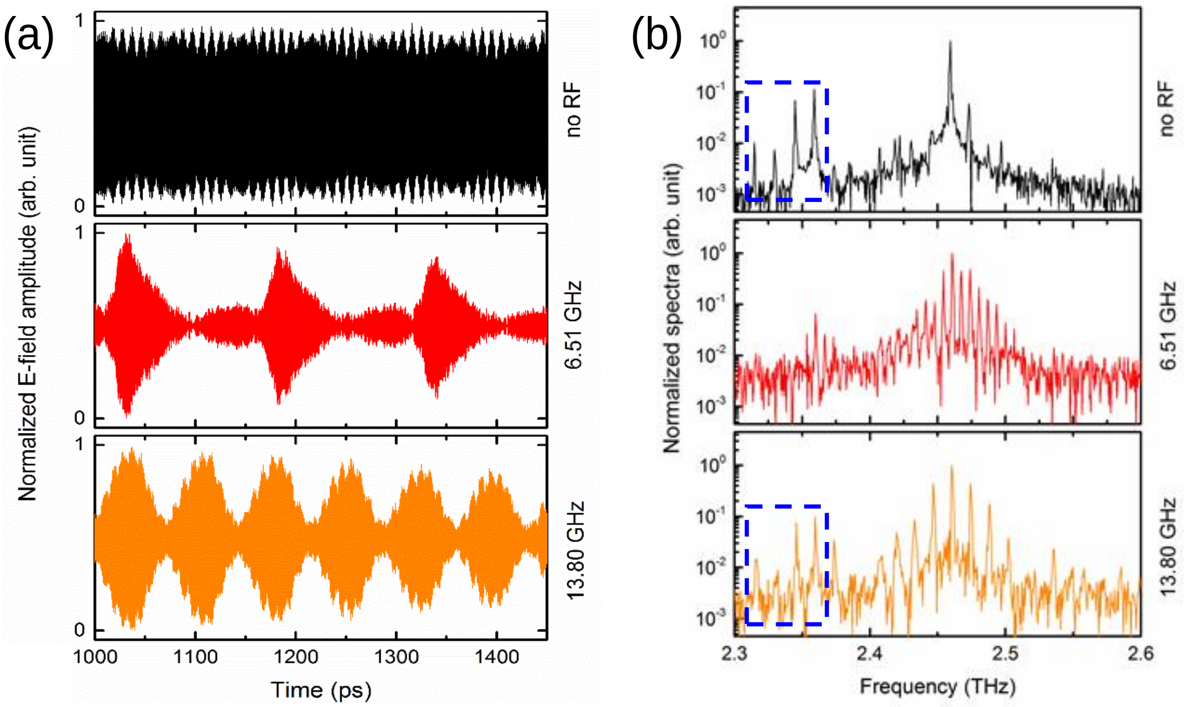

Figure 5.4: (a) Time resolved emission as a function of time for the free-running (black), fundamental modelocking (red) and second harmonic modelocking states (orange) and (b) the corresponding spectra. The modes in the blue boxes highlight the way the mode distribution in the free running case resembles that of the second harmonic modelocking one.

5.2 Spontaneous harmonic emission

5.2.1 Second harmonic spontaneous emission

In the previous section it was discussed that Sample 5 shows a second harmonic beatnote (fig. 5.2b) that is significantly stronger than any of those which may correspond to the fundamental one. Moreover, its free-running spectrum presents a mode spacing at twice the cavity round-trip frequency. While there are only a few lasing modes when the device is set close to threshold, as it has to be for the modelocking experiments, more of them can be brought above threshold for higher biases.

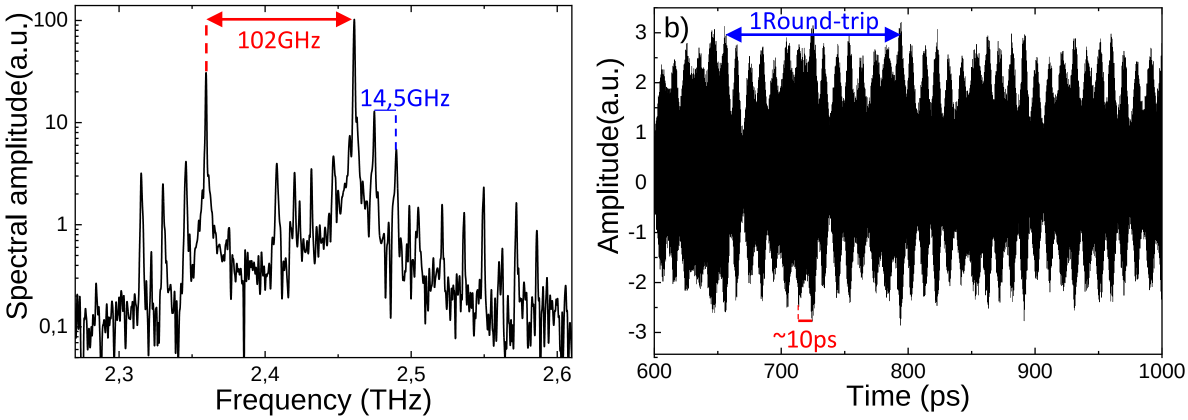

Figure 5.5: (a) Spectrum and (b) corresponding time trace of the electric field emitted by Sample 5 at a bias of 1.09A

Figure 5.5a shows the free-running spectrum for the same device at a bias of 1.09A. Two bands can be identified at 2.35THz and 2.45THz and the emission takes place over a 300GHz range, with many more modes compared to the previous case. The mode separation is at twice the round-trip frequency (~14.5GHz) and this can also be recognized in the corresponding time trace plotted in fig. 5.5b where a modulation at twice the round-trip time is evident. A multitude of short pulses are also visible throughout the entire scan that can be traced back to the ~100GHz separation of the two main modes, thus leading to the presence of a 15th harmonic emission state.

These interesting features result in a fairly complex electric field profile that is considerably different to the one that can be obtained from a frequency modulated laser. This occurs in spite of the observation made in previous publications [56] for which an almost CW emission from QCLs was claimed to be the general case. When the latter condition is not verified, i.e. a strong amplitude modulation of the electric field is present, harmonic emission can be easily identified into the time domain from the periodic repetition of a certain unitary pattern of the emitted field for a number of times per roundtrip that is the order of the harmonic, as already showed in fig. 5.1.

In order to investigate the origin of this periodical amplitude modulation of the electric field profile, we have developed a model that represents the effect of the self-current modulation provided by the beatnote on the emission profile. Some preliminary considerations are necessary and discussed below.

As previously explained, the beatnote is an electrical RF signal generated by the beating of the lasing modes inside the cavity. It has been experimentally demonstrated [123] that the electrical beatnotes of the QCLs has an intensity whose spatial profile in the cavity is not uniform but sinusoidal. In other words, a RF standing wave modulation exists as a result of multimode lasing operation, which in turn is triggered by SHB effects for biases just above the threshold (~1.1 I_{thresh}). Considering the beatnote spectrum of Sample 5, it comes natural to provide a numerical example considering at first the second harmonic case. For such a beatnote, the RF profile it shows in the cavity can be written in space and time as:

$$RF(x,t) = A_{GHz} * cos\left(2\pi\frac{x}{L}\right)\cos\left(2\pi\frac{c}{n_{GHz}L}t\right) \tag{45}$$

where A_{GHz} is the maximum amplitude of the RF modulation at the facet, L is the length of the cavity and n_{GHz} is the refractive index of the material at the frequency of the beatnote. A graphical representation can be found in fig. 5.6. This modulation appears on top of the external bias V_0 applied to the device, so that the total voltage is:

$$V = V_0 + RF(x,t) \tag{46}$$

A generic THz photon P of one mode in the cavity can have its position $x_P(t)$ described at a particular time as

$$x_P(t) = \frac{c}{n_{THz}}t + x_0 \tag{47}$$

where $n_{THz}$is the refractive index seen by the photon and x_0 is the starting position of the photon. The issue of describing the position of this photon after a reflection at one facet can be neglected if the facets have unitary reflectivity and the modulation is symmetric with respect to them. In fact, as showed in fig. 5.6, a photon at a time t_1 is moving along the x_0 axis and its position on the x and x_0 axis is identical. After a reflection at the facet at $x_0 = L$, at time t_2 the position of the photon can be mapped in the interval $L < x < 2L$ without the need of accounting for the inversion of the sign of the velocity which is instead necessary to consider to describe the motion on the x_0 axis.

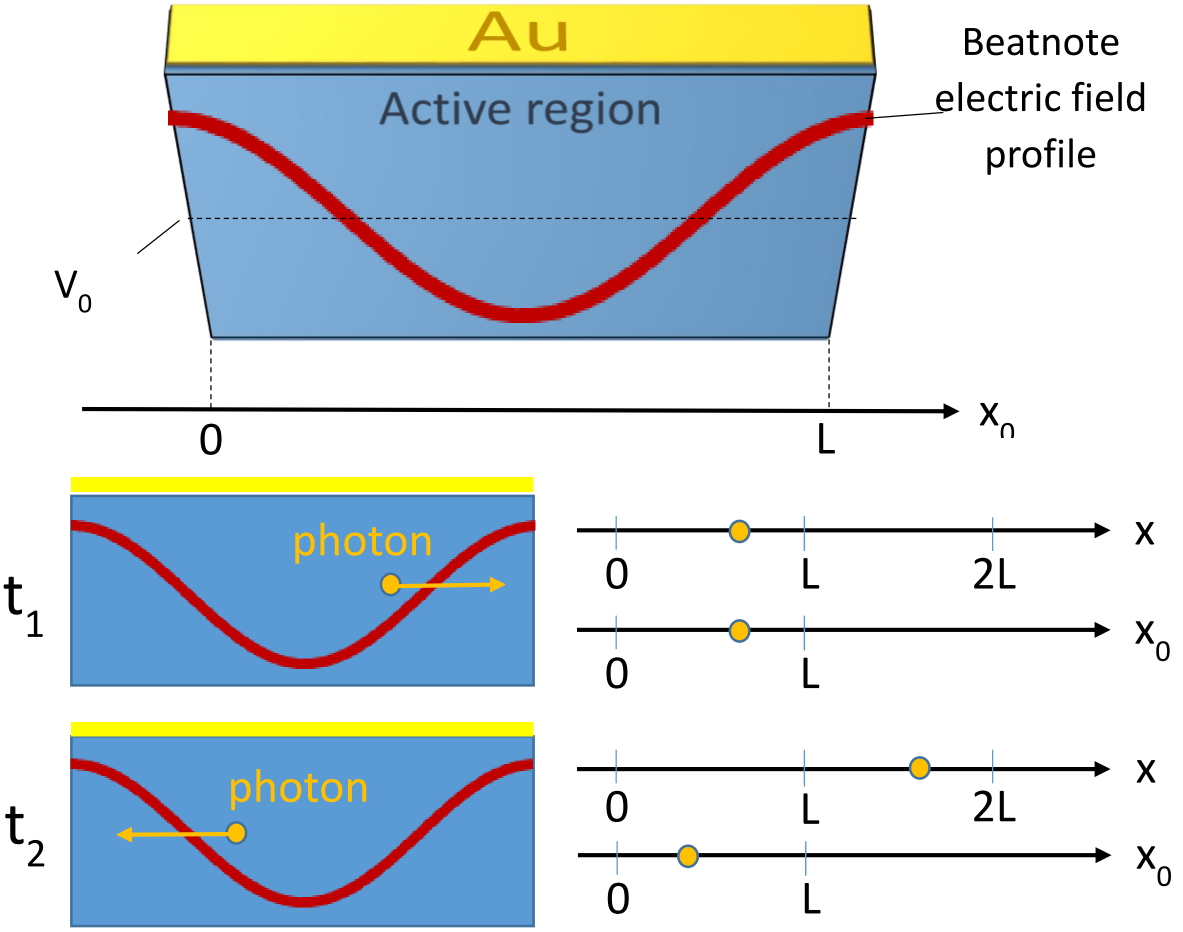

Figure 5.6: Top: schematic of a QCL cavity along the longitudinal direction with the spatial profile of the second harmonic beatnote (in red). Bottom panel: representation of the motion of a photon in the cavity and how it appears along the x axis

Two publications have investigated the relationship between the refractive index experienced by an RF modulation in the GHz range and the THz group velocity refractive index [124] [16]. In particular, the first one of the two shows how the geometrical parameters of the QCL cavity indicate a potential phase-matching condition ($n_{GHz} = n_{THz,group}$) for which a THz wave travels synchronously to a GHz modulation. This means that such a photon at the generic position x in the cavity will see an RF profile that is time independent, and it is then possible to use the expression of its position as a function of time to get rid of the time dependence on the RF modulation expression. One can in fact write:

$$t = (x - x_0)\frac{n_{THz}}{c} \tag{48}$$

$$\begin{aligned} RF(x, x_0) &= A_{GHz} cos\left(2\pi\frac{x}{L}\right)\cos\left(2\pi\frac{c}{n_{GHz}L}(x - x_0)\frac{n_{THz}}{c}\right) = \\ &= A_{GHz} cos\left(2\pi\frac{x}{L}\right)\cos\left(2\pi\frac{(x - x_0)}{L}\right) \end{aligned} \tag{49}$$

or in other words, the profile of the RF modulation can be considered as static and dependent only onto the relative position of the photon with respect to the GHz wave.

This bias modulation, that is static only for the photons which satisfy the phase-matching condition, is present on top of the bias already provided by the QCL that started multimode operation. For the photons that are synchronized to the GHz modulation it is possible to compute the total difference in bias with respect to the one applied that they experience during one round-trip ($2\ L$). We can in fact recast the expression of the RF modulation as:

$$RF(x, x_0) = \frac{A_{GHz}}{2}\left(cos\left[\frac{2\pi}{L}(2x - x_0)\right] + \cos\left(\frac{2\pi}{L}x_0\right)\right) \tag{50}$$

And then integrate from 0 to $2L$

$$\begin{aligned} \int_0^{2L} RF\, dx &= \frac{A_{GHz}}{2}\left(\int_0^{2L} cos\left[\frac{2\pi}{L}(2x - x_0)\right]dx + 2Lcos\left(2\pi\frac{x_0}{L}\right)\right) \\ &= A_{GHz}L\ cos\left(2\pi\frac{x_0}{L}\right) \end{aligned} \tag{51}$$

The average difference in bias ΔV_{2L} per round-trip as a function of the initial position x_0 will then be

$$\Delta V_{2L}(x_0) = \frac{A_{GHz}}{2}\ cos\left(2\pi\frac{x_0}{L}\right) \tag{52}$$

Figure 5.7 displays the corresponding plot which shows how the photons at different points in the cavity see effectively a different bias being applied to the gain region of the QCL. This translates into a different amplification given by the voltage dependence of the gain (i.e. a gain grating) and ultimately to a modulation of the electric field profile in time that is coincident

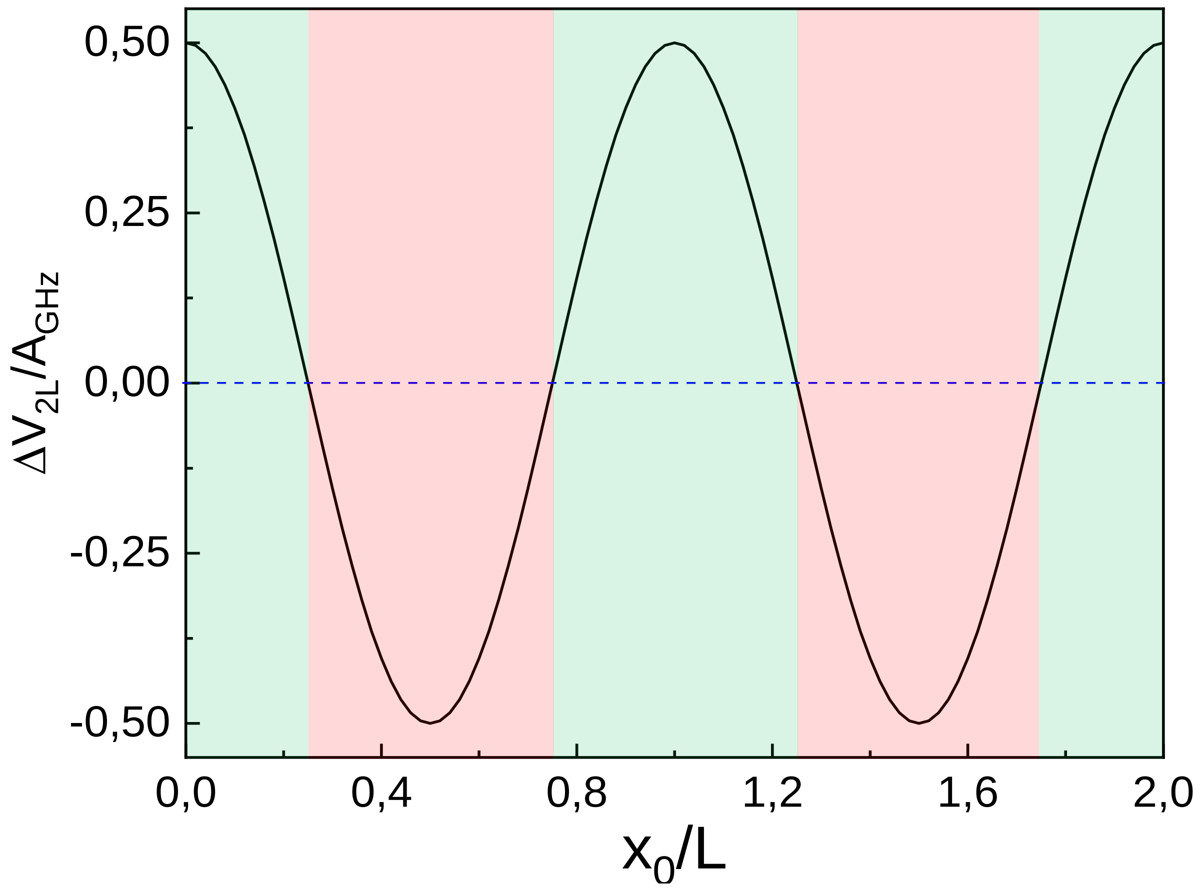

Figure 5.7: Average bias difference per round-trip as seen by photons starting at a spatially specific point of the cavity. The green (red) areas represents the starting points of photons which experience an effective bias higher (lower) than that applied by the external driver.

with the spatial gain gradient. One can see this amplitude modulation of the THz electric field occurring even with a limited intensity of the GHz modulation, such as in the black trace of in fig. 5.4a for which the seeding measurement is performed close to threshold. Conversely, photons which do not satisfy the phase-matching condition will experience an average bias per round-trip that is only determined by the one applied to the cavity. This means that the time profile of their electric field should resemble much more closely a CW output. This latter case is more easily found for MIR QCLs due to the greater difference between the refractive indexes at optical and microwave frequencies and this fact may justify why previous publications referred to the time emission of MIR QCLs as inherently CW-like.

Considering again THz QCLs, the authors of [124] report the presence of the beatnotes of the QCLs at the microwave FP resonances of the cavity of their devices, as showed in fig. 5.8. They attribute this to a self-seeding effect which pulls the round-trip frequency of the QCL and its harmonics to the closest maxima of the microwave resonances. If one of these frequencies is such to satisfy the phase-matching condition, the previously described spatial gain grating is established in the cavity and the electric field is modulated at the corresponding harmonic. This in turn stabilizes the mode spacing at the frequency of the FP resonance very similarly to what is observed in an active modelocking case. The strength of the modulation eventually depends on how well the phase-matching across the modes of the spectrum is established, such that dispersion plays a major role for the stability of this effect. Ultimately, if the phase-matching condition does not occur at any Fabry-Perot resonance of the microwave modulation, the shape of the spectrum will still be dominated by the FWM/SHB mechanism which establishes some mode coherence on its own and favours the emission at the fundamental repetition rate frequency.

Therefore, the control of the harmonic emission properties of the QCLs according to this model relies on the structure of the QCL's waveguide. In particular, the width of the waveguide strongly affects both the group effective index of the THz radiation and the refractive index seen by the GHz modulation (see the inset of fig.5.8). If they are identical for a given frequency close to GHz resonance at the actual width of the waveguide, then the QCL emission should present a strong time modulation at that frequency, ultimately leading to harmonic emission.
Inevitably, the DC-bias applied on the QCL affects the gain, which induces a refractive index change in the THz range of the spectrum as already explained in section **3.1.2**, and the

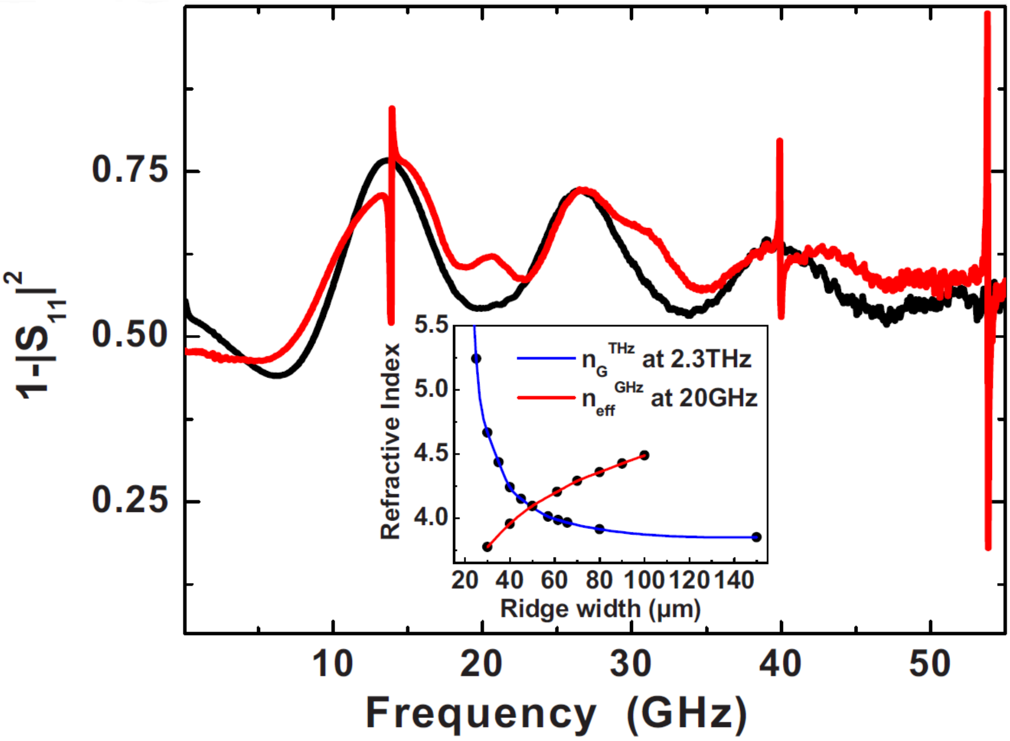

Figure 5.8: Reported $(1-(S11)^2)$ plots in the 0.1–55 GHz range for a 2.65 mm-long THz QCL below threshold (black) and above threshold (red), respectively. Inset: Computed group effective index at 2.3 THz (n_G, blue line) and effective index at 20 GHz (n_{eff} GHz, red line) as a function of the ridge width. Source: [99].

dispersion profile as well as influencing the temperature of the device. It is then expected that when the QCL satisfies this seemingly rare ‘phase-matching condition’, then one should see harmonic emission in the range of biases for which this condition is sufficiently well enforced.

It is also possible to further generalize this 1D theoretical model accounting for the possibility of changing the length of the optical path of the THz waves in order to compensate for a THz group effective index that is lower than the refractive index for the GHz modulation. For a sufficiently wide waveguide, this condition is expected to occur for all the GHz harmonics, as one can see from the inset of fig.5.8. By tuning the THz path length, it may be possible to choose the harmonic for which synchronization is desired. This can be done for example by employing an AR coating on one of the QCL facets and using a mirror to feed the radiation back into the cavity, as represented in fig. 5.9. For the sake of simplicity we will assume the facet without the coating having unitary reflectivity, the facet with the coating having zero reflectivity and the feedback to account for the full emitted radiation. Under these conditions, the system resembles that of the tunable GTI discussed in section **3.3** but with the difference that no GTI effect can occur due to the reflectivity of the output facet of the QCL being extremely low. In the following, the refractive indexes for the THz and GHz waves will be noted n_T and n_G respectively, while the QCL cavity length and the distance of the external mirror from the QCL facet are L_1 and L_2 so that $2(L_1 + L_2) = L_{RT}$.

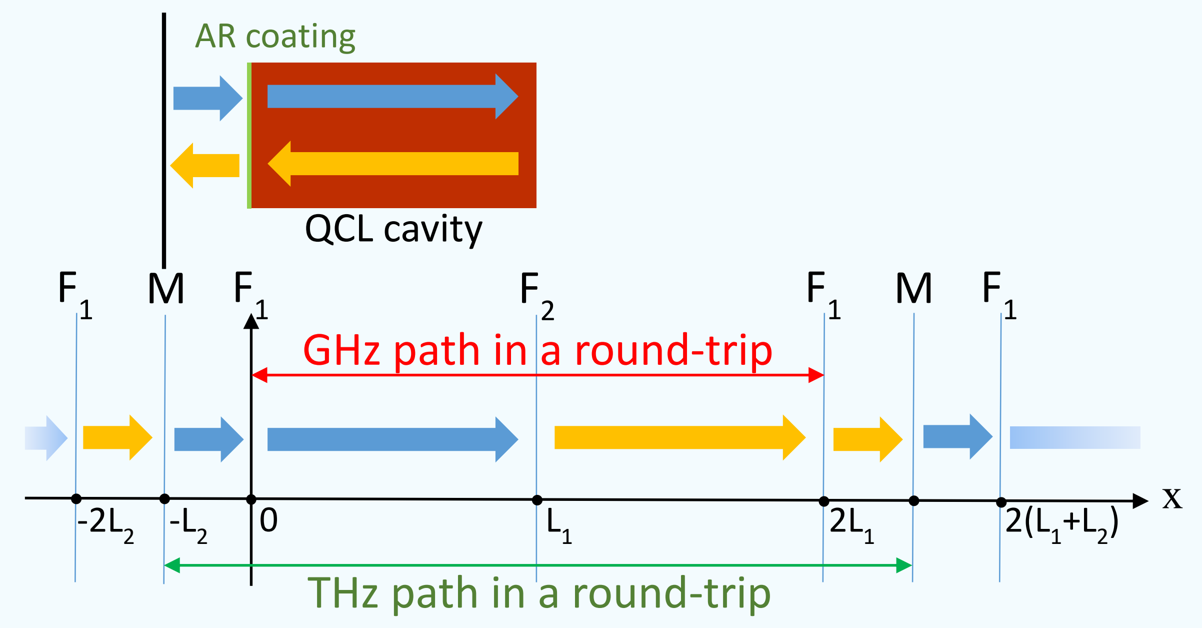

Figure 5.9 : Schematic representation of the QCL with an external mirror (M) configuration. F1 and F2 are the two QCL’s facets having 0 and 1 reflectivity respectively. The Anti-Reflection coating is illustrated in green. The photon position as a function of time is represented along the x axis and the arrows show the actual direction of the propagation.

The photon position as a function of time can then be described by the following expressions :

$$t = (x - x_0)\frac{n_T}{c} \qquad \text{for } 0 < x_0 < 2L_1 \tag{53}$$

$$t = x\frac{n_T}{c} + \frac{(L_{RT} - x_0)}{c} \qquad \text{for } 2L_1 < x_0 < L_{RT} \tag{54}$$

We will also use

$$a = \frac{2\pi}{L_1} \tag{55}$$

$$b = \frac{n_T}{n_G} \tag{56}$$

Combining equations 45 with 53 and 54 we obtain

$$RF(x, x_0) = A_{GHz} * cos(ax)\cos\big(ab(x - x_0)\big) \tag{57}$$

$$RF(x, x_0) = A_{GHz} * cos(ax)\cos\left(abx + a\frac{(L_{RT} - x_0)}{c}\right) \tag{58}$$

which are valid if the condition of synchronization in eq. 59 is satisfied.

$$n_G L_1 = n_T L_1 + L_2 \tag{59}$$

Once again, it is possible to compute the average bias seen by a photon starting at position x_0 integrating over x on one round-trip and dividing by the length (calculations are omitted).

$$\Delta V_{RT} = \frac{bA_{GHz}}{4\pi(b^2 - 1)}[\cos(abx_0) * u + \sin(abx_0) * v] \tag{60}$$

$$\Delta V_{RT} = \frac{bA_{GHz}}{4\pi(b^2 - 1)}\left[\cos\left(a\frac{(x_0 - L_{RT})}{c}\right) * u + \sin\left(a\frac{(x_0 - L_{RT})}{c}\right) * v\right] \tag{61}$$

where eq. 60 accounts for the points $0 < x_0 < 2L_1$ and eq. 61 for $2L_1 < x_0 < L_{RT}$. u and v are respectively defined as:

$$u = \sin(4\pi b) \tag{62}$$

$$v = (1 - \cos(4\pi b)) \tag{63}$$

Since several parameters are involved, we can consider a case similar to that described in [124] to retrieve some realistic values. By assuming a 3.75mm long and 60µm wide QCL, the group velocity THz refractive index is about 4 and the GHz refractive index for the second harmonic (~19GHz) is about 4.2 (see the inset of fig. 5.8). From the synchronization condition we need to use a mirror 0.75mm away from the output facet of the device. We can then plot the static RF profile as a function of x_0 as in fig. 5.10a while the time profile is reported in fig. 5.10b.

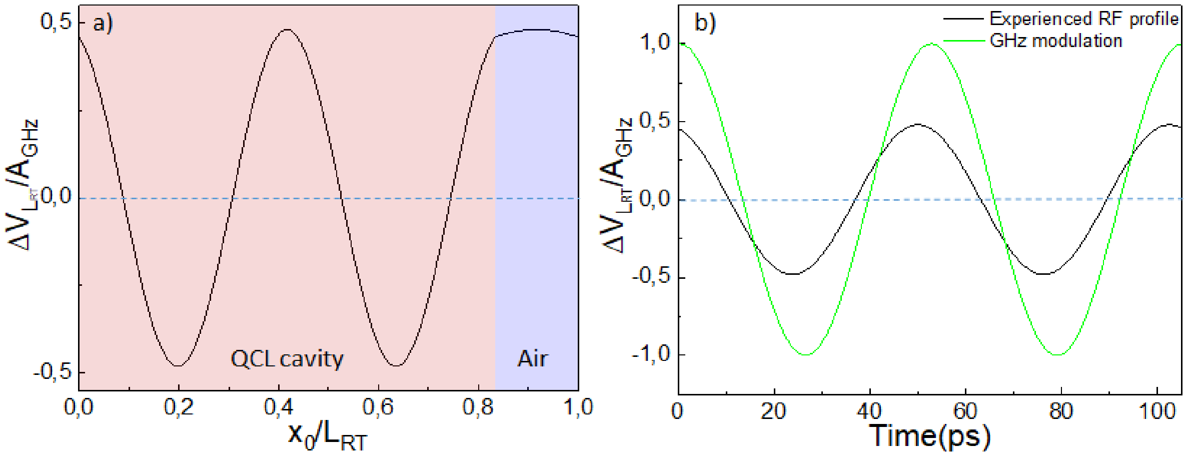

Figure 5.10: a) Average bias difference experienced by a photon starting at position x_0. The red area corresponds to points in the cavity while the blue area to those in the air in between the QCL’s facet and the mirror. b) In black, time profile of the same effective modulation in a) for one roundtrip (105ps). In green it is shown the initial GHz modulation from the beatnote.

Similarly to what was found in the previous case where no mirror is required to achieve THz and GHz waves synchronization, a sinusoidal modulation of the bias effectively experienced by the THz photons is expected to occur at a frequency equal to that of the second harmonic beatnote. That is to say, the THz radiation is modulated in time due to the presence of a gain grating and this modulation is translated in the frequency domain by an enhancement of the second harmonic mode separation. Of course, the amplitude of the bias modulation experienced by the THz photons decreases with the index mismatch, represented by b. Therefore the amplitude modulation of the QCL emission maximized when $b = 1$ which corresponds to the situation where synchronization is established without the need of an external mirror. Nevertheless, according to this simple model it should be possible to induce the appearance of harmonic states in a THz QCL if the synchronization condition is met either by correctly designing the QCL waveguide or thanks to a suitable external feedback. In the latter case, the clear advantage is that one can choose the harmonic state at which the device operates. Currently, no direct testing of this theory has been made yet. This could be done by recording the spectrum of a THz QCL while providing a feedback into its cavity by means of a movable mirror. If synchronization of the THz waves with one of the GHz harmonics occurs for a specific distance of the mirror, there should be a clear spectral signature. Even without an experimental proof available, this model seems to provide an effective and simple explanation of several QCL emission profiles that would be otherwise quite difficult to account for.

Moreover, it is also trivial to extended the model to the case of other harmonics and even to the fundamental frequency case by changing the periodicity of the standing wave expression. In particular, one can consider the synchronization effect described here to be at least one of the factor concurring to generate the profile of the spontaneously pulse emitting QCL described in the previous chapter (Sample 4/66). It was in fact showed that the device operates in a pulsed state, similar to self-modelocking despite the fact that this would not be expected in the presence of fast dynamics. By considering the possibility of synchronization of the THz waves to the GHz modulation at the fundamental frequency, one can immediately see that the emission of one pulse per roundtrip should be expected for a sufficiently strong fundamental beatnote, which is indeed observed (see Annex **3.1.5**). These considerations can also account for the fact that adding dispersion to the spectral range of emission of the QCL does not change the overall THz time profile to CW emission, as it may have been expected if it was strictly due to the coherence of the modes. In fact, if the synchronization holds even in presence of additional dispersion, the envelope of the THz field will still be strongly determined by the profile of the GHz modulation.

Coming back to second harmonic modelocking, it is also interesting to observe that the gain grating of fig. 5.7 resembles the structure proposed in [111] for colliding-pulse modelocking. In fact, if one considers the self-generated RF modulation to be strong enough, and the bias on the QCL to be not too far from threshold, then when the GHz modulation becomes negative this will lead to sections of the QCL active region to be biased below threshold. In particular, equation (37) can be used to retrieve the static profile seen by photons along their propagation in the active region starting from an initial position x_0 (the synchronization condition is assumed to be satisfied). For photons that does not start exactly at the antinodes of the modulation ($x_0 \neq$

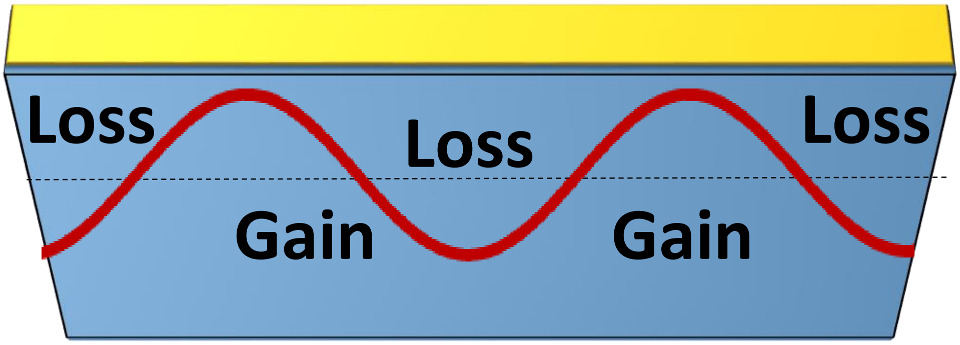

Figure 5.11: Longitudinal section of the QCL cavity with the effective bias profile seen by a THz photon starting at $x_0 = \sim L/4$. For a strong RF modulation, gain and loss regions can be created in the active region of the device according to equation 49.

$n\frac{L}{2}$), an alternation of gain and absorbing regions is experienced at each roundtrip. An example of such a sequence is illustrated in fig. 5.11.

In order to analyze more in detail the actual effect of such a gain profile on the THz emission, numerical simulations based on the open-source software package *mbsolve*[125], [126] have been performed in collaboration with the group of Dr. Christian Jirauschek at the Technische Universität München (TUM). These simulations were used to investigate the electric field evolution in a QCL structure reproducing Sample 5 as closely as possible. The simulation model is based on full wave Maxwell–Bloch (MB) equations [127] [128] for a three level system, i.e. without the rotating wave and slowly varying amplitude approximations, taking into account counter-propagating waves and spatial hole burning.

In this framework, both region types (i.e., gain and absorber) share the same electromagnetic properties, namely the refractive index n, the linear power loss a, the overlap factor Γ and the doping density N. The quantum mechanical model of the electron dynamics is based on a three-level density matrix description. Between the upper and lower lasing level, the energy difference corresponds to the transition frequency f. This lasing transition is further described by the dipole moment d and the dephasing time T_{deph}. Finally, the non-radiative scattering between the energy levels is included using three scattering rates which correspond to the superlattice relaxation time as well as the lower and the upper lasing level lifetime, respectively. The values of the parameters of the material which was not possible to extract from the experiments, were determined by either simulation or by using reasonable values from related

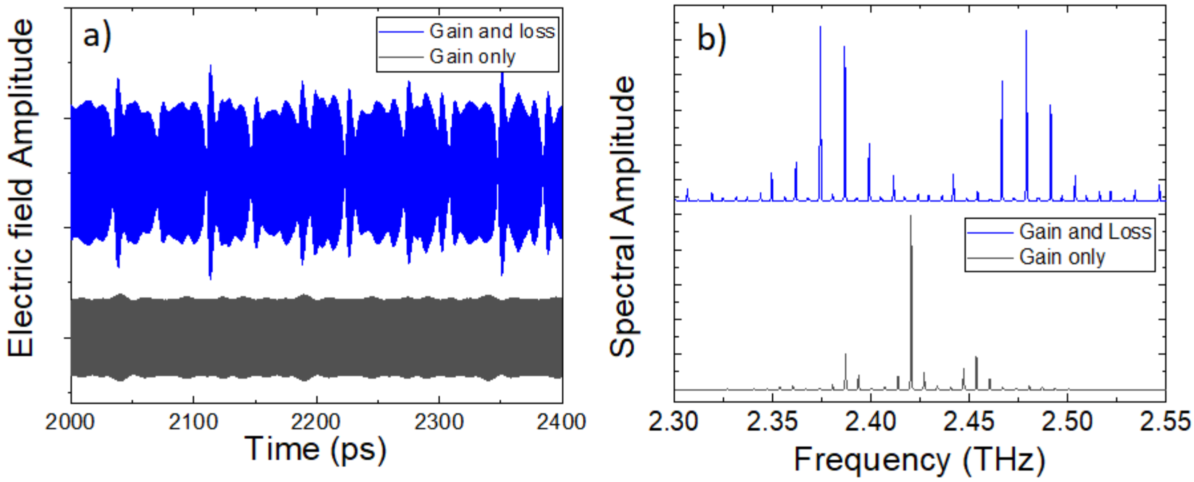

Figure 5.12: (a) Simulated time traces and (b) corresponding spectra for the electric field emission when the whole cavity is above threshold (in black) and when a gain grating sequence is employed (in blue) for the simulated Sample 5

literature [69] [29]. It was then assumed that the gain and loss regions mainly differ in the upper lasing level life time, which determines whether the region acts as gain or as absorber medium.

Simulations of the THz emission were performed in the cases when the active region is fully above threshold and when instead a gain grating is assumed. The length of the loss region was then varied in order to find parameter combinations for which second harmonic behaviour occurs and is clearly visible. We found that a possible combination is the parameter set listed in Table A5.1 in Annex **5**. As one can see from fig. 5.12, the presence of the gain grating is a sufficient but also necessary condition to achieve spontaneous harmonic emission. It has been in fact found that no reasonable choice of parameters for the simulated QCL allow for the onset of this state if the cavity is biased at a constant value, while on contrary there are multiple sets of parameters that allow for second harmonic generation as long as the spontaneous microwave modulation is present. At this regard, it has to be noted that minor differences can be found in the spectra for different choices of the parameters whereas the main features are always conserved. Finally, the simulations could also account for the separation between the two frequency lobes, i.e. the 15th harmonic that was found in the experimental results. Panel (a) shows the time traces, where a strong modulation is present only when the lossy regions are employed, while the corresponding spectra are plotted in panel (b).

The simulations confirm that the influence of the bias grating originated from the beatnote profile is capable of explaining the onset of spontaneous harmonic states in THz QCLs. Moreover, a good agreement was found with the experimental results.
To further confirm our conclusions on Sample 5, harmonic emission at a different order and in a different device will be presented in the following section.

5.2.2 Third harmonic spontaneous emission

Another QCL, Sample 6, was identified to emit at the 3rd harmonic state in free-running and was consequently tested with seeding experiments. While the LIV could be recorded as usual (and it can be found in Annex **3.1.7**), no electrical beatnote was found up to 20GHz, which is the upper limit of the bandwidth of our spectrum analyser. Given that the device is about 2.2mm long, this fact may suggest the presence of spontaneous harmonic emission (or extremely poor mode coherence, which, it will be showed, is not the case). Seeding experiments were consequently performed on Sample 6.

Figure 5.13a shows the free-running spectrum of the device for a bias of 248mA and 30dBm of RF current as it is obtained from the FFT of the recorded time trace plotted in panel (b).

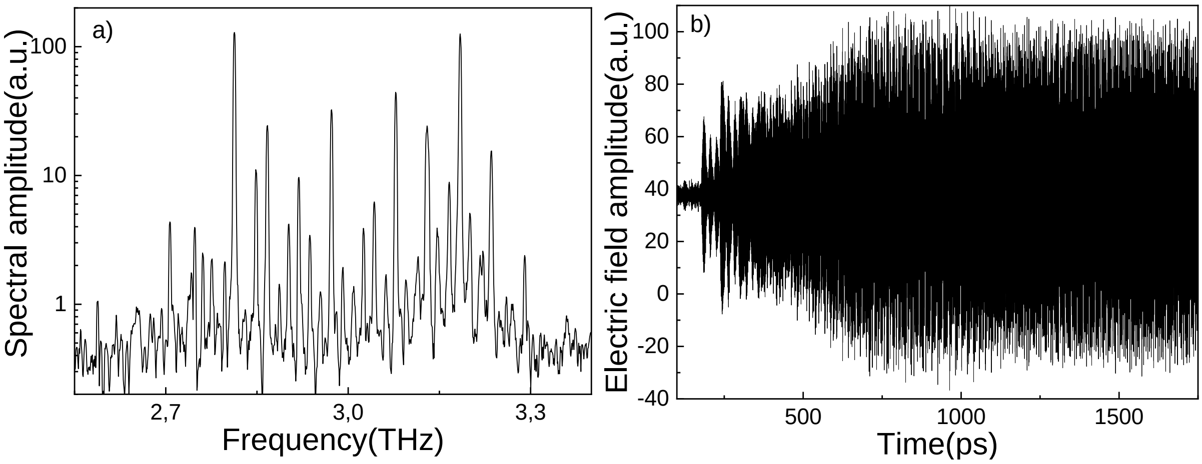

Figure 5.13: (a) FFT spectrum of (b) the electric field time scan of Sample 6 biased at 248mA and 30dBm of RF

When an FFT is applied on the entirety of the trace, the spectrum in panel (a) is obtained. One can see a ~500GHz band with plenty of modes, many of which are separated by the fundamental roundtrip frequency of the device. Such a spectrum may let one assume that the emission of the device does not possess any particularly interesting feature. However, while in general the FFT of the time trace provides all the necessary information about the emission spectrum of the device, it does not allow to distinguish the moment at which a specific spectral component

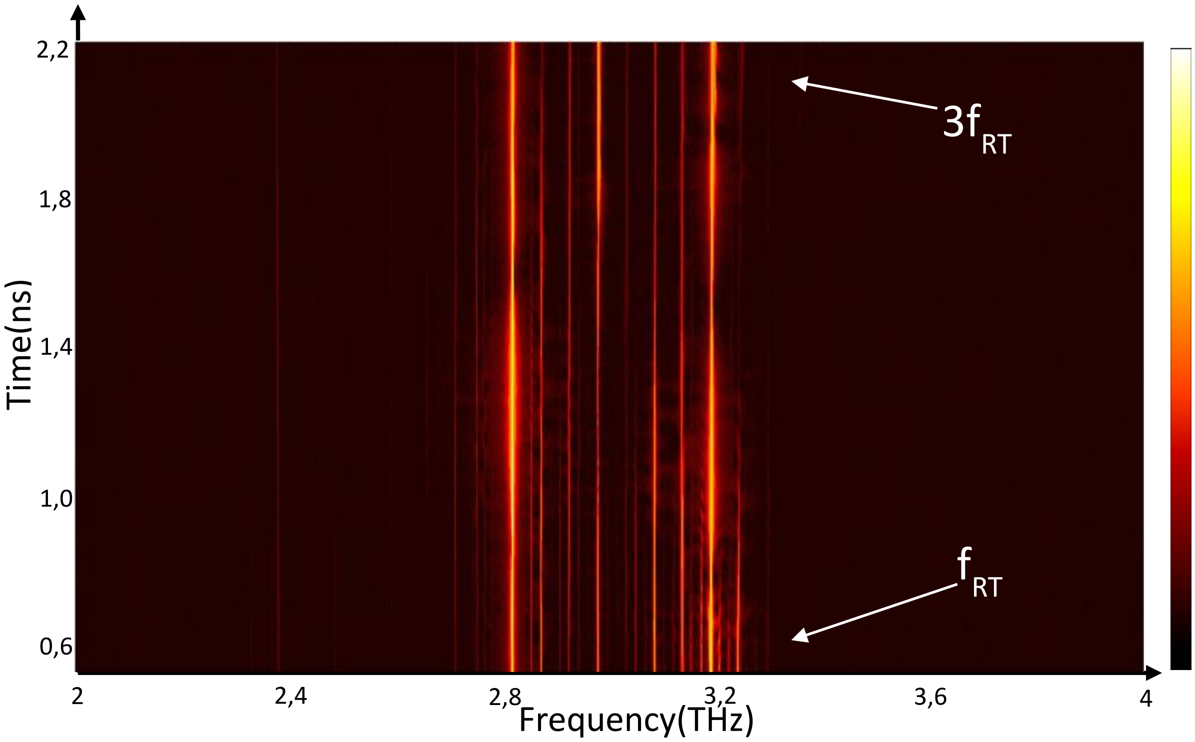

Figure 5.14: Time evolution of the Spectral amplitude emitted by Sample 6. The colour scale indicates higher intensity with brighter tonalities.

appears or disappears in the time domain. It is more accurate then to consider an FFT performed on a smaller range than the whole time trace and to move it across the latter to observe how the spectrum evolves, as already explained. When this is done for a 300ps time window on the previous time scan, the map of fig. 5.14 is obtained. Again, brighter colours indicate a higher intensity of the Fabry-Perot mode. As one can observe, most of the modes that are separated by the fundamental round-trip frequency that can be seen in fig. 5.13a tend to disappear in about 1ns, so that in the long term the spectrum of the device presents only modes with a spacing at the third harmonic. In order to ease the interpretation of the data, the FFT of the time trace around 1.6ns is reported in fig. 5.15a and a detailed view of the electric field profile for 100ps around the same point in time is plotted in panel (b).

The first important observation that one can do regarding the time profile of the electric field emitted by Sample 6 is that despite looking quite similar to a CW output when observed at the

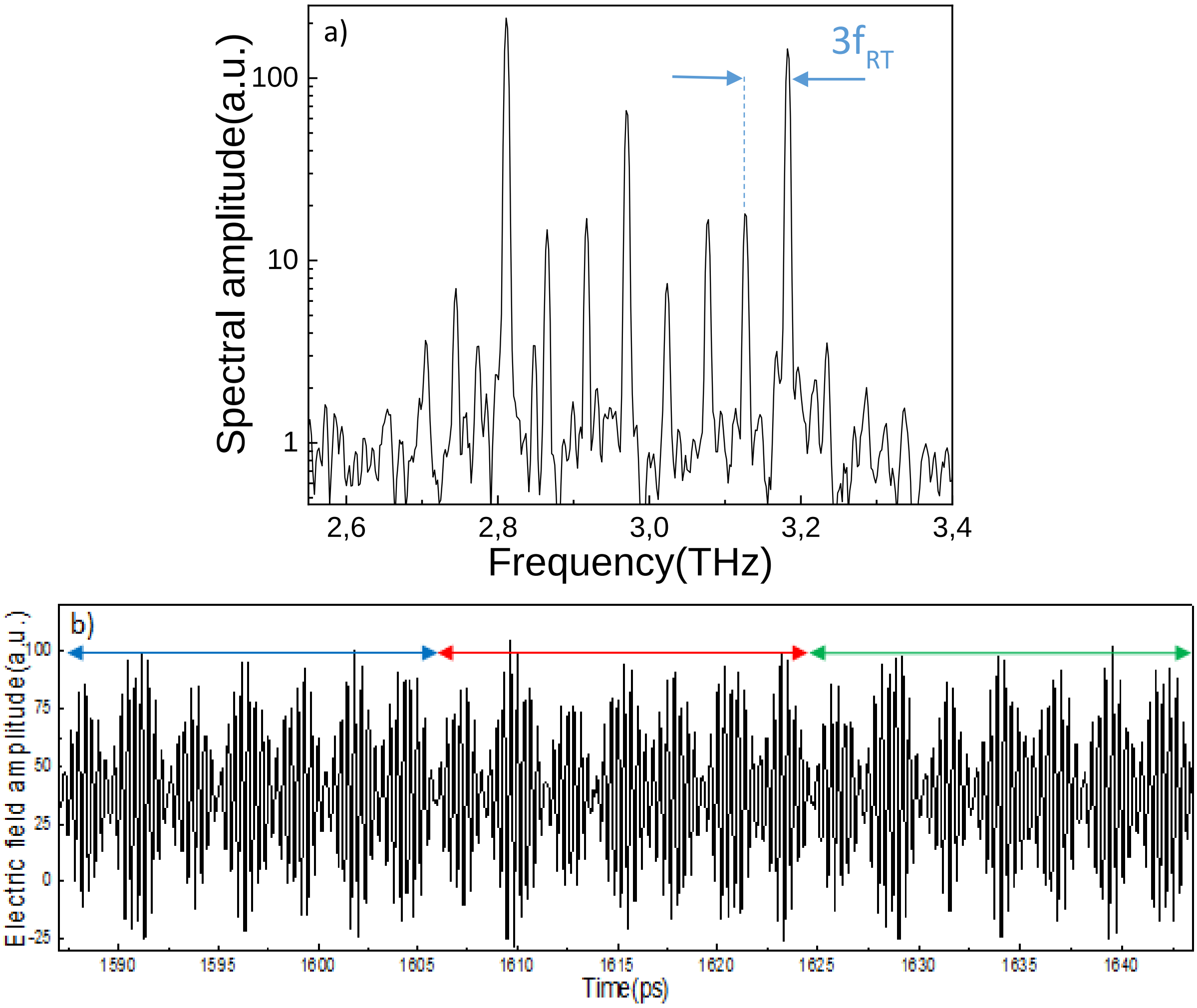

Figure 5.15: (a) FFT of a 300ps window and (b) detail of the electric field profile around 1.6ns of the trace of fig.5.13b. The three groups of pulses composing one round-trip are marked by the coloured arrows.

ns time scale (fig.5.13b), this is absolutely not the case at a closer examination. The features observed in fig. 5.15b in fact resemble very short pulses repeating in almost identical groups. Their origin can be traced back to the interference of the two main modes of the spectrum, at ~2.8THz and ~3.2THz respectively. That is to say, a strong amplitude modulation related to a high order harmonic RF modulation may be the source of such a profile. The uneven distribution of the intensity among the pulses is instead related to the contribution of all the other modes in the spectrum. Three repeated groups of pulses can be identified for each roundtrip which is a consequence of the mode spacing reflecting the third order harmonic nature of the comb produced.

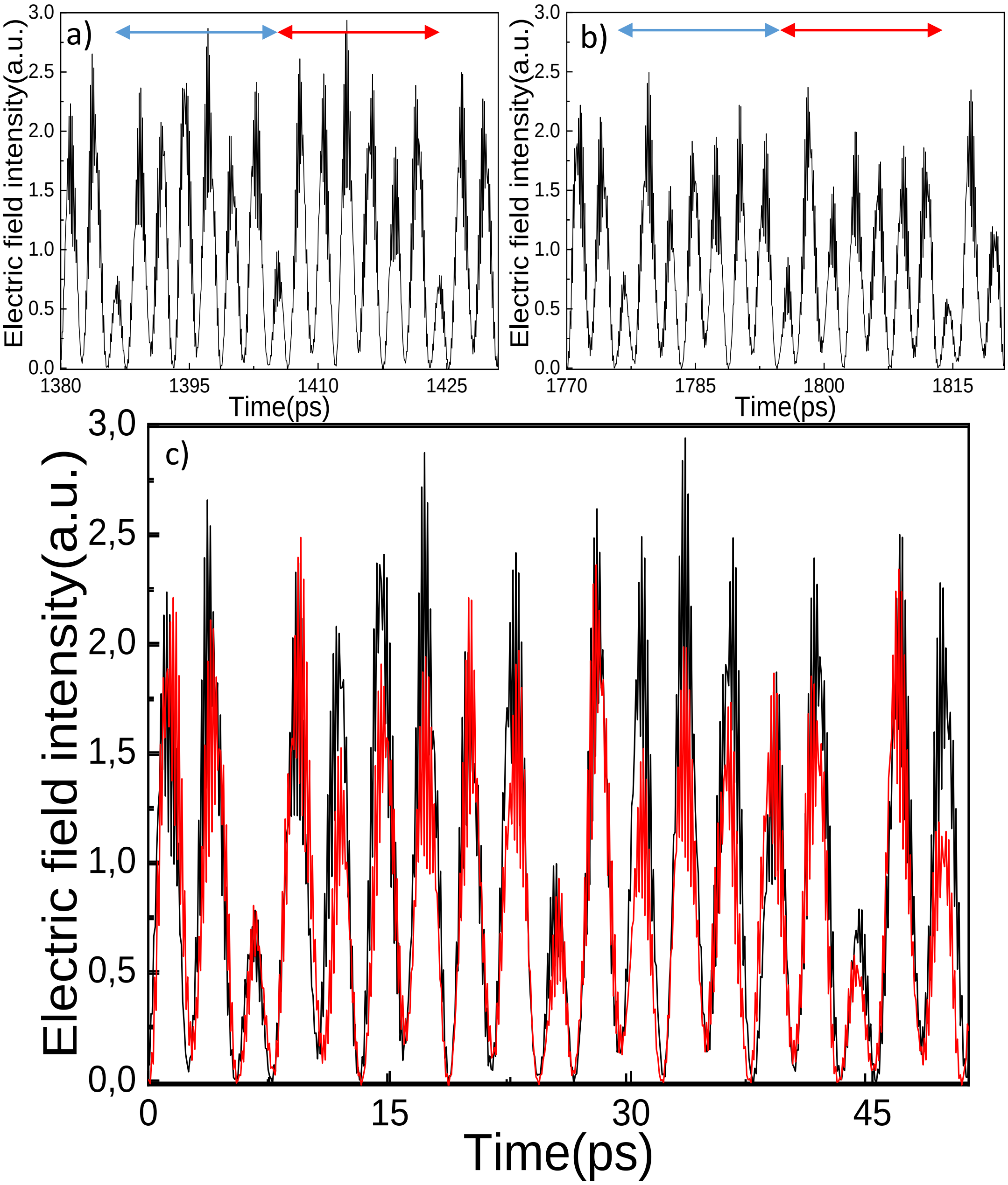

Figure 5.16: Electric field intensity of Sample 6 at (a) ~1.4ns and (b) ~1.8ns. The arrows on top identify each group of pulses. The curves in (c) are the same as in (a) and (b) and their overlap show the time stability of the electric field pattern.

In the intensity profile of the electric field, plotted in fig.5.16 for two time ranges at about 1.4ns (a) and 1.8ns (b), it is instead possible to observe the clear separation between each pulsation. The single pulse can even be shorter than 2ps but such a pulse train as a whole lacks an even distribution of the power among the pulses. While it would be inappropriate to claim harmonic modelocking for the emission of this device as no beatnote could be measured at 45GHz, a third order frequency comb behaviour is a distinct possibility owing to the high time stability of this profile. In any case, the emission profile is clearly not what one would expect if the device was purely frequency-modulated. In fact, a clear capability of the QCL to sustain isolated pulsations can be easily observed. From the point of view of the spectrum, as the results of fig.5.14 show, the QCL does not enter into its harmonic state immediately after the pulse injection, but it takes about 1 to 2ns to acquire an even distribution of the power between the modes while those separated by the fundamental frequency slowly disappear. This is not the case for devices that favour the fundamental state for the emission, as already showed in the introduction for Sample 4/66. Another example can be easily provided by almost any generic QCL. Here another device, Sample 7, has been chosen to provide a second proof of the conventional fundamental-state emission of QCLs. The choice of this specific device is related to its particularly clear spectral evolution in time, that is plotted in fig. 5.17. In this case, which represents the behaviour of most of the QCLs for which no synchronization condition to their GHz modulation is satisfied,

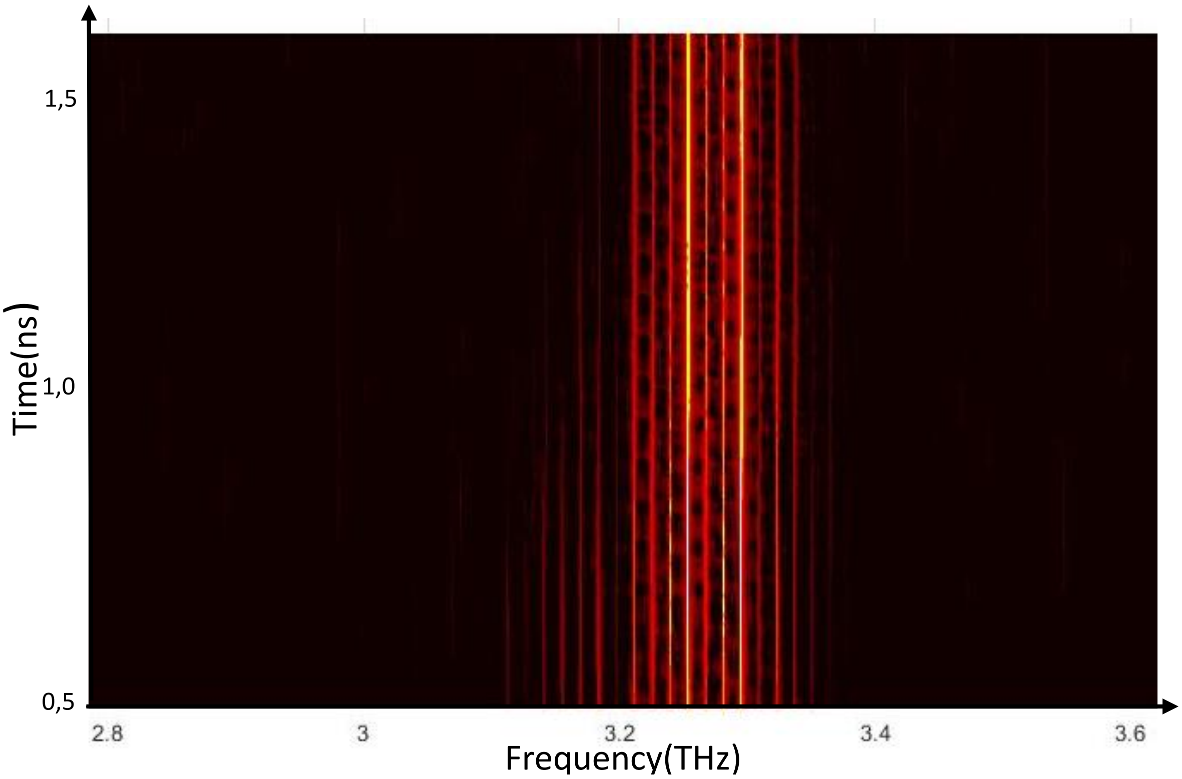

Figure 5.17: Time evolution of the spectrum of a Sample 7 using a time window of 300ps for each FFT showing operation on the fundamental round trip frequency

the mode spacing does not change at all as time goes on, steadily remaining at the fundamental roundtrip frequency for more than 1.7ns. Even though some modes disappear after a few hundreds of ps, they are all located at the sides of the emission band and are not related in any way to the onset of harmonic emission, in stark contrast with what is observed for Sample 6.

In summary, in this section it has been shown that the fast gain recovery time of THz QCLs does not need to be a limiting factor for the generation of short pulsations. This was done by means of time resolved experiments which allowed us to study the ultrafast response of these devices on a ps scale, highlighting the onset of spontaneous harmonic states displaying strong amplitude modulation of the emitted electric field. A theoretical model has been provided which links the amplitude modulation of the QCL emission to a synchronization condition of the THz field to a spontaneous microwave signal. It was also discussed how the ridge dimensions affect the synchronization determining the harmonic order of the emission. A further generalization of this model to a device with an external tunable mirror has suggested a way to trigger and control the harmonic state of a QCL. Future experiments will be performed to test these predictions, as well as the integration of the effect of a microwave modulation in the simulations Finally, the Maxwell-Bloch simulations performed by our collaborators have shown that the gain grating established by the synchronization condition is capable of initiating harmonic emission (and modelocking), further supporting our model.

5.3 Conclusions

In this chapter the ultrafast dynamics of harmonic modelocking in THz QCLs were discussed. Active harmonic modelocking was shown from a 6mm sample with evidence of the locking of the beatnote at twice the round-trip frequency to an external reference. The corresponding spectra also reproduced the frequency of the applied active modulation in their mode spacing. Ultimately, it was demonstrated that a THz QCL can be forced to emit multiple pulsations if a suitable modulation is applied which allows to achieve higher repetition rates and signal to noise ratios from the same device. This showed the QCL flexibility in active modulation to change the separation between the Fabry-Perot modes

Spontaneous harmonic emission was shown for the first time in THz QCLs and the ultrafast temporal response was fully characterized in two different samples. In both cases, a strong amplitude modulation of the emitted electric field was visible on a picosecond time scale, and opens interesting perspectives towards passive modelocking of QCLs. A theoretical model was proposed to explain the physical origin of this phenomenon as a condition of synchronization between the THz electric field emitted by the device and a spontaneous GHz modulation that is generated by the beating of the THz modes. This creates a static non-uniform gain profile for the synchronized THz photons which in turn determines the amplitude modulation of the emitted radiation. It was shown that this can create a sequence of gain and absorber regions in the cavity, reminiscent of a colliding pulse modelocking scheme. Full Maxwell-Bloch simulations performed on this structure were used to reproduce the experimental data.

The time evolution of the emitted THz field was analyzed over nanosecond time scales by means of a moving FFT method. This showed the transition to a harmonic modelocked condition over a relatively long time (>1ns) when the laser reaches steady state from the initial transient that shows spectral emission on the fundamental mode separation.

Third order harmonic emission was also observed in a QCL showing an extremely complex but regular electric field profile and clearly harmonically spaced spectrum. Many short pulsations were shown that indicate a strong amplitude modulation of the emission profile. Several of these pulses displayed a striking duration below 2ps. However, despite their periodical behaviour, the distribution of the power for each pulsation was not uniform thus leading to a diversification of the pulse duration. The strong amplitude modulation which generates these pulsations also demonstrates that spontaneous harmonic emission is considerably different than that of any frequency modulated laser, in contrast with previously reported results [56]. This fact is particularly important with regard to the possibility to achieve passive pulse modelocking in a THz QCL that continues to attract attention.

Finally, the theoretical model was also generalized to account for a change of the THz path length by means of an external mirror. It was found that this should allow to control the harmonic state of the device as long as the synchronization condition can be enforced. Further experiments will be performed in the future on this subject. Moreover, an effort to fully modelize the effect of the microwave modulation into the Maxwell-Bloch simulation frame is currently ongoing.

6

Microwave generation in THz QCLs

Frequency combs are now successfully employed in QCLs where the presence of strong third non-linear susceptibilities enables mode locking via four-wave mixing [129]. It has also been demonstrated in 2007 that giant second order non-linearities can be used in QCLs to generate electromagnetic waves in different spectral regions other than those where the gain was originally designed [130]. The underlying mechanism is intracavity difference-frequency generation (DFG) taking advantage of the high power densities within the QCL cavity. To date, this principle has only been shown for MIR QCLs and has enabled the realization of THz sources operating at room temperature [131]. Moreover, the adoption of a Cherenkov phase-matching scheme and of dual-upper-state active regions has allowed for mW-level peak THz output powers as well, as well as high mid-IR-to-THz conversion efficiency up to 0.8 mW/W^2 [132].

The final chapter of the thesis will treat a phenomenon that has never been reported in THz QCLs: taking free running and modelocked QCLs we show the spontaneous emission of free spece gigahertz (GHz) radiation covering the range from tens to hundreds GHz. The mechanism is based on a similar intracavity DFG process demonstrated in MIR QCLs. Specific experiments are conducted to prove this point and to investigate the capability of engineering GHz lines at specific frequencies. This result opens up the possibility to employ THz QCLs as low-noise RF emitters.

In this chapter, the free-running emission from several samples is considered. More specifically, results from the previously discussed Sample 1 are analyzed with respect to the observed GHz lines in the low frequency part of the spectrum. To confirm the GHz emission, the phenomena was also shown in another sample (Sample 8) based on a previously tested bandstructure. Finally, the capability of enhancing specific GHz lines at very high frequencies was investigated using a THz QCL designed to operate at two THz frequencies (Sample 9). The characteristics of these devices are reported in Table 6.1.

	Sample 1	**Sample 8**	**Sample 9**
Growth code	L1458	L1194	L1194
Processing lab	C2N (Paris)	C2N (Paris)	C2N (Paris)
Active regions (periods)	2.5THz(55) 3THz(40) 3.5THz(40)	2.5THz(200)	2.5THz(200)
Active region scheme	Hybrid structure [94]	LO phonon depopulation [112]	LO phonon depopulation [112]
# wells	9	3	3
Waveguide	Double Metal	Double Metal	Double Metal
Length/width/height	2.9mm/85µm /17µm	1.5mm/60µm /12µm	3mm/68µm /12µm
Side absorbers (width)	6.5µm (metallic)	4µm	4µm

Table 6.1: Characteristics of the samples used in chapter **6.** The dimensions refer to those described in fig.1.9

Chapter 6

6.1 Intracavity generation of microwaves in THz QCLs

6.1.1 Intracavity difference frequency generation in THz QCL

In this section, GHz DFG in THz QCLs is demonstrated for the first time by using free space electro-optic sampling with a TDS system. This phenomenon here consists in the generation of radiation whose frequency is determined by the difference of two exciting frequencies of the QCL interacting with the QCL material. The physical reason underlying this mechanism is a strong second-order non-linearity in the active region of the device.

Before entering into the details of the experimental results, it may be useful to recall that the beatnote is an electrical signal generated on the QCL by the beating of the lasing modes and it is generally used as an indirect proof of frequency comb operation as explained in chapter **1**. It can be considered as a result of a DFG mechanism. Harmonics of the fundamental beatnote have also been showed in section **5.1.2** where their relationship to harmonic emission was investigated. However, only electrical measurements have been performed to measure this beating and no estimation on the possible number of beatnotes produce by a specific QCL have been reported. This is due to the necessity of broadband microwave spectrometers capable of detecting up to hundreds of GHz and the consequential need for high frequency connections. These practical issues, together with the extremely high sensitivity required to detect weak signals at high frequencies, renders difficult the observation of high frequency electrical and optical (free-space) beatnotes (> 40 GHz). Regarding free space detection, this is rendered extremely difficult for the lack of fast detectors in the THz range.

Very recently, free-space emission of an RF signal from a MIR QCL has been published [133]. In this work, it was shown that a QCL can be used as a RF transmitter when coupled to an integrated antenna designed to radiate the signal generated by the electrical beatnote. While interesting, the results were limited to an emitted frequency of 5GHz (the fundamental beatnote).

Here, to overcome the limitations of conventional electrical detection, optical experiments based on electro-optics sampling have been performed that show not only the generation of free space microwave emission stretching to hundreds of GHz, but also considerable output power and without the need of integrating any further component to the QCL's structure. The experiments are similar to the injection seeding investigations presented in previous chapters and was performed on several QCLs to prove the generality of the findings.

The first device investigated was Sample 8, which is a 1.5mm long device with no GTI integrated and which shares a common growth process with Sample 2 (LO phonon depopulation operating at 2.5 THz. Figure 6.1c displays the time trace of the electric field emitted by the free-running device. A 800GHz band centered at 2.4THz with a mode separation of 26 GHz can be seen in panel (a) of the same picture. To measure the microwave emission, a filter was used to remove the THz (see below) to avoid any nonlinearities in the detection. In fig. 6.1b, it is clearly observed that this QCL shows emission over a range of microwave frequencies below 300GHz. In order to verify a relationship with the main THz modes, one can compute the profile of the modes which should result from the difference of the THz lines (red curve) and compare it with the experimental data. More precisely, the red dashed curve of panel (b) is computed by the following formula:

$$I(f_j) = \sum_{j}^{\infty} \left(I(f_i) * I(f_{i-j}) \right) \tag{64}$$

where $I(f_i)$ is the intensity of the generic point at frequency i of the global FFT spectrum. According to this expression, the product of the intensities of each pair of points of the spectrum

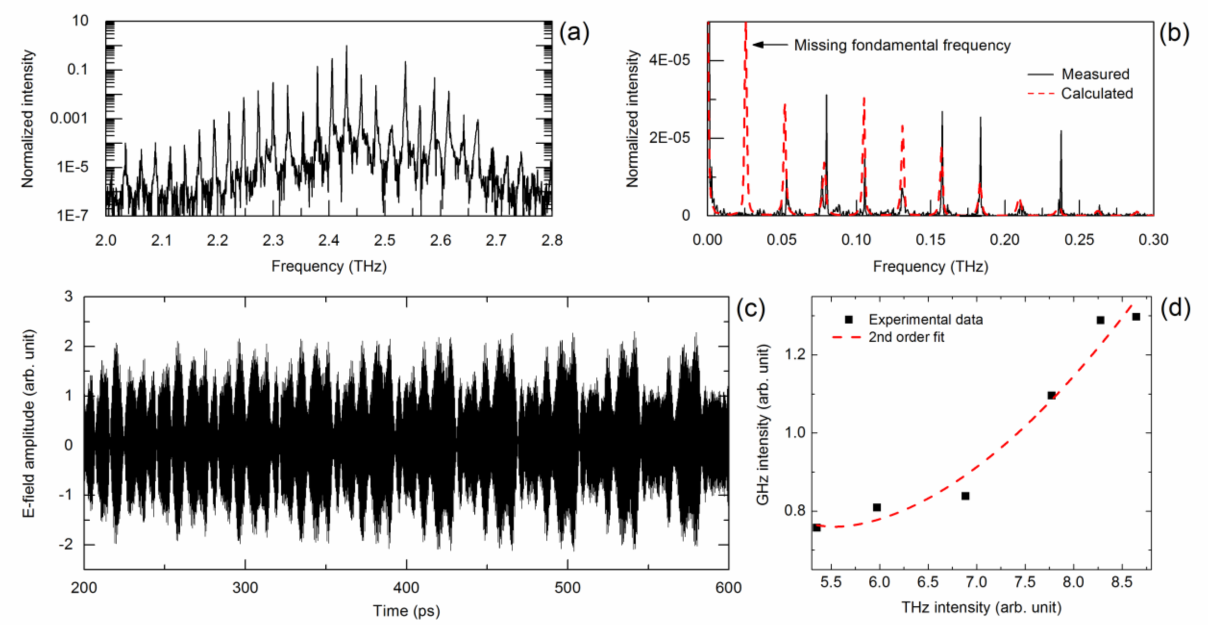

Figure 6.1: (a) Spectrum in the THz and (b) in the GHz range (in black) from Sample 8 in free-running condition measured by injection seeding. The lines calculated assuming a DFG mechanism acting on the THz modes are in red. (c) electric field time trace from which spectra in (a) and (b) are obtained. (d) total GHz intensity as a function of the total THz intensity (black dots) with a second order fit (red dashed line)

separated by a certain frequency f_j is summed together determining the intensity of the point at f_j. A normalization was performed after the computation to easily visualize the calculation with the experimental data. Using the simple expression of equation 64, which is constructed assuming a DFG process, no specific selection of modes is done and all the information in the experimental spectrum are taken into account. Despite not being able to reproduce exactly the real intensity of the modes, this extremely simple formula is showed to predict their expected position with good accuracy. From this point of view, a substantial agreement is reached with the experimental data. Another formula based on the assumption of a FWM process was also tested but was unable to reproduce the mode position, suggesting that it plays no significant role in the generation of GHz modes.

However, no beatnote at the fundamental frequency of 26GHz was detected from these experiments despite the fact that the fundamental beatnote should be the strongest line being produced. Some explanations can be provided for this fact. A possibility is that the spectral resolution of the measurement, which is determined by the length of the time scan (~350MHz for a scan of 2.8ns), may be eventually insufficient to resolve such a thin line with a sufficient signal to noise ratio. Another reason can be attributed to the poor collection of the emitted radiation as a result of limited directionality. It will be showed later, though, that free-space detection of the fundamental beatnote is still possible.

6.1.2 Characteristics of the generation process

Two main aspects have to be examined if an intracavity DFG process is assumed to be the physical mechanism responsible for the generation of millimetric waves in a THz QCL. The first one is that the process is the result of a second order non-linearity. The second, that the phenomenon occurs in the cavity of the device. It is not possible in fact to exclude *a priori* that the THz lines may interact with each other in another element of the setup. In the following, specific experiments are presented that show both aspects to be verified.

In order to demonstrate that the mechanism allowing for the generation of the GHz modes is due to a second order non-linearity, it is necessary to show a quadratic dependence of the intensity of the generated GHz radiation to the THz one as the non-linear efficiency is proportional to the square of the intensity [130]. Figure 6.1d displays (as black squares) the total GHz intensity, as resulting from an integration over the frequency of the intensity spectrum, for different total THz intensities. The latter can be changed by varying the bias current. In red, a power fit is used to prove that this phenomenon is due to the second order non-linear process. The power law fit performed suggests the use of an exponent of 2.32, close to the value of 2 that is expected for a second order process.

To exclude the possibillity of this phenomenon occurring in other components of the setup other than the QCL cavity, a 500GHz optical low-pass filter is put in the TDS along the THz path just after the QCL position. Its transmission function as characterized from TDS experiments can be found in fig 6.2c. If the GHz radiation originates from the laser cavity, only the THz emission should be attenuated. On the contrary, if the detected GHz lines are due to some non-linear effect taking place in the other nonlinear components after the QCL, then these should decrease proportionally to the THz intensity. As fig. 6.2b shows, the intensity of the GHz lines is virtually unchanged, and the two profiles (with and without filter) can be safely plotted on top of each other in linear scale. The THz radiation, on the other hand, gets reduced by the filter

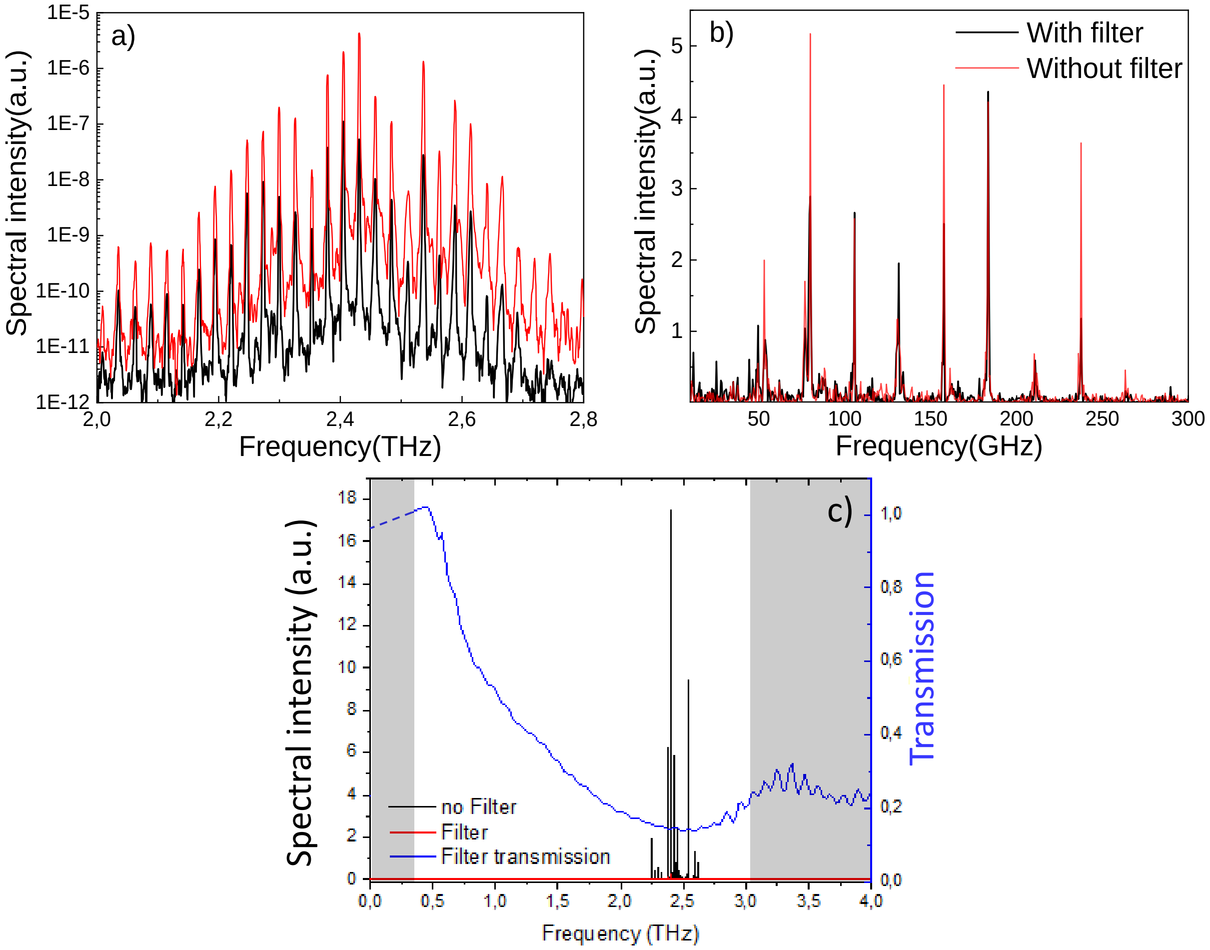

Figure 6.2: Comparison of (a) THz and (b) GHz intensity spectral emission with (in black) or without (in red) a 500GHz low-pass optical filter from Sample 8. (c) Optical filter transmission function (in blue) from TDS characterization and global spectrum of Sample 8 without (black) and with (red) the optical filter. The gray areas denote the ranges for which the characterization of the filter is not reliable due to low signal from the THz source.

of at least one order of magnitude, and comparison becomes possible exclusively on a logarithmic scale, as done in panel (c) of the same picture. This demonstrates that the source of the detected GHz modes must be an intracavity process with its origin in the QCL cavity.

6.1.3 GHz emission engineering

Given our understanding of the nonlinear intracavity phenomenon, it becomes possible to tailor this GHz emission of a THz QCL. Two cases of designed emission are considered in this section: broadband GHz emission and the generation of lines at specific frequencies.

Starting with the tailoring of GHz modes at a specific frequency, fig. 6.3b shows the THz free-running spectrum of Sample 9 having two terahertz bands whose highest modes are separated by 244GHz. The splitting of the spectrum of Sample 9, which has the same active region of Sample 8, into two bands was realized by fibbing a 4μm gap into the top gold layer of the waveguide at a distance of 58μm from one facet. Therefore, a GTI-like structure corresponding to the first type of those described in section **3.2.3** was integrated, which introduces a strong

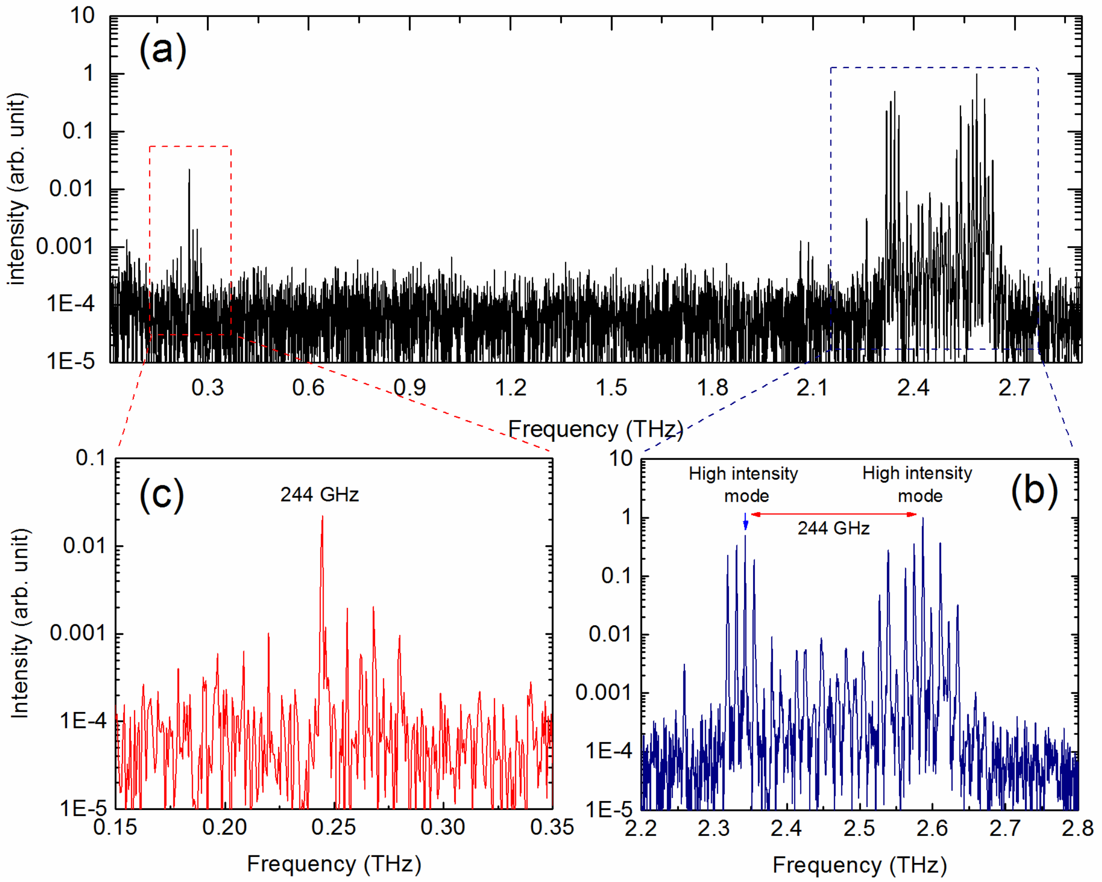

Figure 6.3: (a) Global spectrum of a device having two THz bands separated by ~244GHz; GHz lines are showed in more detail in (c) and the THz bands in (b)

dispersion region in the middle of the emission band of the device (~2.45THz). This reduces the intensity of the central modes of the band, thus splitting it in two smaller bands.
A strong microwave mode at exactly the frequency difference (panel c) is evident in the global spectrum as reported in fig. 6.3a. This already shows that it is possible to design the position of the GHz lines from that of the THz ones. Some additional modes separated by the fundamental round-trip frequency are also visible around the main line at 244GHz. The reason is essentially due to the multimode nature of the emission of Sample 9. The ideal case would be to design a device having only two THz modes separated by the desired distance. In this way, a single GHz line will be generated at the position given by the difference of those of the THz modes.

Other than single mode emission, it is also possible to try to obtain as many GHz modes as the main emission band allows for. To this aim, Sample 1, already described in chapter 4, was employed as a broadband THz source (see fig. 6.4a)) which is expected to generate many GHz lines, as showed in panel (b). GHz emission up to more than 500GHz is detected and once again the position of each line is correctly predicted just by assuming a DFG mechanism acting on the modes of the THz band. It is interesting to notice that the relative intensity of the GHz lines is also reproduced and this is particularly evident above 300GHz.
The upper limit to the frequency of the generated GHz modes is determined by the bandwidth of the device, as the maximum difference of frequency occurs in between the emitted THz lines with the lowest and highest frequency in the main THz band. The intensity of each GHz line is proportional to the number of THz modes beating together to generate it, so an uneven frequency distribution of the modes in the THz band effectively attenuates the GHz ones. Once

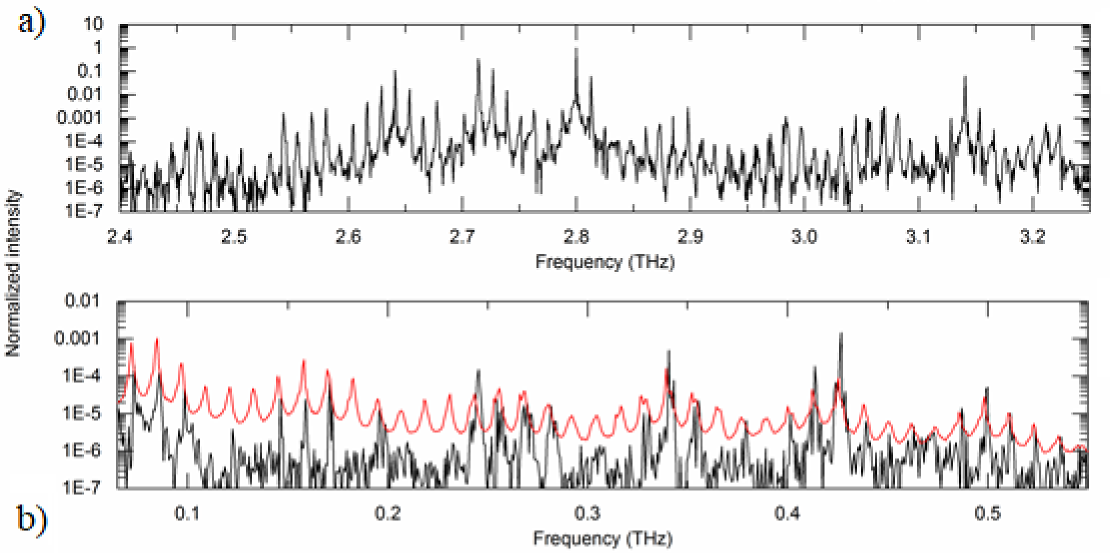

Figure 6.4: (a) THz band of Sample 1 and (b) the resulting GHz emission with the calculated profile calculated according to the analytical formula in red

again, the chromatic dispersion, which is the main factor to account for the frequency distribution of the modes should be minimized to enable the full potential of the DFG process.

As mentioned before, the fundamental beatnote is not detected by electro-optic sampling. Nevertheless, if the length of the laser cavity is sufficiently long, our spectrum analyzer can detect the emission in free space (as long as it radiates). As it is schematically represented in fig. 6.5a, by coupling the spectrum analyzer to a coaxial cable with its core exposed which then acts like an antenna, a signal that is identical to the electrical beatnote is retrieved (panels b and c). This shows that the fundamental line is being emitted by the QCL but it is not detected by the TDS, likely because of the reasons explained previously. It should be noted that the presence of the beatnote indicates a certain coherence between the modes and this would be also expected for the other GHz harmonics.

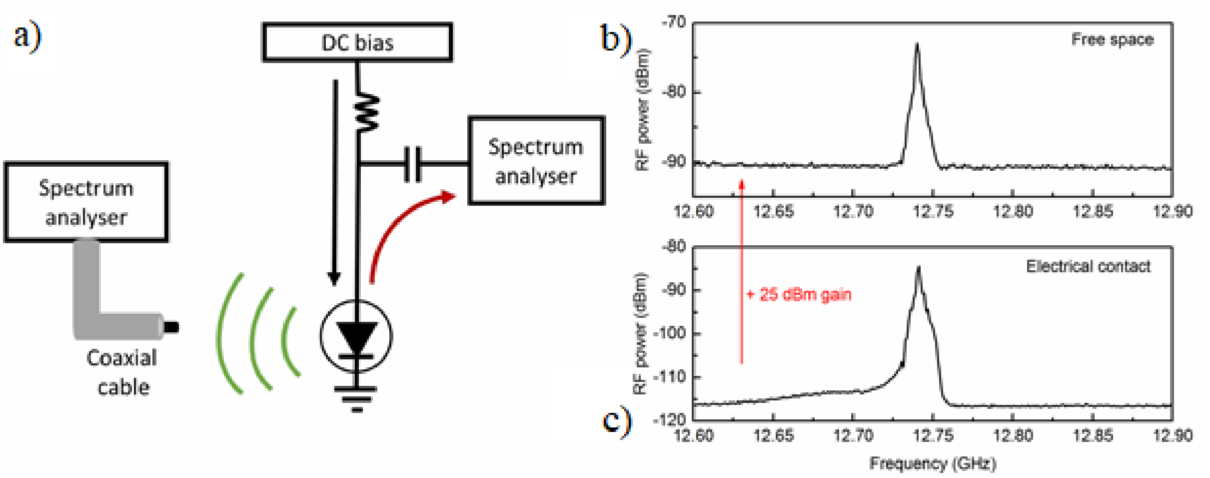

Figure 6.5: (a) Schematic of the setup employed for recording the fundamental beatnote of Sample 1 in free space (b) and with a spectrum analyzer (c)

In summary, it has been demonstrated that THz QCLs have a sufficiently strong second order non-linear susceptibility to efficently downconvert THz emission into the GHz range by means of an intracavity DFG process. This represents the first time these devices are addressed as GHz emitters capable of generating a continuous series of lines from the fundamental one to above 500GHz. This occurs in spite of the absence of a dispersion compensation scheme which should improve the THz lines distribution and enhance the intensity of the GHz modes. The capability of engineering the position of specific lines has also been showed by a dual band device which produces a strong GHz mode at the difference of the central frequencies of the two bands. Finally, the DFG phenomenon has been characterized as an intracavity process, by excluding artifacts and contributions from elements of the setup after the QCL, which shows a quadratic dependence to the THz power, in accordance with the theory.

6.2 GHz emission and THz amplitude modulation

It was widely discussed in chapter **5** that the amplitude modulation of the THz electric field profile can be explained in terms of a synchronization between the THz photons and the self-generated RF modulation originating from the beating of the modes. In the previous section, the generation of GHz modes has been demonstrated in several samples through a DFG process and it was also showed that the position in the spectrum of these modes can be predicted assuming a beating of those in the THz band. It is then reasonable to assume that a relationship between the emitted GHz signal and the modulation of the THz electric field should exist.

We can once again consider the free-running emission of Sample 2, which displayed a broad THz band and many GHz lines. By using a band-pass filter around the THz and GHz bands, as showed in fig. 6.6b by the two coloured areas, we have the time profiles of fig. 6.6a where the GHz electric field in represented in red and the THz one in black. Since the GHz emission is relatively weak, it can be seen in more details in fig. 6.6c. We can notice that after an initial amplification up to 300ps, it decreases in amplitude but then remains constant throughout the entire scan. A more detailed comparison between the GHz and the THz time traces for a short time range reveals a strong correspondence of the oscillations in the amplitude of the THz electric field with the profile of the GHz emission (fig. 6.6d). This is even easier to see in fig. 6.6e if we compare the GHz trace with the upper envelope of the THz electric field. It is immediately evident in fact that the two curves are always in phase. This fact is very important because it demonstrates the synchronization condition described in the previous chapter.

A further proof is given by the spectrum of the envelope of the THz electric field. In fact, due to the band-pass filter which was used to isolate the THz band, it should be expected that no information about the GHz modes can be anymore retrieved from its electric field. Yet, the spectrum of the envelope provides the same GHz lines that are detected from the TDS during the experiments, as showed in fig. 6.6f. This means that not only the THz modes generate the GHz ones through a DFG process, but also that the resulting RF signal strongly affects the THz emission in return.

These results show that the impact of the spontaneously generated microwaves on the emission properties of THz QCLs is much more important than what was thought up to date. The successful control of the electric field profile relies heavily on the design of the RF part of the laser emission. At the same time, this means that there is a way modulate the output of a THz

QCL without the need of active schemes. That is, passive modelocking should be achievable despite the ultra-fast gain recovery time.

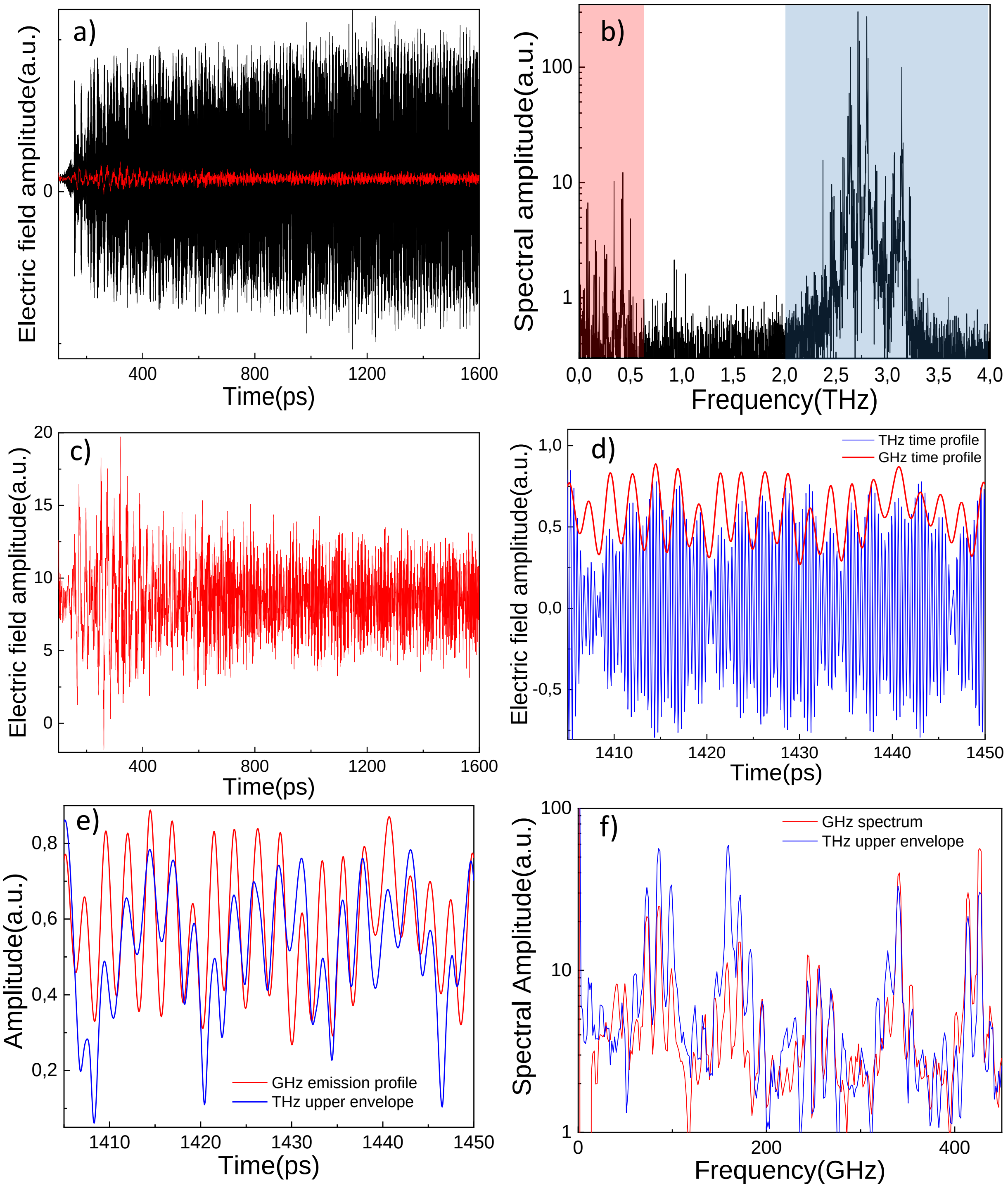

Figure 6.6: (a) Time profile corresponding to the THz (in black) and GHz (red) bands of Sample 2. The band pass filtering around the bands is represented in (b) by the coloured areas. (c) Time profile of the GHz emission. (d) Time profile of the THz band (blue) and GHz band (red) as resulting from the filtering in (b) for a short time range. The amplitude modulation of the THz electric field is clearly influenced by the GHz electric filed profile. (e) Comparison between the THz upper envelope and the GHz time profile for the same time range of (d). (f) Comparison of the spectra of the traces in (e). The strong correspondance between the two is evident.

6.3 Conclusions

In this chapter an intracavity down-conversion process based on Difference Frequency Generation was demonstrated for the first time in THz QCLs as a result of their strong second order non-linear susceptibility. Measurements on three different samples were performed to prove the generality of the phenomenon.

Specific experiments were performed to show that the phenomenon is a second-order non-linear process occurring in the cavity of a THz QCL. These included a 500GHz filter to assess the emission of GHz radiation independently of the THz one and by showing the quadratic dependency of the GHz to the THz intensity. Multiple lines above 500GHz were optically detected and their position in the spectrum could be predicted with a simple analytical elaboration of the profile of the main THz band. It was also proved that the GHz emission can be tailored by exploiting a device with two bands separated by the desired frequency. This means that THz QCLs can be considered as spontaneous GHz sources with a good flexibility in their emission properties and only few limitations which mainly regard their bandwidth in the THz range and their intrinsic dispersion. Increased broadband emission and efficiently compensating the dispersion for the generation of a THz frequency comb will lead to the generation of very narrow and strong GHz lines which are particularly interesting for high frequency telecommunications [133].

The time profile of the GHz emission also showed the synchronization with the THz amplitude modulation, providing a proof to support the theoretical model described in chapter **5**.

It may also be suggested that for a sufficiently broadband device, the emission of a continuous series of lines from a few GHz to several THz may be achievable, thus bridging with a single device the gap from millimetric to micrometric waves and therefore from electronics to optics using a single QCL device. This would require considerable improvements in more spectrally broadband QCLs and in the control of the dispersion over very large ranges of frequencies.

7

General conclusion

In this thesis I have studied the emission dynamics of THz QCLs and employed these devices for the generation of ultrashort THz pulses. This was achieved by means of an ultrafast time-resolved detection scheme that permitted to study QCL operation from the field build up to the steady state with femtosecond precision. The effect of dispersion, as well as the QCL spectral bandwidth, are the key parameters for short pulse generation. Experimental observations have been compared with numerical and electromagnetic simulations to precisely assess the effects of dispersion on the emission properties of these lasers. In particular, a frequency shifting phenomenon was shown owing due to the interplay between active modelocking and the response of an integrated dispersion compensation scheme. By being able to shift from high to low dispersion regimes, I have demonstrated that a stable pulse train with record pulse widths of 3.4ps can be generated from a relatively spectrally narrowband device owing to the combination of dispersion engineering and active modelocking. I have also presented the shortest THz pulse (1.3ps) ever obtained from a QCL exploiting an ultra-broadband design and widely discussed the necessity of dispersion compensation schemes to stabilize the pulse duration. Harmonic active modelocking was also demonstrated for the first time by modulation at a harmonic of the round-trip frequency with the generation of multiple pulses per round-trip, which is beneficial to increase the signal-to-noise ratio as well as showing the flexibility of active modulation in tuning the spectral and emission properties of QCLs.

These are important steps towards the goal of generating sub-picosecond THz pulses that would open up to the possibility of a broader range of applications outside the research domain. In particular, this would impact metrology where a broadband modelocked source could be used to detect multiple gas transitions.

Furthermore, I have shown interesting ultrafast phenomena of THz QCLs that can spontaneously generate pulses and operate in a harmonic modelocked state in free-running condition i.e. without the need of external modulations and represents a type of passive modelocked behaviour. This is contrary to expectations owing to the ultrafast gain dynamics of QCLs. I have proposed a theoretical model to explain these phenomena which is based on the condition of synchronization of the THz waves to the spontaneously generated RF profile originating from the beating of the modes in the QCL cavity. In other words, the free running emission of the laser is modulated by the self-generated RF signal that stabilizes the mode spacing of the THz modes. When the synchronization occurs at a harmonic of the fundamental round-trip frequency, the QCL's spectrum presents modes separated by the frequency of that harmonic. Two devices operating at the second and third harmonic were studied that showed that the transition from the fundamental to the harmonic state requires several round-trips to be completed. If instead the synchronization condition is satisfied for the fundamental round-trip frequency, a strong output modulation with one pulse per round-trip is observed that closely resembles modelocked operation. Beyond a fundamental interest of this peculiar QCL operating state, the capability of passively generating pulses would be a particular advantage as it would avoid the requirement of an external current modulation. In fact, costly and bulky electronic components need to be employed to force a QCL to emit pulses which adds to the complexity of the system.

Finally, I have presented the spontaneous emission of free space microwave radiation stretching from tens to hundreds of gigahertz frequencies through intracavity difference frequency generation. I have demonstrated that the source of this radiation is a second-order non-linear process that takes place in the active region of the device. While the mode beating in the QCL itself has already shown a high frequency electrical signal (i.e. the electrical beatnote), the novelty of my approach is that the GHz radiation was detected through free space optical means i.e. a TDS system, and at much higher frequencies compared to electrical methods. In this way it was possible to prove that THz QCLs are spontaneous RF emitters and that the efficiency of the process is high. Moreover, the presence of strong GHz emission further supports the synchronization model proposed in chapter 5 to explain the source of the amplitude modulation of the QCL's output profile in the spontaneous pulse generation. In the free-running emission profile, the RF profile generated by the beating of the THz modes effects, in return, the THz emission itself creating a cascaded $\chi^{(2)}$ that stabilizes the QCL emission. As well as self-stabilization, this nonlinear process could be potentially used for low noise microwave generation from a modelocked QCL. Indeed, NIR femtosecond lasers are currently used to generate low noise microwave emission for telecommunication applications. Here QCLs would provide advantages owing to their compact dimensions as well as providing a higher quantum efficiency that is determined by the quantum defect.

Bibliography

[1] S. A. Diddams, L. Hollberg, and V. Mbele, 'Molecular fingerprinting with the resolved modes of a femtosecond laser frequency comb', *Nature*, vol. 445, no. 7128, pp. 627–630, Feb. 2007.

[2] M. Hohenleutner *et al.*, 'Real-time observation of interfering crystal electrons in high-harmonic generation', *Nature*, vol. 523, no. 7562, pp. 572–575, Jul. 2015.

[3] Y. Shimotsuma *et al.*, 'Self-Organized Nanogratings in Glass Irradiated by Ultrashort Light Pulses', *Phys. Rev. Lett.*, vol. 91, no. 24, p. 247405, Dec. 2003.

[4] R. Haight et A. V. Carr, *Industrial Applications of Ultrafast Lasers*, vol. Volume 11. WORLD SCIENTIFIC, 2013.

[5] G. Keiser, 'Optical Fiber Communications', in *Wiley Encyclopedia of Telecommunications*, American Cancer Society, 2003.

[6] M. Kuznetsov, 'VECSEL Semiconductor Lasers: A Path to High-Power, Quality Beam and UV to IR Wavelength by Design', in *Semiconductor Disk Lasers*, O. G. Okhotnikov, Ed. Weinheim, Germany: Wiley-VCH Verlag GmbH & Co. KGaA, 2010, pp. 1–71.

[7] Lee, Yun-Shik. (2009). Principles of Terahertz Science and Technology. 10.1007/978-0-387-09540-0.

[8] M. Tonouchi, 'Cutting-edge terahertz technology', *Nat. Photonics*, vol. 1, no. 2, pp. 97–105, Feb. 2007.

[9] B. Ferguson et X.-C. Zhang, « Materials for terahertz science and technology », *Nat. Mater.*, vol. 1, n° 1, p. 26-33, sept. 2002.

[10] N. M. Burford and M. O. El-Shenawee, 'Review of terahertz photoconductive antenna technology', *Opt. Eng.*, vol. 56, no. 1, p. 010901, Jan. 2017.

[11] X. Wu *et al.*, 'Highly efficient generation of 0.2 mJ terahertz pulses in lithium niobate at room temperature with sub-50 fs chirped Ti:sapphire laser pulses', *Opt. Express*, vol. 26, no. 6, pp. 7107–7116, Mar. 2018.

[12] R. Köhler *et al.*, 'Terahertz semiconductor-heterostructure laser', *Nature*, vol. 417, no. 6885, pp. 156–159, May 2002.

[13] Green, RP, Tredicucci, A, Vinh, NQ, Murdin, B, Pidgeon, C, Beere, HE and Ritchie, DA (2009) Gain recovery dynamics of a terahertz quantum cascade laser PHYSICAL REVIEW B, 80 (7), ARTN 0.

[14] S. Barbieri *et al.*, 'Coherent sampling of active mode-locked terahertz quantum cascade lasers and frequency synthesis', *Nat. Photonics*, vol. 5, no. 6, pp. 377–377, Jun. 2011.

[15] J. Maysonnave *et al.*, 'Mode-locking of a terahertz laser by direct phase synchronization', *Opt. Express*, vol. 20, no. 19, pp. 20855–20862, Sep. 2012.

[16] F. Wang *et al.*, 'Generating ultrafast pulses of light from quantum cascade lasers', *Optica*, vol. 2, no. 11, pp. 944–949, Nov. 2015.

[17] F. Wang *et al.*, 'Short Terahertz Pulse Generation from a Dispersion Compensated Modelocked Semiconductor Laser', *Laser Photonics Rev.*, vol. 11, no. 4, p. 1700013, Jul. 2017.

[18] J. Faist, F. Capasso, D. L. Sivco, C. Sirtori, A. L. Hutchinson, and A. Y. Cho, 'Quantum Cascade Laser', *Science*, vol. 264, no. 5158, pp. 553–556, Apr. 1994.

[19] T. Udem, R. Holzwarth, and T. W. Hänsch, 'Optical frequency metrology', *Nature*, vol. 416, no. 6877, pp. 233–237, Mar. 2002.

[20] X. Zhou, X. Zheng, H. Wen, H. Zhang, Y. Guo, and B. Zhou, 'All optical arbitrary waveform generation by optical frequency comb based on cascading intensity modulation', *Opt. Commun.*, vol. 284, no. 15, pp. 3706–3710, Jul. 2011.

[21] M. L. Weichman, P. B. Changala, J. Ye, Z. Chen, M. Yan, and N. Picqué, ‘Broadband molecular spectroscopy with optical frequency combs’, *J. Mol. Spectrosc.*, vol. 355, pp. 66–78, Jan. 2019.

[22] N. R. Newbury, ‘Searching for applications with a fine-tooth comb’, *Nat. Photonics*, vol. 5, pp. 186–188, Apr. 2011.

[23] F. Adler *et al.*, ‘Phase-locked two-branch erbium-doped fiber laser system for long-term precision measurements of optical frequencies’, *Opt. Express*, vol. 12, no. 24, p. 5872, 2004.

[24] W. E. Lamb, « Theory of an Optical Maser », *Phys. Rev.*, vol. 134, n° 6A, p. A1429-A1450, juin 1964.

[25] L. E. Hargrove, R. L. Fork, and M. A. Pollack, ‘LOCKING OF He–Ne LASER MODES INDUCED BY SYNCHRONOUS INTRACAVITY MODULATION’, *Appl. Phys. Lett.*, vol. 5, no. 1, pp. 4–5, Jul. 1964.

[26] R. W. Boyd, *Nonlinear Optics, Third Edition*, 3rd éd. Orlando, FL, USA: Academic Press, Inc., 2008.

[27] E. P. Ippen, C. V. Shank, et A. Dienes, « Passive mode locking of the cw dye laser », *Appl. Phys. Lett.*, vol. 21, n° 8, p. 348-350, oct. 1972.

[28] J. Maysonnave, K. Maussang, J. Freeman, N. Jukam, J. Madéo, P. Cavalié, R. Rungsawang, S. Khanna, E. Linfield, A. Davies, H. Beere, D. Ritchie, S. Dhillon, and J. Tignon, "Mode-locking of a terahertz laser by direct phase synchronization," Opt. Express 20, 20855-20862 (2012).

[29] J. R. Freeman, J. Maysonnave, H. E. Beere, D. A. Ritchie, J. Tignon, and S. S. Dhillon, ‘Electric field sampling of modelocked pulses from a quantum cascade laser’, *Opt. Express*, vol. 21, no. 13, pp. 16162–16169, Jul. 2013.

[30] P. von Allmen, M. Berz, G. Petrocelli, F.-K. Reinhart, et G. Harbeke, « Inter-sub-band absorption in GaAs/AlGaAs quantum wells between 4.2 K and room temperature », *Semicond. Sci. Technol.*, vol. 3, n° 12, p. 1211-1216, déc. 1988.

[31] W. W. Chow and S. W. Koch, *Semiconductor-Laser Fundamentals: Physics of the Gain Materials*. Berlin Heidelberg: Springer-Verlag, 1999.

[32] L. A. Coldren *et al.*, ‘Diode Lasers and Photonic Integrated Circuits, 2nd Edition | Photonics & Lasers | General & Introductory Electrical & Electronics Engineering | Subjects | Wiley’.

[33] A. Lyakh, R. Maulini, A. Tsekoun, R. Go, and C. K. N. Patel, ‘Multiwatt long wavelength quantum cascade lasers based on high strain composition with 70% injection efficiency’, *Opt. Express*, vol. 20, no. 22, pp. 24272–24279, Oct. 2012.

[34] Y. Bai, N. Bandyopadhyay, S. Tsao, S. Slivken, and M. Razeghi, ‘Room temperature quantum cascade lasers with 27% wall plug efficiency’, *Appl. Phys. Lett.*, vol. 98, no. 18, p. 181102, May 2011.

[35] J. S. Yu, S. Slivken, A. Evans, L. Doris, and M. Razeghi, ‘High-power continuous-wave operation of a 6 μm quantum-cascade laser at room temperature’, *Appl. Phys. Lett.*, vol. 83, no. 13, pp. 2503–2505, Sep. 2003.

[36] J. Faist *et al.*, ‘High-power continuous-wave quantum cascade lasers’, *IEEE J. Quantum Electron.*, vol. 34, no. 2, pp. 336–343, Feb. 1998.

[37] H. Kroemer, *Quantum mechanics: for engineering, materials science, and applied physics*. Englewood Cliffs, N.J.: Prentice Hall, 1994.

[38] M. S. Vitiello *et al.*, « Quantum-limited frequency fluctuations in a terahertz laser », *Nat. Photonics*, vol. 6, n° 8, p. 525-528, août 2012.

[39] J. Faist, *Quantum Cascade Lasers*. Oxford, New York: Oxford University Press, 2013.

[40] J. Faist, M. Beck, T. Aellen, and E. Gini, ‘Quantum-cascade lasers based on a bound-to-continuum transition’, *Appl. Phys. Lett.*, vol. 78, no. 2, pp. 147–149, Jan. 2001.

[41] B. S. Williams, S. Kumar, H. Callebaut, Q. Hu, and J. L. Reno, ‘Terahertz quantum-cascade laser at λ≈100 μm using metal waveguide for mode confinement’, *Appl. Phys. Lett.*, vol. 83, no. 11, pp. 2124–2126, Sep. 2003.

[42] G. Bastard, ‘Wave mechanics applied to semiconductor heterostructures /’, c1988. .

[43] V. Liverini *et al.*, ‘Room-temperature transverse-electric polarized intersubband electroluminescence from InAs/AlInAs quantum dashes’, *Appl. Phys. Lett.*, vol. 101, no. 26, p. 261113, Dec. 2012.

[44] C. Worrall *et al.*, ‘Continuous wave operation of a superlattic quantum cascade laser emitting at 2 THz’, *Opt. Express*, vol. 14, no. 1, pp. 171–181, Jan. 2006.

[45] B. S. Williams, S. Kumar, H. Callebaut, Q. Hu, et J. L. Reno, « Terahertz quantum-cascade laser operating up to 137 K », *Appl. Phys. Lett.*, vol. 83, n° 25, p. 5142-5144, déc. 2003.

[46] L. Bosco, M. Franckié, G. Scalari, M. Beck, A. Wacker, and J. Faist, ‘Thermoelectrically cooled THz quantum cascade laser operating up to 210 K’, *Appl. Phys. Lett.*, vol. 115, no. 1, p. 010601, Jul. 2019.

[47] M. I. Amanti *et al.*, ‘Bound-to-continuum terahertz quantum cascade laser with a single-quantum-well phonon extraction/injection stage’, *New J. Phys.*, vol. 11, no. 12, p. 125022, Dec. 2009.

[48] B. S. Williams, « Terahertz quantum-cascade lasers », *Nat. Photonics*, vol. 1, n° 9, p. 517-525, sept. 2007.

[49] C. Sirtori, F. Capasso, J. Faist, A. L. Hutchinson, D. L. Sivco and A. Y. Cho, "Resonant tunneling in quantum cascade lasers," in *IEEE Journal of Quantum Electronics*, vol. 34, no. 9, pp. 1722-1729, Sept. 1998.

[50] J. A. Fan *et al.*, ‘Wide-ridge metal-metal terahertz quantum cascade lasers with high-order lateral mode suppression’, *Appl. Phys. Lett.*, vol. 92, no. 3, p. 031106, Jan. 2008.

[51] D. Bachmann *et al.*, ‘Short pulse generation and mode control of broadband terahertz quantum cascade lasers’, *Optica*, vol. 3, no. 10, p. 1087, Oct. 2016.

[52] K. Unterrainer *et al.*, ‘Quantum cascade lasers with double metal-semiconductor waveguide resonators’, *Appl. Phys. Lett.*, vol. 80, no. 17, pp. 3060–3062, Apr. 2002.

[53] Aristeidou, Antonis et al. “The evolution of corneal and refractive surgery with the femtosecond laser.” *Eye and vision (London, England)* vol. 2 12. 14 Jul. 2015.

[54] J. Zhang, A. Cerkauskaite, R. Drevinskas, A. Patel, M. Beresna, and P. Kazansky, ‘Eternal 5D data storage by ultrafast laser writing in glass’, 2016.

[55] A. Hugi, G. Villares, S. Blaser, H. C. Liu, and J. Faist, ‘Mid-infrared frequency comb based on a quantum cascade laser’, *Nature*, vol. 492, no. 7428, pp. 229–233, Dec. 2012.

[56] D. Kazakov *et al.*, ‘Self-starting harmonic frequency comb generation in a quantum cascade laser’, *Nat. Photonics*, vol. 11, no. 12, pp. 789–792, Dec. 2017.

[57] J. B. Khurgin, Y. Dikmelik, A. Hugi, and J. Faist, ‘Coherent frequency combs produced by self frequency modulation in quantum cascade lasers’, *Appl. Phys. Lett.*, vol. 104, no. 8, p. 081118, Feb. 2014.

[58] C. Hönninger, R. Paschotta, F. Morier-Genoud, M. Moser, and U. Keller, ‘Q-switching stability limits of continuous-wave passive mode locking’, *JOSA B*, vol. 16, no. 1, pp. 46–56, Jan. 1999.

[59] R. Paschotta, A. Schlatter, S. C. Zeller, H. R. Telle, and U. Keller, ‘Optical phase noise and carrier-envelope offset noise of mode-locked lasers’, *Appl. Phys. B*, vol. 82, no. 2, pp. 265–273, Feb. 2006.

[60] N. Picqué and T. W. Hänsch, ‘Frequency comb spectroscopy’, *Nat. Photonics*, vol. 13, no. 3, pp. 146–157, Mar. 2019.

[61] L. Consolino *et al.*, ‘Fully phase-stabilized quantum cascade laser frequency comb’, *Nat. Commun.*, vol. 10, no. 1, pp. 1–7, Jul. 2019.

[62] F. Adler, K. C. Cossel, M. J. Thorpe, I. Hartl, M. E. Fermann, and J. Ye, ‘Phase-stabilized, 1.5 W frequency comb at 2.8–4.8 µm’, *Opt. Lett.*, vol. 34, no. 9, pp. 1330–1332, May 2009.

[63] T. J. Kippenberg, R. Holzwarth, et S. A. Diddams, « Microresonator-Based Optical Frequency Combs », *Science*, vol. 332, n° 6029, p. 555, avr. 2011.

[64] P. Del’Haye, A. Schliesser, O. Arcizet, T. Wilken, R. Holzwarth, et T. J. Kippenberg, « Optical frequency comb generation from a monolithic microresonator », *Nature*, vol. 450, n° 7173, p. 1214-1217, déc. 2007.

[65] D. Burghoff *et al.*, ‘Terahertz laser frequency combs’, *Nat. Photonics*, vol. 8, no. 6, pp. 462–467, Jun. 2014.

[66] A. Mottaghizadeh *et al.*, ‘5-ps-long terahertz pulses from an active-mode-locked quantum cascade laser’, *Optica*, vol. 4, no. 1, p. 168, Jan. 2017.

[67] D. Burghoff, Y. Yang, J. L. Reno, and Q. Hu, ‘Dispersion dynamics of quantum cascade lasers’, *Optica*, vol. 3, no. 12, p. 1362, Dec. 2016.

[68] G. Villares *et al.*, ‘Dispersion engineering of quantum cascade laser frequency combs’, *Optica*, vol. 3, no. 3, p. 252, Mar. 2016.

[69] D. Oustinov *et al.*, ‘Phase seeding of a terahertz quantum cascade laser’, *Nat. Commun.*, vol. 1, no. 1, p. 69, Dec. 2010.

[70] A. Rogalski and F. Sizov, ‘Terahertz detectors and focal plane arrays’, *Opto-Electron. Rev.*, vol. 19, no. 3, pp. 346–404, 2011.

[71] J. Yan *et al.*, « Dual-gated bilayer graphene hot-electron bolometer », *Nat. Nanotechnol.*, vol. 7, n° 7, p. 472-478, juill. 2012.

[72] D. Burghoff, Y. Yang, D. J. Hayton, J.-R. Gao, J. L. Reno, and Q. Hu, ‘Evaluating the coherence and time-domain profile of quantum cascade laser frequency combs’, *Opt. Express*, vol. 23, no. 2, p. 1190, Jan. 2015.

[73] I.-C. Benea-Chelmus, C. Bonzon, C. Maissen, G. Scalari, M. Beck, and J. Faist, ‘Subcycle measurement of intensity correlations in the terahertz frequency range’, *Phys. Rev. A*, vol. 93, no. 4, p. 043812, Apr. 2016.

[74] M. van Exter, C. Fattinger, and D. Grischkowsky, ‘Terahertz time-domain spectroscopy of water vapor’, *Opt. Lett.*, vol. 14, no. 20, pp. 1128–1130, Oct. 1989.

[75] N. Jukam *et al.*, « Terahertz time domain spectroscopy of phonon-depopulation based quantum cascade lasers », *Appl. Phys. Lett.*, vol. 94, n° 25, p. 251108, juin 2009.

[76] Madéo, J.; Jukam, N.; Oustinov, D.; Rosticher, M.; Rungsawang, R.; Tignon, J.; Dhillon, S.S.: 'Frequency tunable terahertz interdigitated photoconductive antennas', Electronics Letters, 2010, 46, (9), p. 611-613.

[77] Q. Wu et X. -C. Zhang, « Free-space electro-optic sampling of terahertz beams », *Appl. Phys. Lett.*, vol. 67, n° 24, p. 3523-3525, déc. 1995.

[78] H. Zhong, N. Karpowicz, et X.-C. Zhang, « Terahertz emission profile from laser-induced air plasma », *Appl. Phys. Lett.*, vol. 88, n° 26, p. 261103, juin 2006.

[79] K. Maussang *et al.*, ‘Monolithic echo-less photoconductive switches as a high-resolution detector for terahertz time-domain spectroscopy’, *Appl. Phys. Lett.*, vol. 110, no. 14, p. 141102, Apr. 2017.

[80] P. J. Hale *et al.*, ‘Broadband THz generation using interdigitated photoconductive antennas with a 15 fs, high power oscillator’, in *CLEO: 2013*, 2013, pp. 1–2.

[81] P. U. Jepsen, R. H. Jacobsen, and S. R. Keiding, ‘Generation and detection of terahertz pulses from biased semiconductor antennas’, *JOSA B*, vol. 13, no. 11, pp. 2424–2436, Nov. 1996.

[82] J. Dai, J. Liu and X. Zhang, "Terahertz Wave Air Photonics: Terahertz Wave Generation and Detection With Laser-Induced Gas Plasma," in *IEEE Journal of Selected Topics in Quantum Electronics*, vol. 17, no. 1, pp. 183-190, Jan.-Feb. 2011.

[83] Q. Wu, M. Litz, et X. -C. Zhang, « Broadband detection capability of ZnTe electro-optic field detectors », *Appl. Phys. Lett.*, vol. 68, n° 21, p. 2924-2926, mai 1996.

[84] Q. Wu et X.-C. Zhang, « 7 terahertz broadband GaP electro-optic sensor », *Appl. Phys. Lett.*, vol. 70, n° 14, p. 1784-1786, avr. 1997.

[85] I. N. D. III and I. N. Duling, *Compact Sources of Ultrashort Pulses*. Cambridge University Press, 1995.

[86] R. Roy, P. A. Schulz, and A. Walther, 'Acousto-optic modulator as an electronically selectable unidirectional device in a ring laser', *Opt. Lett.*, vol. 12, no. 9, pp. 672–674, Sep. 1987.

[87] P. A. Schulz, 'Single-frequency Ti:Al/sub 2/O/sub 3/ ring laser', *IEEE J. Quantum Electron.*, vol. 24, no. 6, pp. 1039–1044, Jun. 1988.

[88] T. L. Paoli and J. E. Ripper, 'Direct modulation of semiconductor lasers', *Proc. IEEE*, vol. 58, no. 10, pp. 1457–1465, Oct. 1970.

[89] P. Gellie *et al.*, 'Injection-locking of terahertz quantum cascade lasers up to 35GHz using RF amplitude modulation', *Opt. Express*, vol. 18, no. 20, pp. 20799–20816, Sep. 2010.

[90] W. J. Witteman, 'Passive Mode Locking', in *The CO2 Laser*, W. J. Witteman, Ed. Berlin, Heidelberg: Springer Berlin Heidelberg, 1987, pp. 251–266.

[91] E. P. Ippen, 'Principles of passive mode locking', *Appl. Phys. B*, vol. 58, no. 3, pp. 159–170, Mar. 1994.

[92] S. Chen and J. Wang, 'Self-starting issues of passive self-focusing mode locking', *Opt. Lett.*, vol. 16, no. 21, pp. 1689–1691, Nov. 1991.

[93] P. J. Delfyett, A. Dienes, J. P. Heritage, M. Y. Hong, and Y. H. Chang, 'Femtosecond hybrid mode-locked semiconductor laser and amplifier dynamics', *Appl. Phys. B*, vol. 58, no. 3, pp. 183–195, Mar. 1994.

[94] M. Wienold, L. Schrottke, M. Giehler, R. Hey, W. Anders, and H. T. Grahn, 'Low-voltage terahertz quantum-cascade lasers based on LO-phonon-assisted interminiband transitions', *Electron. Lett.*, vol. 45, no. 20, pp. 1030–1031, Sep. 2009.

[95] D. Bachmann *et al.*, 'Dispersion in a broadband terahertz quantum cascade laser', *Appl. Phys. Lett.*, vol. 109, p. 221107, Nov. 2016.

[96] F. Wooten, 'Optical Properties of Solids', p. 270.

[97] J. Liu, *Photonic Devices*. Cambridge University Press, 2009.

[98] L. Jumpertz, *Nonlinear Photonics in Mid-infrared Quantum Cascade Lasers*. Springer International Publishing, 2017.

[99] Y. Bidaux, F. Kapsalidis, P. Jouy, M. Beck, and J. Faist, 'Coupled-waveguides for dispersion compensation in semiconductor lasers', *ArXiv171109116 Phys.*, Nov. 2017.

[100] M. Rösch *et al.*, 'Heterogeneous terahertz quantum cascade lasers exceeding 1.9 THz spectral bandwidth and featuring dual comb operation', *Nanophotonics*, vol. 7, no. 1, pp. 237–242, Jan. 2018.

[101] Y. Bidaux *et al.*, 'Plasmon-enhanced waveguide for dispersion compensation in mid-infrared quantum cascade laser frequency combs', *Opt. Lett.*, vol. 42, no. 8, p. 1604, Apr. 2017.

[102] M. Sezen, 'Focused Ion Beams (FIB) — Novel Methodologies and Recent Applications for Multidisciplinary Sciences', *Mod. Electron Microsc. Phys. Life Sci.*, Feb. 2016.

[103] T. Fobbe *et al.*, 'Broadband terahertz dispersion control in hybrid waveguides', *Opt. Express*, vol. 24, p. 22319, Sep. 2016.

[104] J. Hillbrand, P. Jouy, M. Beck, and J. Faist, 'Tunable dispersion compensation of quantum cascade laser frequency combs', *Opt. Lett.*, vol. 43, no. 8, pp. 1746–1749, Apr. 2018.

[105] X. Qi *et al.*, ‘Mode Selection and Tuning Mechanisms in Coupled-Cavity Terahertz Quantum Cascade Lasers’, *IEEE J. Sel. Top. Quantum Electron.*, vol. 23, no. 4, pp. 1–12, Jul. 2017.

[106] N. G. Usechak and G. P. Agrawal, ‘Semi-analytic technique for analyzing mode-locked lasers’, *Opt. Express*, vol. 13, no. 6, p. 2075, 2005.

[107] I. Kundu *et al.*, ‘Ultrafast switch-on dynamics of frequency-tuneable semiconductor lasers’, *Nat. Commun.*, vol. 9, no. 1, p. 3076, Aug. 2018.

[108] Xiaoqiong Qi, Gary Agnew, Iman Kundu, Thomas Taimre, Yah Leng Lim, Karl Bertling, Paul Dean, Andrew Grier, Alexander Valavanis, Edmund H. Linfield, A. Giles Davies, Dragan Indjin, and Aleksandar D. Rakić, "Multi-spectral terahertz sensing: proposal for a coupled-cavity quantum cascade laser based optical feedback interferometer," Opt. Express 25, 10153-10165 (2017).

[109] F. X. Kärtner, D. Kopf, and U. Keller, ‘Solitary-pulse stabilization and shortening in actively mode-locked lasers’, *JOSA B*, vol. 12, no. 3, pp. 486–496, Mar. 1995.

[110] H. Choi *et al.*, ‘Femtosecond dynamics of resonant tunneling and superlattice relaxation in quantum cascade lasers’, *Appl. Phys. Lett.*, vol. 92, no. 12, p. 122114, Mar. 2008.

[111] P. Tzenov *et al.*, ‘Passive and hybrid mode locking in multi-section terahertz quantum cascade lasers’, *New J. Phys.*, vol. 20, no. 5, p. 053055, May 2018.

[112] S. Fathololoumi *et al.*, ‘Terahertz quantum cascade lasers operating up to ∼ 200 K with optimized oscillator strength and improved injection tunneling’, *Opt. Express*, vol. 20, no. 4, pp. 3866–3876, Feb. 2012.

[113] H. A. Haus, ‘Mode-locking of lasers’, *IEEE J. Sel. Top. Quantum Electron.*, vol. 6, no. 6, pp. 1173–1185, Nov. 2000.

[114] M. A. Talukder and C. R. Menyuk, ‘Self-induced transparency modelocking of quantum cascade lasers in the presence of saturable nonlinearity and group velocity dispersion’, *Opt. Express*, vol. 18, no. 6, p. 5639, Mar. 2010.

[115] V. Gkortsas *et al.*, ‘Dynamics of actively mode-locked Quantum Cascade Lasers’, *Opt. Express*, vol. 18, pp. 13616–30, Jun. 2010.

[116] M. Rösch, G. Scalari, M. Beck, et J. Faist, « Octave-spanning semiconductor laser », *Nat. Photonics*, vol. 9, p. 42, nov. 2014.

[117] L. H. Li *et al.*, ‘Broadband heterogeneous terahertz frequency quantum cascade laser’, *Electron. Lett.*, vol. 54, no. 21, pp. 1229–1231, 2018.

[118] N. Jukam *et al.*, ‘Gain Measurements of THz Quantum Cascade Lasers using THz Time-Domain Spectroscopy’, *IEEE J. Sel. Top. Quantum Electron.*, vol. 14, no. 2, pp. 436–442, 2008.

[119] A. Gordon *et al.*, ‘Multimode regimes in quantum cascade lasers: From coherent instabilities to spatial hole burning’, *Phys. Rev. A*, vol. 77, no. 5, p. 053804, May 2008.

[120] M. Piccardo *et al.*, ‘Widely tunable harmonic frequency comb in a quantum cascade laser’, *Appl. Phys. Lett.*, vol. 113, no. 3, p. 031104, Jul. 2018.

[121] Q. Lu, F. Wang, D. Wu, S. Slivken, and M. Razeghi, ‘Room temperature terahertz semiconductor frequency comb’, *Nat. Commun.*, vol. 10, no. 1, pp. 1–7, Jun. 2019.

[122] H. Li *et al.*, ‘Dynamics of ultra-broadband terahertz quantum cascade lasers for comb operation’, *Opt. Express*, vol. 23, no. 26, pp. 33270–33294, Dec. 2015.

[123] M. Piccardo *et al.*, ‘Time-dependent population inversion gratings in laser frequency combs’, *Optica*, vol. 5, no. 4, p. 475, Apr. 2018.

[124] W. Maineult *et al.*, ‘Microwave modulation of terahertz quantum cascade lasers: a transmission-line approach’, *Appl. Phys. Lett.*, vol. 96, no. 2, p. 021108, Jan. 2010.

[125] M. Riesch and C. Jirauschek, ‘An open-source solver tool for the Maxwell-Bloch equations’, *https://github.com/mriesch-tum/mbsolve*, 2017.

[126] M. Riesch, N. Tchipev, S. Senninger, H.-J. Bungartz, and C. Jirauschek, ‘Performance evaluation of numerical methods for the Maxwell–Liouville–von Neumann equations’, *Opt. Quantum Electron.*, vol. 50, no. 2, p. 112, Feb. 2018.

[127] C. Jirauschek et T. Kubis, « Modeling techniques for quantum cascade lasers », *Appl. Phys. Rev.*, vol. 1, n^o 1, p. 011307, févr. 2014.

[128] C. Jirauschek, M. Riesch, and P. Tzenov, ‘Optoelectronic Device Simulations Based on Macroscopic Maxwell–Bloch Equations’, *Adv. Theory Simul.*, vol. 2, no. 8, p. 1900018, 2019.

[129] P. Friedli *et al.*, ‘Four-wave mixing in a quantum cascade laser amplifier’, *Appl. Phys. Lett.*, vol. 102, no. 22, p. 222104, Jun. 2013.

[130] M. A. Belkin *et al.*, ‘Terahertz quantum-cascade-laser source based on intracavity difference-frequency generation’, *Nat. Photonics*, vol. 1, no. 5, pp. 288–292, May 2007.

[131] K. Fujita *et al.*, ‘Recent progress in terahertz difference-frequency quantum cascade laser sources’, *Nanophotonics*, vol. 7, no. 11, pp. 1795–1817, Oct. 2018.

[132] K. Fujita, M. Hitaka, A. Ito, M. Yamanishi, T. Dougakiuchi, and T. Edamura, ‘Ultra-broadband room-temperature terahertz quantum cascade laser sources based on difference frequency generation’, *Opt. Express*, vol. 24, no. 15, p. 16357, Jul. 2016.

[133] M. Piccardo *et al.*, ‘Radio frequency transmitter based on a laser frequency comb’, *Proc. Natl. Acad. Sci.*, vol. 116, no. 19, pp. 9181–9185, May 2019.

[134] P. Tzenov, D. Burghoff, Q. Hu, and C. Jirauschek, ‘Time domain modeling of terahertz quantum cascade lasers for frequency comb generation’, *Opt. Express*, vol. 24, no. 20, pp. 23232–23247, Oct. 2016.

Annex 1

A1.1 Quantum cascade laser fabrication process

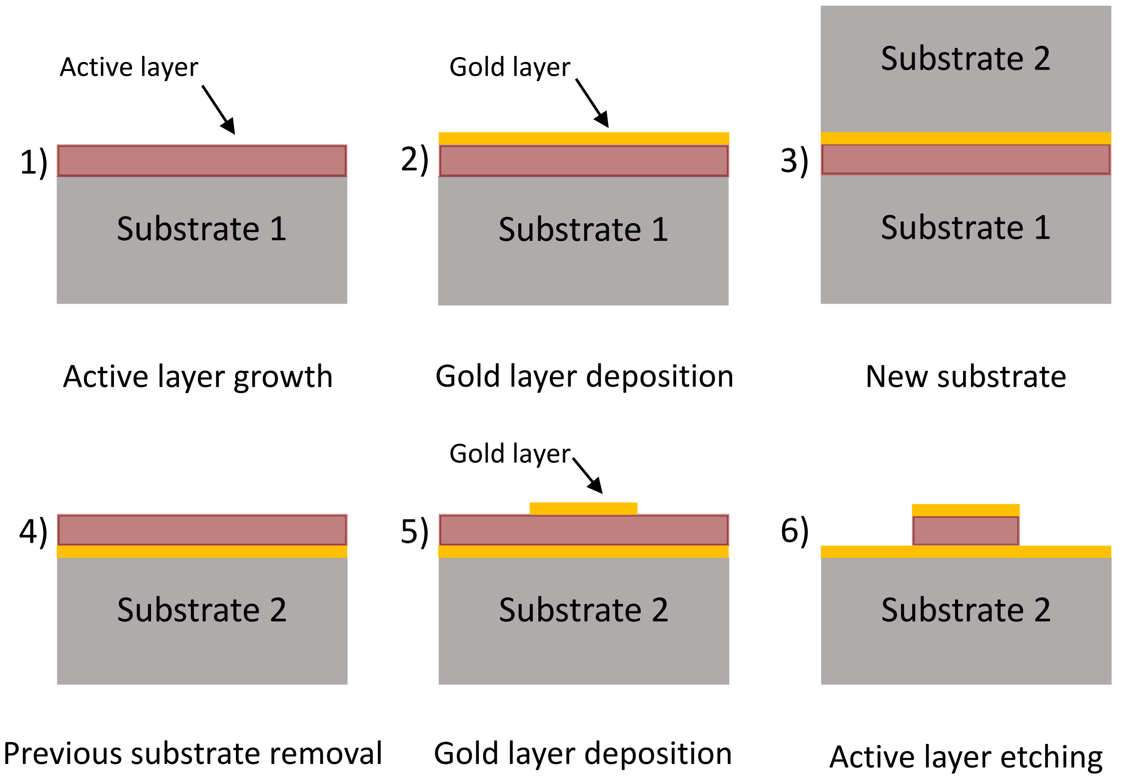

Figure A1: Illustration of the main steps for the fabrication of a THz QCL with a double-metal waveguide

Figure A1 shows schematically the main steps of the process which leads to a complete double-metal device. In the first step the ~10μm thick active region is deposited by MBE on a GaAs substrate. After that, a Ti/Au layer with a thickness of ~300 nm is deposited on the active layer as illustrated in 2). In third step, a host GaAs substrate is wafer-bonded to the Ti/Au layer of the QCL substrate. In 4) the original GaAs substrate is removed using physical thinning and selective etching. This is followed by the deposition of a ~300-nm Ti/Au thick layer having the width chosen for the waveguide on top of active region, as shown in 5). Finally, the active region is etched (chemical or dry etching) so that only the part covered by the top metal is spared. The device is then ready to be dimensioned, mounted and bonded.

Annex 2

A2.1 Imaginary part of the refractive index of GaAs

The expression of the imaginary part of the refractive index is

$$k(\omega) = \sqrt{\frac{\sqrt{\varepsilon_1^2(\omega) + \varepsilon_2^2(\omega)} - \varepsilon_1(\omega)}{2}}$$

and it is plotted in figure A2.1 from the same parameters employed in section **3.1**.

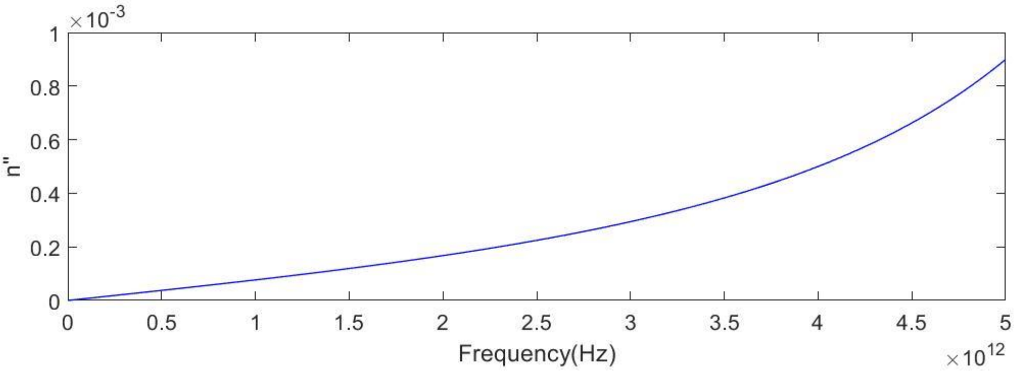

Figure A2.1: Imaginary part of the refractive index from the Drude-Lorentz model

A2.2 Tunable GTI with an external spherical mirror

The effect of an external spherical mirror on the dispersion introduced to a THz QCL was simulated in the 2D Comsol environment. Figure A2.2a shows an example of the resulting electric field intensity at a frequency of 3.5THz and a mirror distance to the facet of 190µm. A frequency sweep to recover the phase of the reflected field results in the dispersion profile of fig. A2.2b. As one can see, the dispersion profile is very similar to that of an ideal GTI. The increase of dispersion for higher frequencies is associated to a better back-coupling into the QCL waveguide.

Fig.2.2c reports the linewidth of the beatnote of Sample 1 without the tunable GTI (in black) and when the tunable GTI is used on-resonance (in red). The reduction of the linewidth in the second case demonstrates a significant improvement in the mode distribution that is achieved thanks to the compensation of dispersion.

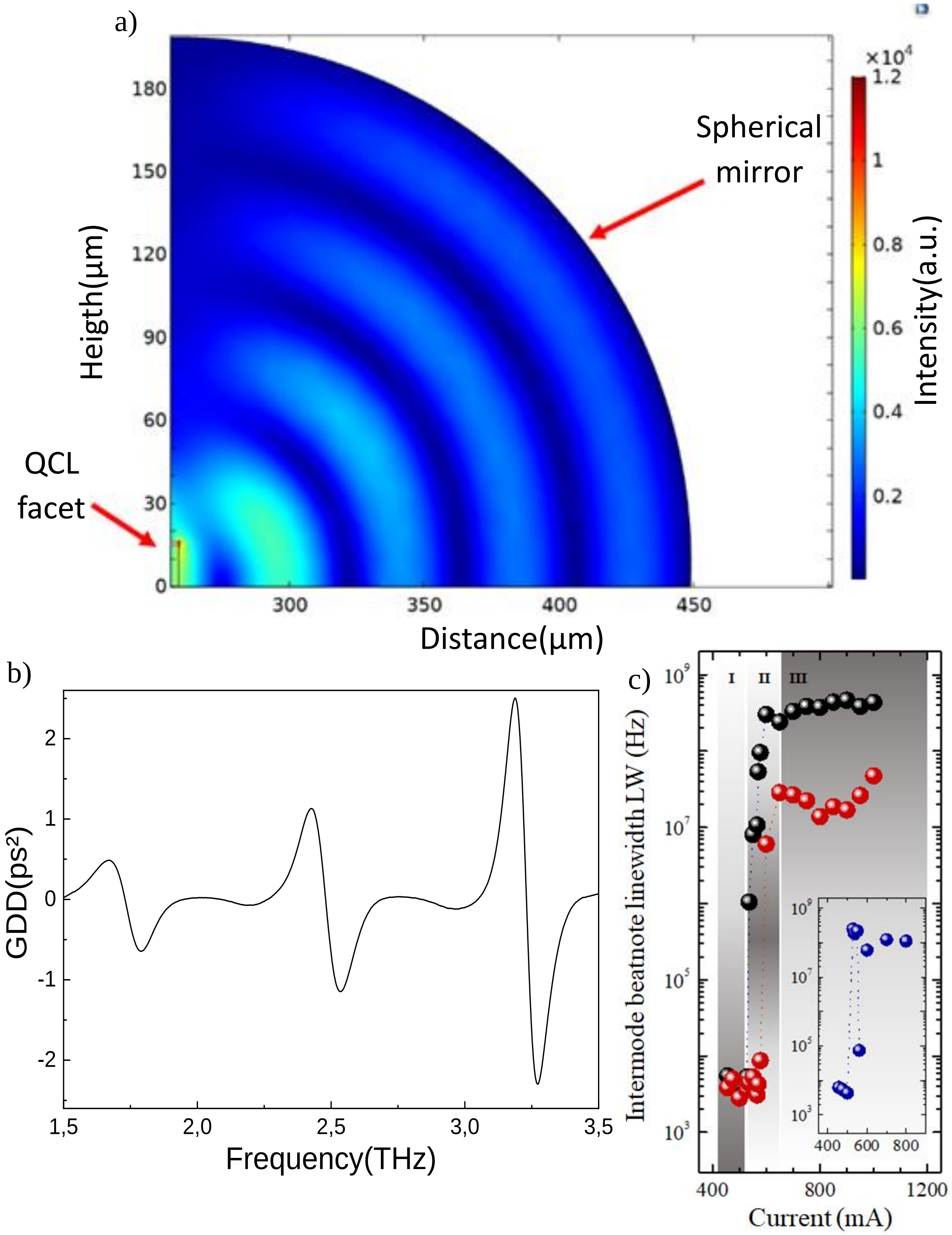

Figure A2.2: (a) Spatial distribution of the electric field emitted by a THz QCL at 3.5THz in presence of a perfectly reflecting external spherical mirror positioned at 190µm from the QCL's facet. (b) Dispersion profile introduced by a spherical gold mirror positioned at 190µm from a QCL facet. This profile has been obtained from the phase of the scattering parameter S11 read at the facet of the device. (c) Sample 1 beatnote linewidth as a function of bias without the tunable GTI (in black) or when the tunable GTI is on-resonance (in red). The linewidth enhancement is evident in particular after 600mA.

Annex 3

A3.1.1 LIV and beatnote map of Sample 1

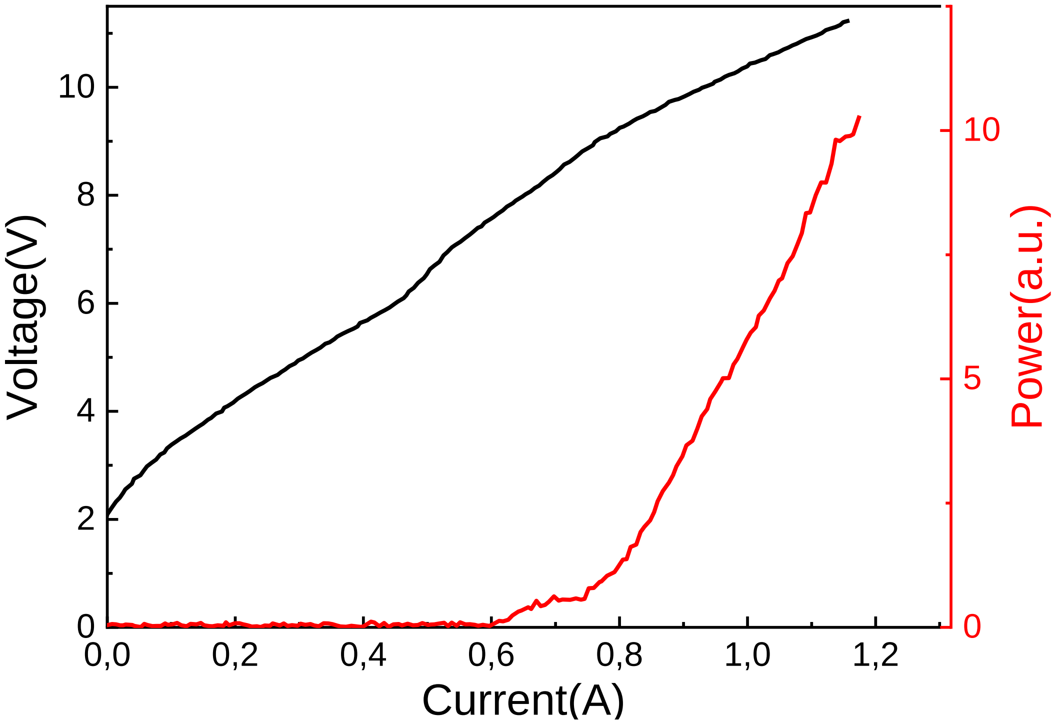

Figure A3.1: LIV of Sample 1 (L1458) at 20K - 25kHz bias frequency – 10% duty cycle

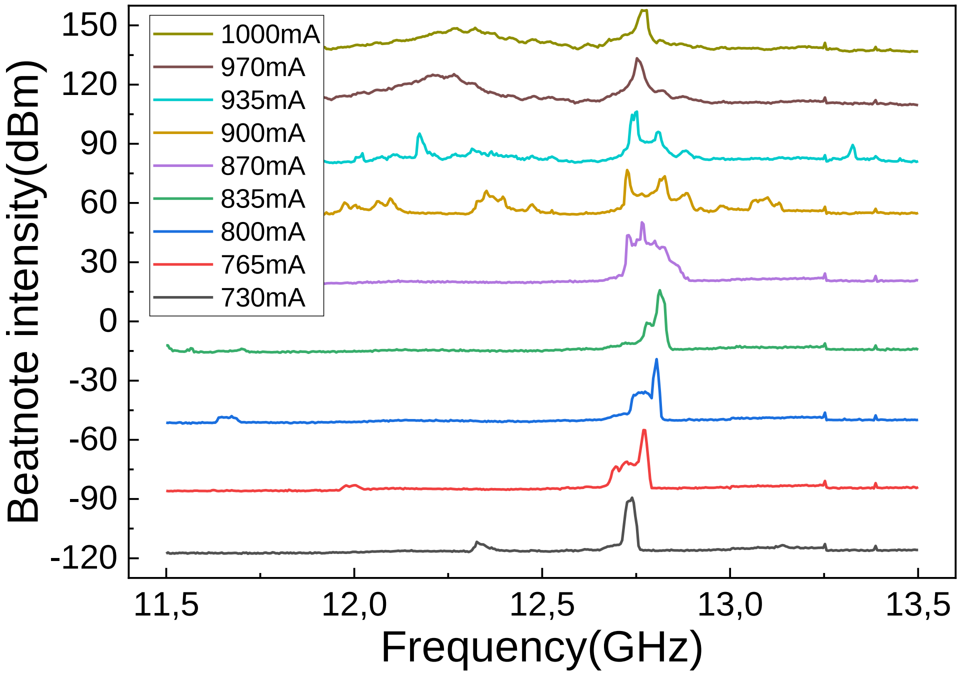

Figure A3.2: Beatnote map of Sample 1 at 20K - 25kHz bias frequency – 5% duty cycle

A3.1.2 LIV and beatnote map of Sample 2

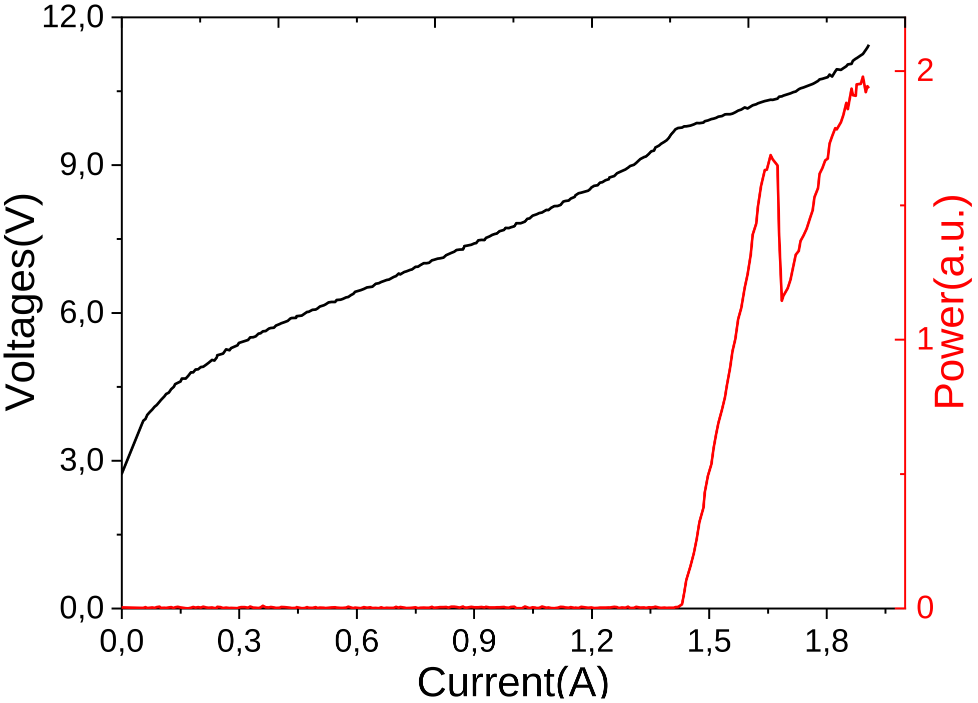

Figure A3.3: LIV of Sample 2 (L1194) at 20K - 20kHz bias frequency – 10% duty cycle

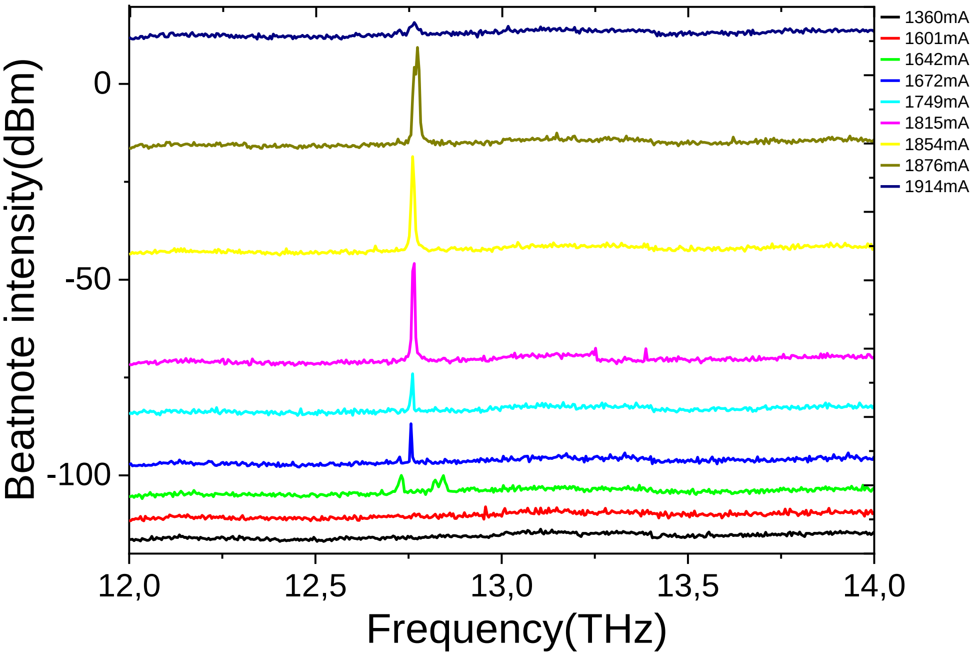

Figure A3.4: Beatnote map of sample 2 at 20K - 20kHz bias frequency – 2% duty cycle

A3.1.3 LIV and beatnote map of Sample 3

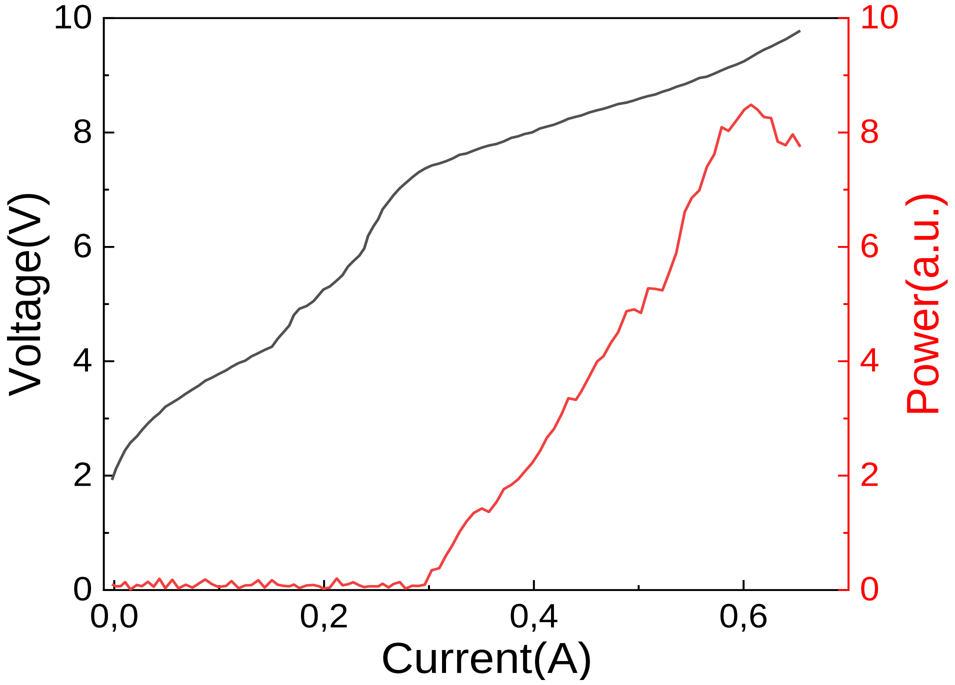

Figure A3.5: LIV of Sample 3 (L1369) at 20K - 25kHz bias frequency – 5% duty cycle

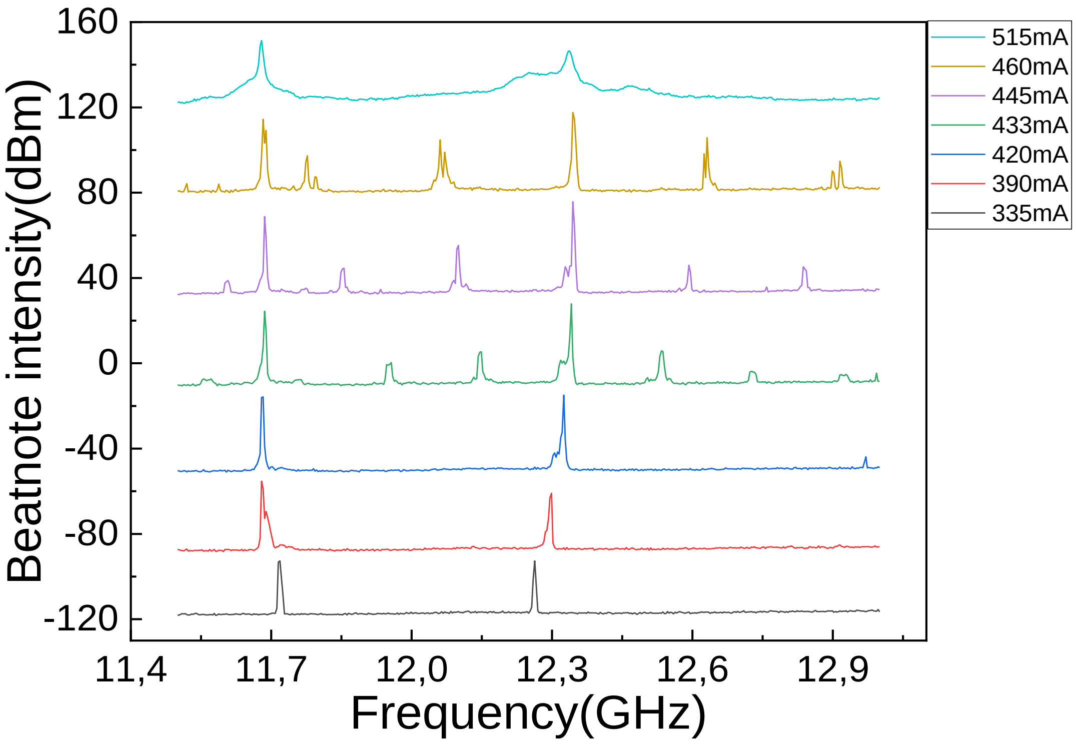

Figure A3.6: Beatnote map of Sample 3 at 20K - 25kHz bias frequency – 5% duty cycle

A3.1.4 LIV and beatnote map of Sample 4

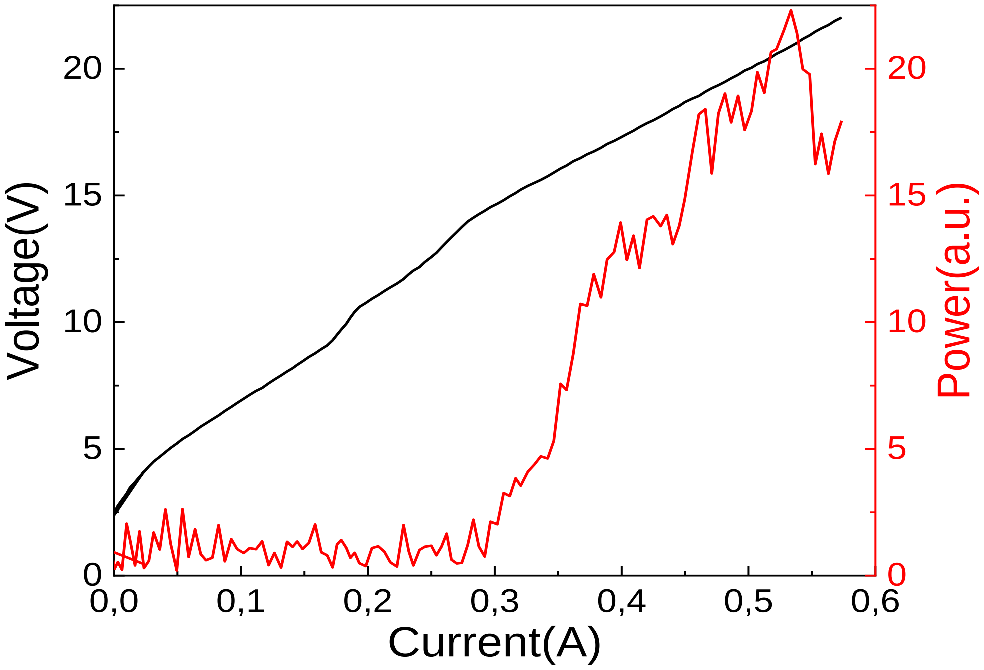

Figure A3.7: LIV of Sample 4 (L1388) at 20K - 25kHz bias frequency – 10% duty cycle

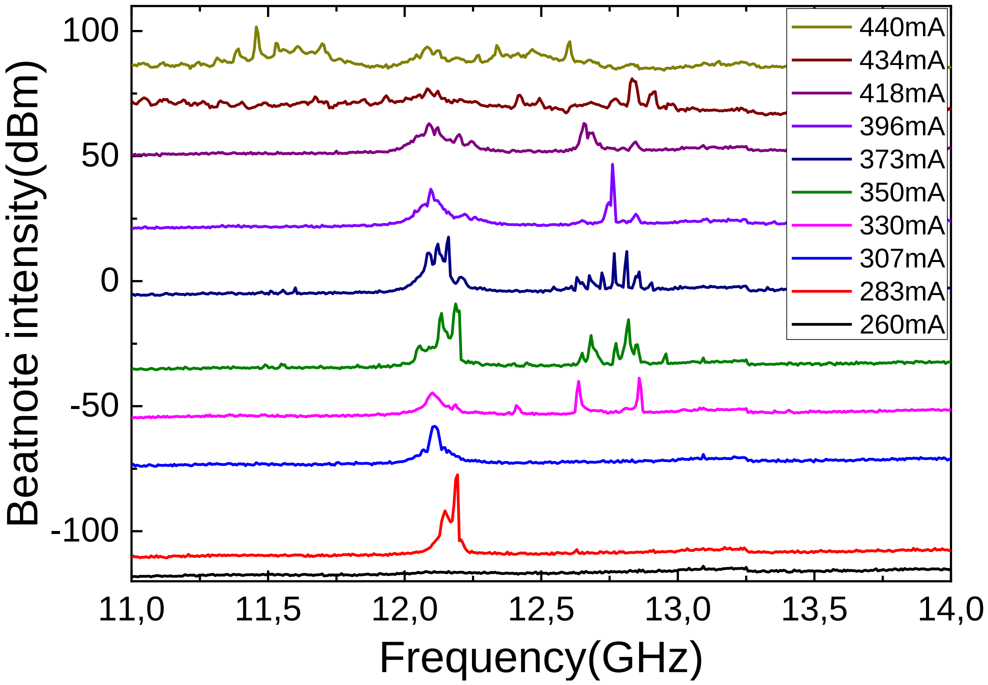

Figure A3.8: Beatnote map of Sample 4 at 20K - 25kHz bias frequency – 5% duty cycle

A3.1.5 LIV and beatnote map of Sample 4/66

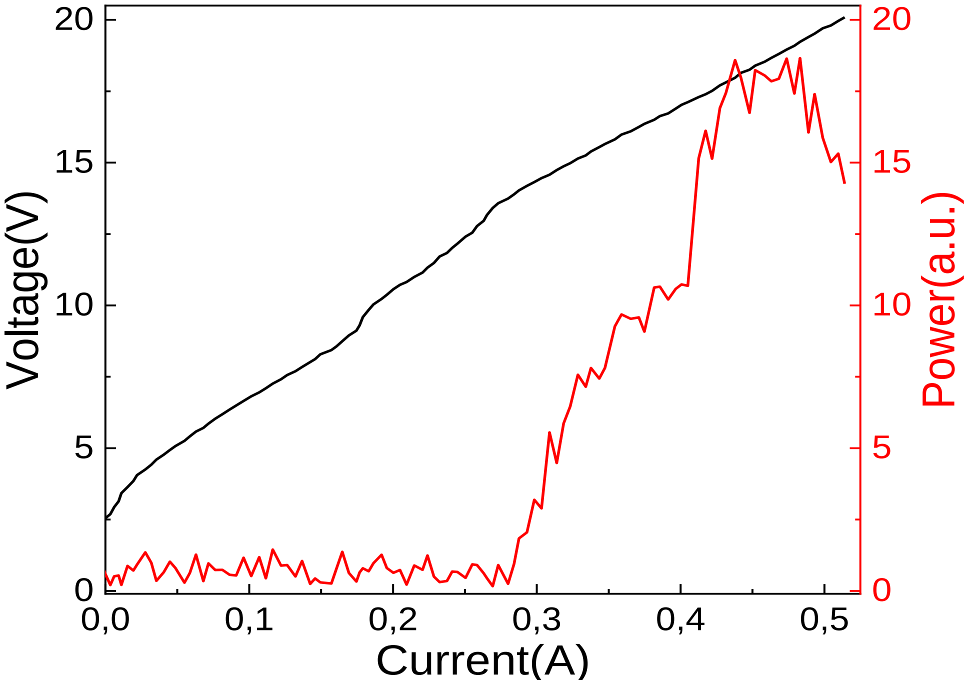

Figure A3.9: LIV of Sample 4/66 at 20K - 25kHz bias frequency – 10% duty cycle

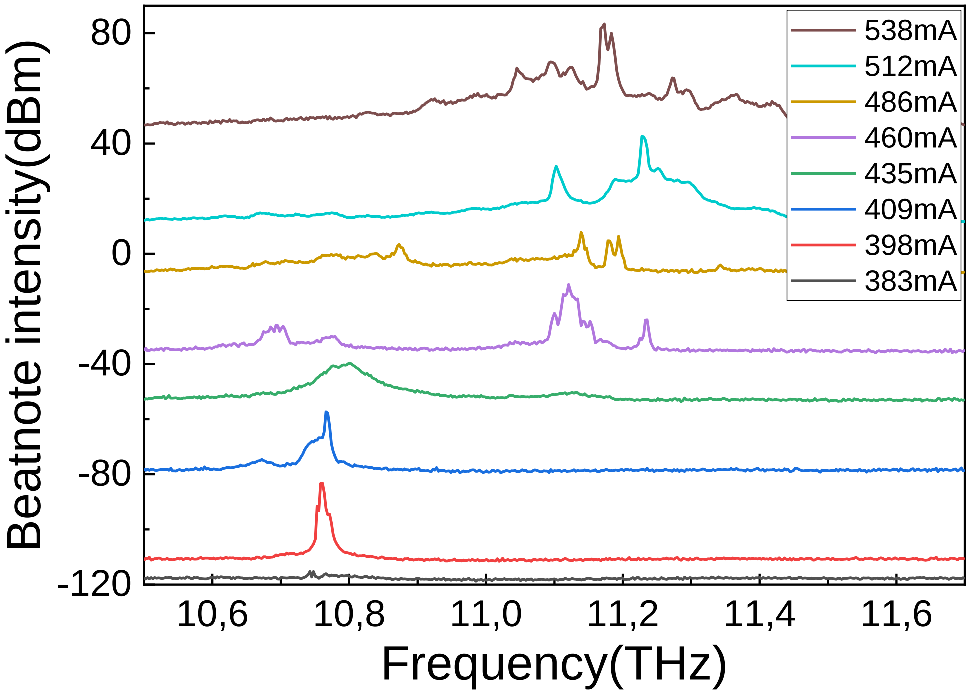

Figure A3.10: Beatnote map of Sample 4/66 at 20K - 25kHz bias frequency – 5% duty cycle

A3.1.6 LIV and beatnote map of Sample 5

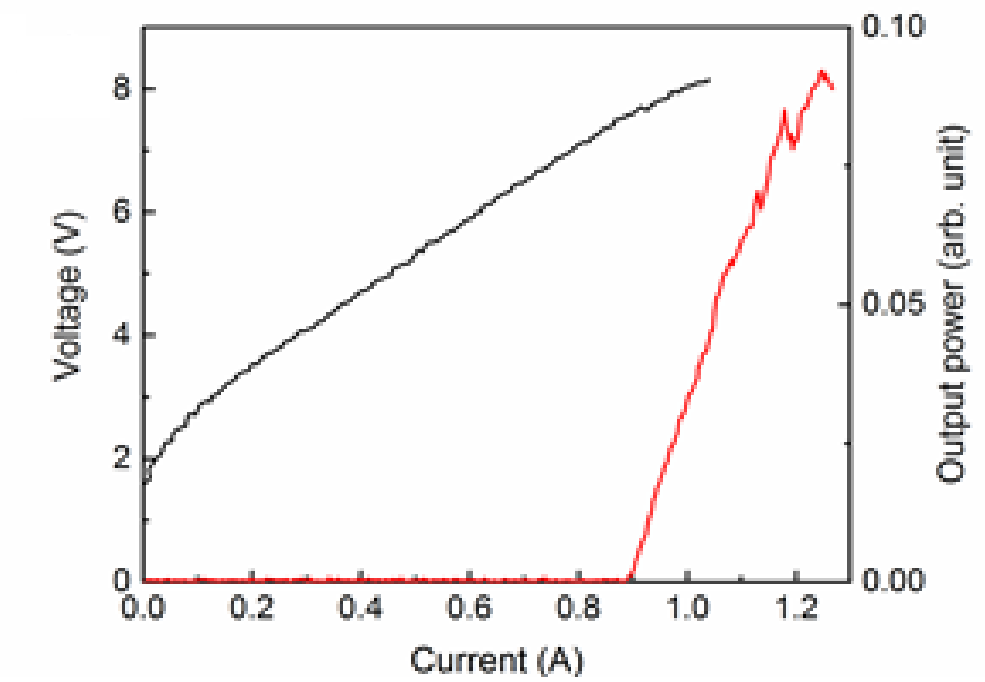

Figure A3.11: LIV of Sample 5 at 20K - 25kHz bias frequency – 5% duty cycle

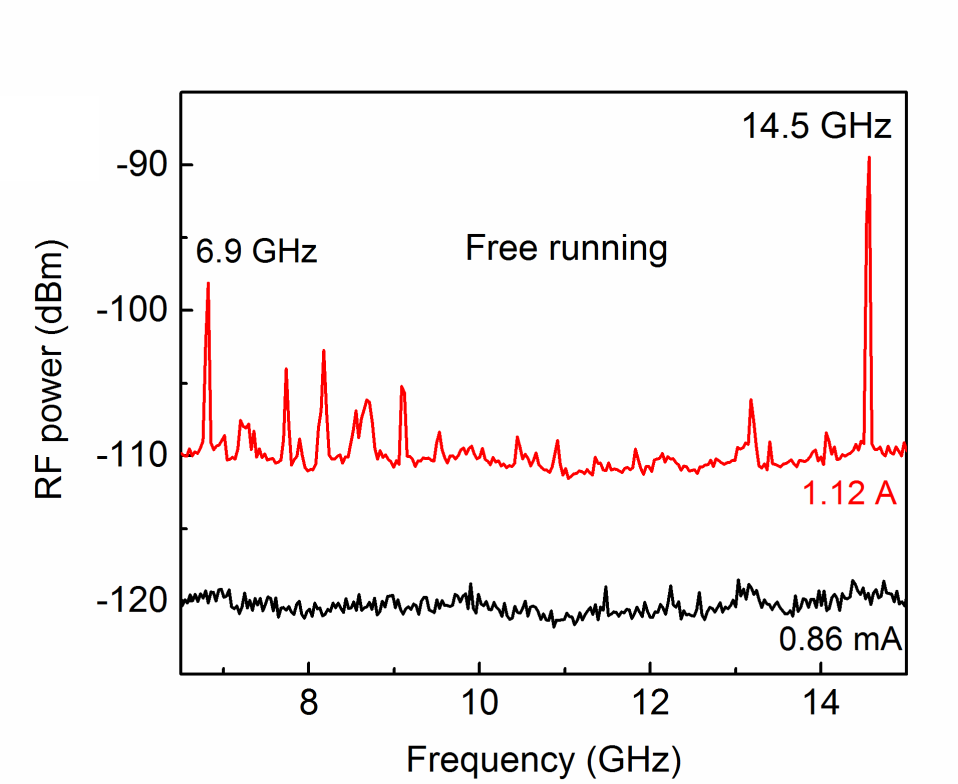

Figure A3.12: Beatnote spectrum of Sample 5 at 20K - 25kHz bias frequency – 5% duty cycle

A3.1.7 LIV and beatnote map of Sample 6

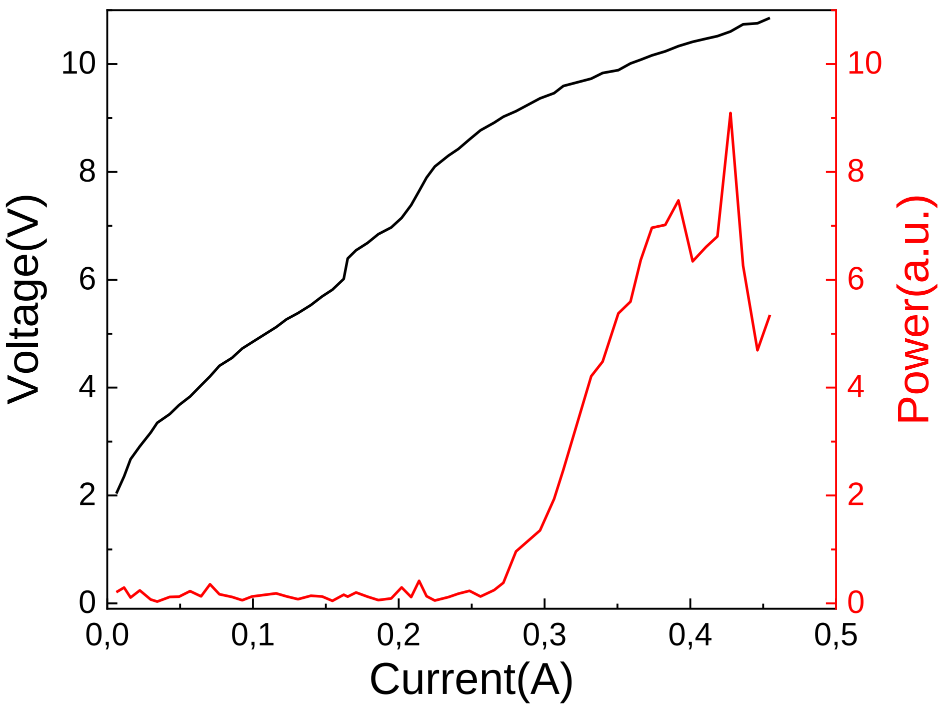

Figure A3.13: LIV of Sample 6 at 20K - 25kHz bias frequency – 10% duty cycle

No beatnote could be found at any bias for Sample 6 up to 20GHz, which is the limit of detection for our spectrum analyzer. This suggests that the device operates at a harmonic of the fundamental beatnote. The experimental results demonstrate that this is the case, and that the modes of the device are separated by three times the fundamental round-trip frequency.

A3.1.8 LIV and beatnote map of Sample 7

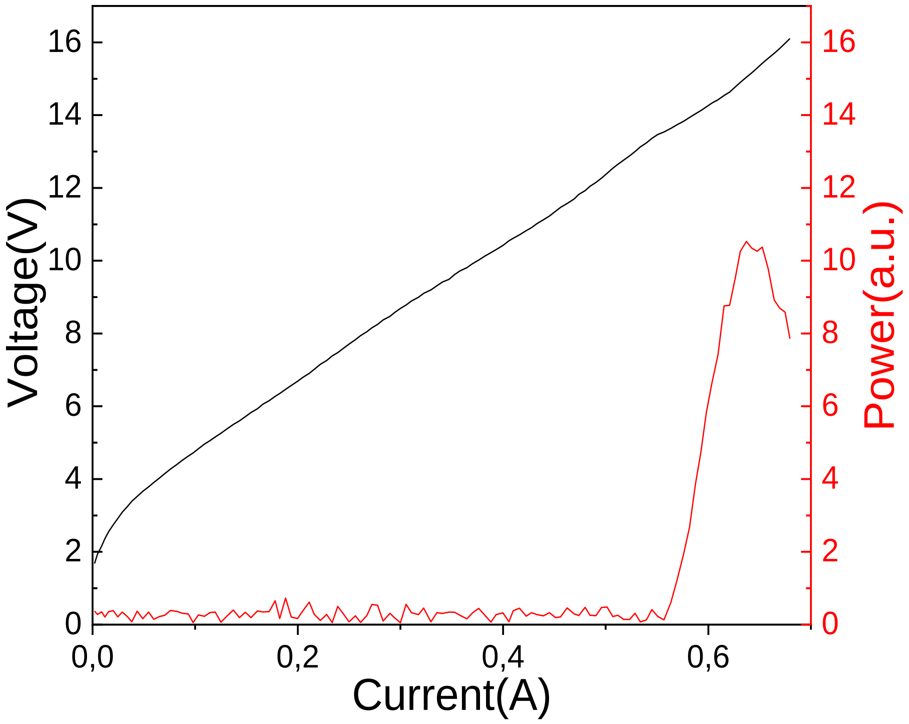

Figure A3.14: LIV of Sample 7 at 10K - 20kHz bias frequency – 9% duty cycle

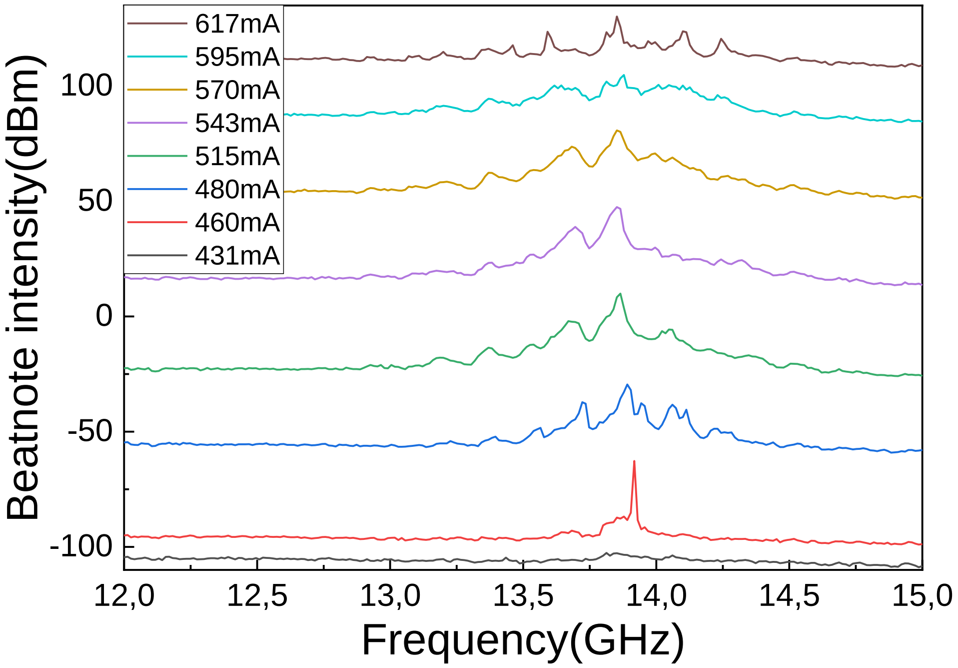

Figure A3.15: Beatnote map of Sample 7 at 10K - 20kHz bias frequency – 9% duty cycle

A3.1.9 LIV and beatnote map of Sample 8

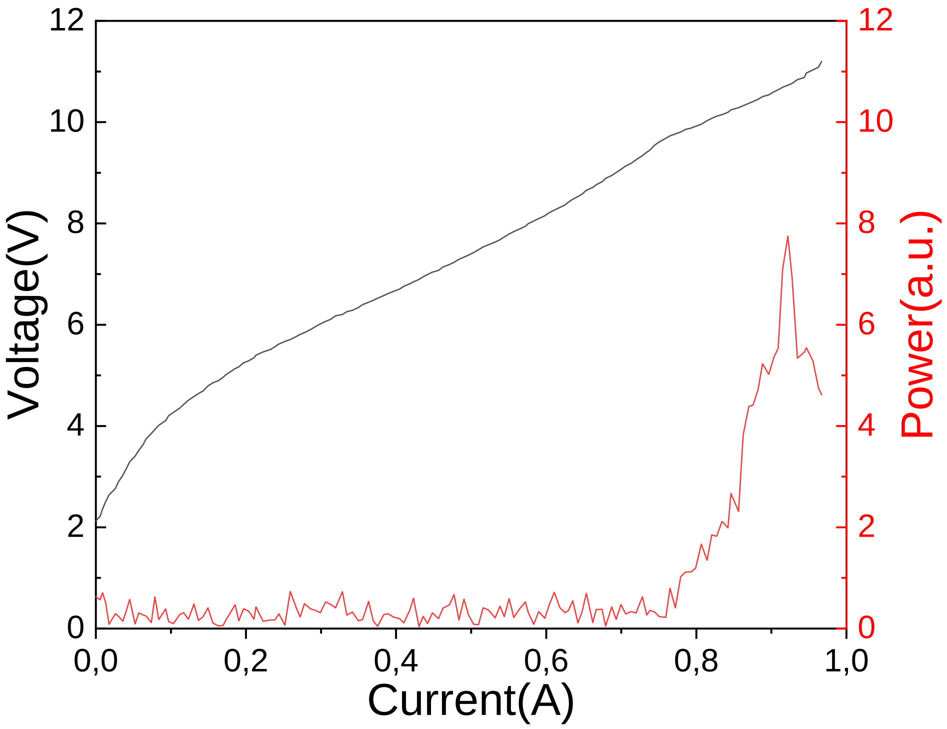

Figure A3.16: LIV of Sample 8 at 10K - 25kHz bias frequency – 10% duty cycle

Since Sample 8 is only 1.5mm long, the expected frequency of its fundamental beatnote is at ~26GHz. No beatnote was found at any bias up to 20GHz that is the upper limit of the bandwidth of our spectrum analyzer.

A3.1.10 LIV and beatnote map of Sample 9

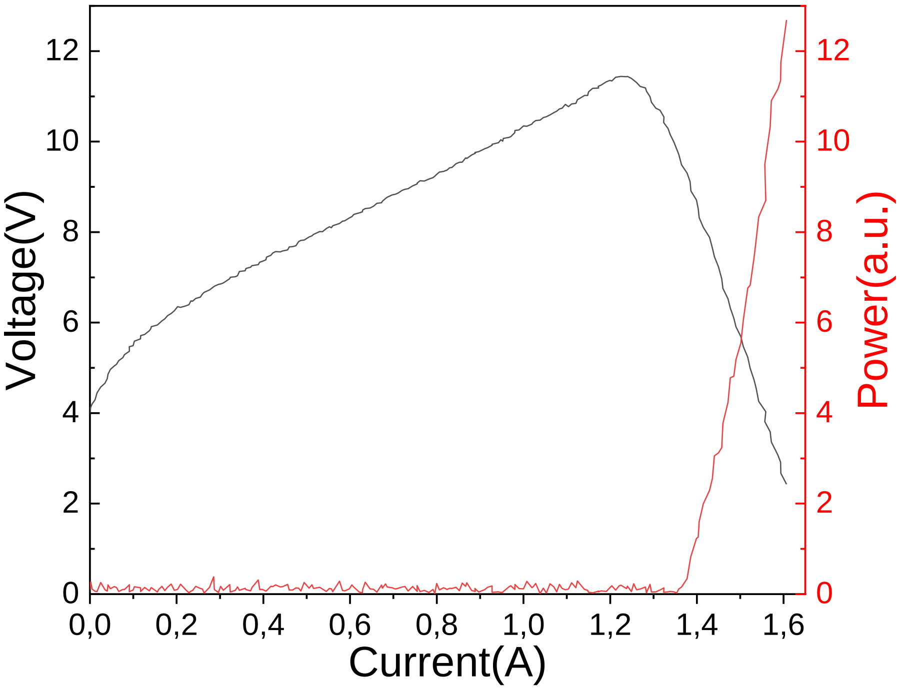

Figure A3.17: LIV of Sample 9 at 10K - 20kHz bias frequency – 6% duty cycle. The voltage drop at 1.2A is related to a malfunctioning of the current probe for high voltages.

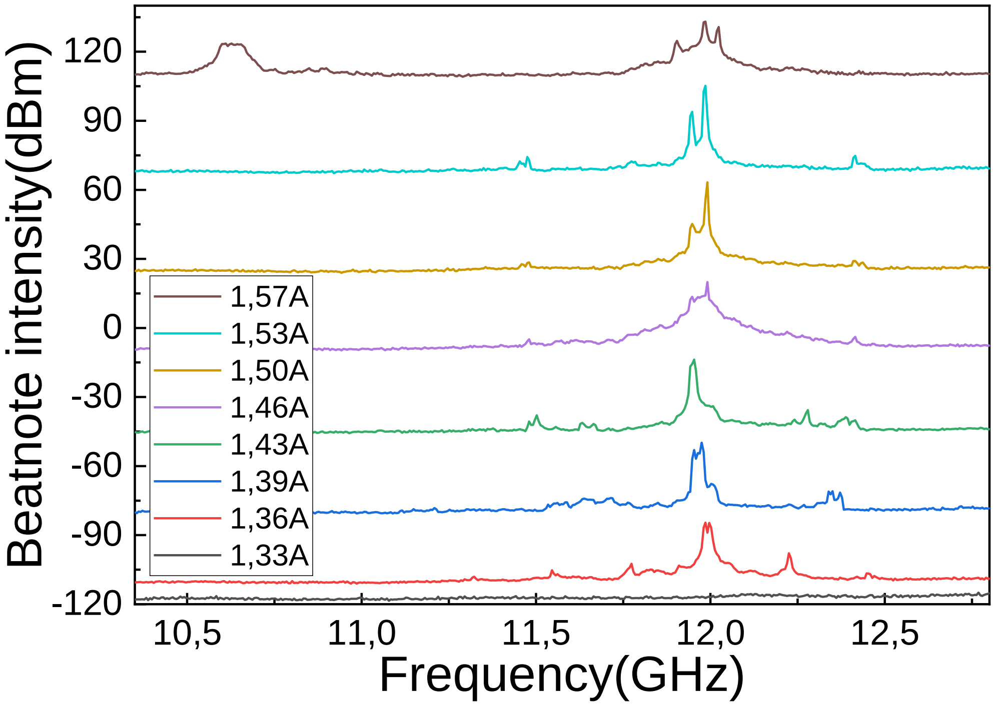

Figure A3.18: Beatnote map of Sample 9 at 10K - 20kHz bias frequency – 6% duty cycle

Annex 4

A4.1 Free-running traces and spectra of Sample 3

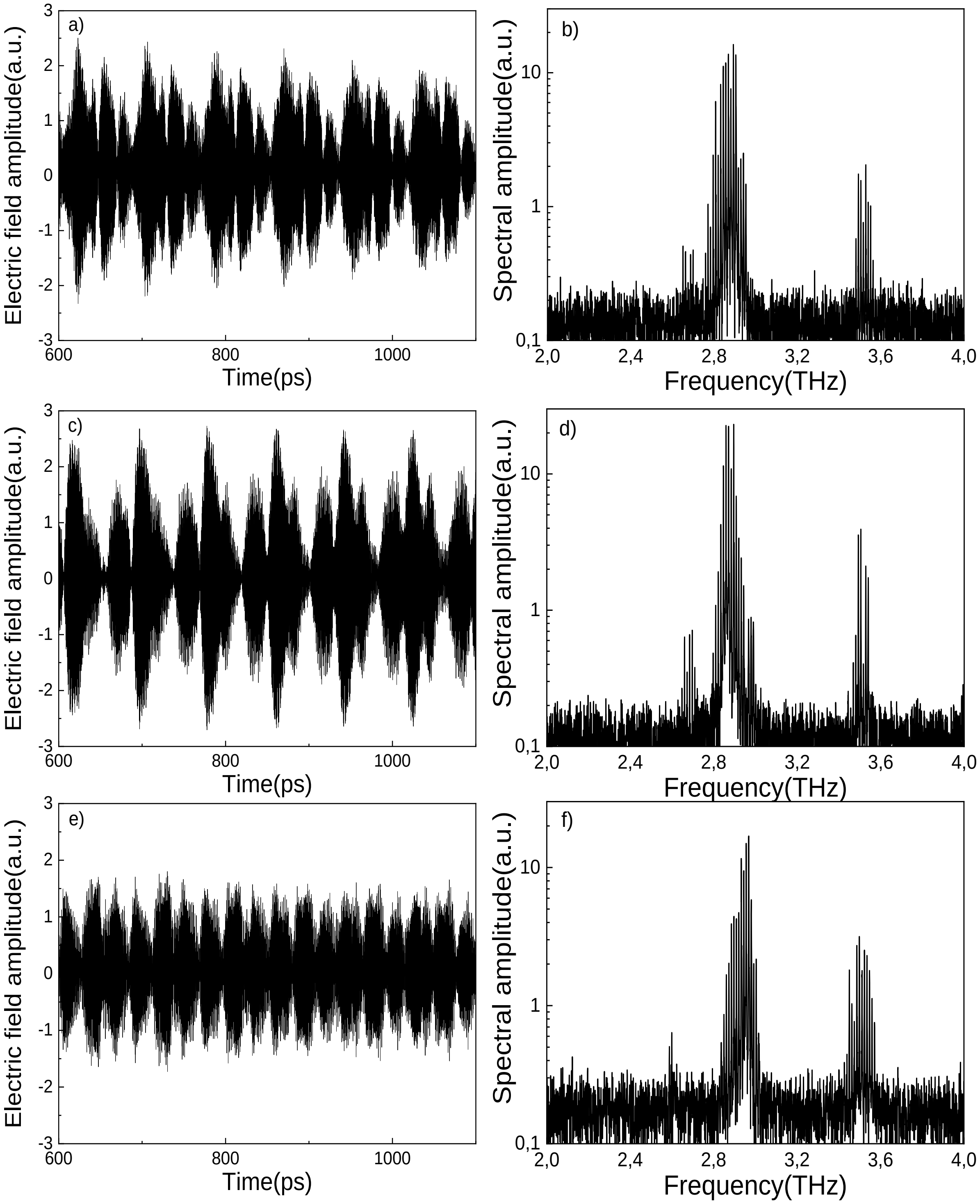

Figure A4.1: Free-running time traces (left panels) and spectra (right panels) for the Sample 3 devices with the 36.1µm (a-b), 37.1µm (c-d) and 38.3µm (e-f) integrated GTI

A4.2 Sample 3 with an integrated 36.1μm GTI – active modelocking time trace

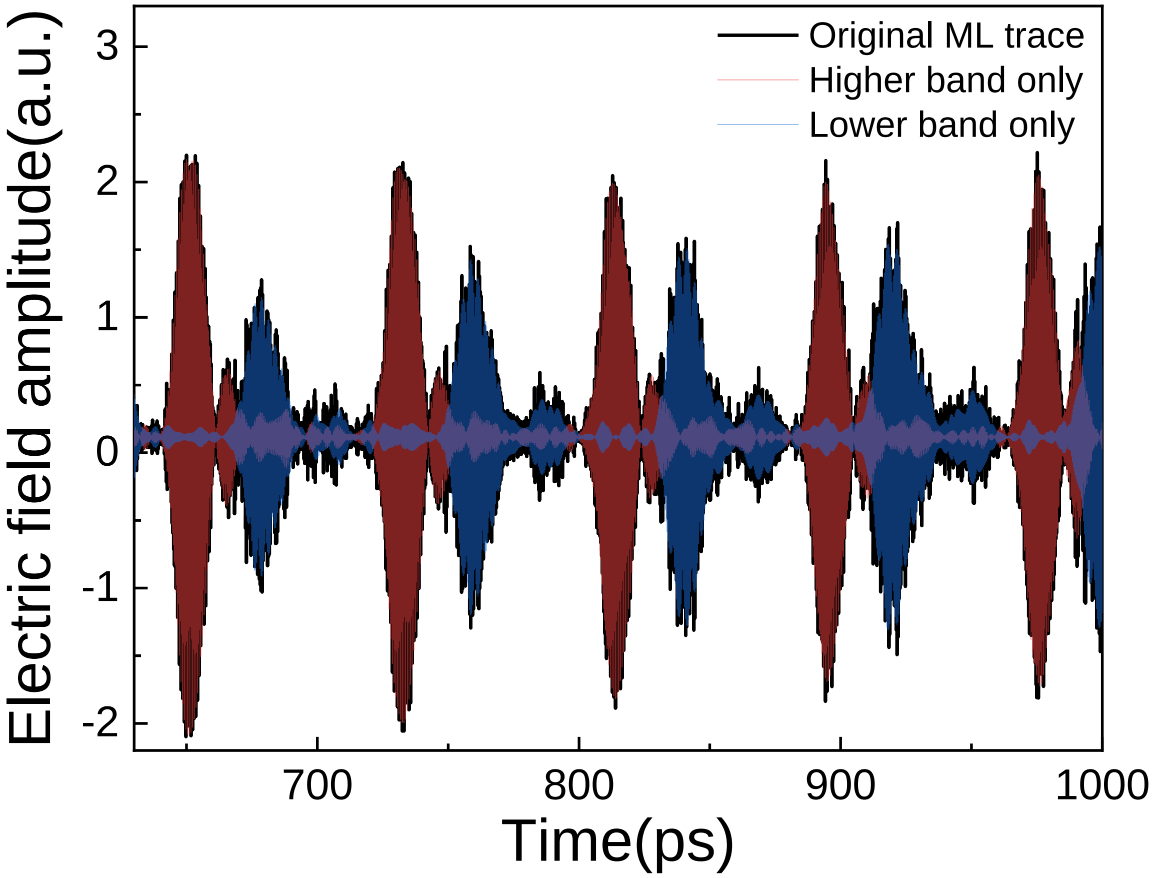

Figure A4.2: Modelocking time trace of Sample 3 with an integrated 36.1μm GTI

This time trace shows the profile of the electric field emitted by the Sample 3 with the integrated 36.1μm GTI. Two pulses per round-trip are visible. When a low pass filter is used to eliminate the upper band of the spectrum of this trace, only the second pulse remains. Vice versa, when only the upper band is kept, the first pulse produces a nice modelocking trace of ~6ps pulses. Since the two bands are separated in the spectrum by the high dispersion region introduced by the GTI, this can be interpreted as a phase offset between the two combs that are produced by the bands of the spectrum. In other words, a constant spacing and a fixed phase offset is enforced by the active modelocking mechanism, but the offset is not the same for both bands. In the time domain this means that the modes of one band will be in-phase at a different time with respect to those of the other. Since we know that a full roundtrip corresponds to a phase rotation of 2π, it is also possible to estimate the difference of their offset phases, which is about 0.638π in this case.

As a side note, it is interesting that the case of this modelocking trace perfectly corresponds to the thought experiments deviced by D. Burghoff et al in [72]. In their work, it was discussed how measurements with a SWIFTS can be used to retrieve time-domain information from the knowledge of the relative phases between the modes of a comb. The presence of spectral gaps, however, make it impossible to know which is the phase difference between the last mode of the low-frequency comb and the first mode of the high-frequency one. Therefore, no way exists to establish unambiguously the time profile in the range where the modes overlap.

Thanks to our TDS measurement, instead, not only it is possible to access this information with extremely high resolution, but its time evolution can also be assessed.

Annex 5

Annex 5.1 – Harmonic emission simulation model

In order to understand the measured harmonic time and spectral behaviour using simulation tools, a model of the quantum cascade laser structure was set up that consists of different gain and absorber regions along the propagation direction. The different regions aim to capture the influence of the microwave beatnote field on the active region. It was found that the setup consisting of a 0.75 mm absorber, 1.5 mm gain, 1.5 mm absorber, 1.5 mm gain, and 0.75 mm absorber captures two characteristics of the measured result, namely the spacing of the different modes (equals $2f_{RT}$) and the distance between the two frequency lobes (15th harmonic).

Quantity	Symbol	Value (Gain)	Value (Loss)	Unit	Source
Refractive index	**n**	3.6	3.6		{4}
Linear Power Loss	α	16	16	cm^{-1}	{1}
Overlap Factor	Γ	1.0	1.0		{4}
Doping Density	**N**	5.585e+15	5.585e+15	cm^{-3}	{4}
Transition Frequency	**f**	2.415	2.415	THz	{5}
Dipole Moment	**d**	4.4	4.4	nm	{5}
Dephasing time	T_{deph}	600	600	fs	{1}
Superlattice time	τ_{12}	30	30	ps	{1}
Lower level lifetime	τ_{31}	3	3	ps	{1}
Upper laser lifetime	τ_{23}	10	2	ps	{1}

Table A5.1: Parameters of the numerical simulation. The source entry indicates how the parameter in question was determined: {4} known material parameter, {5} determined by simulation, {1} chosen in the scope of parameter exploration (range of reasonable parameter values from literature [134]).